UAB
Universitat Autònoma de Barcelona

Bioinspired and Biomimetic Micro/nanoparticles for Medical Applications

Ivana Cavaliere

Universitat Autònoma de Barcelona

Department of Chemistry

Faculty of Science

Bioinspired and Biomimetic Micro/nanoparticles for Medical Applications

Ivana Cavaliere

PhD Thesis

PhD in Materials Science

2023

Supervisors:
Dr. Daniel Ruiz Molina
Dr. Claudio Roscini

Tutor:
Dr. Daniel Ruiz Molina

Memòria presentada per aspirar al Grau de Doctor per Ivana Cavaliere.

Ivana Cavaliere

Vist i plau,

Dr. Daniel Ruiz Molina

Dr. Claudio Roscini

Bellaterra, 30 de Marzo 2023

Abstract

Nature, and in particular the human body, offers countless inspiration sources. Translating its unique properties to synthetic materials has been the driving force of several studies up to today. Biomimetic and bioinspired micro/nanoparticles represent remarkable tools for this aim; however, since the complexity of biological systems, different features and attributes, such as size, shape, and surface properties, need to be evaluated.

The aim of this thesis is to develop a set of several biomimetic and bioinspired particles to address different biomedical problems currently affecting public health. Three main topics have been explored in this thesis.

First, an innovative system has been proposed as a new class of vaccine for bacteria that would represent a precious aid by limiting the spread of the increasing antibiotic resistance. For this, biocompatible polylactic acid microparticles have been developed to reproduce bacteria morphologies; the anisotropic shape of bacteria was evaluated as a biomimetic key factor for the specific stimulation of the immune system. Inspired by *Pseudomonas aeruginosa*, the combination of its structural properties, such as size and shape, with its immunogenicity, obtained by using antigens, has allowed achieving a significant immune activation in an *in vivo* model.

Secondly, powerful therapeutic and theragnostic tools have been proposed for their employment in the fight against cancer. Polymeric particles were combined with bioinspired magnetic nanocubes, and microparticles displaying an ellipsoidal shape, like magnetotactic bacteria, or spherical nanoparticles possessing a liquid core, were separately studied. The responsiveness of both types of particles under the influence of an external magnetic field was evaluated; in the case of spherical nanoparticles, in combination with light responsiveness, it was employed for thermal treatment and nanothermometry, and in the ellipsoidal one, for rotational stimulation.

Finally, neuromelanin-like nanoparticles have been designed as excellent dopamine delivery systems with unique advantages for Parkinson's disease treatment. Supramolecular interaction and metal-ligand coordination have been exploited to develop two different systems, primarily constituted by dopamine. Iron was used as the metal node in both cases due to its biocompatibility and possible use as a contrast agent in magnetic resonance imaging. Outstanding amounts of dopamine were successfully encapsulated with non-covalent bonding, allowing its release. The drug delivery efficiency was further exploited by studying an innovative administration route, the intranasal, *in vitro* or *in vivo.*

Considering the multidisciplinarity of this thesis, each part has been carried out in collaboration with experts in different fields from various research centers.

Table of Contents

Chapter 1

1. General Introduction

1.1 Biomimetic micro/nanoparticles

Nature has always offered sources of inspiration in several fields and for several applications. In material sciences, particularly in nanotechnology, there are countless studies that have employed bioinspired approaches or designed biomimetic materials.[1] Bioinspired strategies aim to reproduce or repeat natural features, not necessarily being equal to them, while biomimetic ones propose to imitate them. Moreover, it has been proposed an additional classification based on two categories; the first one, defined as functional biomimetic synthesis, aims to achieve specific properties of natural materials, while the other, instead, named process biomimetic synthesis, proposes to mimic the synthesis routes or processes of natural materials.[2] Nevertheless, the terminology often overlaps, and "biomimetic" or "bioinspired" have been used interchangeably.

In biological applications, the need to find new bioinspired or biomedical approaches arises from the fact that, despite the outstanding success and studies about nanoparticles, only a few have reached clinical use. This is mainly due to the failure of specific targeting, as to the great ability of the human body to eliminate any foreign materials. However, red blood cells are able to circulate in the bloodstream freely, and immune cells can actively reach a specific site when needed; moreover, viruses or bacteria escape the immune system circulating unnoticed within the body.[3] Inspiration or mimicry in micro or nanoparticles can be towards the materials components and constituents of biological materials, but also to their structure properties, such as sizes and shapes, or their functionalities (Figure 1.1).[3]

Materials:

Synthetic materials, which have been extensively employed for the fabrication of particles thanks to their important advantages, such as flexibility, are generally not biomimetic. Therefore, efforts have been made to find more biomimicking materials in terms of chemical structure or physical properties. The promising new polymer synthesis strategies allow for obtaining more natural-like materials, such as stimuli-responsive polymers, since biological polymer can adapt their structure in function to external stimuli.[4] These properties, for instance, could exploit the potential of particles for controlled drug delivery. Moreover, the combination of synthetic and natural materials, such as peptides or proteins, has been studied as an emerging strategy to obtain responsive biomimetic materials. Furthermore, the ability of natural materials to form supramolecular structures, such as in vesicles, can also be a source of inspiration.[4,5]

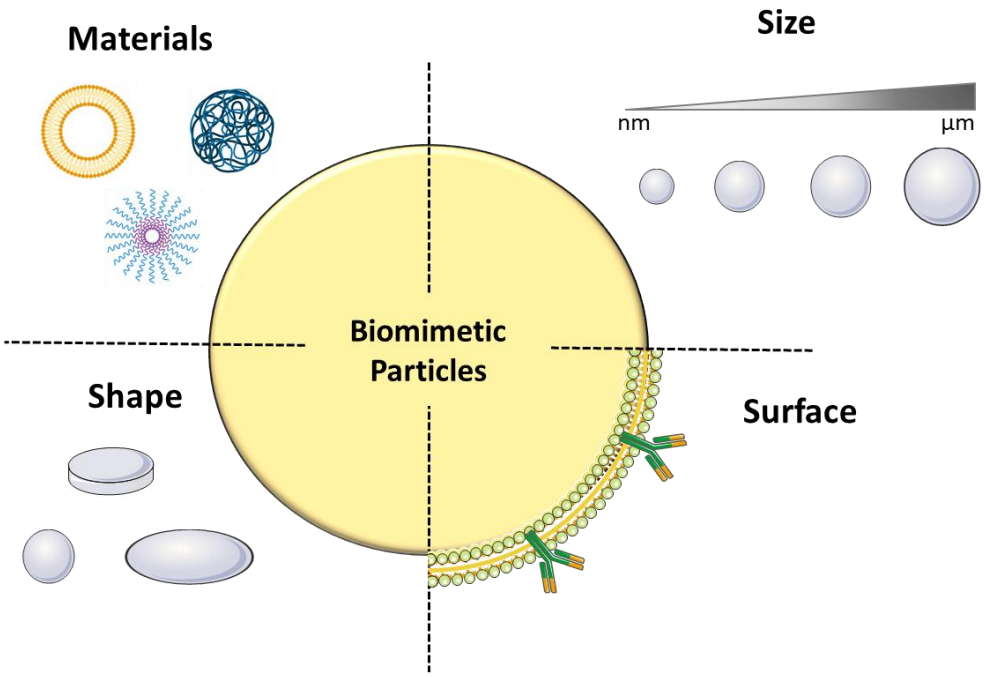

Figure 1.1: Schematic representation of possible biomimetic features in particles.

Size:

The reduced size of particles allows them to be in the same cellular range (microdimension) or even smaller, being able to enter them and take place in biological processes (nanodimension). Some examples of microparticles are the artificial antigen presenting cells (aAPC), which intend to mimic the functionalities of the natural cells, aiming to stimulate the T-cells of the immune system.[6] The immunological system can also recognize the specific size of the pathogens; this is particularly clear if the wide variability of virus size is considered, which could generate a different immune response. Therefore, when a new vaccine, relying on the use of nanoparticles, is aimed to be developed, it is crucial to consider the size of the virus to maximize its efficiency[7]. The aforementioned are just some examples of biomimetic micro or nanoparticles that have been reported up-today.

Shape

The geometry of particles is another inspiration source for biological applications; cells, bacteria, or viruses display a batch of different shapes. Cells interact differently between them or with pathogens, which also depends on their shape. For example, along with a specific size, an anisotropic shape would help on the generation of aAPC. Non-spherical shapes, particularly elongated ones, promote the interaction with T-cells, ascribable to the higher contact surface between them.[8] Moreover, the shape drastically influences the particle's fate in the body; indeed, it has been demonstrated that non-spherical

particles can avoid macrophages internalization.[9] It has been postulated that immune cells are able to recognize their specific target by geometry; this consideration arises from the fact that bacteria present a tremendous variability in terms of shapes, and each of them generates different and specific immune responses.[10] Another bioinspiration for non-spherical shape comes from the red blood cells, which have a discoidal and biconcave shape, providing unique deformability properties. Several studies have been reported with the aim to mimic this peculiar shape, showing how the shape significantly influences particles' biodistribution,[11] having an extended blood circulation time.[12,13]

Surface

Clearly, the surface of nano and microparticles is the feature that mainly affects their interaction with cells. Different strategies have been proposed to obtain biomimetic surfaces to combine the physicochemical properties of synthetic materials with inherited biological functionalities.[14] On one side, by bottom-up approaches, it is possible to decorate the particle's surface with biological molecules, such as lipids and proteins, including antibodies, by chemical modification or physical adsorption to enhance their biocompatibility, blood circulation, and specific targeting;[14,15] other examples are based on the functionalization with antigens obtained by pathogens for vaccine development.[16,17] On the other side, through top-down approaches, it is possible to entirely coat the surface of particles with cellular membranes in order to emulate cells. This emerging approach provides unique properties which would not be achievable by conventional particle's surface functionalization.[10,14] The cell surface coating has been applied for several types of cells, and in general relies on a two-step process, the extraction of the cellular membrane and the combination with particles. Usually, the extraction requires some relatively complex processes to guarantee the elimination of all intracellular components, while the second step can be performed by physical extrusion or by ultrasonication.[14] The most reported example is regarding the coating with red-blood cells membrane or the usage of outer membrane vesicles (OMVs) of bacteria. The former strategy would provide great potential to particles to overcome biological barriers, rendering them free to circulate in the blood vessels and to escape the immune system.[3,18] The OMVs are lipid-bilayer vesicles enriched with various bioactive molecules like proteins and nucleic acids; they are naturally produced by GRAM-negative bacteria and have a diameter between 20 and 400 nm.[19] They exhibit a similar chemical behavior to the bacterium but with reduced immunogenicity and pathogenicity, therefore being considered safer.[14] Both gold[20] and polymer particles[21] have been efficiently coated with OMV, and they have found application for antibacterial vaccine development,[22] antibiotic delivery system,[23] and immunotherapy.[24] Other cell membranes have also been studied for particle's coating.[25,26]

Aryal and co-workers efficiently coated discoidal particles (between 1 and 3 μm) with the isolated membrane of red blood cells,[12] demonstrating high biocompatibility and an extended blood circulation half-life in mice compared to discoidal particles with no coating, as well as showing a unique pharmacokinetics and biodistribution pattern.[12] In a similar work in 2020, Ben-Akiva *et al*. combined the anisotropic shape of particles with cell membrane coating.[27] Particularly, they fabricated ellipsoidal polymeric nanoparticles (240 nm diameter) and subsequently coated them with the membrane extracted from red blood cells. The synergistic effect provided an outstanding reduction of particles clearance from the blood, allowing a better pharmacokinetic profile, which would improve the therapeutic efficiency of an eventual encapsulated drug.[27]

In summary, bionspiration has been a continuous source of novel nanocarriers for drug delivery. However, much work is still needed before full implementations is achieved. In this Thesis we have concentrated mainly in two different families on nanoparticles, more precisely Neumeromelanin and Barteria-like systems. Both are described next.

1.2 Neuromelanin-like nanoparticles for intranasal dopamine delivery

1.2.1 Parkinson's disease and dopamine

Dopamine or 3,4-dihydroxyphenethylamine (DA) plays several important roles as a neuromodulator. DA is mainly produced in the cytoplasm by a two-step synthesis; hydroxylation of tyrosine into levodopa (L-DOPA) and subsequent catalyzed decarboxylation.[28] Once produced, DA is rapidly stored in synaptic vesicles by VMAT-2 proteins, where the acid pH ensures its chemical stability. Under stimulation, these vesicles release their DA content into the synaptic cleft, where the neurotransmitter can bind to DA receptors of post-synaptic neurons or be reinternalized by presynaptic DA-auto receptors.[29] Therefore, the DA level is closely regulated by neurons. When its quantity in the cytosol exceeds, it is promptly converted into less toxic species, the 3,4-dihydroxyphenylacetic acid (DOPAC) and hydrogen peroxide, by monoamine oxidase B enzyme (MAO) first and aldehyde dehydrogenase (ALDH) later. DOPAC is then degraded by catechol-O-methyltransferase (COMT) into homovanillic acid (HVA) once taken up by glia cells (Figure 1.2).[29,30] Of course, DA metabolism is far more complicated, and several other pathways can be undertaken for its degradation. Unfortunately, early progressive death of dopaminergic neurons, mainly in the substantia nigra pars compacta, results in a drastic reduction of DA physiological level in the brain[31] and consequently in Parkinson's disease (PD), the second most common neurodegenerative disorder affecting more than 10 million people worldwide.[32] The common symptoms

of PD are resting tremors, bradykinesia, rigidity, and postural instability. Other non-motor features cognitive impairment and dementia, depression, psychosis, and sleep disturbances, also significantly affect the patient's quality of life.[33]

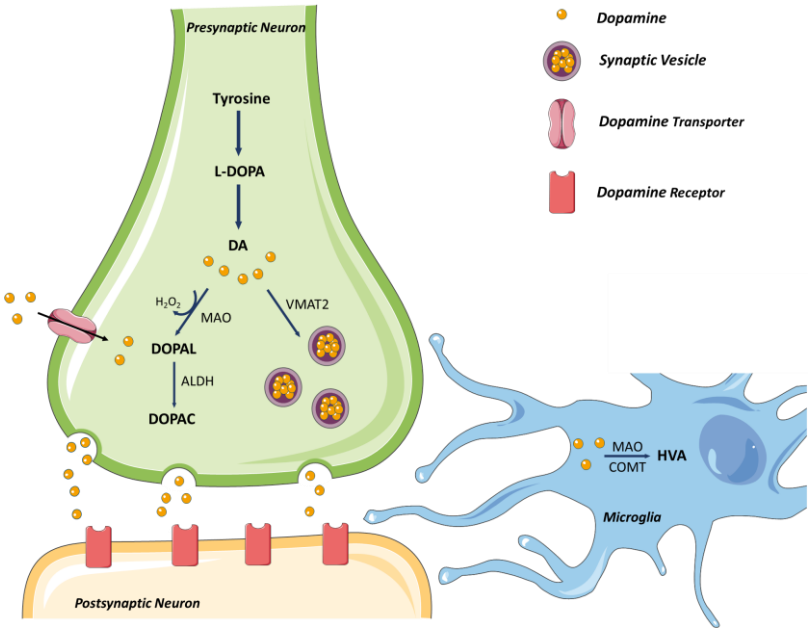

Figure 1.2: Schematic representation of DA metabolism in presynaptic and postsynaptic neurons. *L-DOPA*: levodopa; *DA*: dopamine; *DOPAL*: 3,4-Dihydroxyphenylacetaldehyde; *DOPAC*: 3,4-Dihydroxyphenylacetic acid; *MAO*: monoamine oxidase B enzyme; *ALDH*: aldehyde dehydrogenase; *COMT*: catechol-O-methyltransferase; *HVA*: homovanillic acid. Reproduced and adapted from [30].

The exact causes and the pathogenesis of PD are still unknown, although it is believed that it could be induced by a combination of environmental and genetic factors.[34] Aging is evaluated as a significant common risk associated with neuroinflammation, mitochondrial impairment, and oxidative stress.[35] All catecholamines can be easily and quickly oxidized, with the potential formation of several cytotoxic molecules, including superoxide anions, hydroxyl radicals, and reactive quinones, that could cause cells damages.

Despite the intense research and the considerable number of studies, PD is still uncurable. Current therapies can only ameliorate patients' conditions by mitigating the symptoms. More recent approaches include gene therapy, immunotherapy, behavioral therapy, and the use of DA antagonists or DA inhibitors, like MAO-B/COMT.[36] Nevertheless, the gold treatment chosen nowadays to rebalance neurons' correct functions is DA replacement. However, the direct administration of DA is still challenging as it cannot directly reach the brain. This last one is protected by a biological barrier, mainly

constituted by three types of cells forming strong tight junctions, called the blood-brain barrier (BBB). For this reason, the primary treatment for PD relies on using L-DOPA, a DA precursor that can cross the BBB and shows the ability to alleviate symptoms. However, this precursor is not the drug itself, and it is associated with severe side effects. Its prolonged use is linked with the appearance of involuntary movements, called drug-induced dyskinesia, and motor fluctuations, that in some cases can be more debilitating than the disease itself.[37]

1.2.2 Dopamine nanodelivery systems

It is evident then how crucial it is to find new PD therapies alternative to L-DOPA by efficiently delivering therapeutic amounts of DA. For this, DA encapsulation in nanoparticles or nanocapsules would allow a controlled release over time, reducing doses and increasing the neurons selectivity. Furthermore, as DA quickly oxidizes, it is essential to protect it from the environment to avoid the loss of its therapeutic effect while avoiding toxicity in the surrounding tissues. Finally, whenever a proper nanoparticle size, hydrophobic character, and surface charge are selected, they would also allow crossing the BBB without chemically modifying the drug.[38]

For instance, Laquintana and co-workers functionalized DA-loaded liposomes (182 nm average diameter and an encapsulation efficiency of 35%) with transferrin, whose receptor is localized on the endothelia surface of brain capillaries that form the BBB.[39] The liposomes were able to permeate through an *in vitro* BBB model constituted by an endothelial cell membrane, by exploiting a receptor-mediated endocytosis mechanism.[39] In a similar work, Kahana *et al*. functionalized DA-loaded liposomes (90-120 nm) with a peptide that is recognized by specific transporters located in the BBB and observed a significant increase of DA levels in the striatal of mice, rats, and mini-pigs.[40] Pahuja *et al*. in their work employed poly(D,L-lactic-co-glycolic acid) (PLGA) nanoparticles loaded with DA, which crossed the BBB of a 6-hydroxydopamine (6-OHDA) induced rat model of PD after intravenous administration (Figure 1.3 B).[41] Accordingly, single and double doses of nanoparticles significantly reversed neurobehavioral abnormalities in parkinsonian rats, demonstrating an important therapeutic efficiency of DA-loaded PLGA nanoparticles even though its low loading efficiency (LE) of 12% w/w.[41] In a more recent work, Mortari and co-workers developed DA-containing PLGA nanoparticles (353 and 497 nm) combined with bovine serum albumin (BSA) and a fluorophore marker.[42] The BSA facilitates BBB crossing via receptor-mediated pathways and reduce the clearance of the nanoparticles by reducing the binding of endogenous proteins from blood circulation. With the fluorescent marker nanoparticles were primarily located in the striatum and hippocampal of mice. Moreover, these nanoparticles appeared able

to improve the motor symptoms of lesioned mice (6-OHDA).[42] Finally, Qu *et al.* proposed an innovative encapsulating DA in mice blood exosomes (70-100 nm), resulting in a LE of 15.97% (Figure 1.3 B).[43] These are endogenous spherical vesicles with an inherent ability to cross the BBB, as they expressed transferrin receptors on their surface, while ensuring high biocompatibility and low toxicity. Interestingly, an accumulation of exosomes in the brain of mice after injection was found showing significant therapeutic effects and a reduced systemic toxicity in PD mouse model.[43]

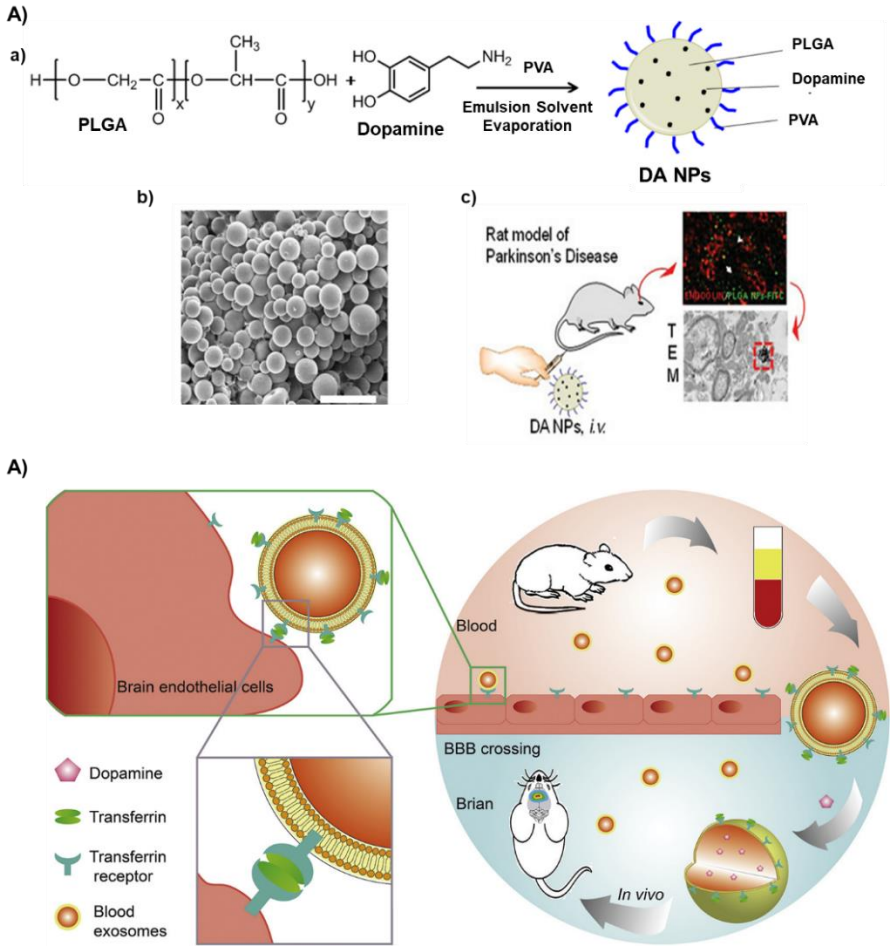

Figure 1.3: A) a) Schematic representation of DA-loaded PLGA nanoparticles (DA NPs)**,** b) Scanning electron microscopy of nanoparticles, and c) schematic representation of intravenous injection (i.v.) of nanoparticles and their accumulation in the brain of mice. (PVA: polyvinyl alcohol, scale bar: 20 µm). Adapted from [41]. B) Schematic representation of DA-loaded exosomes and ability to cross the BBB after intravenous injection in mice by transferrin-transferrin receptor interaction. Reproduced from [43].

All in all, several DA delivery systems have been proposed until today in the literature though all them are still characterized by a reduced DA loading, a real limitation for a prolonged treatment requiring repeated administrations. Therefore, developing novel nanocarriers with enhanced encapsulation yields

while preserving all previously described characteristics remains a main objective. Herein we hypothesize that neuromelanin (NM)-inspired nanoparticles could be an excellent approach to this aim.

1.2.3 Neuromelanin

NM is a natural pigment located prevalently in the dopaminergic or noradrenergic neurons formed upon autoxidation of DA. A tentative formation route is reported in Figure 1.4, where no enzymatic participation is needed.[29]

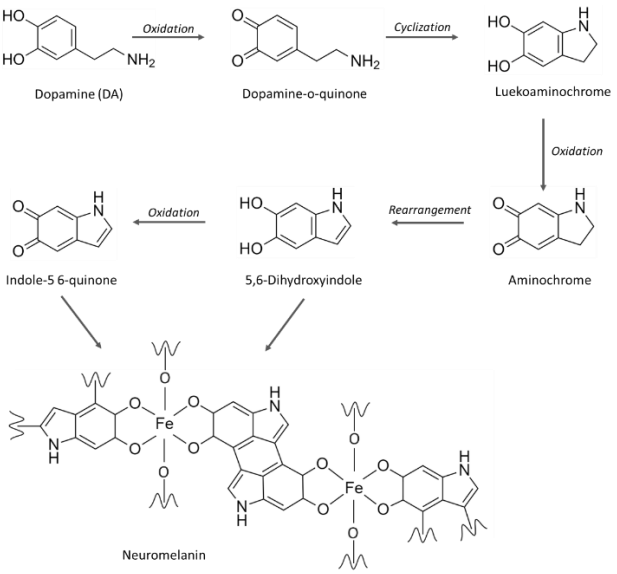

Figure 1.4: Possible oxidative pathway for NM formation and its attempted structure. Recreated from [29].

Its actual physiological role is still unknown, but it seems to act as a complementary protective element subtracting transition metals, like iron, or catechol derivatives and hydroxyl radicals, even though other studies also pointed out that neurons more susceptible to degeneration are the more pigmented ones.[44] In any case, the most relevant feature of these nanoparticles is their high DA content, representing, therefore, a source of bioinspiration for developing novel nanoparticles.

Over time, several synthetic approaches to obtain melanin-based materials have been proposed. Most of them are based on the synthesis of polydopamine (PDA), as they share many physicochemical properties, chemical functionalities, and structural similarities.[45] These nanoparticles exhibit high biocompatibility, long-term stability and can act as a photothermal agent, converting near-infrared radiation into heat.[46] For this reason, PDA has vast applications in several fields, e.g., energy storage systems, environmental technology, and biomaterial science.[47] PDA nanoparticles have been synthesized

starting from DA, in several ways; by its spontaneous autoxidation induced by pH, by its chemical oxidation, mainly induced by sodium hydroxide (NaOH) or ammonium hydroxide (NH_4OH), or by enzymatic polymerization.[48] However, its actual formation mechanism is still far from being well understood, though it is assumed that DA quickly oxidizes and polymerizes, forming different oligomers that interconnect between them by weak interactions, such as hydrogen bonding, van der Waals interactions, and π-π stacking. A good amount of DA also may remain unpolymerized and stacked in polydopamine.[49] On the other side, π-cation interactions between hydrophobic aromatic rings and protonated amines may have a leading role in the progressive assembly of polydopamine.[50] Illustration of possible polydopamine formation mechanisms is depicted in Figure 1.5.

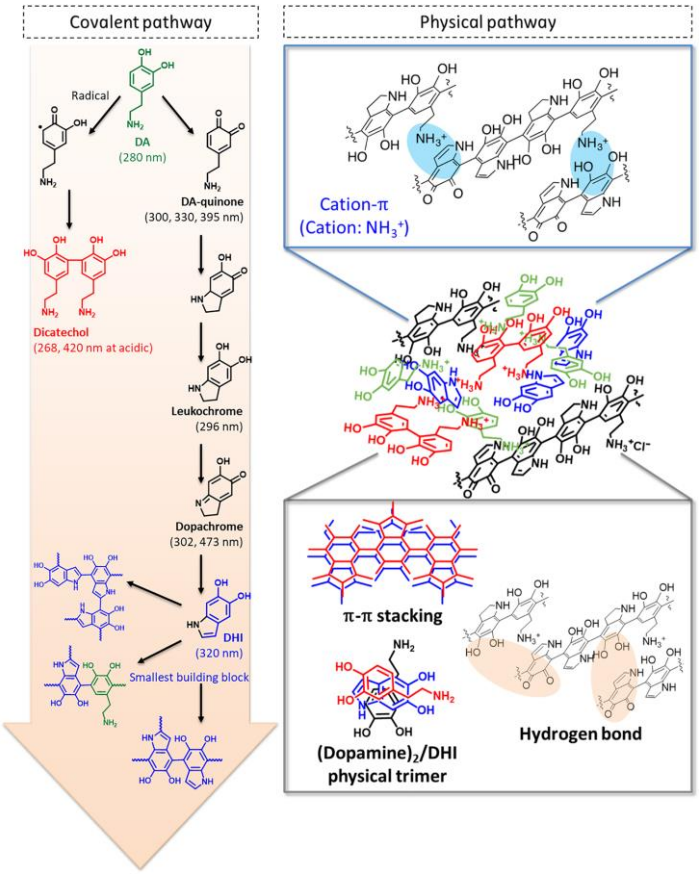

Figure 1.5: PDA mechanisms formation. The oxidation chain of DA with its intermediates and correspondents' absorbance wavelengths are represented, and the covalent polymerization pathway is reported on the left side. The physical pathway is reported on the right side, as the supramolecular interactions of formed oligomers or trimers [50].

Though many examples of PDA-like materials have been described in the literature, there is no iron content in comparison with NM, which entraps high iron contents by coordination with catechol groups and is stored in an inactive form to prevent Fenton's reaction.[51] For this reason, in recent years, new

approaches have been proposed to obtain a new class of melanin-like particles that entrap iron. Among them, three main strategies can be recognized (Figure 1.6):

1. *Post-doping reaction*. Iron (or other metals) is added after the formation of PDA nanoparticles by self-oxidation of DA. Through this method, it is possible to control the morphology and size of nanoparticles. However, despite the use of large excess of iron and long reaction times, the metal loading is difficult to be controlled, as iron can be chelated only at the few access sites close to the surface of nanoparticles.[52] For instance, Zhang and co-workers,[53] and Chen *et al*.[54] reported ultrasmall PEG-coated polydopamine nanoparticles with iron-melanin binding sites available to act as a contrast agent or therapeutic agents against cancer.[53,54]
2. *One-pot or pre-doping reaction*. In this strategy, first iron-DA tris complexes are formed by tuning the pH during the polymerization process, so the nanoparticles are formed by a simple one-pot reaction with continuous metal incorporation, leading to a much higher LE[52]. This strategy does not need template particles and occurs in mild conditions. For instance, Lu and co-workers studied the effect of iron/DA ratio on the chemical structures of nanoparticles by a comparison with empty polydopamine ones.[55] Alternatively, Wang *et al*., incorporated different metals and studied the reaction conditions, such as the reaction time, iron and DA concentrations, and pH, for tuning the iron content, morphology, and size of nanoparticles.[56] This strategy has been widely applied due to its ability to increase and modulate the doping levels of iron in nanoparticles[57,58]
3. *Metal-ion exchange reaction*. This strategy was developed by Gianneschi group, and it consists in the use of manganese-chelated PDA nanoparticles as a stable precursor and then using another metal, like gadolinium, as the replacement source. This strategy allows to obtain uniform nanoparticles with good stability.[59] This method is a complementary strategy to the pre-doping one, and it could be extended to several other metal ions; however, the exchange metal should have a stronger binding affinity than the pre-doped one.[52]

A schematic representation of the three approaches is shown in Figure 1.6. All in all, different approaches have been reported for the synthesis of NM-like nanoparticles; however, as previously described, all of them involved the reaction of DA, so they cannot be used for its controlled delivery. To overcome this limitation without losing all the advantages and positive features of NM, in this work we propose the use of iron-DA supramolecular nanoparticles.

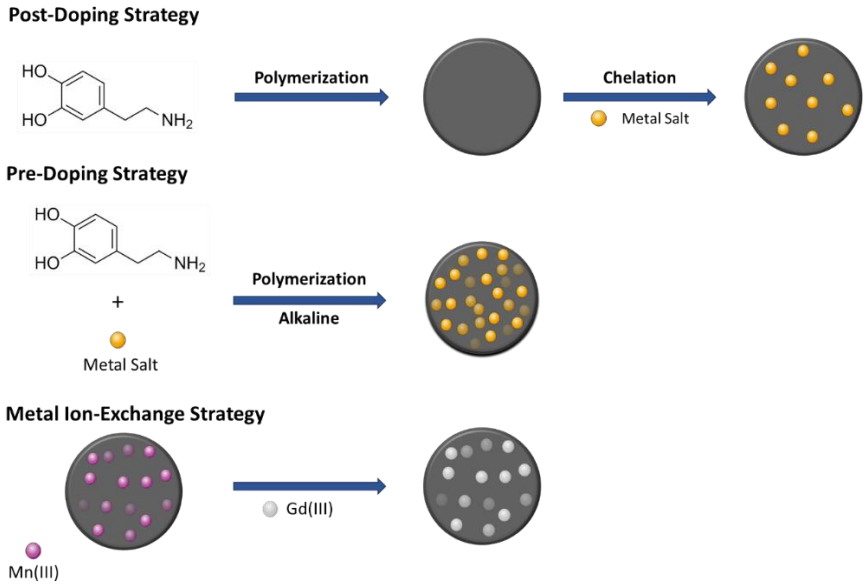

Figure 1.6: Schematic representation of the three general synthesis strategies for NM-like nanoparticles chelated with metal ions. Reproduced from [52].

1.2.4 Supramolecular nanoparticles

Supramolecular nanostructures are generated by noncovalent interactions among building molecules via bottom-up spontaneous and tunable self-assembling. Thus, it is possible to avoid multiple synthesis steps and complicated purification processes typical of other nanosystems. Furthermore, the reaction solvent is usually water, especially when biological molecules are involved, making the synthesis green and with a reduced cost.[60] In any case, supramolecular nanoparticles are characterized by a thermodynamic equilibrium, in which they continuously assemble and disassemble upon small changes in the ambient conditions, offering a unique advantage for drug delivery. The minimum shift in pH, ionic strength, temperature, or solvent polarity, can drastically result in the disruption or change in the structure of nanoparticles.[61] Moreover, their morphology, such as size and shape, can be easily and precisely modulated by the molecular design or assembly condition.[62,63]

The different noncovalent interactions that can be used with this aim are shown in Figure 1.7. Supramolecular interactions can be of different nature, involving hydrogen bonding, π-π stacking, van der Waals forces, hydrophobic interactions, electrostatic interactions, metal-ligand coordination, and host–guest chemistry. For instance, countless studies have employed hydrophobic effects to obtain supramolecular nanoparticles, using amphiphilic molecules that spontaneously self-assemble in water to form nanostructures, such as micelles, liposomes, polymersomes, among others.[64] As for electrostatic

interaction, layer-by-layer is the most followed method to obtain supramolecular nanoparticles through the consecutive deposition of charged polymers (polyelectrolytes). Furthermore, by properly choosing polyelectrolytes, it is possible to modulate the final surface charge of the nanoparticle so colloidal stability.[65] Another approach is host-guest interaction consisting in the inclusion of a molecule, the guest, into another one, the host, through a facile and reversible manner led by noncovalent interactions. The host-guest complexes are in a thermodynamic equilibrium with continuous formation or dissociation depending on the properties of the host and guest, but also on the environmental conditions.[62] Macrocyclic host molecules, particularly cyclodextrins, are undoubtedly the most used in host-guest chemistry. Thanks to the typical cone-shaped structure and the hydrophobic interior, it can act as host molecule allowing the inclusion of different hydrophobic molecules.[66] The size of the guest molecule is important for a proper interaction with the host, as it can incur in satirical obstruction if too big, or they cannot efficiently interact with each other if too small.[64] Another approach is based on using the drug as a building unit. In this case, as the majority of commercially available drugs are hydrophobic, the drug can directly self-assemble and form nanoparticles, acting as both drug and drug carrier. The formation and the final properties would depend only on the drug itself.[61,63]

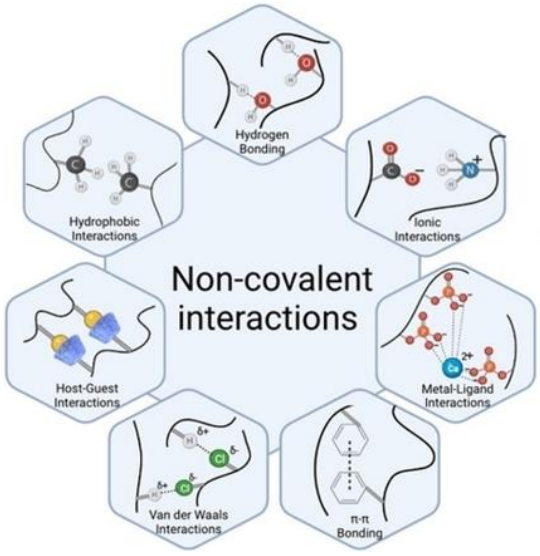

Figure 1.7: Schematic representation of supramolecular interactions [67].

One of the most explored categories of supramolecular nanomaterials is the one constituted by recoverable hydrogels, in which crosslinking is made by hydrogen-bonding or electrostatic interactions. The final structure and properties can be fine-tuned with different crosslinking interactions obtaining a highly hydrated three-dimensional network with exceptional biocompatibility and unique mechanical

properties suitable for drug delivery or tissue regeneration.[67] For instqnce, chitosan has been employed for hydrogel synthesis as its excellent biocompatibility. Trapani and co-workers preprepared chitosan nanoparticles loaded with DA by ionic gelation method; nanoparticles showed the ability to cross an MDCKII-MDR1epithelial cell monolayer, recommended as an *in vitro* model for the human BBB. Furthermore, they found a prompt and pulsate release of DA in the striatum of rats after intraperitoneal injection.[68]

Liposomes are another excellent example of supramolecular nanoparticles; thanks to their intrinsic biocompatibility and easy preparation, they have been studied for several years. Furthermore, they have already been approved by FDA, and have passed numerous clinical trials.[69] Both hydrogels and liposomes have been employed for DA delivery. Trapani *et al*. used liposomes to protect DA from oxidation to demonstrate their potentiality as a delivery system. They corroborated the neurotransmitter location in the core of the lipid particles, leading to complete oxidative stability for DA. However, the encapsulation efficiency was very low (~7% w/w).[70] Kahana *et al*., instead, functionalized liposomes with a specific peptide, able to be recognized by receptors of the blood-brain barrier (BBB), having a direct delivery of DA.[40] The authors synthesized 100 nm liposomes with DA content of around 10-15 µg for mg of nanoparticles. They demonstrated the ability of their system to deliver DA to the brain of mice after intra-peritoneal injection.[40]

Finally, another class of supramolecular nanoparticles that have received significant attention for biomedical applications is constituted by nanostructured coordination polymers (NCPs). These nanoparticles are formed after the coordination of metal ions with organic ligands and their self-assembly at the nanoscale.[71] Remarkably, the drug or biomolecule of interest can constitute one of the main building blocks of NCPs, ensuring a high loading efficiency. Herein we hypothesize that the synthesis of DA-containing NCPS in high contents would represent a novel and efficient therapeutic tool for PD and all the associated benefits, including higher therapeutic efficacy and doses reduction.

1.2.5 Intranasal administration

Finally, in addition to the proper selection of the nanocarrier, the delivery approach turns out to be also very relevant. Among them, the non-invasive intranasal administration (IN) route is getting increasing attention as a direct access to the brain through the trigeminal and olfactory pathways while avoiding the BBB. Accordingly, it is expected to favor dose reduction, enhanced drug safety, and rapid onset of action. Even more importantly, IN drug delivery avoids gastrointestinal and hepatic elimination, drastically reducing side effects and enhancing drug efficiency compared with conventional

administration routes.[48] The real and exact mechanism in the nose-to-brain delivery is still not fully elucidated. Most probably, three main pathways are involved: the systemic, the olfactory nerve, and the trigeminal nerve pathway (Figure 1.8). The first pathway is considered an indirect route, and it occurs when drugs are directly absorbed by the nasal cavity's vascular system and transported in the systemic circulation. Here, drugs undergo a mechanism like intravenous injection, and they can cross the BBB if their properties allow them. Alternatively, the axons of olfactory sensor neurons directly extend in the olfactory epithelium, where drugs can access the brain mainly by (i) paracellular pathway between epithelial cells or extra-neuronal transport; (ii) intracellular pathway after internalization into neurons, and (iii) transcellular transport through epithelial cells. The paracellular and extra-neuronal pathways occur especially thanks to clefts left by the continuous turnover of olfactory cells, which is considered the predominant and faster ones. The intracellular pathway can take place within some hours after administration, being a much slower process, more likely it is not significantly involved in the transportation of drugs to the brain (Figure 1.8).[72,73] Finally, two branches of the trigeminal nerve directly innervate the nasal cavity, being a possible direct access to the brain for drugs.[74] Here again, both intracellular and extracellular transportation may be involved. This last mechanism has been less studied and is considered less relevant.[72]

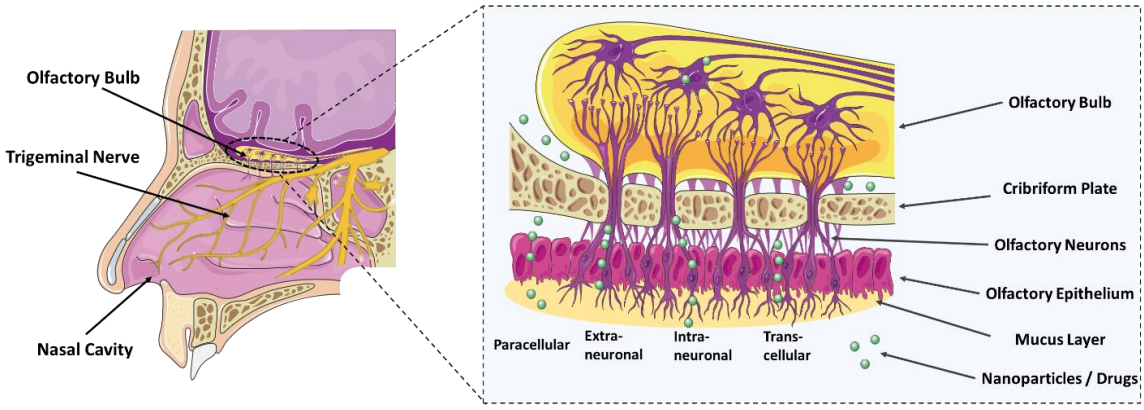

Figure 1.8: Illustration of direct nose-to-brain administration. Nasal cavity representation (left), and internalization mechanisms of nanoparticles through the olfactory bulb (right). Reproduced from [75].

Despite the numerous advantages of intranasal administration, not every drug can reach the brain, mainly due to its enzymatic degradation and the physical clearance mechanism. The first line of defense that particles encounter when entering the nasal cavity is the mucus, which is highly present in the nose. Mucus is a viscous, highly hydrated (more than 90% of water) gel constituted by mucins - a heterogeneous group of glycoproteins with high molecular weight- and a small fraction of lipids and

salts. It forms a three-dimensional network with variable mesh dimensions, around 20-200 nm. Inhaled particulates, or foreign pathogens, are entrapped in the mucus and transported by ciliated cells to the nasopharynx to be swollen and then deactivated by acid and enzyme-mediated lysis. This process represents mucociliary clearance, the primary protective mechanism. Usually, it is a fast and continuous process, taking around 15 minutes. [74,76] So, to have a proficient intranasal delivery system, the retention time in the nasal cavity must be modulated to reach the olfactory and trigeminal nerves. It must permeate enough time adhered to the mucus in order not to be immediately expelled by exhalation; but at the same time, it has not to remain stacked in it, to not be removed by mucociliary clearance.

Several parameters, like composition, size, surface chemistry, or hydrophobicity/hydrophobicity properties, can be tuned to obtain mucoadhesive or mucopenetrating nanoparticles. The surface chemistry of nanoparticles, particularly their surface charge, appears to be one of the more influential parameters. The mucus presents an overall negative charge at the native pH, due to the isoelectric point of mucins.[77] Positively charged nanoparticles are expected to interact closely with mucus through electrostatic interactions. Furthermore, hydrophobic nanoparticles can present enhanced adhesion thanks to their interaction and formation of hydrophobic bonding with domains of mucins. Many studies have employed natural polymers to modify the surfaces of particles, for instance, with chitosan to have mucoadhesive systems or with polyethylene glycol to have mucus-penetrating properties.[78] Size has been shown to affect mucus interaction as well. However, its role appeared to be tricky and dependent on multiple factors. In principle, smallest particles could diffuse better in the mucus mesh and easily interact with it, even though larger particles are known to have increased retention. However, when the dimension of particles reaches the micrometer range, they could incur steric obstruction, preventing their mucus penetration. However, the relation between size and the enhanced penetration properties appears not to be linear with particles dimension; this is presumably related to the high heterogeneity in size and morphology of mucus mesh. For example, small particles can remain entrapped in mucus dead-end pockets and be removed by mucus turnover.[79]

Up today, few examples of IN DA administration or DA delivery have been reported, demonstrating that DA itself has the ability of reach the brain following the olfactory pathway.[80] Fewer studies have reported of DA delivery systems for IN. For instance, Tang *et al*., functionalized polymeric nanoparticles with borneol and lactoferrin as strong biological ligand. Nanoparticles with average dimensions of 175 nm and entrapment efficiency of 25% w/w were intranasally administrated in rats restoring striatum lesions while decreasing apomorphine-induced contralateral rotations.[81] Trapani et. al studied different chitosan nanoparticles as potential carriers for the direct nose-to-brain delivery of DA. Chitosan, along with its mucoadhesive properties, can induce the tight junction opening between apical cells. In their

work, the authors obtained particles with different sizes, ranging from 214 nm to over 1000 nm, and DA association efficiency (from 19 to 54% w/w). They chose the best formulation as the one with the closest pH to the nasal cavity one, and intranasally administered it to rats. They found that the repeat administration of chitosan nanoparticles in the right nostril resulted in a significant DA increase in the right striatum, almost up to 46% compared to the left one.[82]

1.3 Bacterium-like particles against antibiotic resistance

1.3.1 Antibiotic resistance: the use of vaccines for its prevention

Antibiotic resistance is considered one of the major health threats globally, already causing hundreds of thousands of deaths yearly.[83] Moreover, the problem is worrisome, and it is projected to cause more than 300 million deaths in the next 30 years.[84] Antibiotic resistance can be due to innate resistance, which is the bacteria's inherent lack of susceptibility to antibiotics due to a genetic modification with no contact with the drug. This modification can be spontaneous or inherited by a horizontal gene transfer (the acquisition of foreign DNA). In the presence of an antibiotic, the mutant bacteria have a higher survival rate than the rest of the population, leading to proliferation. Furthermore, they can spread in the same individual or be transferred to other organisms.[83,84] Conversely, secondary or acquired resistance can be developed, which occurs after the interaction with antibiotics. In this case, the responsible genes are not located in chromosomes but in small DNA molecules present in the cytoplasm, known as plasmids. These molecules can be transferred among bacteria mainly by conjugation and transduction (direct contact of two bacterial cells or the involvement of bacterial virus, respectively) and can contain more resistance genes for different antibiotics.[83,84]

The mechanisms by which bacteria actuate antibiotic resistance can be different, such as the direct prevention of its access, by reducing the membrane permeability or increasing its efflux, by inactivation due to chemical modifications, or by directly modifying or protecting the target.[85] Finding new strategies to avoid antibiotics is crucially needed, being as well one of the major global challenges for public health.

An important and powerful aid in this fight is represented by vaccines. Vaccination prevents the establishment of infectious diseases or drastically reduces their severity by training the immune system to recognize a specific pathogen and trigger a specific immune response against it.[86] Vaccination would establish what is called "herd immunity" (a large portion of the population gets immune to a disease), which significantly reduces the transmission of pathogenic bacteria and, therefore, directly decreases the number of cases of resistant diseases; secondly, it would result in the reduction of antibiotic use, limiting

the consequent resistance development (Figure 1.9).[87,88] Moreover, vaccines, contrary to antibiotics, are effective before bacteria multiply and spread, and can be specific for more than one target simultaneously.[89]

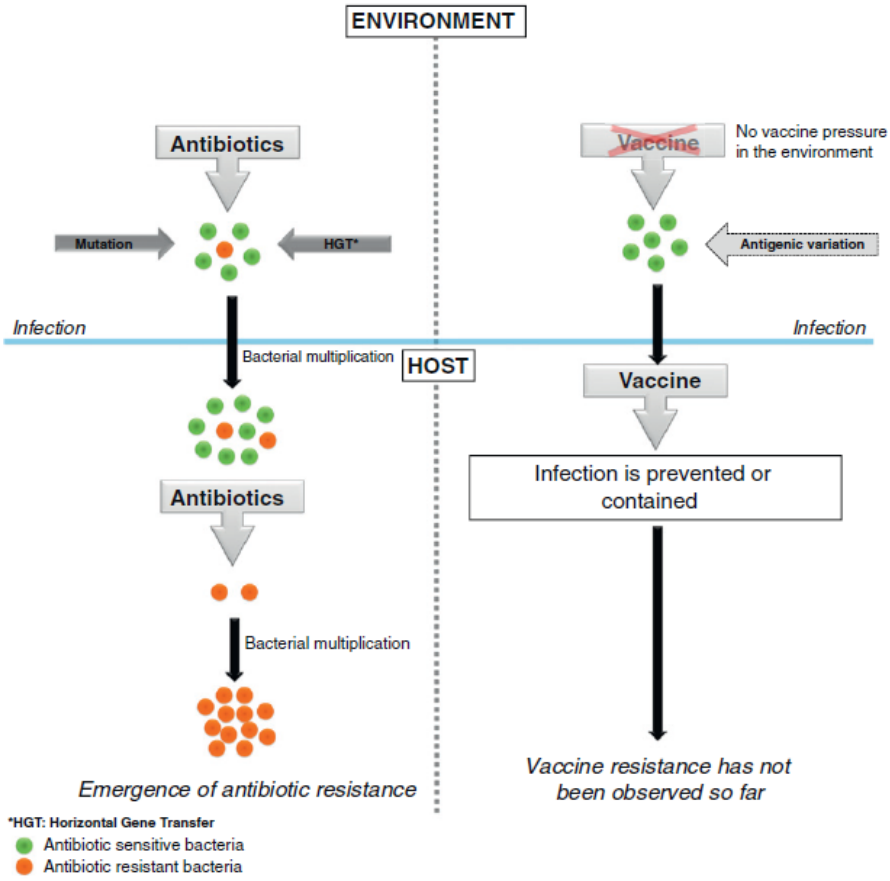

Figure 1.9: Schematic representation of the reduced antibiotic resistance spreading when vaccination is employed. Reported from [87].

Generally, bacterial vaccines can be classified into four groups:[90]

i) Toxoids, which are chemically inactivated toxins from bacteria.

ii) Subunit vaccines, which consist of a single antigen of the bacterium.

iii) Killed whole-cell vaccines, constituted by entire inactivated bacterial cells.

iv) Attenuated vaccines, based on live bacteria which have been modified in order to reduce their virulence and prevent the onset of the disease mediated by them.

Among them, attenuated vaccines can induce the strongest immune response with a considerably longer duration. However, they are associated with the crucial risk of reactivation, which would reverse

their inactivity and induce the disease. Subunit vaccines are much safer as microorganisms are not administrated, exhibiting, regardless, reduced immunogenicity. Indeed, they are commonly employed in combination with adjuvants, which are substances able to boost the vaccine-mediated immune response. As their immune system stimulation is unspecific, they can be used for different bacterium-specific vaccines.[90]

The development of vaccines is of particular relevance for hospital-acquired (nosocomial) infections as they represent a primary cause of death, and it has been demonstrated how almost all the bacteria responsible for these infections are already resistant to at least one of the antibiotics used for their treatment.[87] Among them, *Pseudomonas aeruginosa* has been ranked as one of the three top critical pathogens, for which new treatments are urgently needed.[91] *Pseudomonas aeruginosa* is a virulent opportunistic GRAM-negative bacterium that is able to infect and colonize almost all the body systems in humans, thanks to its tremendous adaptative ability. [91,92] Despite the huge efforts spent over the last 50 years to find efficient vaccination against this bacterium, no licensed vaccines are available nowadays, and the few successful candidates (using well-known virulence factors as vaccine antigens) have failed in clinical trials.[89,91] This lack of promising vaccines can be associated with intrinsic limitations, such as low immunogenicity or the risk of reactivation of traditional vaccination.

1.3.2 Micro/nanoparticles in vaccination

Micro/nanoparticles can represent a new strategy to enhance the efficacy of traditional vaccines and overcome their drawbacks, taking advantage of their inevitable interaction with the immune system. Indeed, micro/nanoparticles have been employed to develop new vaccines, particularly to improve the immunogenicity of antigens.[93] Moreover, they could co-deliver an adjuvant, where the co-localization with antigens would help the enhanced immune response generation. The adjuvant can be encapsulated into the particles or attached to their surface; although, particles can also act as adjuvants themselves,[94] showing an immune stimulation power even stronger than the one of traditional adjuvants.[95] Nevertheless, the use of nanotechnology would also help to specifically target the lymphoid tissue generating enduring immune response and drastically reduce side effects, requiring lower doses.[16,96] The antigens can also be encapsulated in the particles. This strategy would have the advantages of protecting them from degradation, increasing their stability, and controlling their release, which would result in the regulation of the type of induced immune response.[95] On the other side, another possible approach is the attachment of the antigens on the surface of particles in order to maximize and facilitate their interaction with the receptors of the immune system cells, presenting the antigens in a more biomimetic way, and

provoking a more similar response to the one of the pathogen.[16,17] The surface functionalization of micro/nanoparticles with antigens can be performed by simple adsorption or by covalent bonding.[16]

Several kinds of particles have been employed as both antigen delivery systems and adjuvants, constituted by inorganic materials, like gold[97] and silica nanoparticles,[98] or by organic materials, like polymers[99] and lipids.[100] Among them, polymeric particles, particularly polylactic acid (PLA) and poly(lactic-co-glycolic acid) (PLG), have raised great attention as a promising strategy, enhancing immune system response, mostly for their straightforward and low-cost production, biocompatibility, efficiency, and simple surface functionalization,[16] and they have shown significant adjuvant effects. [99,101]

Several parameters, such as size, chemical surface, and shape, can be tuned to modulate the interactions between particles and the immune system. Particles with different dimensions would interact with various elements of the immune system through different pathways, having distinct effects and being able to promote the humoral or the cellular response, or both.[102] However, controversial and not consistent results have been reported about particles size,[93] which have been studied in a broad range, form very small particles (20 nm) to considerably larger ones (150 nm).[103,104] Some studies have reported how smaller particles were able to induce a more robust immune response, while others demonstrated that larger ones would be more potent immune modulators.[105,106]Therefore, tuning of particle size is crucial for the development of a new particles-based vaccine. However, its effect could be further dependent on other properties, such as the antigen concentration, its loading method (encapsulation or surface functionalization), or the route of administration. [93,107]

Another fundamental aspect that would need to be considered is that usually bacteria present a wide range of geometries, which would contribute to their virulence. In the same way, particle shape could influence their persistence time in the bloodstream and, particularly, their cell internalization.[108] For instance, a series of studies performed in Mitragotri's laboratory, the authors evaluated the interaction between macrophages and particles of several geometries, discovering that the shape plays a predominant role in the fate of phagocytosis (Figure 1.10).[9] More precisely, the internalization or the cell spreading over the particles depended on their orientation in the starting contact point, fact attributed to the difficulties encountered by macrophages to create the actine structure needed for phagocytosis, when the local curvature with particles was larger. As the actine remodeling is a high-consumption metabolic activity, the phagocytosis would be successful only for particles with a small contact surface, while if it was too wide, the phagocytosis could be completely inhibited.[9] Particularly, they further evaluated the macrophages' interaction with particles by exploiting the shape effect, considering a worm-like geometry. This shape was able to enhance the phagocytosis inhibition since the internalization was possible only when the contact occurred by the two extremities of the particles, which presented the

highest curvature; when the attachment happened at any other point of the particles, it did not result in the internalization.[109]

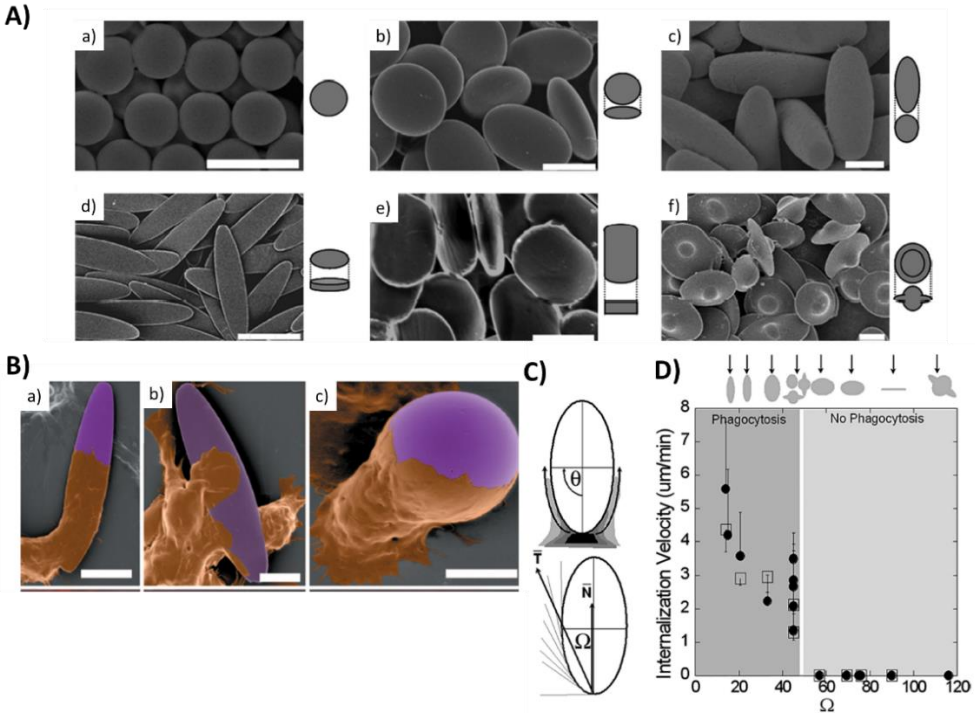

Figure 1.10: A) Scanning electron microscopy and 3D illustrations of microparticles with different shapes: a) Spheres, b) Oblate ellipsoids, c) Prolate ellipsoids, d) Elliptical disks, e) Rectangular disks, and f) "UFOs" (scale bar: 5 μm). B) Scanning electron micrographs and actin staining of a) cells attached at the end of an ellipsoidal particle (scale bar: 10 μm), b) cells attached at the flat side of an ellipsoidal particle (scale bar: 5 μm) c) a cell attached to a spherical particle (scale bar: 5 μm) (cells in brown, and particles in pourple). C) Definition of Ω, as generalized and quantitative parameter for the evaluation of particles shape in phagocytosis, defined as the angle between N (the membrane normal at the initial contact point) and the vector T (whose angle represents the mean direction of tangents to the counter of particles, starting from the initial contact point to the center line of the particle). D) Dependence of phagocytosis (express as internalization velocity) on the shape of particles (considering their Ω). Reported from [9].

Even more interesting would be to stimulate or modulate the adaptative immune system with the particle shape. These cells, known to be antigen presenting cells, have a main role in regulating the immune system, being a messenger between innate and adaptative defenses. In their recent and promising work, Moore *et al.* developed a novel injectable vaccine platform composed of biodegradable ribbon-like particles, which were called "microconfetti" (Figure 1.11).[110] Particles were obtained by mechanical fragmentation of fiber obtained by the electrospinning of acetalated dextran polymer, and their length and width were modulated in order to obtain "small" (0.67 x 10.2 μm), "medium" (1.28 x 20.7 μm), and

"large" (5.67 x 90.2 µm) microconfetti. Their surface was further functionalized with the model antigen ovalbumin by physical adsorption, which resulted in the high and specific activation of T-cells *in vitro*.[110]

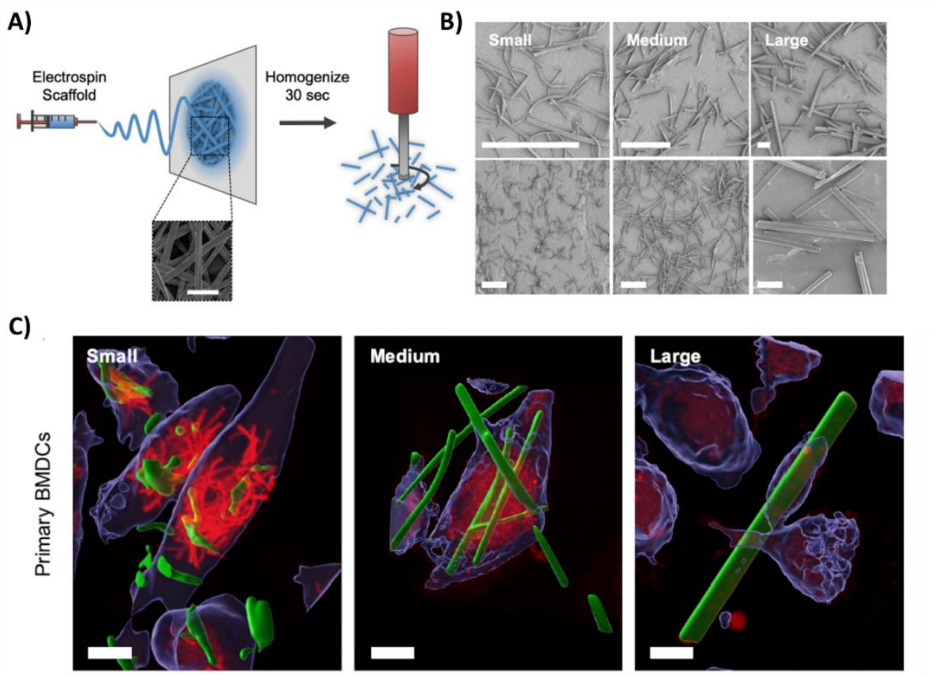

Figure 1.11: A) Schematic representation of microconfetti fabrication by electrospinning (scale bar: 5 µm). B) Scanning electron microscopy of microconfetti with different dimensions (scale bar: 25 µm). C) Confocal microscopy images of microconfetti (green) internalized by antigen presenting cells (BMDCs) (scale bar: 10 µm). Reported from [110].

In two additional works performed by Green and co-workers, spherical polymeric (PLGA) particles were used to directly induce the activation of the adaptative immune system.[111,112] In particular, they obtained ellipsoidal microparticles (>10 µm) whose surface was functionalized with an antigen, and they called them "artificial antigen presenting cell" (Figure 1.12 A). They demonstrated how non-spherical particles were able to significantly enhance the activity of T-cells over the spherical counterpart, which was associated with an increased interaction between particles and cells, observed by confocal microscopy.[111] In a similar work, published in 2015, the authors produced the same particles, but scaled at nanometric size (225 nm) (Figure 1.12 B). Again, the antigen-specific T-cell response was significantly pronounced for ellipsoidal particles, though they observed a strong antigen concentration-dependent response.[112] These results suggest that shape, rather than size, is a major parameter to be evaluated and modulated when a specific immune response is desired.

Up to today, most studies, independently on the size or shape of particles employed, have focused on using model antigens such as ovalbumin or bovine serum albumin. Only few examples of more specific antigens from more infective pathogens are reported.[101]

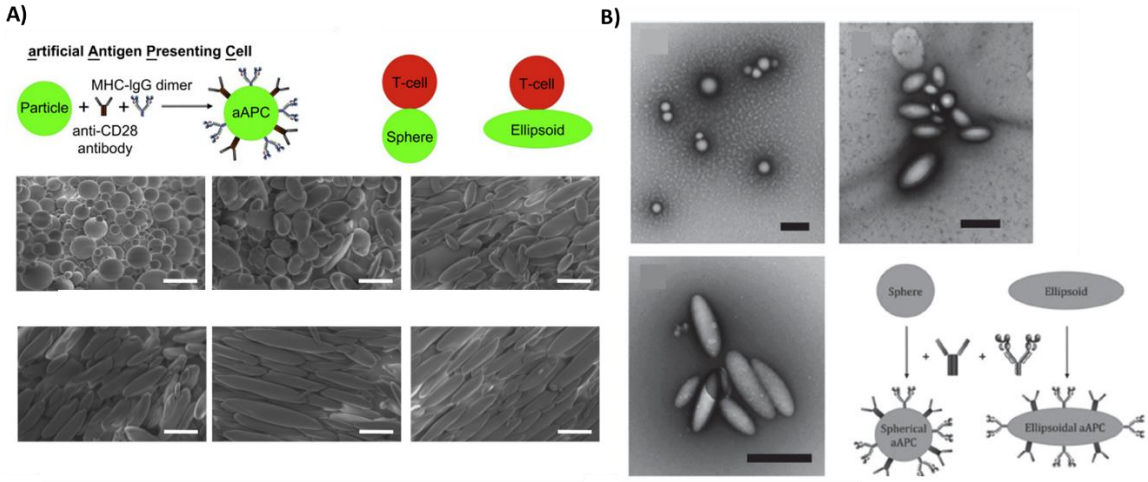

Figure 1.12: Schematic representation of artificial antigen presenting cells and scanning electron microscopy images of spherical and ellipsoidal particles with different major axis dimension. A) microparticles (scale bar: 10 µm) [111], B) nanoparticles (scale bar: 500 nm) [112].

Particularly for *Pseudomona aeruginosa*, some examples of new approaches for vaccine development have been reported.[113,114] Schaefers at el. co-encapsulated in PLGA particles the secretion protein PoPB of the bacterium along with its chaperon protein (PcrH).[115] They obtained nanoparticles of 600-700 nm, with approximately 2% protein loading, demonstrated nanoparticle/antigen synergy enhancing (4-5 fold in comparison to mice immunized only with empty PLGA or pure antigen), showing a higher T-immune cells activation as a higher survival after the reinfection with a lethal dose of *Pseudomonas aeruginosa*.[115] In another work, Ardestani and co-workers obtained similar results by chemically binding a *Pseudomonas aeruginosa* antigen, the exotoxin-A, to PLGA particles.[116] In parallel, Gao *et al*. encapsulated an immunogenic epitope from Pseudomonas aeruginosa in PLGA nanoparticles, coated with the cellular membrane of macrophages. These vehicles demonstrated great potential as nano-vaccine against the bacterium *in vivo*, inducing high immune response and protecting the mice with a surprisingly higher efficiency than the epitope itself.[117]

All the studies reported for *Pseudomonas aeruginosa*, have involved the employment of spherical nanoparticles; no examples of the employment of different shapes have been reported. Moreover, all the studies and attempts performed until today lack specificity and particularly mimicry toward the bacterium. Indeed, considering this bacterium's elongated shape, studying the effect of ellipsoidal particles would be of primary interest. Hence, by combining the immunogenic power of *Pseudomonas aeruginosa* antigens, the particles adjuvant effect and the enchantment properties of particles shape, we

proposed a new and more biomimetic approach that would represent a new powerful class of vaccination, potentially opening new possibilities for preventing and facing bacterial infections.

1.4 Magnetotactic bacteria: magnetic bacterium-like particles

1.4.1 Iron oxide nanoparticles in cancer treatment

Cancer, defined as the uncontrolled abnormal growth of cells, is still a major health challenge worldwilde, by being a primary cause of death. Current treatments include surgery, chemotherapy, radiation therapy, and targeted therapy. However, they still present great limitations and significant side effects.[118] So, the need for the implementation of new and efficient treatments is clearly urgent. Iron oxide magnetic nanoparticles (IOMNPs), usually magnetite (Fe_3O_4) and its oxide maghemite (γ-Fe_2O_3), are undoubtedly the most used family of magnetic nanoparticles in cancer treatment due to their higher biocompatibility and stability.[119] Some of the main advantages are described next.

Synthesis. IOMNPs can be synthesized by different methods; the more extensively used are thermal decomposition and co-precipitation.[118] Concerning dimensions, IOMNPs present a critical size, around 20-30 nm, which could cause the passage from superparamagnetic behavior to ferromagnetic one. If particles are small enough, they can act as a single magnetic domain presenting a random magnetic moment, resulting in a null overall average magnetization when a low-frequency external magnetic field is removed. On the contrary, ferromagnetic materials show residual magnetization after the effect of an external magnetic field. Since attractive reciprocal forces among ferromagnetic nanoparticles could lead to the formation of bigger aggregates, a superparamagnetic behavior is desired in biomedical applications to avoid risks during their blood circulation after intravenous administration.[120,121] It is also possible to achieve IOMNPs with different geometries playing with the synthetic conditions, such as nanocubes, nanorods, nanowires, nanodisks, and nanoflowers (Figure 1.13). This directly affects the magnetic anisotropy and magnetic behavior [122,123] as well as the final interaction with cells.[124]

Biocompatibility. Usually, IOMNPs are covered by a biocompatible stabilizing shell that reduces any residual toxicity while protecting them from undesired aggregation.[121] Moreover, IOMNPs can be coated with organic polymers, surfactants or inorganic materials such as silica,[118] which are used to fine tune the pharmacokinetic profile, extend their half-life and conjugate different biomolecules on the surface to favor biocompatibility. On top of that, thanks to their small dimension IOMNPs can be easily uptake and then retained by the tumor through enhanced permeability and retention (EPR), meaning they could accumulate in tumoral tissue.[121] This fact can be even favored by taking advantage of their magnetic

behavior, by guiding them, once administrated, with an external magnetic field. Magnetic targeting consists of attracting nanoparticles in the tumor region by locally applying a magnetic field.[120] This specific drug delivery would drastically avoid the side effects of chemotherapy and reduce drug doses while improving their half-life.[118]

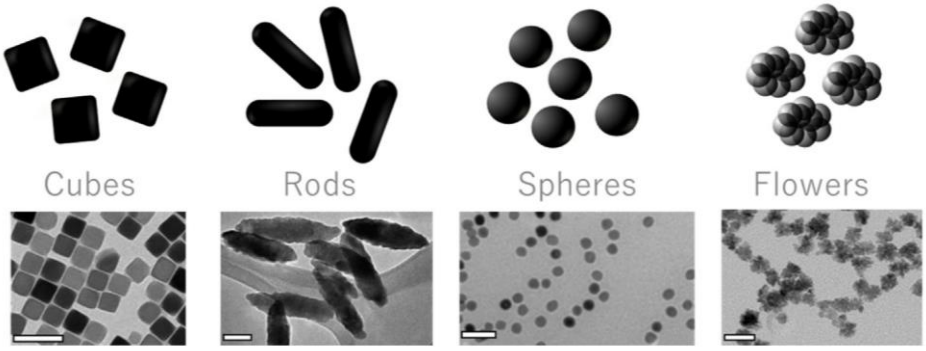

Figure 1.13: Most common morphologies of IOMNPs made of magnetite or maghemite (scale bar: 50 nm) Reported from [125].

Theranostics. The superparamagnetic properties of IOMNPs enhance the transverse relaxation time (T2), providing images with improved contrast and clarity, along with reducing the doses needed to be injected.[120] Along with this, IOMNPs can be employed to treat cancer by converting light irradiation or alternating magnetic fields into heat, the so-called hyperthermia treatment where the local tumor temperature is increased between 39-45 °C, inducing cancer cells apoptosis. In this range, cancer cells have been demonstrated to be more sensitive than healthy ones primarily because of their higher metabolic rate and their lower ability in heat dissipation due to their disordered vascularization. Higher temperatures (47-50 °C) can also be considered, which would induce violent necrosis of cancer cells through their direct disruption. However, this thermal ablation is less used as these high temperatures could damage healthy tissues.[126] Moreover, the thermal treatment made them more responsive to traditional therapies, such as chemotherapy or radiotherapy, increasing their efficacy.[120,127] Next, we discuss the two different approaches for nanoparticles stimulation, which could be induced by light irradiation (photothermia) or by a magnetic field (magnetic hyperthermia) (Figure 1.14).

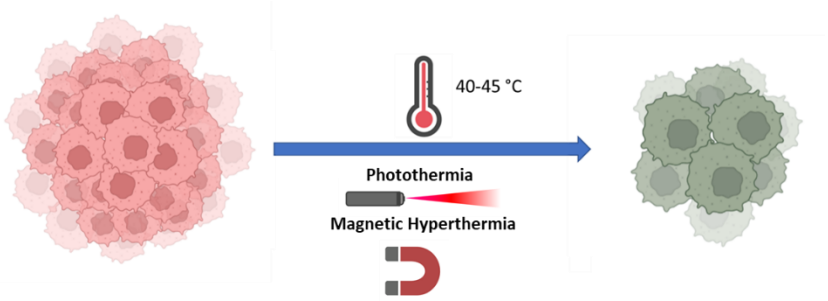

Figure 1.14: Schematic representation of cancer cells death induced by heating, induced by light irradiation (photothermia) or by exposure to a magnetic field (magnetic hyperthermia).

1.4.2 Light induced and magnetic hyperthermia

Light-induced hyperthermia (Photothermia) is based on the use of photothermal agents, which can convert light into heat with high efficiency. The most employed photothermal agents are generally metal materials, such as gold, which exhibit local surface plasmon resonance (LSPR). Under electromagnetic irradiation, the electrons of the conduction band on the surface of these materials go into resonance, i.e., they start oscillating synchronized to the stimulus irradiation. Therefore, once the electron transition is recovered, energy is released through a non-radiative process leading to a temperature increase.[128] More recently IOMNPs have shown a remarkable ability to induce heat generation under near-infrared (NIR) infrared irradiation.[129] Indeed, they present a broad absorption spectrum from visible to NIR region, where the heating capacity is mainly due to an iron to ligand charge transfer.[130] This is one of their main advantages; biomolecules and water exhibit minimal absorption at this wavelength range, known as the biological window, so there is a higher penetration. On top of that, even though NIR source needs higher irradiation density, the broad absorption spectrum of IOMNPs made them efficient nanoheaters.[131]

The final temperature reached in the tumor depends mainly on the IOMNPs concentration and the dosage of the incident light (exposure time, intensity, and continues or pulsed stimulation), and conversion efficiency. This last one depends on the size and shape of IOMNPs. For example, it has been shown that the anisotropy obtained by the aggregation of IOMNPs in small clusters significantly improves light absorption and, therefore, heat generation.[132] Furthermore, nanocubes have been demonstrated to act as a promising photothermal agent, with characteristics close to gold nanoparticles, generating a temperature increase of 7-9°C in *in vitro* experiments.[130]

The main limitation of photothermal therapy is the intrinsic limited tissue penetration even employing a light source within the biological window, reason why this technique is mostly feasible for more superficial tumors.[131] This limitation can be overcome with the thermal activation of the IOMNPs using

an alternating magnetic field. Magnetic hyperthermia, contrary to photothermia, is not limited by the tumor location, as magnetic fields can penetrate the body with homogeneity and minimum attenuation, though it requires high frequencies and particle concentrations are required.[133] In this regime, the IOMNPs show a dissipative hysteresis loop in the magnetization process (magnetization vs magnetic field). This frequency-dependent behavior allows IOMNPs to be applied as nanoheaters in biological applications since they can be localized in the tumor region.[134] IOMNPs lose their magnetization after removal of the external magnetic field by two possible mechanisms: Neel relaxation, which consists of the rapid change of magnetic moments, and Brownian relaxation, constituted by the movement of nanoparticles. The predominant mechanism depends on the IOMNPs intrinsic properties and the surrounding medium characteristics, even though both could co-occur. However, in viscous biological media, or when high magnetic field amplitudes are applied, the Neel relaxation is most favorable and predominant.[135] The heating efficiency of IOMNPs is estimated by the specific absorption rate (SAR), which quantifies the magnetic energy transferred into heat. As heat generation is directly dependent on the hysteresis loop, a lot of interest has been focused on the attempt to expand it without excessively increasing the magnetic field frequencies. Having IOMNPs with high SAR would guarantee efficient hyperthermia while reducing the required doses.[126,135] Saturation magnetization can be increased by improving the crystallinity quality of nanoparticles, or by tuning their size and shape. Particularly, modulating the magnetic anisotropy, which could be dictated by crystalline or shape anisotropies, would significantly improve IOMNPs heating efficiencie.[123,127] Non-spherical particles, such as nanocubes or nanorods, have shown higher SAR values. Nanocubes are considered one of the most efficient nanoheaters,[136] as the elongated shape of nanorods is still a challenge to be achieved under 100 nm.[123]

Despite the great advances of both hyperthermia therapies achieved until today, further works is still needed. Specifically, the local temperature measurement is required for the corroboration of therapy efficacy. Moreover, the modulation of magnetic anisotropy in IOMNPs is still challenged to be achieved with tunability.

1.4.3 Magnetic anisotropy

Beyond heat release, the physical and mechanical rotation of the IOMNPs can be also used to kill cancer cells. How can it be possible? Anisotropic IOMNPs have the magnetic moment locked in the so-called easy magnetization axis, so rotation of the field induces a rotation of all aligned nanoparticles.[137] More specifically, if we apply a homogenous low-frequency magnetic field (a few tens of Hz) it is enough to induce a continuous rotation or vibration of IOMNPs considering the high viscosity of the environment

while avoiding a temperature increase. On the other side, the uniformity of the magnetic field is important to guarantee the rotation of particles and not the translation. Mechanical oscillation of IOMNPs may generate physical harmful effects on cancer cells by provoking the rupture of cellular membranes or cause direct damage to the cytoskeleton or lysosomes, which would activate the apoptosis pathway.[137] Moreover, during oscillation, IOMNPs are subjected to consequent stretching, compression, or shear forces that can be transferred to the macromolecules attached to their surfaces, which can be structurally deformed resulting in their misregulation.[138] The application of this mechanical effect in biology has been studied since its first appearance in 2010 and has become an emerging approach in cancer treatment.[139] Once again, the efficiency of the magneto-transduction into mechanical effect depends on IOMNPs properties, like size and shape. Nowadays, disk-shape particles are probably the most used and have been extensively applied, demonstrating their ability to induce mechanical stress into tumor cells.[137,140] However, cubic IOMNPs or small chain aggregates of spherical ones have also been studied.[137,141] However, the fine tuning of anisotropic shape with controlled magnetic properties is still challenging.

Once more, magnetic nanoparticles with fine tuned properties are present in nature, which could represent a source of inspiration. This is the case of magnetotactic bacteria which generate magnetite nanoparticles in their interior through a genetically regulated bio-mineralization process of iron crystals (Figure 1.15 A,B). The single IOMNPs could present different shapes: roughly cubic, elongated prismatic and bullet-shaped. Their dimension can also change between 35-120 nm (Figure 1.15 C,D). The magnetic crystals present a single magnetic domain separately, meaning they are permanently magnetic at room temperature, but their alignment provides a complex magnetic dipole to the bacterium, which allows its orientation.[142] Then, aquatic bacteria can align along the Earth's magnetic field (magnetotaxis) and actively swim along this direction thanks to their flagella.[143,144] The number of IOMNPs within a magnetotactic bacteria varies from 10 to 30, covered by a phospholipid bilayer and usually arranged in chains along the bacterium axis, the so called magnetosome.[143] Overall, IOMNPs of magnetotactic bacteria present unique properties, such as a well-defined morphology with a narrow size distribution, showing a high chemical purity with few crystallographic defects.[144] Moreover, they are coated with a biocompatible layer which makes them stable once dispersed in water and helping their surface functionalization.[145] Moreover, they have not shown toxic effects in both *in vivo* and *in vitro* studies.[145]

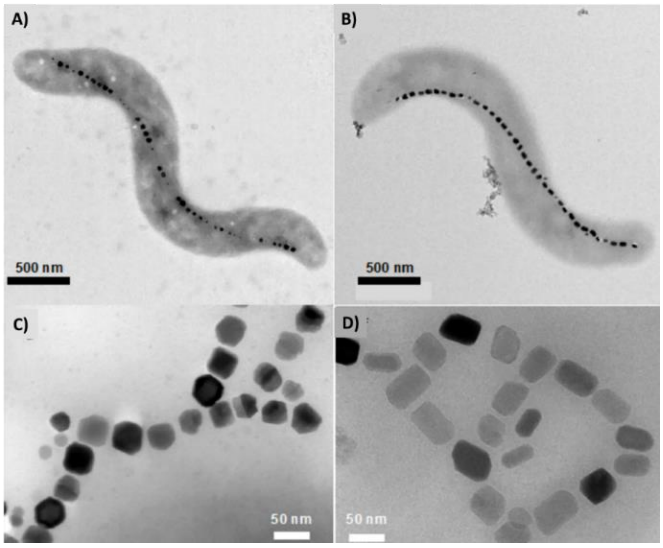

Figure 1.15: Transmission electron microscopy images of A,B) two different magnetotactic bacteria, and C,D) their isolated magnetosomes. Adapted from [146].

Worth to mention, the manipulability of magnetotactic bacteria through a magnetic field has been used to actively and selectively guide them to the tumor. Moreover, their ability to move thanks to the flagella is an additional advantage; as these bacteria prefer living in low oxygen concentrations in natural conditions, the tumor targeting, which presents hypoxia, would be enhanced.[143,147] Additionally, additional surface functionalization of magnetosomes has been employed to deliver anticancer drugs, such as doxorubicin or cytosine arabinosid.[143] Furthermore, they have shown great potential to act as a powerful magnetic hyperthermia agent. Indeed, their alignment along the external magnetic field would enhance their heating efficiency.[145 147]

However, the applicability of magnetotactic bacteria presents several drawbacks. First, their culturing conditions are complex and expensive. Moreover, IOMNPs are challenging to be collected with a well-defined shape and at high concentrations, requiring long purification processes which make their scalability unachievable.[143] Therefore, developing biomimetic or bioinspired magnetotactic bacteria has attracted significant attention. With this aim, Martí *et al*. deposited IOMNPs on the surface of some bacteria present in natural human microbiota, showing similar shapes and dimensions to magnetotactic ones, obtaining what they called "artificial magnetic bacteria".[148] By applying an external magnetic field, they obtained ordered magnetic nanostructures, where the presence of the bacterium as a platform allowed them to avoid their uncontrolled aggregation. The authors found some differences in the magnetic behavior, and the external magnetic field required for the alignment of the artificial bacterium was much higher compared to the Earth's one. However, controlling the amount of iron per bacterium was possible, which represents an important advantage.[148] In a more recent work, Yao and co-workers

deposited IOMNPs on the surfaces of a commonly used magnetotactic bacterium intending to regulate their magnetic sensitivity, making them responsive to different magnetic fields, leading to the applicability in a broader range of possibilities.[149]

On top of the previous target, herein we also hypothesize that the encapsulation of the IOMNPs within oil close-shell magnetotactic bacteria-like particles instead of solid nanoparticles would allow us for additional uses uses such as nanothermometry. The oil allows for the motion of the NCs in a controlled environment while the polymeric shell protects if from mixing with the cytosol. Indeed, an important goal is the real-time monitoring of temperature increases induced by hyperthermia. Knowing the exact heating localization is crucial to limit harmful side effects on healthy tissues and verify treatment efficacy. Thus, the development of real-time thermometers, able to precisely detect minimum temperature variations, and being at the nanometric scale to access the heating regions in the body, has been exploited in recent years.[150] Currently, the examples reported are based on the use of luminescent probes by evaluating their lifetime or fluorescence shifts.[151] However, these molecules could induce cytotoxic effects and are subjected to the intrinsic limitation of chemical stability, caused by photobleaching or blinking, or to external limitation due to the absorption and scattering of the human body.[152] An interesting alternative is to exploit the temperature dependence magnetic susceptibility of the IOMNPs itself, by evaluating the magnetization variation at different frequencies.[153,154] For instance, IOMNP Brownian relaxation is strongly influenced by the viscosity of the surrounding medium, which in turn is strongly temperature dependent. Overall, the higher the viscosity the higher the delay (phase lag) directly reflected in the amplitude of the IOMNPs harmonic response. By measuring these amplitudes and using a calibration curve, it is possible to estimate the local viscosity [155,156] so the temperature.[157] The main limitation is that as low frequencies are needed, it is possible to detect changes only by using high particles concentration.[158]

To avoid such concentration dependence, it is possible to take advantage of the same IOMNP magneto-optical properties.[152] Indeed, considering that the polarization plane of light is modified on passing through a magnetic field, the variation of the light plane with the amplitude and the phase lag of the IOMNP harmonics can be used to study temperature variations. For instance, Sepulveda and co-workers used a polarized laser at 808 nm as the light source for both the optical measurement and heat generation. By measuring the phase lag, which is independent from IOMNPs concentration, the authors measured very low variations of the viscosity upon temperature changes with an incredibly low detection limit (0.08 °C in water).[152] However, the main limitation for its practical implementation is the lack of

defined and precise information about the intracellular matrix viscosity, which is highly variable and unpredictable.

Scope of the thesis

Several biomedical challenges are still unresolved and require an immediate solution. Taking inspiration or mimicking the unique properties that biological systems display would represent an exceptional approach. In this thesis, various micro and nanoparticle have been proposed as tools for three main areas: i) vaccine development, ii) cancer treatment, and iii) Parkinson's disease therapy. For these purposes, polymeric particles or supramolecular chemistry have been employed, and the bioinspiration sources were taken by bacteria and neuromelanin.

Three main cha can be recognized in this thesis, divided into three main chapters:

- Chapter 3: *Pseudomonas aeruginosa*-like microparticles are designed aiming to enhance the immune response activation by the non-spherical shape.
- Chapter 4: Bioinspired and biomimetic magnetic particles, resembling magnetotactic bacteria or magnetosome crystals, are intended for cancer therapy. The elongated shape and magnetic behavior of the bacteria are proposed on one side, while core-shell spherical particles with encapsulated magnetosomes crystals-like nanocubes are planned on the other.
- In Chapter 5: Dopamine and iron, neuromelanin main constituents, are structured in two different types of nanoparticles by coordination chemistry, being inspired by the chemical structure and supramolecular nature of neuromelanin.

1.5 References

1. Akagi, T., Cabral, H. & Mi, P. Bio-inspired nanomaterials for biomedical innovation. *Sci. Technol. Adv. Mater.* **21**, 420–421 (2020).
2. Zan, G. & Wu, Q. Biomimetic and Bioinspired Synthesis of Nanomaterials/Nanostructures. *Adv. Mater.* **28**, 2099–2147 (2016).
3. Parodi, A. *et al.* Bio-inspired engineering of cell- and virus-like nanoparticles for drug delivery. *Biomaterials* **147**, 155–168 (2017).
4. Pasparakis, G., Krasnogor, N., Cronin, L., Davis, B. G. & Alexander, C. Controlled polymer synthesis—from biomimicry towards synthetic biology. *Chem Soc Rev* **39**, 286–300 (2010).
5. Pasparakis, G. & Alexander, C. Sweet Talking Double Hydrophilic Block Copolymer Vesicles. *Angew. Chem. Int. Ed.* **47**, 4847–4850 (2008).

6. Steenblock, E. R. & Fahmy, T. M. A Comprehensive Platform for Ex Vivo T-cell Expansion Based on Biodegradable Polymeric Artificial Antigen-presenting Cells. *Mol. Ther.* **16**, 765–772 (2008).
7. Bachmann, M. F. & Jennings, G. T. Vaccine delivery: a matter of size, geometry, kinetics and molecular patterns. *Nat. Rev. Immunol.* **10**, 787–796 (2010).
8. Wauters, A. C. *et al.* Artificial Antigen-Presenting Cell Topology Dictates T Cell Activation. *ACS Nano* **16**, 15072–15085 (2022).
9. Champion, J. A. & Mitragotri, S. Role of target geometry in phagocytosis. *Proc. Natl. Acad. Sci.* **103**, 4930–4934 (2006).
10. Meyer, R. A., Sunshine, J. C. & Green, J. J. Biomimetic particles as therapeutics. *Trends Biotechnol.* **33**, 514–524 (2015).
11. Hayashi, K., Yamada, S., Hayashi, H., Sakamoto, W. & Yogo, T. Red blood cell-like particles with the ability to avoid lung and spleen accumulation for the treatment of liver fibrosis. *Biomaterials* **156**, 45–55 (2018).
12. Nguyen, T. D. T. *et al.* Biomimetic surface modification of discoidal polymeric particles. *Nanomedicine Nanotechnol. Biol. Med.* **16**, 79–87 (2019).
13. Wang, J. *et al.* Shape matters: Morphologically biomimetic particles for improved drug delivery. *Chem. Eng. J.* **410**, 127849 (2021).
14. Xu, X., Li, T. & Jin, K. Bioinspired and Biomimetic Nanomedicines for Targeted Cancer Therapy. *Pharmaceutics* **14**, 1109 (2022).
15. Sanità, G., Carrese, B. & Lamberti, A. Nanoparticle Surface Functionalization: How to Improve Biocompatibility and Cellular Internalization. *Front. Mol. Biosci.* **7**, 587012 (2020).
16. Pati, R., Shevtsov, M. & Sonawane, A. Nanoparticle Vaccines Against Infectious Diseases. *Front. Immunol.* **9**, 2224 (2018).
17. Gregory, A. E., Titball, R. & Williamson, D. Vaccine delivery using nanoparticles. *Front. Cell. Infect. Microbiol.* **3**, (2013).
18. Luk, B. T. *et al.* Safe and Immunocompatible Nanocarriers Cloaked in RBC Membranes for Drug Delivery to Treat Solid Tumors. *Theranostics* **6**, 1004–1011 (2016).
19. Toyofuku, M., Nomura, N. & Eberl, L. Types and origins of bacterial membrane vesicles. *Nat. Rev. Microbiol.* **17**, 13–24 (2019).
20. Gao, W. *et al.* Modulating Antibacterial Immunity via Bacterial Membrane-Coated Nanoparticles. *Nano Lett.* **15**, 1403–1409 (2015).
21. Zhang, Y. *et al.* Inhibition of Pathogen Adhesion by Bacterial Outer Membrane-Coated Nanoparticles. *Angew. Chem. Int. Ed.* **58**, 11404–11408 (2019).
22. Angsantikul, P., Thamphiwatana, S., Gao, W. & Zhang, L. Cell Membrane-Coated Nanoparticles As an Emerging Antibacterial Vaccine Platform. *Vaccines* **3**, 814–828 (2015).
23. Gao, F., Xu, L., Yang, B., Fan, F. & Yang, L. Kill the Real with the Fake: Eliminate Intracellular *Staphylococcus aureus* Using Nanoparticle Coated with Its Extracellular Vesicle Membrane as Active-Targeting Drug Carrier. *ACS Infect. Dis.* **5**, 218–227 (2019).
24. Long, Q. *et al.* Engineered bacterial membrane vesicles are promising carriers for vaccine design and tumor immunotherapy. *Adv. Drug Deliv. Rev.* **186**, 114321 (2022).
25. Kroll, A. V., Fang, R. H. & Zhang, L. Biointerfacing and Applications of Cell Membrane-Coated Nanoparticles. *Bioconjug. Chem.* **28**, 23–32 (2017).
26. Zeng, Y. *et al.* Cell membrane coated-nanoparticles for cancer immunotherapy. *Acta Pharm. Sin. B*

12, 3233–3254 (2022).
27. Ben-Akiva, E. *et al.* Biomimetic anisotropic polymeric nanoparticles coated with red blood cell membranes for enhanced circulation and toxin removal. *Sci. Adv.* **6**, eaay9035 (2020).
28. Zhang, S., Wang, R. & Wang, G. Impact of Dopamine Oxidation on Dopaminergic Neurodegeneration. *ACS Chem. Neurosci.* **10**, 945–953 (2019).
29. Bisaglia, M., Mammi, S. & Bubacco, L. Kinetic and Structural Analysis of the Early Oxidation Products of Dopamine. *J. Biol. Chem.* **282**, 15597–15605 (2007).
30. Meiser, J., Weindl, D. & Hiller, K. Complexity of dopamine metabolism. *Cell Commun. Signal.* **11**, 34 (2013).
31. Alabrahim, O. A. A. & Azzazy, H. M. E.-S. Polymeric nanoparticles for dopamine and levodopa replacement in Parkinson's disease. *Nanoscale Adv.* **4**, 5233–5244 (2022).
32. AlMahadin, G. *et al.* Parkinson's disease: current assessment methods and wearable devices for evaluation of movement disorder motor symptoms - a patient and healthcare professional perspective. *BMC Neurol.* **20**, 419 (2020).
33. Poewe, W. *et al.* Parkinson disease. *Nat. Rev. Dis. Primer* **3**, 17013 (2017).
34. Rodríguez-Nogales, C., Garbayo, E., Carmona-Abellán, M. M., Luquin, M. R. & Blanco-Prieto, M. J. Brain aging and Parkinson's disease: New therapeutic approaches using drug delivery systems. *Maturitas* **84**, 25–31 (2016).
35. Hindle, J. V. Ageing, neurodegeneration and Parkinson's disease. *Age Ageing* **39**, 156–161 (2010).
36. Shankar, J., K.M, G. & Wilson, B. Potential applications of nanomedicine for treating Parkinson's disease. *J. Drug Deliv. Sci. Technol.* **66**, 102793 (2021).
37. Aviles-Olmos, I., Kefalopoulou, Z. & Foltynie, T. Understanding and Prevention of "Therapy-" Induced Dyskinesias. *Park. Dis.* **2012**, 1–9 (2012).
38. Lombardo, S. M., Schneider, M., Türeli, A. E. & Günday Türeli, N. Key for crossing the BBB with nanoparticles: the rational design. *Beilstein J. Nanotechnol.* **11**, 866–883 (2020).
39. Lopalco, A. *et al.* Transferrin Functionalized Liposomes Loading Dopamine HCl: Development and Permeability Studies across an In Vitro Model of Human Blood–Brain Barrier. *Nanomaterials* **8**, 178 (2018).
40. Kahana, M. *et al.* Liposome-based targeting of dopamine to the brain: a novel approach for the treatment of Parkinson's disease. *Mol. Psychiatry* **26**, 2626–2632 (2021).
41. Pahuja, R. *et al.* Trans-Blood Brain Barrier Delivery of Dopamine-Loaded Nanoparticles Reverses Functional Deficits in Parkinsonian Rats. *ACS Nano* **9**, 4850–4871 (2015).
42. Monge-Fuentes, V. *et al.* Dopamine-loaded nanoparticle systems circumvent the blood–brain barrier restoring motor function in mouse model for Parkinson's Disease. *Sci. Rep.* **11**, 15185 (2021).
43. Qu, M. *et al.* Dopamine-loaded blood exosomes targeted to brain for better treatment of Parkinson's disease. *J. Controlled Release* **287**, 156–166 (2018).
44. Zecca, L. *et al.* Iron, neuromelanin and ferritin content in the substantia nigra of normal subjects at different ages: consequences for iron storage and neurodegenerative processes: Nigral iron, neuromelanin and ferritin. *J. Neurochem.* **76**, 1766–1773 (2001).
45. Chen, C.-T., Martin-Martinez, F. J., Jung, G. S. & Buehler, M. J. Polydopamine and eumelanin molecular structures investigated with ab initio calculations. *Chem. Sci.* **8**, 1631–1641 (2017).
46. Chen, Y. *et al.* Polydopamine-based coordination nanocomplex for T1/T2 dual mode magnetic

resonance imaging-guided chemo-photothermal synergistic therapy. *Biomaterials* **77**, 198–206 (2016).
47. You, I. *et al.* Polydopamine coating in organic solvent for material-independent immobilization of water-insoluble molecules and avoidance of substrate hydrolysis. *J. Ind. Eng. Chem.* **46**, 379–385 (2017).
48. Park, J., Moon, H. & Hong, S. Recent advances in melanin-like nanomaterials in biomedical applications: a mini review. *Biomater. Res.* **23**, 24 (2019).
49. Hong, S. *et al.* Non-Covalent Self-Assembly and Covalent Polymerization Co-Contribute to Polydopamine Formation. *Adv. Funct. Mater.* **22**, 4711–4717 (2012).
50. Hong, S., Wang, Y., Park, S. Y. & Lee, H. Progressive fuzzy cation-π assembly of biological catecholamines. *Sci. Adv.* **4**, eaat7457 (2018).
51. Zucca, F. A. *et al.* Neuromelanin of the Human Substantia Nigra: An Update. *Neurotox. Res.* **25**, 13–23 (2014).
52. Wang, Z., Zou, Y., Li, Y. & Cheng, Y. Metal-Containing Polydopamine Nanomaterials: Catalysis, Energy, and Theranostics. *Small* **16**, 1907042 (2020).
53. Chen, A. *et al.* The effect of metal ions on endogenous melanin nanoparticles used as magnetic resonance imaging contrast agents. *Biomater. Sci.* **8**, 379–390 (2020).
54. Chen, L. *et al.* Fe^{2+} /Fe^{3+} Ions Chelated with Ultrasmall Polydopamine Nanoparticles Induce Ferroptosis for Cancer Therapy. *ACS Biomater. Sci. Eng.* **5**, 4861–4869 (2019).
55. Ang, J. M. *et al.* One-Pot Synthesis of Fe(III)–Polydopamine Complex Nanospheres: Morphological Evolution, Mechanism, and Application of the Carbonized Hybrid Nanospheres in Catalysis and Zn–Air Battery. *Langmuir* **32**, 9265–9275 (2016).
56. Wang, Z. *et al.* Tunable, Metal-Loaded Polydopamine Nanoparticles Analyzed by Magnetometry. *Chem. Mater.* **29**, 8195–8201 (2017).
57. Li, Y. *et al.* Structure and Function of Iron-Loaded Synthetic Melanin. *ACS Nano* **10**, 10186–10194 (2016).
58. Zhang, L., Wang, Q., Jian, R.-K. & Wang, D.-Y. Bioinspired iron-loaded polydopamine nanospheres as green flame retardants for epoxy resin *via* free radical scavenging and catalytic charring. *J. Mater. Chem. A* **8**, 2529–2538 (2020).
59. Lemaster, J. E. *et al.* Gadolinium Doping Enhances the Photoacoustic Signal of Synthetic Melanin Nanoparticles: A Dual Modality Contrast Agent for Stem Cell Imaging. *Chem. Mater.* **31**, 251–259 (2019).
60. Zayed, J. M., Nouvel, N., Rauwald, U. & Scherman, O. A. Chemical complexity—supramolecular self-assembly of synthetic and biological building blocks in water. *Chem. Soc. Rev.* **39**, 2806 (2010).
61. Webber, M. J. & Langer, R. Drug delivery by supramolecular design. *Chem. Soc. Rev.* **46**, 6600–6620 (2017).
62. Ma, X. & Zhao, Y. Biomedical Applications of Supramolecular Systems Based on Host–Guest Interactions. *Chem. Rev.* **115**, 7794–7839 (2015).
63. Lin, R. & Cui, H. Supramolecular nanostructures as drug carriers. *Curr. Opin. Chem. Eng.* **7**, 75–83 (2015).
64. Stoffelen, C. & Huskens, J. Soft Supramolecular Nanoparticles by Noncovalent and Host-Guest Interactions. *Small* **12**, 96–119 (2016).
65. Oh, K. S. *et al.* The multilayer nanoparticles formed by layer by layer approach for cancer-targeting

therapy. *J. Controlled Release* **165**, 9–15 (2013).
66. Mejia-Ariza, R., Graña-Suárez, L., Verboom, W. & Huskens, J. Cyclodextrin-based supramolecular nanoparticles for biomedical applications. *J. Mater. Chem. B* **5**, 36–52 (2017).
67. Omar, J., Ponsford, D., Dreiss, C. A., Lee, T. & Loh, X. J. Supramolecular Hydrogels: Design Strategies and Contemporary Biomedical Applications. *Chem. – Asian J.* **17**, (2022).
68. Trapani, A. *et al.* Characterization and evaluation of chitosan nanoparticles for dopamine brain delivery. *Int. J. Pharm.* **419**, 296–307 (2011).
69. Bulbake, U., Doppalapudi, S., Kommineni, N. & Khan, W. Liposomal Formulations in Clinical Use: An Updated Review. *Pharmaceutics* **9**, 12 (2017).
70. Trapani, A. *et al.* Protection of dopamine towards autoxidation reaction by encapsulation into non-coated- or chitosan- or thiolated chitosan-coated-liposomes. *Colloids Surf. B Biointerfaces* **170**, 11–19 (2018).
71. Suárez-García, S. *et al.* Antitumour activity of coordination polymer nanoparticles. *Coord. Chem. Rev.* **441**, 213977 (2021).
72. Samaridou, E. & Alonso, M. J. Nose-to-brain peptide delivery – The potential of nanotechnology. *Bioorg. Med. Chem.* **26**, 2888–2905 (2018).
73. Bharadwaj, V. N., Tzabazis, A. Z., Klukinov, M., Manering, N. A. & Yeomans, D. C. Intranasal Administration for Pain: Oxytocin and Other Polypeptides. *Pharmaceutics* **13**, 1088 (2021).
74. Lofts, A., Abu-Hijleh, F., Rigg, N., Mishra, R. K. & Hoare, T. Using the Intranasal Route to Administer Drugs to Treat Neurological and Psychiatric Illnesses: Rationale, Successes, and Future Needs. *CNS Drugs* **36**, 739–770 (2022).
75. Cui, J. *et al.* Gather wisdom to overcome barriers: Well-designed nano-drug delivery systems for treating gliomas. *Acta Pharm. Sin. B* **12**, 1100–1125 (2022).
76. Bourganis, V., Kammona, O., Alexopoulos, A. & Kiparissides, C. Recent advances in carrier mediated nose-to-brain delivery of pharmaceutics. *Eur. J. Pharm. Biopharm.* **128**, 337–362 (2018).
77. Boegh, M. & Nielsen, H. M. Mucus as a Barrier to Drug Delivery - Understanding and Mimicking the Barrier Properties. *Basic Clin. Pharmacol. Toxicol.* **116**, 179–186 (2015).
78. Sonvico, F. *et al.* Surface-Modified Nanocarriers for Nose-to-Brain Delivery: From Bioadhesion to Targeting. *Pharmaceutics* **10**, 34 (2018).
79. Sosnik, A., das Neves, J. & Sarmento, B. Mucoadhesive polymers in the design of nano-drug delivery systems for administration by non-parenteral routes: A review. *Prog. Polym. Sci.* **39**, 2030–2075 (2014).
80. Dahlin, M., Bergman, U., Jansson, B., Björk, E. & Brittebo, E. Transfer of Dopamine in the Olfactory Pathway Following Nasal Administration in Mice. *Pharm. Res.* **17**, 737–742 (2000).
81. Tang, S. *et al.* Brain-targeted intranasal delivery of dopamine with borneol and lactoferrin co-modified nanoparticles for treating Parkinson's disease. *Drug Deliv.* **26**, 700–707 (2019).
82. Di Gioia, S. *et al.* Intranasal delivery of dopamine to the striatum using glycol chitosan/sulfobutylether-β-cyclodextrin based nanoparticles. *Eur. J. Pharm. Biopharm.* **94**, 180–193 (2015).
83. Urban-Chmiel, R. *et al.* Antibiotic Resistance in Bacteria—A Review. *Antibiotics* **11**, 1079 (2022).
84. Munita, J. M. & Arias, C. A. Mechanisms of Antibiotic Resistance. *Microbiol. Spectr.* **4**, 4.2.15 (2016).
85. Blair, J. M. A., Webber, M. A., Baylay, A. J., Ogbolu, D. O. & Piddock, L. J. V. Molecular

mechanisms of antibiotic resistance. *Nat. Rev. Microbiol.* **13**, 42–51 (2015).
86. Jansen, K. U., Knirsch, C. & Anderson, A. S. The role of vaccines in preventing bacterial antimicrobial resistance. *Nat. Med.* **24**, 10–19 (2018).
87. Mishra, R. P., Oviedo-Orta, E., Prachi, P., Rappuoli, R. & Bagnoli, F. Vaccines and antibiotic resistance. *Curr. Opin. Microbiol.* **15**, 596–602 (2012).
88. Atkins, K. E. & Lipsitch, M. Can antibiotic resistance be reduced by vaccinating against respiratory disease? *Lancet Respir. Med.* **6**, 820–821 (2018).
89. Micoli, F., Bagnoli, F., Rappuoli, R. & Serruto, D. The role of vaccines in combatting antimicrobial resistance. *Nat. Rev. Microbiol.* **19**, 287–302 (2021).
90. Giesker, K. & Hensel, M. Bacterial Vaccines. in *Reference Module in Biomedical Sciences* B9780128012383000000 (Elsevier, 2014). doi:10.1016/B978-0-12-801238-3.00141-0.
91. Killough, M., Rodgers, A. M. & Ingram, R. J. Pseudomonas aeruginosa: Recent Advances in Vaccine Development. *Vaccines* **10**, 1100 (2022).
92. Torrents, E., Poplawski, A. & Sjöberg, B.-M. Two Proteins Mediate Class II Ribonucleotide Reductase Activity in Pseudomonas aeruginosa. *J. Biol. Chem.* **280**, 16571–16578 (2005).
93. Oyewumi, M. O., Kumar, A. & Cui, Z. Nano-microparticles as immune adjuvants: correlating particle sizes and the resultant immune responses. *Expert Rev. Vaccines* **9**, 1095–1107 (2010).
94. Zhou, J., Kroll, A. V., Holay, M., Fang, R. H. & Zhang, L. Biomimetic Nanotechnology toward Personalized Vaccines. *Adv. Mater.* **32**, 1901255 (2020).
95. Gheibi Hayat, S. M. & Darroudi, M. Nanovaccine: A novel approach in immunization. *J. Cell. Physiol.* **234**, 12530–12536 (2019).
96. Gutjahr, A. *et al.* Biodegradable Polymeric Nanoparticles-Based Vaccine Adjuvants for Lymph Nodes Targeting. *Vaccines* **4**, 34 (2016).
97. Niikura, K. *et al.* Gold Nanoparticles as a Vaccine Platform: Influence of Size and Shape on Immunological Responses *in Vitro* and *in Vivo*. *ACS Nano* **7**, 3926–3938 (2013).
98. Skrastina, D. *et al.* Silica Nanoparticles as the Adjuvant for the Immunisation of Mice Using Hepatitis B Core Virus-Like Particles. *PLoS ONE* **9**, e114006 (2014).
99. Ben-Akiva, E., Est Witte, S., Meyer, R. A., Rhodes, K. R. & Green, J. J. Polymeric micro- and nanoparticles for immune modulation. *Biomater. Sci.* **7**, 14–30 (2019).
100. Tyagi, R. K., Garg, N. K. & Sahu, T. Vaccination Strategies against Malaria: novel carrier(s) more than a tour de force. *J. Controlled Release* **162**, 242–254 (2012).
101. Pavot, V. *et al.* Poly(lactic acid) and poly(lactic- *co* -glycolic acid) particles as versatile carrier platforms for vaccine delivery. *Nanomed.* **9**, 2703–2718 (2014).
102. Najafi-Hajivar, S. *et al.* Overview on experimental models of interactions between nanoparticles and the immune system. *Biomed. Pharmacother.* **83**, 1365–1378 (2016).
103. Fifis, T. *et al.* Size-Dependent Immunogenicity: Therapeutic and Protective Properties of Nano-Vaccines against Tumors. *J. Immunol.* **173**, 3148–3154 (2004).
104. Johansen, P. Towards clinical testing of a single-administration tetanus vaccine based on PLA/PLGA microspheres. *Vaccine* **19**, 1047–1054 (2000).
105. Katare, Y. K., Muthukumaran, T. & Panda, A. K. Influence of particle size, antigen load, dose and additional adjuvant on the immune response from antigen loaded PLA microparticles. *Int. J. Pharm.* **301**, 149–160 (2005).
106. Kanchan, V. & Panda, A. K. Interactions of antigen-loaded polylactide particles with

macrophages and their correlation with the immune response. *Biomaterials* **28**, 5344–5357 (2007).
107. Johansen, P. Ambiguities in the preclinical quality assessment of microparticulate vaccines. *Trends Biotechnol.* **18**, 203–211 (2000).
108. Doshi, N. & Mitragotri, S. Macrophages Recognize Size and Shape of Their Targets. *PLoS ONE* **5**, e10051 (2010).
109. Champion, J. A. & Mitragotri, S. Shape Induced Inhibition of Phagocytosis of Polymer Particles. *Pharm. Res.* **26**, 244–249 (2009).
110. Moore, K. M. *et al.* Injectable, Ribbon-Like Microconfetti Biopolymer Platform for Vaccine Applications. *ACS Appl. Mater. Interfaces* **12**, 38950–38961 (2020).
111. Sunshine, J. C., Perica, K., Schneck, J. P. & Green, J. J. Particle shape dependence of CD8+ T cell activation by artificial antigen presenting cells. *Biomaterials* **35**, 269–277 (2014).
112. Meyer, R. A. *et al.* Biodegradable Nanoellipsoidal Artificial Antigen Presenting Cells for Antigen Specific T-Cell Activation. *Small* **11**, 1519–1525 (2015).
113. Azimi, S. & Safari Zanjani, L. Immunization against Pseudomonas aeruginosa using Alg-PLGA nano-vaccine. *Iran. J. Basic Med. Sci.* **24**, (2021).
114. Maleki, M., Azimi, S. & Salouti, M. Protective effect of two new nanovaccines against Pseudomonas aeruginosa based on LPS and OPS: A comparison study. *Immunobiology* **227**, 152278 (2022).
115. Schaefers, M. M. *et al.* PLGA-encapsulation of the Pseudomonas aeruginosa PopB vaccine antigen improves Th17 responses and confers protection against experimental acute pneumonia. *Vaccine* **36**, 6926–6932 (2018).
116. Safari Zanjani, L., Shapouri, R., Dezfulian, M., Mahdavi, M. & Shafiee Ardestani, M. Exotoxin A-PLGA nanoconjugate vaccine against Pseudomonas aeruginosa infection: protectivity in murine model. *World J. Microbiol. Biotechnol.* **35**, 94 (2019).
117. Gao, C. *et al.* A novel structurally identified epitope delivered by macrophage membrane-coated PLGA nanoparticles elicits protection against Pseudomonas aeruginosa. *J. Nanobiotechnology* **20**, 532 (2022).
118. Li, X., Li, W., Wang, M. & Liao, Z. Magnetic nanoparticles for cancer theranostics: Advances and prospects. *J. Controlled Release* **335**, 437–448 (2021).
119. Shubayev, V. I., Pisanic, T. R. & Jin, S. Magnetic nanoparticles for theragnostics. *Adv. Drug Deliv. Rev.* **61**, 467–477 (2009).
120. Cole, A. J., Yang, V. C. & David, A. E. Cancer theranostics: the rise of targeted magnetic nanoparticles. *Trends Biotechnol.* **29**, 323–332 (2011).
121. Singh, A. & Sahoo, S. K. Magnetic nanoparticles: a novel platform for cancer theranostics. *Drug Discov. Today* **19**, 474–481 (2014).
122. Roca, A. G. *et al.* Design strategies for shape-controlled magnetic iron oxide nanoparticles. *Adv. Drug Deliv. Rev.* **138**, 68–104 (2019).
123. Ovejero, J. G., Spizzo, F., Morales, M. P. & Del Bianco, L. Mixing iron oxide nanoparticles with different shape and size for tunable magneto-heating performance. *Nanoscale* **13**, 5714–5729 (2021).
124. Ferreira, M., Sousa, J., Pais, A. & Vitorino, C. The Role of Magnetic Nanoparticles in Cancer Nanotheranostics. *Materials* **13**, 266 (2020).
125. de la Encarnación, C., Jimenez de Aberasturi, D. & Liz-Marzán, L. M. Multifunctional

plasmonic-magnetic nanoparticles for bioimaging and hyperthermia. *Adv. Drug Deliv. Rev.* **189**, 114484 (2022).
126. Alromi, D., Madani, S. & Seifalian, A. Emerging Application of Magnetic Nanoparticles for Diagnosis and Treatment of Cancer. *Polymers* **13**, 4146 (2021).
127. Nemati, Z. *et al.* Improving the Heating Efficiency of Iron Oxide Nanoparticles by Tuning Their Shape and Size. *J. Phys. Chem. C* **122**, 2367–2381 (2018).
128. Sharma, S. K., Shrivastava, N., Rossi, F., Tung, L. D. & Thanh, N. T. K. Nanoparticles-based magnetic and photo induced hyperthermia for cancer treatment. *Nano Today* **29**, 100795 (2019).
129. Chu, M. *et al.* Near-infrared laser light mediated cancer therapy by photothermal effect of Fe3O4 magnetic nanoparticles. *Biomaterials* **34**, 4078–4088 (2013).
130. Espinosa, A. *et al.* Duality of Iron Oxide Nanoparticles in Cancer Therapy: Amplification of Heating Efficiency by Magnetic Hyperthermia and Photothermal Bimodal Treatment. *ACS Nano* **10**, 2436–2446 (2016).
131. Estelrich, J. & Busquets, M. Iron Oxide Nanoparticles in Photothermal Therapy. *Molecules* **23**, 1567 (2018).
132. Nemec, S. *et al.* Comparison of Iron Oxide Nanoparticles in Photothermia and Magnetic Hyperthermia: Effects of Clustering and Silica Encapsulation on Nanoparticles' Heating Yield. *Appl. Sci.* **10**, 7322 (2020).
133. Shivanna, A. T., Dash, B. S. & Chen, J.-P. Functionalized Magnetic Nanoparticles for Alternating Magnetic Field- or Near Infrared Light-Induced Cancer Therapies. *Micromachines* **13**, 1279 (2022).
134. Egea-Benavente, D., Ovejero, J. G., Morales, M. del P. & Barber, D. F. Understanding MNPs Behaviour in Response to AMF in Biological Milieus and the Effects at the Cellular Level: Implications for a Rational Design That Drives Magnetic Hyperthermia Therapy toward Clinical Implementation. *Cancers* **13**, 4583 (2021).
135. Farzin, A., Etesami, S. A., Quint, J., Memic, A. & Tamayol, A. Magnetic Nanoparticles in Cancer Therapy and Diagnosis. *Adv. Healthc. Mater.* **9**, 1901058 (2020).
136. Guardia, P. *et al.* Water-Soluble Iron Oxide Nanocubes with High Values of Specific Absorption Rate for Cancer Cell Hyperthermia Treatment. *ACS Nano* **6**, 3080–3091 (2012).
137. Naud, C. *et al.* Cancer treatment by magneto-mechanical effect of particles, a review. *Nanoscale Adv.* **2**, 3632–3655 (2020).
138. Nikitin, A. A., Ivanova, A. V., Semkina, A. S., Lazareva, P. A. & Abakumov, M. A. Magneto-Mechanical Approach in Biomedicine: Benefits, Challenges, and Future Perspectives. *Int. J. Mol. Sci.* **23**, 11134 (2022).
139. Kim, D.-H. *et al.* Biofunctionalized magnetic-vortex microdiscs for targeted cancer-cell destruction. *Nat. Mater.* **9**, 165–171 (2010).
140. Mansell, R. *et al.* Magnetic particles with perpendicular anisotropy for mechanical cancer cell destruction. *Sci. Rep.* **7**, 4257 (2017).
141. Shen, Y. *et al.* Elongated Nanoparticle Aggregates in Cancer Cells for Mechanical Destruction with Low Frequency Rotating Magnetic Field. *Theranostics* **7**, 1735–1748 (2017).
142. Taher, Z. *et al.* Magnetosomes and Magnetosome Mimics: Preparation, Cancer Cell Uptake and Functionalization for Future Cancer Therapies. *Pharmaceutics* **13**, 367 (2021).
143. Kuzajewska, D., Wszołek, A., Żwierełło, W., Kirczuk, L. & Maruszewska, A. Magnetotactic

Bacteria and Magnetosomes as Smart Drug Delivery Systems: A New Weapon on the Battlefield with Cancer? *Biology* **9**, 102 (2020).

144. Vargas, G. *et al.* Applications of Magnetotactic Bacteria, Magnetosomes and Magnetosome Crystals in Biotechnology and Nanotechnology: Mini-Review. *Molecules* **23**, 2438 (2018).
145. Kotakadi, S. M., Borelli, D. P. R. & Nannepaga, J. S. Therapeutic Applications of Magnetotactic Bacteria and Magnetosomes: A Review Emphasizing on the Cancer Treatment. *Front. Bioeng. Biotechnol.* **10**, 789016 (2022).
146. Fdez-Gubieda, M. L. *et al.* Magnetotactic bacteria for cancer therapy. *J. Appl. Phys.* **128**, 070902 (2020).
147. Gandia, D. *et al.* Unlocking the Potential of Magnetotactic Bacteria as Magnetic Hyperthermia Agents. *Small* **15**, 1902626 (2019).
148. Martín, M. *et al.* Artificial Magnetic Bacteria: Living Magnets at Room Temperature. *Adv. Funct. Mater.* **24**, 3489–3493 (2014).
149. Li, Q. *et al.* Nanoparticle-Regulated Semiartificial Magnetotactic Bacteria with Tunable Magnetic Moment and Magnetic Sensitivity. *Small* **15**, 1900427 (2019).
150. Wu, K. *et al.* Magnetic Particle Spectroscopy: A Short Review of Applications Using Magnetic Nanoparticles. *ACS Appl. Nano Mater.* **3**, 4972–4989 (2020).
151. Zhou, J., del Rosal, B., Jaque, D., Uchiyama, S. & Jin, D. Advances and challenges for fluorescence nanothermometry. *Nat. Methods* **17**, 967–980 (2020).
152. Li, Z. *et al.* Simultaneous Local Heating/Thermometry Based on Plasmonic Magnetochromic Nanoheaters. *Small* **14**, 1800868 (2018).
153. Zhong, J., Liu, W., Kong, L. & Morais, P. C. A new approach for highly accurate, remote temperature probing using magnetic nanoparticles. *Sci. Rep.* **4**, 6338 (2014).
154. Zhong, J., Liu, W., Jiang, L., Yang, M. & Morais, P. C. Real-time magnetic nanothermometry: The use of magnetization of magnetic nanoparticles assessed under low frequency triangle-wave magnetic fields. *Rev. Sci. Instrum.* **85**, 094905 (2014).
155. Wu, K. *et al.* Superparamagnetic nanoparticle-based viscosity test. *Appl. Phys. Lett.* **107**, 053701 (2015).
156. Zhong, J., Schilling, M. & Ludwig, F. Magnetic nanoparticle thermometry independent of Brownian relaxation. *J. Phys. Appl. Phys.* **51**, 015001 (2018).
157. Perreard, I. M. *et al.* Temperature of the magnetic nanoparticle microenvironment: estimation from relaxation times. *Phys. Med. Biol.* **59**, 1109–1119 (2014).
158. Elrefai, A. L., Yoshida, T. & Enpuku, K. Effect of viscosity on harmonics signals of magnetic nanoparticles for thermometry application. *J. Magn. Magn. Mater.* **491**, 165480 (2019).

Chapter 2

Objectives

Micro/nanoparticles were aimed to be designed and developed for their application in different biomedical fields. As a general approach, the bioinspired or the aimed biomimetic features are translated to the designed synthetic micro/nanoparticles, and their applicability for the specific biomedical application is tested.

Specifically, three main objectives were set:

- The generation of surface-functionalized ellipsoidal particles for vaccine development.
- The development of neuromelanin-like nanoparticles for Parkinson's disease treatment by using coordination and supramolecular interactions.
- The synthesis of core-shell nanoparticles or ellipsoidal microparticles with magnetic and/or photoresponsive properties for cancer therapy.

For each of them, the specific tasks were aimed:

- Design and development of the specific size, shape, and structure of particles.
- Characterization and evaluation of physicochemical properties.
- Assessment of biological or therapeutical effects *in vitro* or *in vivo.*

Chapter 3

3. Neuromelanin-like nanoparticles as dopamine delivery system for Parkinson's disease treatment.

In this chapter, divided into two sections, bioinspired neuromelanin nanoparticles were designed by coordination chemistry. In both cases, iron and dopamine were used as constitutive materials to obtain new Parkinson's treatments by dopamine delivery after intranasal administration. On one side, nanoparticles made by supramolecular interactions of tris iron-dopamine complexes were accomplished. Their morphological and chemical characterization was carried out, and their applicability for intranasal administration was evaluated employing a cell culture model (RPMI 2650) of nasal tissue. The ability of nanoparticles to cross the cell monolayer of the nasal cells model was slightly lower than free dopamine but still considered a therapeutic amount.

In the second part, nanostructured coordination polymers were synthesized. The colloidal stability was evaluated under different conditions, and a growth factor was successfully encapsulated. The almost absence of reactive oxygen production was demonstrated *in vitro* using a dopaminergic cell line. Finally, their therapeutic effect was evaluated *in vivo* in a parkinsonian rat model after intranasal administration.

In both cases, an outstanding encapsulated amount of dopamine was found, being one of the main nanoparticle's components. Moreover, non-covalent bonding was involved, allowing the release of dopamine with preserved therapeutical properties.

The first part of this work was carried out in collaboration with Dr. José das Neves, from the Nanomedicines & Translational Drug Delivery group of the i3S institute (Instituto de Investigação e Inovação em Saúde da Universidade do Porto).

The second part of the work was done in collaboration with the Protein Engineering and Nanomedicine group led by Dr. Julia Lorenzo, from the Institute of Biotechnology and Biomedicine.

3.1 Introduction

3.1.1 Coordination polymer nanoparticles in biomedicine

Coordination polymers (CP) are hybrid materials constituted by metal ions and organic bridging linkers via coordination bonds. Depending on the extending dimension of the CP, they can form 1D, 2D, or 3D structures (Figure 3.1).1 During polymer structuration, other noncovalent interactions can take place, such as hydrogen-bonding, π-π stacking, and van der Waals forces, which further influence the final structure.2,3 These materials offer the possibility to design a plethora of new structures and compositions thanks to their chemical and functional versatility, flexible structure, and morphology, while the directional metal-ligand interactions lead to easy miniaturization at the nanoscale.[4] Furthermore, the incorporation of metal ions could provide these materials with magnetic, electronic, optical, or catalytic properties.

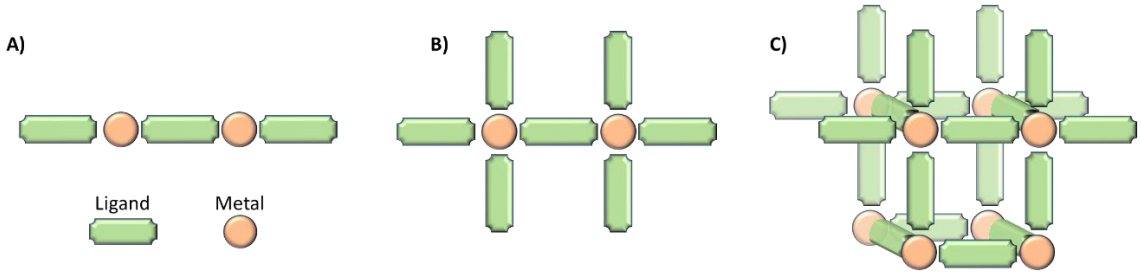

Figure 3.1: Schematic representation of dimensional structuration of CP: A) 1D, B) 2D, and C) 3D.

Nanometric CPs can be divided into nanoscale metal-organic frameworks (NMOFs) or nanoscale coordination polymers (NCPs). The NMOFs are highly ordered and porous crystalline structures, while the NCPs are amorphous systems that can be porous or nonporous. Thanks to their versatility, both have found huge success in the last years, with applications in several fields, including gas storage, nonlinear optics, sensing, and catalysis.[5] Notably, NMOFs/NCPs have attracted significant attention in nanomedicine due to their unique properties and advantages compared to other nanocarriers. First, being constituted by coordination interactions and not by covalent bonds, they can be easily biodegraded, while the choice of non-toxic metals made these nanoparticles biologically safe.[2] Secondly, the tunable composition and structure allow the synthesis of nanomaterials with different chemical properties, sizes, and shapes. Finally, NMOFs/NCPs have an excellent loading efficiency for several functional molecules.[6]

The common methods used for NMOFs and NCPs synthesis can be categorized into four general approaches: nanoscale precipitation, solvothermal, surfactant-templated or reverse microemulsion, and surfactant-templated solvothermal reactions (Figure 3.2). Usually, the first method generates only amorphous materials, while the others can lead to both amorphous or crystalline materials.[6]

- *Nanoscale precipitation method.* It consists in a simple one-pot reaction and is the most used approach for NCPs synthesis. It is based on out-of-equilibrium conditions where the single precursor ligands are soluble in the solvent used, while the polymer formed by their coordination is not and therefore it precipitate.[6] The resulting NCPs precipitate in the form of spherical particles to minimize the interfacial free energy between their surface and the solvent.[5] Different synthetic parameters can be adjusted to modulate the average dimensions of NCPs, such as pH, time, or stirring rate. Moreover, through external stimuli like ultrasonication, finer control over nanoparticles size could be achieved.[7]

- *Solvothermal Method*. It is usually applied for NMOFs synthesis and relies on the control of the nucleation and growth of crystals by employing high temperatures and pressures over time. These conditions, indeed, increase the solubility of the precursors and facilitate their interactions during the synthesis. Temperature can be provided by conventional heating, ultrasound, or microwaves,[8] and the reaction can occur in heated sealed containers, reactors, or autoclaves.

- *Surfactant-Templated Method*. In this method, surfactants are employed to stabilize water droplets in a nonpolar organic solvent. The microemulsion droplets act as nano-cells in which the precursors can coordinate with each other.[9] The surfactant-water ratio can influence the morphology or size of NMOFs or NCPs.[8]

- *Surfactant-Templated Solvothermal Method*. Surfactants can be used as a template during synthesis under solvothermal conditions. In this case, as the heating destroys the microemulsion, the stabilizers are not incorporated in the final formulation. However, they still play a fundamental role in defining the final coordination rate and morphology of NMOFs/NCPs.[10]

- *Other Approaches*. Other strategies have been employed for the synthesis of NMOFs or NCPs, like Dip-Pen Nanolithography which allows a direct growth of materials on surfaces through the

precise deposition of the precursors.[11] Another emerging approach is microfluidics, which provides fine and sophisticated control over synthetic parameters.[12]

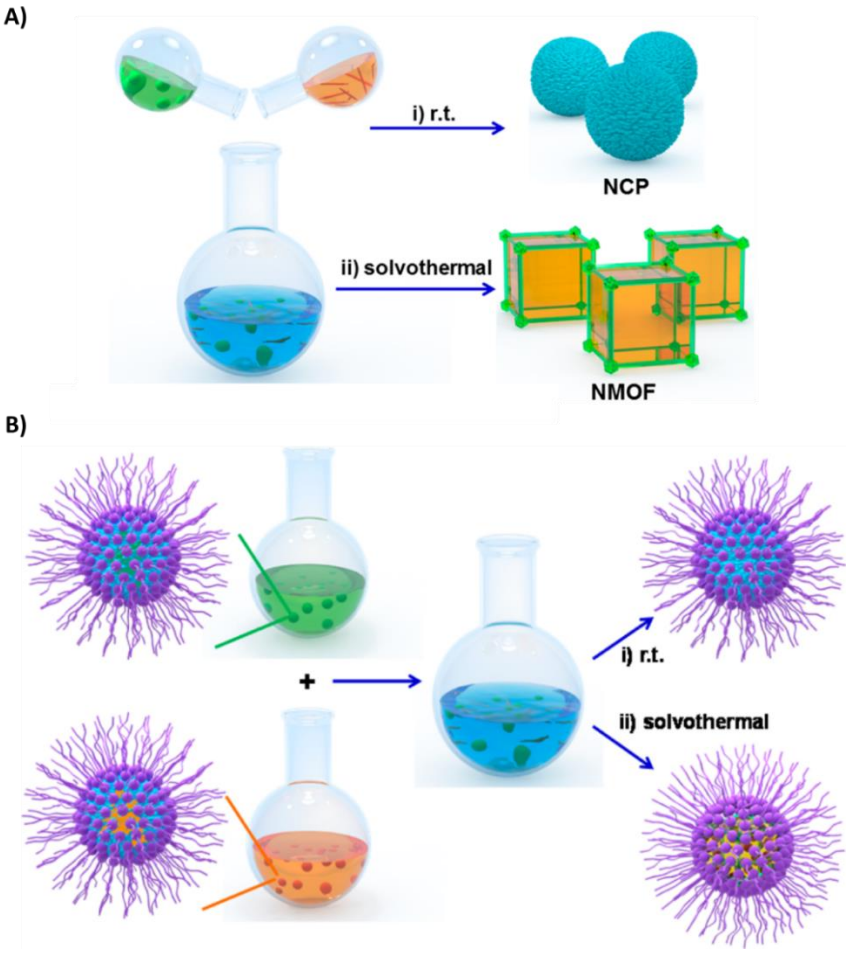

Figure 3.2: Schematic illustrations of common approaches for NCPs and NMOFs synthesis. A) i) Nanoscale precipitation method and ii) solvothermal method. B) i) Surfactant-templated method and ii) surfactant-templated solvothermal method. Reproduced from [6].

NMOFs have been the most studied CP over the past years. They present an exceptional surface area thanks to their inherent porosity, which provide an outstanding loading capacity. Furthermore, the crystallinity nature facilitates their chemical analysis and theoretical modeling.[13] On the other side, NCPs have attracted great attention since their first appearance in 2005.[14] Despite their less predictable structure and composition, as amorphous materials, they present several advantages over their crystalline counterpart, especially for their application in nanomedicine. First, they usually present a spherical shape and are obtained mainly by simple, low-cost, fully reproducible, and scalable reactions made at room temperature. The use of high temperatures in biomedical applications could represent a significant

limitation, since thermosensitive drugs or bioactive molecules, like proteins, can lose their activity.[9] Furthermore, they show good colloidal stability, easy surface functionalization, and control over the release.[15]

Two main encapsulation strategies can be recognized for NCPs. In the chemical entrapment, the active molecule or agent (e.g. drug) is directly incorporated in the NCPs structure, either as a bioactive metal ion or organic ligands[15] (Figure 3.3 A). In the second approach, the agents of interest can be physically entrapped in the structure of the nanoparticle during the NCPs formation via covalent or noncovalent interactions[6] (Figure 3.3 B). In the first case, an excellent loading efficiency with good distribution uniformity within the nanoparticles matrix can be achieved, though the morphology and size of the final nanoparticles could be more challenging to control, and precautions to avoid the degradation of the active molecule during synthesis must be taken. Upon physical encapsulation, NCPs tend to maintain the same morphological properties as the unloaded ones, allowing a easier modulation over the structural and morphological properties. However, the payloads (defined as the ratio of the amount of drug in the nanoparticles and the total weight of nanoparticles) and encapsulation efficiencies (defined as the amount of cargo encapsulated compared to the loaded quantity before the synthesis) accomplished with physical encapsulation strongly depend on the physicochemical properties of cargo molecules and their compatibility with the NCPs polymer matrix and often results in lower values.[5]

As expected, NCPs particles obtained through physical and chemical encapsulation also undergo two different release mechanisms of the cargo. In the case of physical entrapment, the active drug/molecule diffuses through the NCPs matrix, while in the chemical entrapment, the release occurs through the degradation of nanoparticles.[16] Following both approaches, several anticancer drugs, such as doxorubicin,[17] methotrexate,[18] and particularly platinum drugs (FDA approved cisplatin, carboplatin, and oxaliplatin) have been successfully encapsulated within NCPs with outstanding loading efficiency.[19]

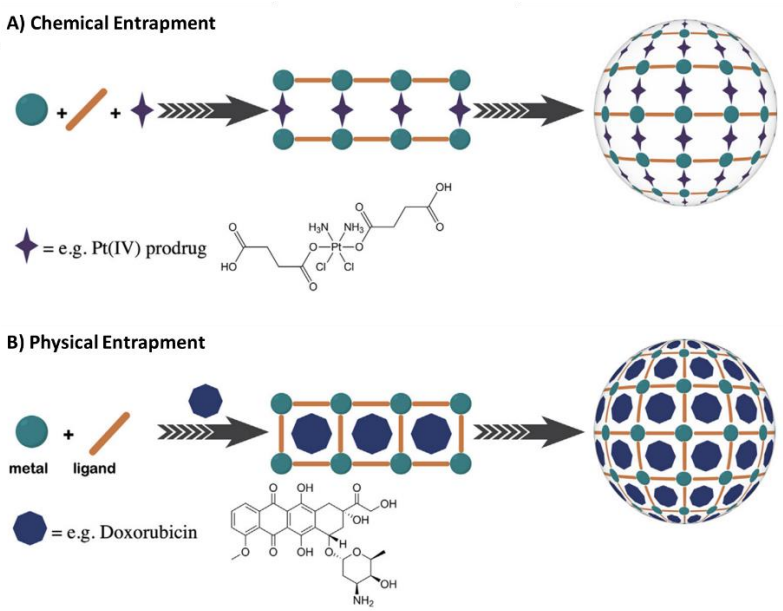

Figure 3.3: Schematic representation of the two different encapsulation strategies for NCPs for two different anticancer drugs. A) Chemical entrapment, and B) physical entrapment. Adapted from [15].

NCPs have been applied in photodynamic or photothermal therapies. They allow localizing photosensitizers or photothermal agents in the cancer region and thus selective confinement of the light effect, inducing the killing of only cancer cells and avoiding harmful effects for healthy tissues.[6] In NCPs designed for photodynamic therapy, the photosensitizers, i.e. molecules able to generate reactive oxygen species (ROS) under light irradiation at specific wavelengths, can be incorporated as ligands during NCPs synthesis.[10,20] In NCPs for photothermal therapy, inorganic or organic photothermal agents, which produce heat upon light irradiation, causing cancer cells' death, can constitute one of the polymeric components.[21]

On top of that, by incorporating metals, NCPs act as excellent imagining probes for different modalities, like magnetic resonance imaging (MRI), computerized tomography (CT) imaging, and optical imaging, improving those already described in the literature or even the commercial ones. Indeed, MRI contrast agents can improve image quality, modifying the relaxation times of water protons when the magnetic field is applied. However, common contrast agents need to be used at high concentrations to have enough contrast between healthy and diseased tissues, risking toxicity effects for the patients. On the contrary, NCPs could enhance the sensitivity without inducing harmful effects and act as dual T1/T2 contrast agents thanks to the incorporation of iron or gadolinium and manganese ions.[22,23]

However, despite the potential uses in different applications, only a few studies have been reported about the employment of CPs for Parkinson's disease (PD) therapy or diagnosis. In their work, Cheng *et al.* reported NCPs for PD treatment for the first time. In this case, they choose the natural molecule

curcumin as a therapeutic agent.[24] Curcumin is known to have excellent antioxidant and anti-inflammatory abilities and can ameliorate PD symptoms. The authors synthesized ultrasmall NCPs by coordinating the symmetric phenolic hydroxyl groups of curcumin and ferric ions. The resulting nanoparticles, stabilized with PVP and functionalized with a fluorescent molecule, had dimensions of 10 nm and great enzyme-like activities, both *in vitro* and *in vivo*. The authors tested the ability of NCPs to cross the blood brain barrier (BBB) through an *in vitro* model of endothelial bEnd.3 cells monolayer. Curcumin nanoparticles showed important neuroprotective effects against PD model cells, which were obtained by treating SH-SY5Y cells with 1-methyl-4-phenylpyridinium neurotoxic to inhibit mitochondrial redox functions. Moreover, after intravenous injection in mice, particles accumulated in the brain after 4 and 8 h. Induced mice PD model exhibited significant improvement in exercise ability after treatment with curcumin NCPs having a pronounced amelioration in the energy metabolism of the brain, by their scavenging activity (Figure 3.4).[24]

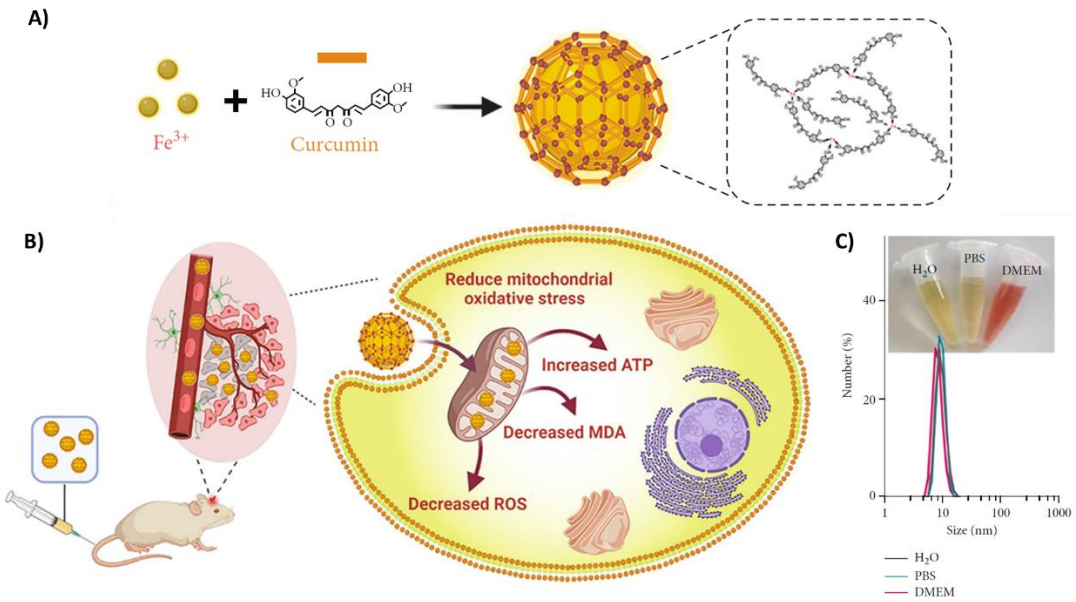

Figure 3.4: Schematic representation of A) curcumin-iron NCPs formation, and B) delivery of NCPs across the BBB after intravenous administration and their antiparkinsonian effects (ATP: adenosine triphosphate, MDA: malondialdehyde, ROS: reactive oxygen species). C) Size distribution measured by dynamic light scattering of NCPs in water, phosphate buffer (PBS), and cell cellular medium (DMEM); adapted from [24].

To the best of our knowledge, no other studies have been reported about NCPs for PD therapy, especially for dopamine (DA) delivery. The only example of use of coordination polymers, particularly MOFs, for DA replacement therapy is the work of Pinna *et al.*, published in 2018.[25] Their MOFs were

synthesized by inducing the growth of MIL-88A (fumaric acid-iron) around polymeric magnetic particles. The final size of MOFs varied between 3 and 6 μm. The magnetic properties were desired to manipulate the movement of the particles in the nasal cavity to reach the olfactory nerve. The authors demonstrate the ability of this system to prevent DA oxidation with an excellent loading efficiency (payload, LE) (0.61 mg/mg^{-1}) while having a sustained and controlled release. Moreover, these MOFs did not induce any cytotoxic effect on PC12 cell line, showing excellent biocompatibility. No significant level of DA was found in the extracellular environment, as DA probably underwent multiple chemical reactions. The intracellular DA amount increased in comparison to the control (with no treatment), and was slightly higher than the treatment with free DA.[25] It is interesting to underline that in this work the authors achieved one of the greatest DA LE up to today. Nevertheless, this system still needs further investigation to improve its *in vitro* and *in vivo* ability to increase physiological levels of DA.

Herein we propose to exploit the ability of catechols to coordinate iron to form DA-based NCPs. For this, an exceptionally high amount of encapsulated DA is expected. Furthermore, DA would be bound through non-covalent and reversible interactions, allowing its release *in vitro* and *in vivo.*

3.1.2 Iron-dopamine complexes

The ability of catechols to coordinate with metal ions is well-known and studied.[26,27] Notably, the complexation with iron is presented in various natural materials.[28,29] As mentioned in the Introduction section, neuromelanin is rich in iron content. The mussel byssus cuticle is another example of natural material presenting Fe-catecholate complexes. These provide enhanced mechanical, adhesives, and self-healing properties.

The bond between catechol and iron occurs through the coordination between the electron cloud on oxygen atoms of the hydroxyl groups and the vacant d-orbitals of the Fe(III) ions. The strength of this coordination bond is known to be of the magnitude of covalent ones.[29,30]

Catechol-metal coordination is responsive to the environment, especially dependent on the pH. Indeed, catechol can form mono, bis, or tris complexes with iron ions varying the pH (Figure 3.5). Moreover, each coordination state is characterized by a specific pH and a specific color and can be easily monitored by UV-vis spectroscopy. At pH lower than 5.6, mono-complexes are formed, with green color (λ_{max} = 710-730 nm); between pH 5.6 and 9.1, instead, bis catechol complexes are formed, with a blue-violet color (λ_{max} = 570-580 nm); finally, at basic pH higher than 9.1, the tris coordination occurs, with a purple-red color (λ_{max} = 480-490 nm). [31,32]

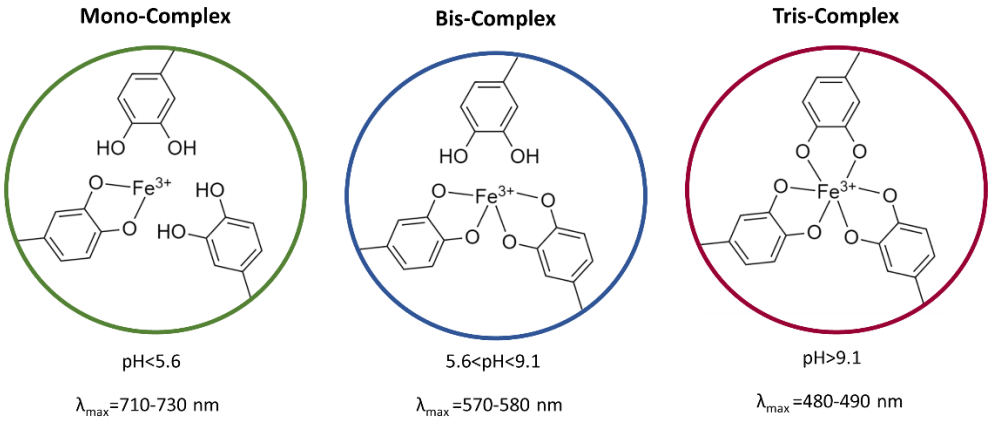

Figure 3.5: Schematic representation of catechol and ferric ions complexes at different pH, with the corresponding maximum absorbance. Reproduced from [33].

The spontaneous self-assembly driven by iron-catechol coordination has been applied to obtain functional materials, like coating or nanoparticles. Remarkably, several bioadhesives have been studied and synthesized inspired by mussels.[34] However, as the spontaneous oxidation and crosslink of DA easily occur, the control over the formation of nanoparticles is challenging,[35,36] requiring most of the time an initial template s needed.[37]Significant efforts have been put in the last years to exploit the metal coordination crosslinking in the synthesis of protein and polymeric hydrogel nanoparticles. Some examples of the formation of solid nanoparticles or hollow nanocapsules with control over morphology and size are reported.[35,36,38] In all cases, the nanostructures were obtained through the synergy between polymer self-assembly and catechol–metal ion coordination. Such coordination has been employed to realize pH-responsive hydrogels taking inspiration from the mussel foot properties.[33,39] Jin Kim *et al.* used this principle to control the delivery of doxorubicin by stimuli response. In their work, they obtained mussel-derived adhesive protein nanoparticles modified with stoichiometric iron-dopamine complexes, which both constitute the stimuli-responsive unit as the crosslinker.[40]

3.2 Objectives

Parkinson's disease is one of the principal neurodegenerative diseases, affecting the lives of millions of people worldwide. The current treatments, based on DA replacement, exhibit several drawbacks, and the new nano-delivery systems proposed today still show considerable limitations, such as the difficulties in reaching the brain and the low DA content. Therefore, the need to find new efficient solutions is urgent.

Herein, we proposed two possible strategies to achieve more suitable DA loading, and by the synergy with a new administration route, the intranasal, an essential improvement in Parkinson's therapy is expected. Inspired by natural neuromelanin, the main components for both type of nanoparticles have been selected as DA and iron. Considering the ability of DA to coordinate, the possibility of obtaining neuromelanin-like supramolecular nanoparticles was investigated.

Even though the original intention was to accomplish NCPs, a first strategy based on a more accessible synthetic approach and presenting a simpler chemical structure was evaluated. Nanoparticles based on iron-DA tris coordination complexes nanostructured by supramolecular interactions between the non-linked complexes were prepared and studied in this work (Figure 3.6). These nanoparticles would offer a considerable DA cargo, as mainly constituted only by it. The nanostructuration would protect DA from oxidation and allow its sustainer release. The synthesis optimization has been performed with the aim of achieving the highest reversible tri-complexation yield while avoiding polydopamine formation. Indeed, the absence of irreversible covalent bonding involving DA (in DA polymerization) is crucial for its delivery. Moreover, their potentiality for intranasal administration has been evaluated. This method resulted quite innovative and straightforward; however, chemical lability can be expected.

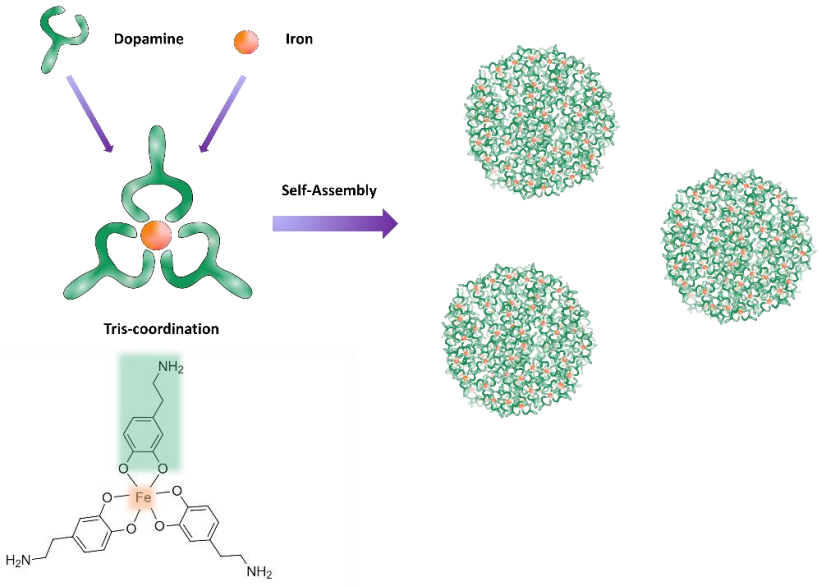

Figure 3.6: Schematic representation of DA-based supramolecular nanoparticles.

Therefore, a second strategy was explored based on the original idea to achieve NCPs, in which higher chemical stability is expected. A slightly more complex synthetic route was designed, where iron and DA form bis-coordination, while a second ligand (1,4-bis(imidazol-1-ylmethyl)benzene, Bix) also coordinates with iron, contributing to the formation of NCPs (Figure 3.7). Here, the amount of leaded DA is expected to be still elevated. Special attention has been paid to the reproducibility of the NCPs protocol's synthesis, size optimization, and chemical characterization. Moreover, reactive oxygen species (ROS) generation in dopaminergic cells and the investigation of NCPs internalization mechanisms have also been evaluated. Considering the multidisciplinarity of this work, it has been carried out in collaboration with experts from different research centers. Dr. Javier Pardo has performed an extensive part of the work, and the *in vitro* studies have been carried out at the Institut de Biotecnologia i de Biomedicina (IBB) in collaboration with the Protein Engineering and Nanomedicine group led by Prof. Julia Lorenzo. Moreover, animal studies were performed in the Vall d'Hebron Research Institute, to corroborate the intranasal administration applicability of these nanoparticles.

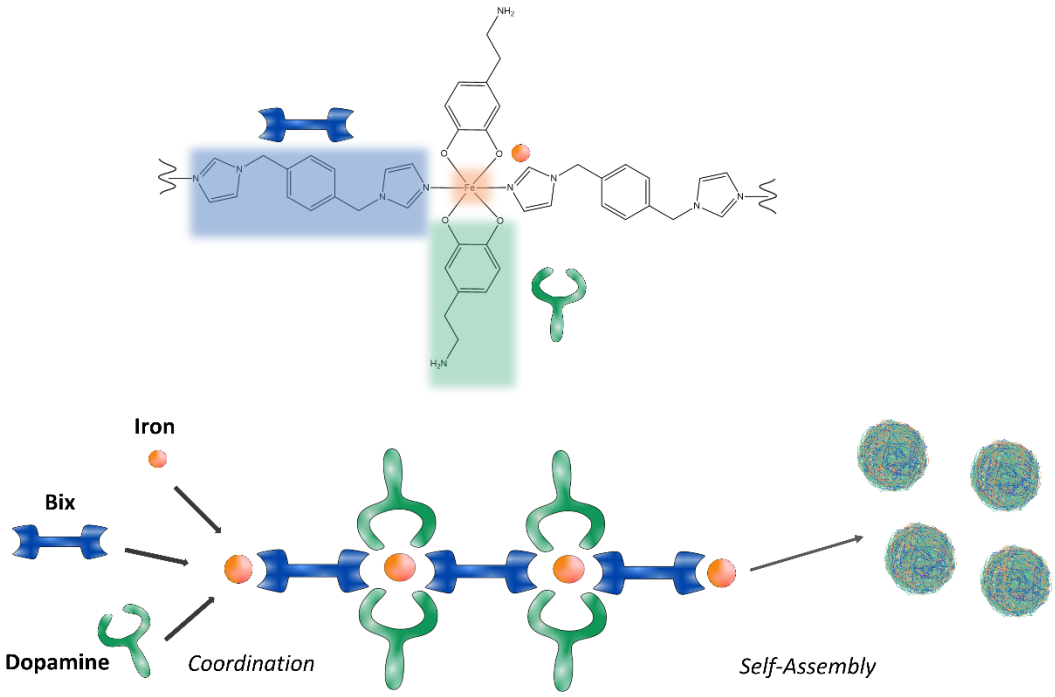

Figure 3.7: Schematic representation of synthetic rout for DA-based NCPs.

3.3 Supramolecular nanoparticles based on tris-coordination complexes and their application for dopamine delivery

3.3.1 Synthesis of supramolecular nanoparticles

The synthesis of neuromelanin-like iron-dopamine nanoparticles (Fe-DA-NPs) was designed through a simple one-pot solution reaction, where Fe was added to DA solution (Figure 3.8), following a similar procedure as NCPs synthesis.[41]

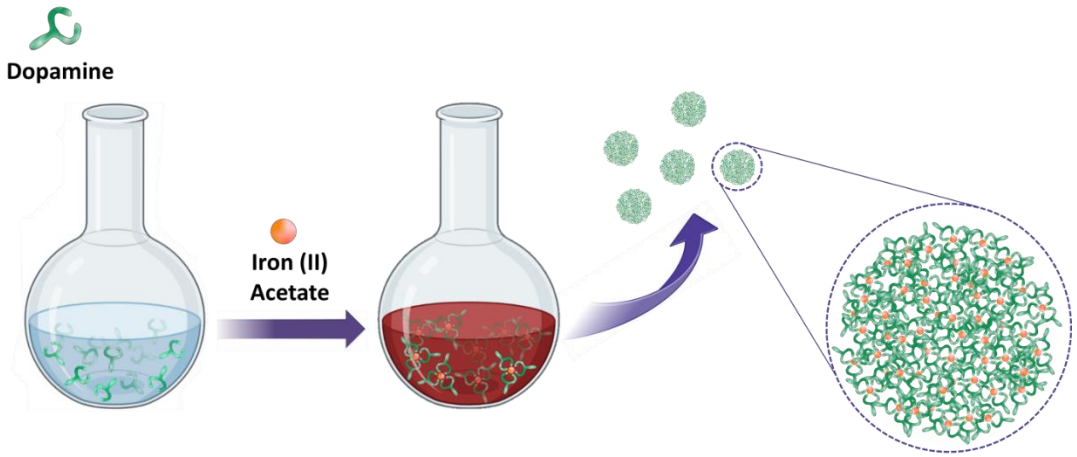

Figure 3.8: Schematic representation of Fe-DA-NPs synthesis. Iron(II) acetate is added to a DA solution in sodium tetraborate buffer, causing the immediate color change and the consequent particles' formation.

Tris complexation between Fe and DA is well known to have a characteristic color as dark purple/red wine, and it takes place at pH higher than 9, as mentioned in the introduction. Furthermore, DA tends to oxidize quickly and then polymerize once dissolved in basic buffers. Therefore, the particles' synthesis has been optimized to have the desired reaction color while protecting from or avoiding DA oxidation. The desired tri-coordination and the described color was aimed to be maintained even after dilutions in water. To corroborate the tri-complexes formation and the absence of polydopamine, UV-vis spectroscopy was employed during synthesis optimization as sensitive and reliable method to monitor catechol-metal coordination. Indeed, the appearance of the characteristic absorption band at 490 nm[32,42] and the absence of black color and a broad absorption from UV to near-infrared (NIR) spectral regions confirm the successful complexation between Fe and DA and the absence of polydopamine respectively.

Several parameters were optimized for these purposes.

i) pH: the basic condition of the synthesis buffer has been modulated to have a final pH of 9. In the synthetic process, DA hydrochloride was employed, which led to a drastic decrease in the pH once dissolved. Thus, a solvent with a higher starting pH was needed. However, when buffers with pH around 10-12 were employed, DA solution rapidly changed color, turning brown, suggesting a fast DA polymerization. Therefore, the pH was modulated with the addition of a few microliters of 1M NaOH solution after the coordination of DA with iron started.

ii) Inert atmosphere: argon was used to avoid oxygen presence, slowing down the oxidation of DA, favoring the formation of supramolecular particles. However, no differences were observed at the end of the reaction with or without inert atmosphere.

iii) Iron salt: as the first choice, iron(III) chloride was chosen for neuromelanin-like particles' synthesis. However, a green color was observed after the iron addition to DA solution, typical for a mono-coordination of DA to the iron. With the use of iron(III) nitrate, instead, the tris coordination was ensured, though no nanostructuration was observed. Finally, iron(II) acetate was used, showing better results since the desired color (and spectral) change and formation of NPs were both achieved.

iv) Reaction media: different buffers were used to obtain a chemically stable tris-complexation.

- Tris buffer was initially chosen for its wide use in the synthesis of polydopamine-doped nanoparticles. At the beginning of the reaction, the purple color appeared, but it turned black after a short time.
- In ethanol (EtOH), the pH tuning was more complex, and a blue color was observed during the synthesis, indicating a bis coordination.
- When sodium bicarbonate was used, a black color was noticed after dilution in water, followed by a slow precipitation process, which can be ascribe to polydopamine formation.
- Sodium tetraborate (commercially known as Borax) appeared to be the best buffer, as it prevents DA oxidation.[43] In all the previous buffers studied, when DA was dissolved, the color gradually turned yellow in a relatively short time (less than 15 minutes). In contrast, when Borax was employed, the yellow color appeared after much longer time, giving a colorless DA solution for almost 30 minutes. After iron addition, the color changed immediately to purple (Figure 3.9 A), and it was maintained after the dilution in water (Figure 3.9 B). Therefore, sodium tetraborate was chosen as the buffer for the synthesis of nanoparticles.

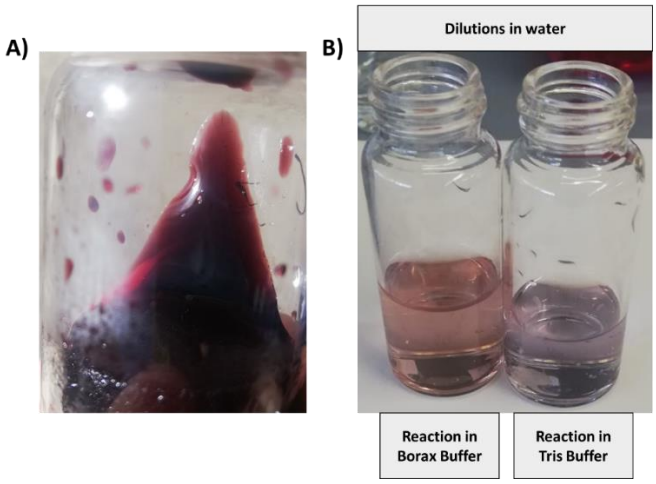

Figure 3.9: A) Picture of Fe-DA-NPs after the synthesis in sodium tetraborate buffer. B) Pictures of Fe-DA-NPs synthesized in sodium tetraborate buffer (left sample) or Tris buffer (right sample) after dilution in water.

The tris coordination was confirmed by UV-vis spectroscopy, after the dilution of Fe-DA-NPs in different media (Figure 3.10). In PBS (pH 7.4) and sodium tetraborate buffers (pH 9), a peak at λ_{max} = 285 nm, ascribed to DA, appeared,[44] while it redshifted to λ_{max} = 290 nm in water. On the other hand, the absorption band position related to the complex varied depending on the medium, from λ_{max} = 555 nm in PBS (closer to the bis-catechol iron complex, 570-580 nm), λ_{max} = 505 nm in sodium tetraborate (which lays between the bis and tris complexes) and λ_{max} = 495 in water, being the closest to the tris-coordinated absorption band, confirming its choice as buffer for nanoparticles synthesis.

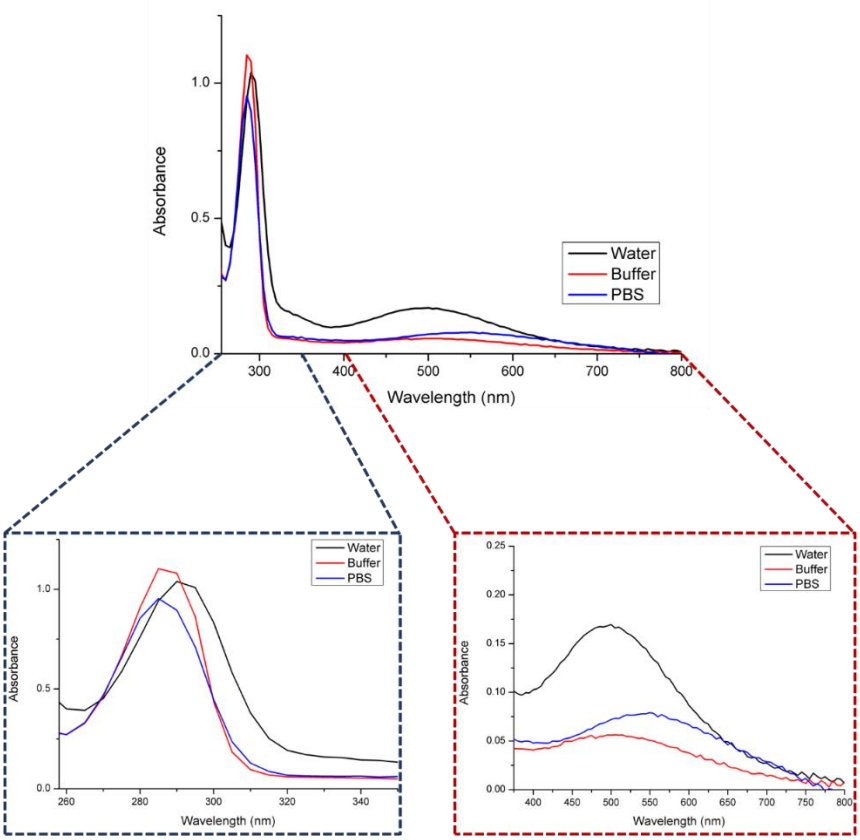

Figure 3.10: Absorbance spectra of Fe-DA-NPs dispersed in different buffers: water (black line), sodium tetraborate buffer (red line), and PBS (blue line); zoom-in spectra (blue and red boxes).

During the synthesis, it was possible to observe the formation of a fine black precipitate, which was removed by filtration, leading to a completely transparent solution. The fine black precipitate removed by filtration after Fe-DA-NPs synthesis was also investigated by scanning electron microscopy (SEM). Figure 3.11 shows the presence of tiny particles, around 30-50 nm diameter, ascribed to the formation of iron-oxide nanoparticles due to the interaction between Fe and NaOH.[45] It was also confirmed by the significant percentage of iron detected by EDX.

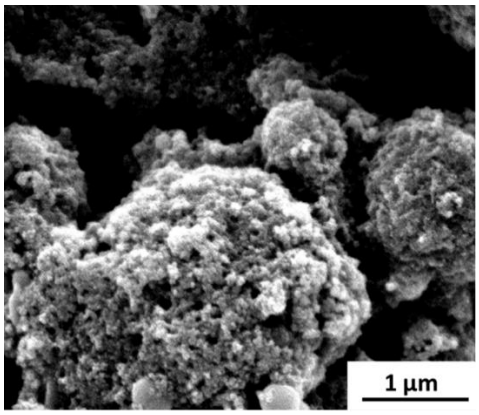

Figure 3.11: SEM images of precipitated removed by filtration after Fe-DA-NPs synthesis.

3.3.2 Morphology and size

To study the dimensions and size distribution of Fe-DA-NPs, the hydrodynamic diameter was measured by dynamic light scattering (DLS) (Figure 3.12 A). The hydrodynamic diameter of NPs was 201.8 ± 30.1 nm, with PDI of 0.185. However, DLS did not reveal a reliable technique for the characterization. Indeed, problems of reproducibility and stability were faced during measurements, most probably because of the intense color of the samples or the large dilution applied to minimize the absorption. Nanoparticles tracking analysis (NTA), using a NanoSight, was employed to evaluate the size and the concentration of Fe-DA-NPs. This method allows to see NPs moving in suspension and, by following their trajectory during time, the particles size can be determined. Figure 3.12 B shows a major NPs population with size of 70-80 nm, and a minor one with diameter around 100-150 nm, for an overall diameter average of 117.3 ± 2.2 nm. Particles had a total concentration of $112 \times 10^8 \pm 3.3 \times 10^7$ particles/ml. Figure 3.12 C shows three frames of the collected video by NanoSight, where the movements of nanoparticles are recognized. Furthermore, after NanoSight analysis, the absorption spectrum of the nanoparticles suspension was collected, and no differences were found with the spectrum obtained before the measurements, indicating that the nanoparticles detected by the Nanosight were not made by polydopamine.

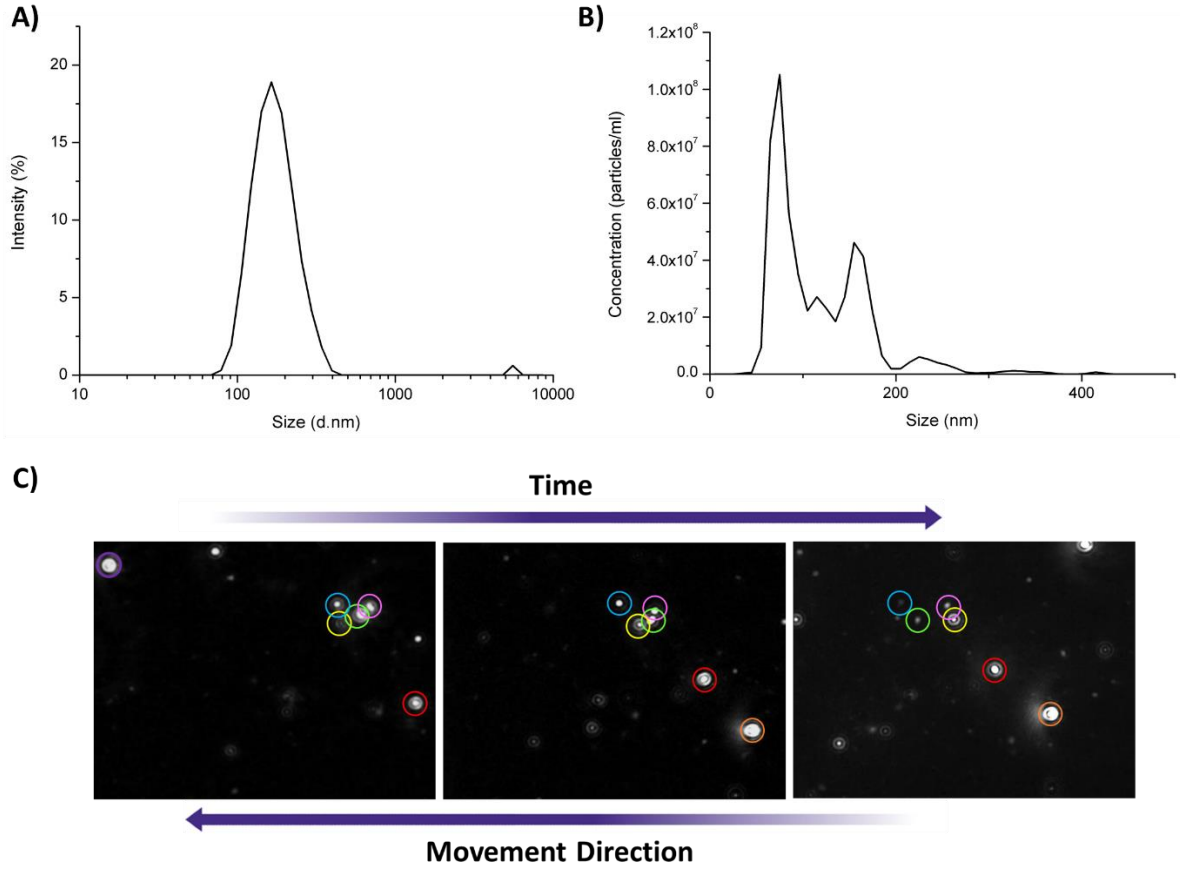

Figure 3.12: A) DLS measurement and B) NTA analysis of Fe-DA-NPs re-dispersed in water, C) three frames of recollected video by NanoSight. Each particle is recognized and marked with a colored circle and its movement is followed over time.

To confirm the morphology and size of Fe-DA-NPs, SEM was employed. As shown in Figure 3.13 A,B, spherical nanoparticles, of 90-120 nm diameter, with smooth surface, were obtained. This dimension appeared to correspond to the main population for all samples observed. However, some larger particles (300 nm) were also found. This heterogeneity in dimensions was first justified by assuming that larger particles were obtained from DA polymerization, which could occur due to water dilution or air exposure during the sample drying. Hence, to corroborate it, samples not subjected to dilution or turned to solid powder through oxygen-free freeze-drying, were also examined by SEM. In both cases, nanoparticles with the same morphology and size dimension were obtained, with also the presence of some larger particles. Furthermore, the freeze-dried nanoparticles appeared to be as light purple powder, easily dispersable in water, which evidences the absence of polydopamine. Indeed, solid-state polydopamine-iron nanoparticles appear to be a black paste with adhesive features and completely not dispersable in water.[46] It is also important to mention SEM also showed a significant contribution from crystals (Figure 3.13 E) coming from the presence of sodium tetraborate. Moreover, non-structured

material was found, most probably constituted by free DA (Figure 3.13 F). This is possibly due to the fact that Fe-DA-NPs did not undergo to cleaning process before SEM analysis.

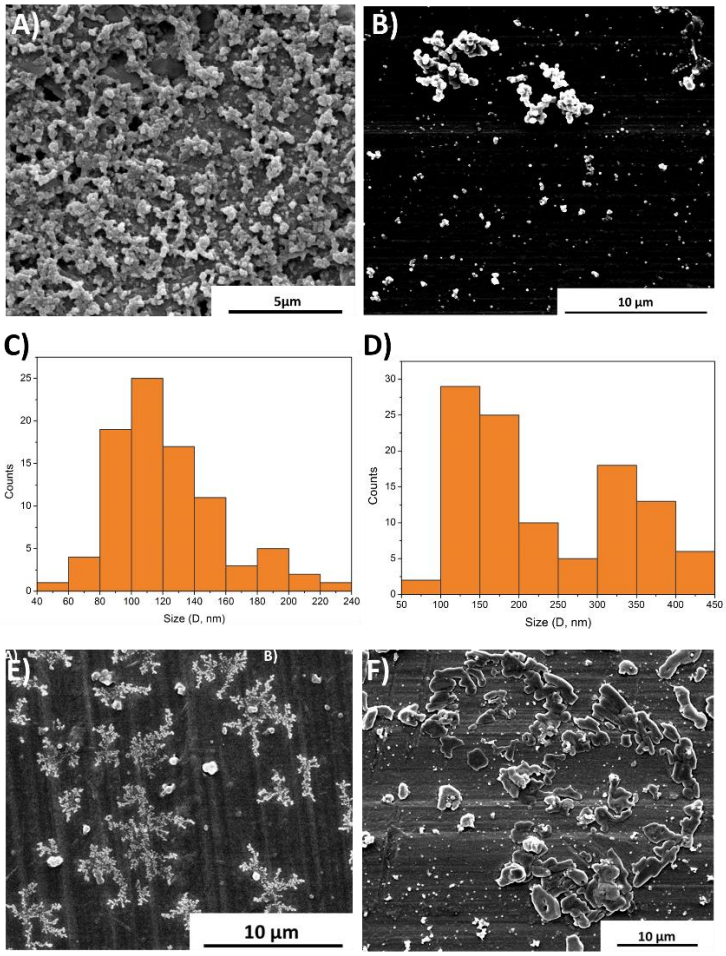

Figure 3.13: A-B) SEM images of Fe-DA-NPs with correspondent size distribution (C-D). SEM image of E) crystals of salts formed after water evaporation and F) unstructured materials.

3.3.3 Chemical characterization

a) Spectroscopy characterization

To quantify the amount of DA present in Fe-DA-NPs UV-vis spectroscopy was employed, following a method already reported.[47] A stock solution of DA was prepared by dissolving in an aqueous solution of HCl, used to avoid its oxidation and polymerization, and ensuring the linearity of the absorption signal. The absorbance values at 280 nm of different dilutions of DA were measured and plotted against

concentration. NPs were completely degraded by the same acid conditions, and the absorption spectrum was recorded, where the band at 450 nm disappeared and the band at 280 nm was used for DA quantification. The LE of DA was 22% w/w; this value is comparable to the ones already reported in the literature, appearing relatively low.[48,49] However, when the entrapment efficiency (EE) was calculated, it appeared to be remarkably high, equal to 81% w/w. This discrepancy in values comes from the overestimation of NPs total weight. Indeed, the contribution of sodium tetraborate salt is also considered in the calculation. Thus, as the salt weight is excluded from it, the actual DA cargo can be considered much higher. DA amount was also determined with high-pressure liquid chromatography with electrochemical detection (HPLC-ECD). Through this method, which is highly sensitive it was determined a LE of 33% w/w.

On the other hand, the presence of Fe in Fe-DA-NPs was confirmed by EDX and quantified by inductively coupled plasma-optical emission spectroscopy (ICP-OES). A small amount of iron was found, resulting in a LE of 0.47% w/w. This low value is ascribed by the fact that most of the metal used during the synthesis is filtered in the form of iron oxide nanoparticles aggregates. The measured Fe/DA molar ratio (1:14) resulted much smaller than the theoretical value (1:3), which indicates an excess of DA in the NPs and its encapsulation, not only as chemically tris-coordinated moieties, but also as free molecules physically entrapped in the NP matrix. Most probably, a high amount of the DA is entrapped in the middle of nanoparticles during their formation by molecular interaction between free and coordinated DA. However, since DA is considered the desired drug to be delivered for PD's treatment, having an extra load can be considered a positive aspect.

Through Fourier-transform infrared spectroscopy (FT-IR) spectroscopy of the Fe-DA-NPs (Figure 3.14); the coordination of DA to Fe was confirmed by the presence of the peak between 1200-1280 cm^{-1}, associated to the C-O stretching from catechol after coordination. Furthermore, from the comparison with the FTIR spectrum of free DA, the stretching of the amine group of DA at 3340 cm^{-1} was also identified in the NPs, while the bending vibration shifted from 1616 to 1597 cm^{-1}. The broad band at 3000-3500 cm^{-1}, associated to the stretching of –OH groups is still detectable in the particles spectrum, which was ascribed to the DA molecules not coordinated.. Additionally, a contribution from sodium tetraborate can also be recognized by the peaks in the range of 900-1000 cm^{-1}.

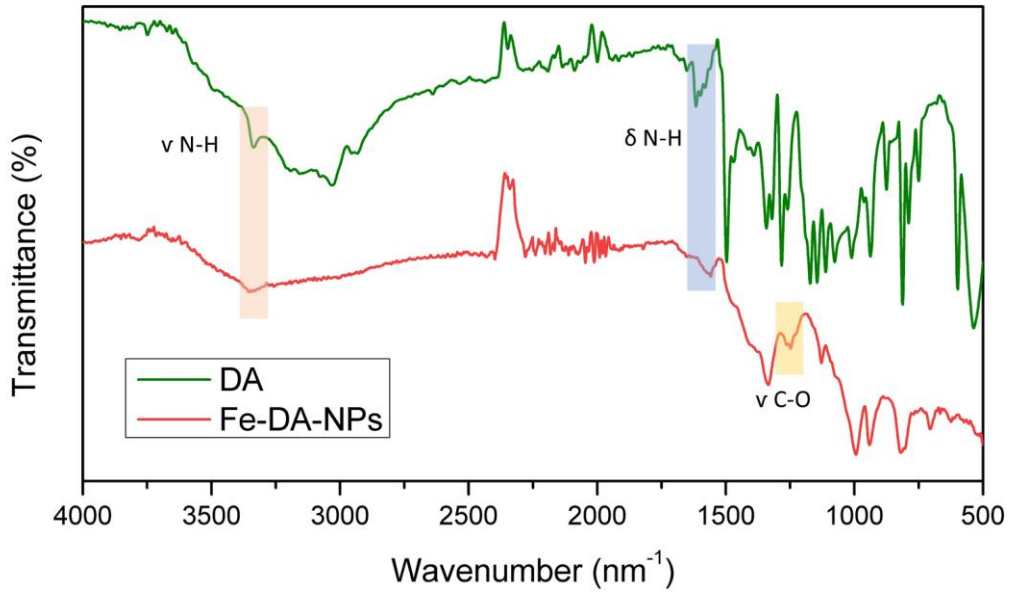

Figure 3.14: FT-IR spectra of DA (green line) and Fe-DA-NPs (red line) (ν: stretching; δ: bending).

b) Chemical stability of the Fe-DA-NPs

To further investigate the chemical stability of Fe-DA-NPs, the absorbance UV-Vis spectrum was measured over time after dilution in water (20 µl in 2 ml). It is important to study the stability after dilution as Fe-DA-NPs would result more expose to oxidation and polymerization and being closer to the biological environment. Water was initially chosen as a milder condition for DA polymerization or oxidation induction (Figure 3.15 A). The band at 495 nm was used to monitor the potential discoordination and/or the polymerization of DA. After one hour, only a small shift to 490 nm was observed, suggesting how the tris coordination of nanoparticles is preserved. However, 2 h later, the spectrum changed, with an additional shift to 480 nm and an increase of absorbance all over the spectrum. At 3 h, the coordination band was no longer appreciable, and the absorption spectrum increased all over the measured range basically changing its baseline and suggesting an increase of light scattering. This tendency was ascribed to the formation of polydopamine which precipitated as nanoparticles, producing light scattering.[50]

This behavior was not observed when the NPs suspension was kept for 3 h in the initial condition, obtained right after the synthesis, at higher concentration, and then diluted in deionized water (Figure 3.15 B). However, when the diluted solution was left for 5 h, it turned from brownish to black (Figure 3.15 C). These findings suggest that Fe-DA-NPs can be considered chemically stable for almost one hour after dilution. Furthermore, this stability is not affected and is preserved for more than 5 h if no dilution

is made. Indeed, before dilution, Fe-DA-NPs were at a higher concentration (X mg/ml), which could act as a self-protection from oxidation. Indeed, nanoparticles would results less exposed to the environment, with a reduced interaction with water molecules.

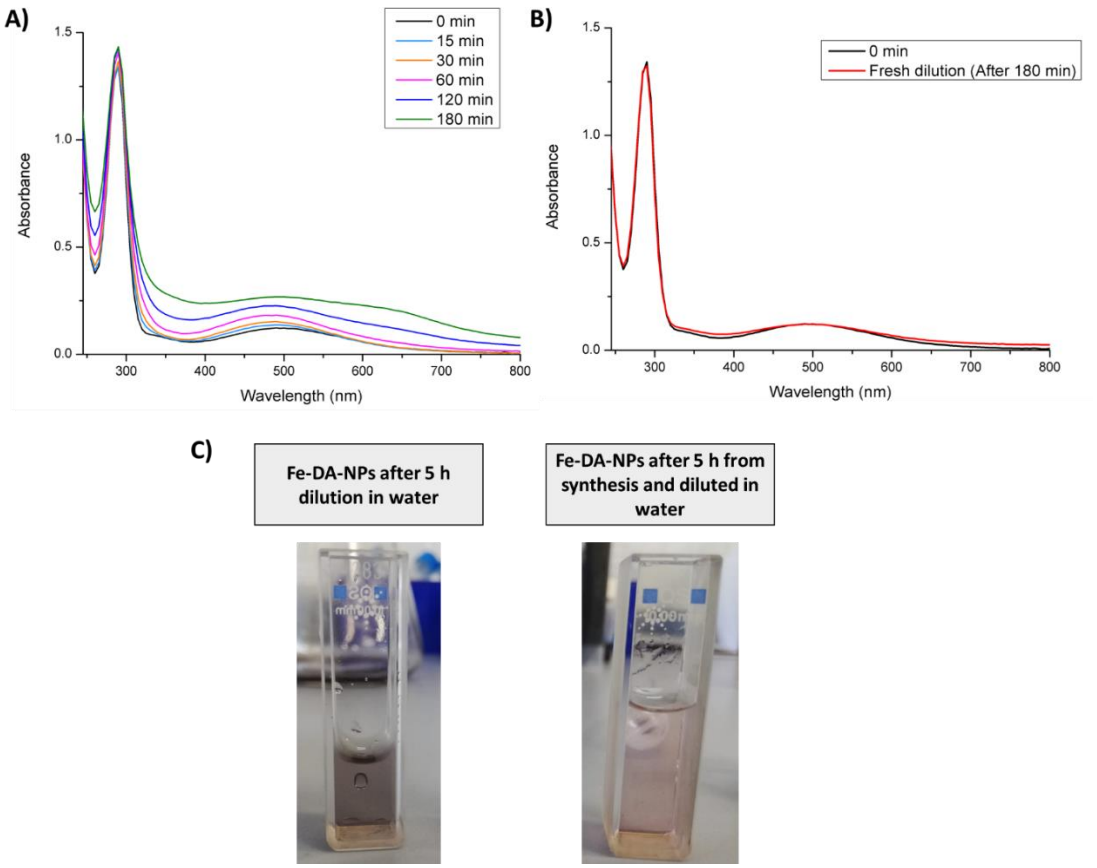

Figure 3.15: Absorbance spectra of Fe-DA-NPs A) measured every 15 minutes after the addition of 20 µl of NPs in 2 ml of deionized water, B) measured after the same dilution in water (20 µl in 2 ml), immediately after particles' synthesis, (black line) or making a fresh dilution after 180 minutes (red line). C) Pictures of samples after 5 h from the dilution in water (left sample) or after making a new dilution at 5 h from the synthesis (right sample).

Once obtained the Fe-DA-NPs and studied their stability, their properties were investigated for DA release and their possible use as contras agent.

c) Release profile study

The DA release from Fe-DA-NPs was evaluated through a dialysis bag method (Figure 3.16). The study was performed in simulated nasal mucus, a buffer mimetic to the nasal physiological condition, where particles would face the first biological barrier before reaching the brain. The salts and pH (6.2)

were selected as the closest to the nasal mucosa ones, following a receipt reported in the literature.[51] The natural antioxidant, ascorbic acid, was added at high concentration to prevent DA oxidation. Aliquots of the solution outside the dialysis bag were collected at different times, and the released DA amount quantified by HPLC-EDC. The accumulated DA was plotted against time (Figure 3.16). Since an excess of DA was quantified at the end of the release study, resulting in a collected DA amount slightly over the expected 100% w/w, the amount of released DA at each time was normalized respect to the overall collected DA at the end of the study, when all the DA was considered released. After only 15 minutes, a burst release was observed, with almost 40% w/w of DA found outside the bag, while after 2 h almost 90% w/w of DA was collected. A fast release of the drug of interest is usually considered a disadvantage as it would reduce its possibilities to reach the site of interest within the carrier, decreasing the efficient dose.[52] However, for intranasal administration this releasing represents a much more limited problem. Fe-DA-NPs are expected to be in contact and interact with epithelial cells for a short time, and quickly reach the brain. Therefore, the majority of DA releasing would most probably occurred already in the brain. Moreover, if some DA would be released in the nasal cavity, it could still be able to reach the brain separately, following a different route.

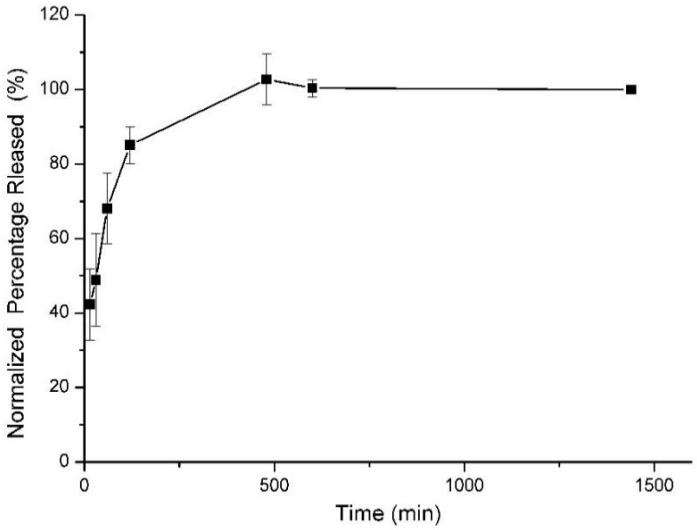

Figure 3.16: DA release profile of Fe-DA-NPs in simulated nasal buffer at pH 6.2 and 37 °C, normalize respect to the DA amount at the last time point (24 h).

d) Relaxivity properties

Fe-DA-NPs were also investigated as a diagnostic tool, by acting as contrast agent in MRI. The longitudinal (r_1) and the transversal (r_2) relaxivity values were determined for nanoparticles at different concentrations by acquiring T1-weighted (T_{1w}) and T2-weighted (T_{2w}) images. These values were obtained by calculating the linear regression slope of plotted R_1 and R_2 (the reverse of T_{1w} and T_{2w}, respectively) against iron concentration. For the measurements, Fe-DA-NPs were dispersed in a PBS solution with 1% (w/v) of agarose, a reported medium used to mimic the environment and viscosity of biological tissues.[23] The phantoms images and the calculated r_1 and r_2 are reported in Figure 3.17. The T_{1w} images showed good contrast, with phantoms becoming lighter as the iron concentration increased. The corresponding r_1 value resulted 1.76 $mM^{-1}s^{-1}$, relatively lower compared to commercial gadolinium contrast agent values (4 $mM^{-1}s^{-1}$ for adolinium-diethylenetriamine penta-acetic acid,Gd-DTA),[53] but close to others found for different Fe-based NCPs (2 - 4 $mM^{-1}s^{-1}$) .[37,22] On the other hand, a notable high r_2 value was found (13.02 $mM^{-1}s^{-1}$), comparable to other Fe-based systems (10 - 12 $mM^{-1}s^{-1}$) but much higher than commercial contrast agents (4 $mM^{-1}s^{-1}$). [22,53] However, less appreciable differences were found in T_{2w} images by varying iron concentrations. Indeed, it is important to mention that T_{2w} images were acquired by employing an echo time (TE) much longer than the one usually applied in *in vivo* application.[23] Despite this discrepancy, which was also found in literature,[37] Fe-DA-NPs appeared to be a good candidate as a novel T_2 contrast agent; however further investigation is needed. Moreover, to evaluate the use of Fe-DA-NPs as a dual contrast agent, the ratio r_2/r_1 was evaluated. It is known that depending on if the ratio is higher than 10 or lower than 2, the material behaves as a T2 contrast or T1 contrast agent, respectively.[54] In our case, an intermediate value of 7.42 was found, indicating how Fe-DA-NPs could act as excellent dual-modal MRI agent in.

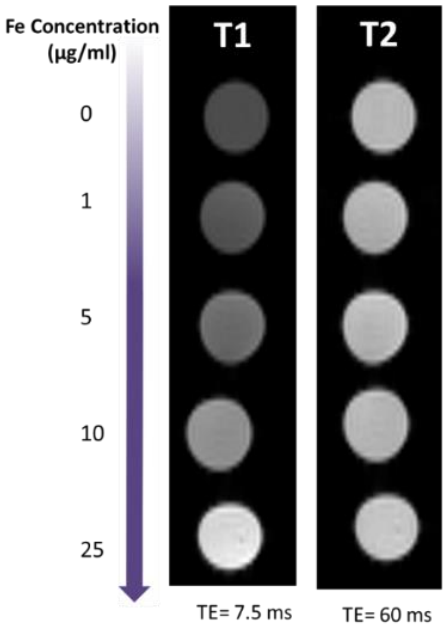

r1 (mMs^{-1})	r2 (mMs^{-1})	r2/r1
1.76 ± 0.03	13.02 ± 0.22	7.42

Figure 3.17: MRI phantoms images of Fe-DA-NPs at increasing Fe concentration immobilized in agarose (left side). Table with the calculated MRI relaxivity values (r_1 and r_2) and their ratio for Fe-DA-NPs (right side).

3.3.4 *In vitro* experiments

This part of the work was made in collaboration with the Nanomedicines & Translational Drug Delivery group led Prof. Bruno Sarmento and the experiments were performed at the i3S institute (Portugal), under the supervision of Dr. José Das Neves.

a) Cytotoxic effects on nasal cell line

The final application of Fe-DA-NPs is their use as PD's treatment through intranasal administration. It is clear how the use of a cell culture model would help to assess NPs toxic effect on the nasal epithelium and thus understand their potential applicability for intranasal administration. The commercially available RPMI 2650 cell line has been used with this aim. These cells were initially obtained in 1962 from an anaplastic squamous cell carcinoma of the human nasal septum.[55] This cell line has been mostly used as a model for drug metabolism studies and toxicity assay since it presents properties and similarities close to the normal human nasal epithelium, such as identical metabolic activity and the production of different cytokeratins.[56,57] In this work, RPMI 2650 were grown in culture medium and were used between passages 25 and 35. To test the toxicity effect of Fe-DA-NPs, the resazurin assay was

employed after the cells were treated (for 24 h) with increasing concentrations of the NPs, while free DA was used as control. As shown in Figure 3.18, both DA and NPs did not produce any toxicity effect at low concentrations. A slight reduction in cell viability is appreciable only when a DA equivalent concentration of 100 µg/ml was used, in the case of Fe-DA-NPs. The slight excess over 100% viability was correlated to the cell proliferation that would occur during the 24 h of incubation, which could overcompensate the low cell death, as previously reported.[58] At the highest concentration (1000 µg/ml), DA and NPs showed distinct effects. Indeed, DA induced a drastic reduction in cell viability (up to 47%). This result aligns with similar findings reported in the literature for other cell lines, like HeLa[59] or PC12[60]. This increase in cell death was ascribed to the direct damages caused by DA oxidation.[59] As explained in the introduction, reactive oxygen species (ROS), like hydrogen peroxide, ion superoxide, or active quinones, can be generated upon DA oxidation, contributing to the cells oxidative stress or mitochondrial dysfunction with the consequent cells' death.[55] In the case of NPs, the cytotoxic effect of the highest concentration is more contained, showing a cell viability reduction equal to 68%. This difference could probably be ascribed to the delay in DA exposure due to its delayed release from Fe-DA-NPs, in agreement with previous results.[47] Overall, Fe-DA-NPs show low toxicity effects to RPMI2650 cells, making their intranasal administration suitable.

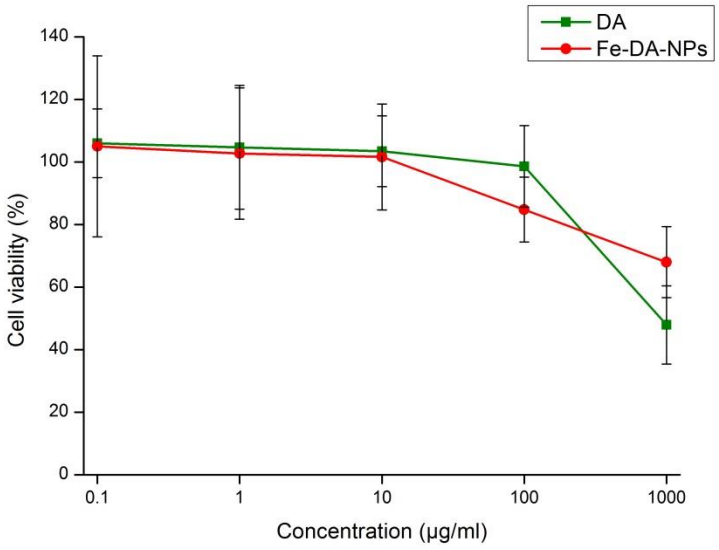

Figure 3.18: Cytotoxic effect of DA (green line) and Fe-DA-NPs (red line) on RPMI2650 after 24 h treatment. Cell viability is expressed as percentage of control (no treatment) and is evaluated at increasing equivalent concentrations of DA. Data are shown as mean ± standard deviation (n=4).

b) Permeability study across a nasal cell-monolayer model

In vitro permeation studies of Fe-DA-NPs were performed against a RPMI 2650 cell monolayer. Though the use of this cell line as an *in vitro* model may be somehow controversial as it is not yet elucidated if they can form tight junctions and for its low ability to differentiate or produce mucus, these cells offer good standardization and unlimited availability, and, above all, they have shown functional barrier properties.[57,61] In this work, the RPMI 2650 cell monolayers were formed by using Millipore transwell. These inserts are made by a polymeric membrane that divides the plate wells in two parts, the upper part known as the apical side and the bottom one as the basolateral side (see Figure 3.19 A). The membrane pore size is chosen accordingly to the cells dimensions to avoid their fall into the basolateral side, and to the size of the studied nanoparticles to not obstruct their passage, therefore, a pore size of 1 µm was selected in this work. In a permeability study, nanoparticles are put in contact with cell membranes from the apical side, and their passage through the membrane is followed by recollecting aliquots from the basolateral one. Several culture conditions were optimized in this work to obtain dense and intact monolayers. To monitor the cell membrane formation and wellness, transepithelial electric resistance (TEER), the electrical resistance across cell monolayers was measured (Figure 3.20). It is reported that air-liquid interfaces (ALI), where cells are left in contact with air from the apical side, reproduce better natural conditions and lead to stronger junctions between cells.[62] In our case, this strategy has shown the growth of a denser confluent cell monolayer with higher TEER values after a few days from the medium removal. However, a cell detachment was consistently observed, leading to the monolayer disassembly. A possible reason for cell detachment could be due to membrane manipulation, for example, while measuring the TEER, or some leaks of the medium from the basolateral side could occur, which dragged the cells.

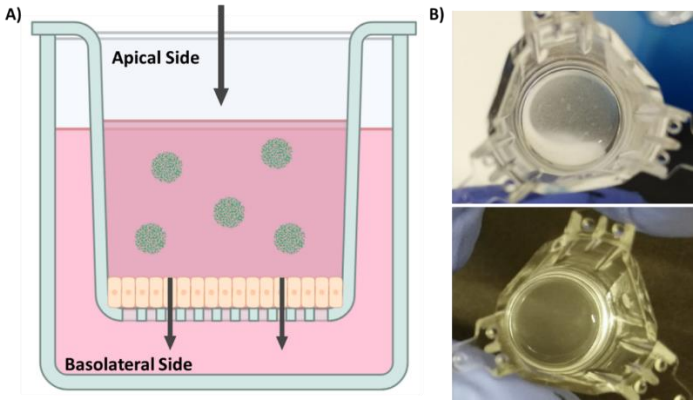

Figure 3.19: A) Schematic illustration of RPMI 2650 cell monolayer grown on a hanging insert after the addition Fe-DA-NPs. B) Pictures of cells' membranes after 14 days of culturing.

To guarantee the absence of any damages to the membranes, the use of a liquid-liquid interface (LLI) was thus preferred, despite its relatively lower TEER values and less biomimetic characteristics. Furthermore, similar permeability for ALI and LLI has been shown in the past.[63] In several works, two weeks are chosen for the cell monolayer formation.[61, 64,65] Starting from day seven, the TEER was measured every three days, showing values between 37 and 43 Ωcm^2, with no significant increase over time (Figure 3.20). These values are close to the natural nasal tissue one and in agreement with other studies.[55,61,66]

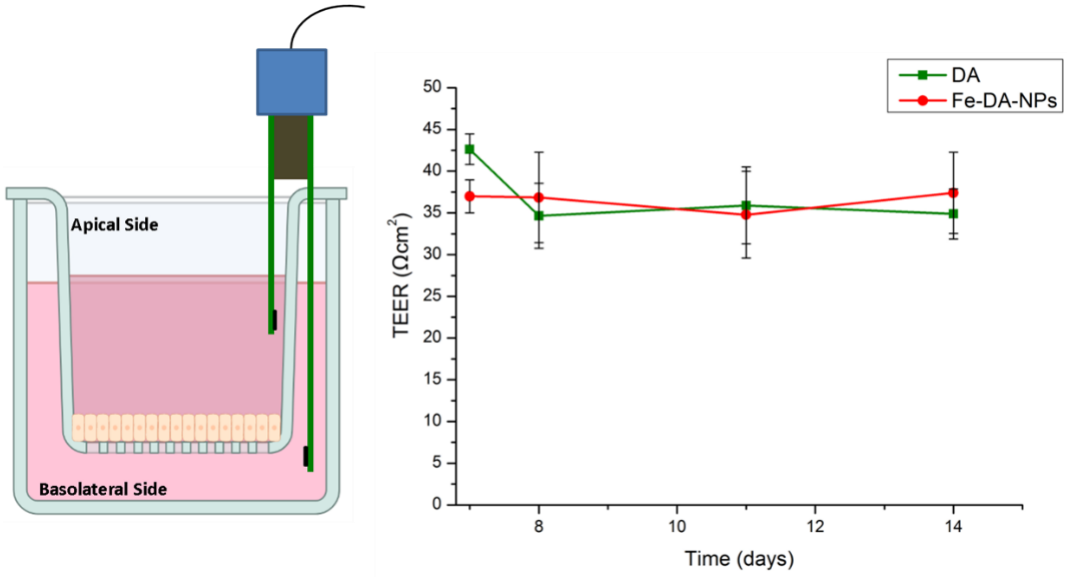

Figure 3.20: A) Schematic TEER measurement representation. B) TEER values of RPMI2650 cell monolayers cultured in LLI over time. Measurements were made for different membranes used for passive transport study of: DA (green line), and Fe-DA-NPs (red line). Values are represented as means ± standard deviation (n=4).

On day 14, the permeability study was performed. The medium from the apical side was replaced with a diluted solution of DA or suspension of Fe-DA-NPs at the DA equivalent concentration of 10 µg/ml. This concentration was chosen accordingly to the cytotoxicity results (Figure 3.18), which showed complete cell viability. Aliquots from the basolateral side were collected, at different times, for 3 h, and the amount of DA passed through the cells monolayer was quantified by HPLC-EDC. The TEER values were measured for all the membranes during the study (Figure 3.21 A, inset). Since they are subjected to stress, agitation, exposure to air, and the addition of particles, minor damages with the consequent reduction of TEER were considered acceptable.

As shown in Figure 3.21 A, after 3 h, up to 11% (w/w) and 6% (w/w) of total DA passed in the case of free DA and NPs, respectively. Furthermore, the apparent permeability (Papp) of DA (for both free DA and Fe-DA-NPs treatment) was calculated, as reported in the experimental section. This value gives information regarding the ability of drugs to permeate cell membranes. As expected, the value of free DA ($4.66 \times 10^{-6} \pm 0.52 \times 10^{-6}$ cm/s) almost doubled the value calculated for NPs ($2.6 \times 10^{-6} \pm 1.7 \times 10^{-6}$ cm/s) (Figure 3.21 B). The different behavior and the reduced drug permeation for Fe-DA-NPs could be ascribed to different reasons. During 1 hour, both samples follow the same permeability profile. This could be associated with the free DA present in Fe-DA-NPs, which would probably be the first to cross the cells monolayer. More significant differences in the permeation trends could be observed at longer times, with a sustained release of DA from NPs due to a delay in DA availability. Indeed, at 1 h, only the 66% (w/w) of DA is released (Figure 3.16). For future works, it would be interesting to evaluate permeation studies at longer times to understand if the profiles of DA and Fe-DA-NPs would reach closer values.

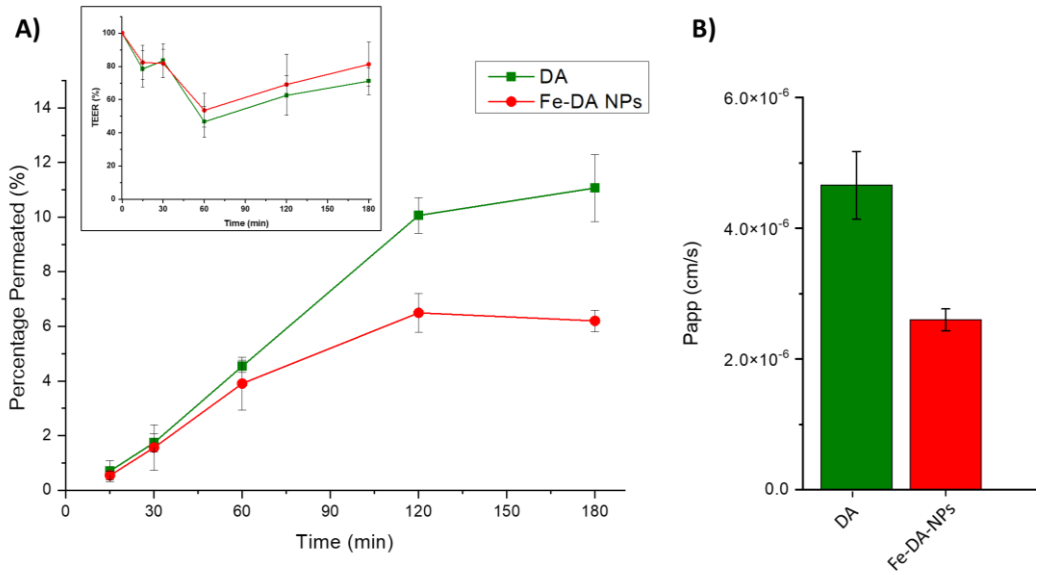

Figure 3.21: A) Permeation profile of DA through the RPMI2650 cell monolayer over 3 h, after the treatment with free DA (green line) and Fe-DA-NPs (red line). TEER values measured during the study are reported as insert. B) Apparent permeability (Papp) values for free DA and Fe-DA-NPs.

3.4 Dopamine nanoscale coordination polymers: a promising strategy for Parkinson's diseases therapy

3.4.1 Synthesis of coordination polymer nanoparticles

In this work, DA-based coordination polymer nanoparticles (DA-NCPs), have been obtained through the solvent-induced precipitation method, following a protocol already optimized by Dr. Nador, a former member of the group. These DA-NCPs were formed by iron, as the central node for the polymerization, DA as lateral ligand and Bix as bifunctional ligand, responsible for the binding of Fe nodes (Figure 3.22), The synthesis consisted of a simple one-pot reaction where Fe was added to an ethanol solution of DA and Bix. After iron addition, the reaction immediately turns black/violet with the presence of a fine precipitate, as consequence of the NCPs formation. The color observed was ascribed to the formation of bis-catechol iron coordination.[31] Finally, precipitation was induced by centrifugation resulting in a black solid.

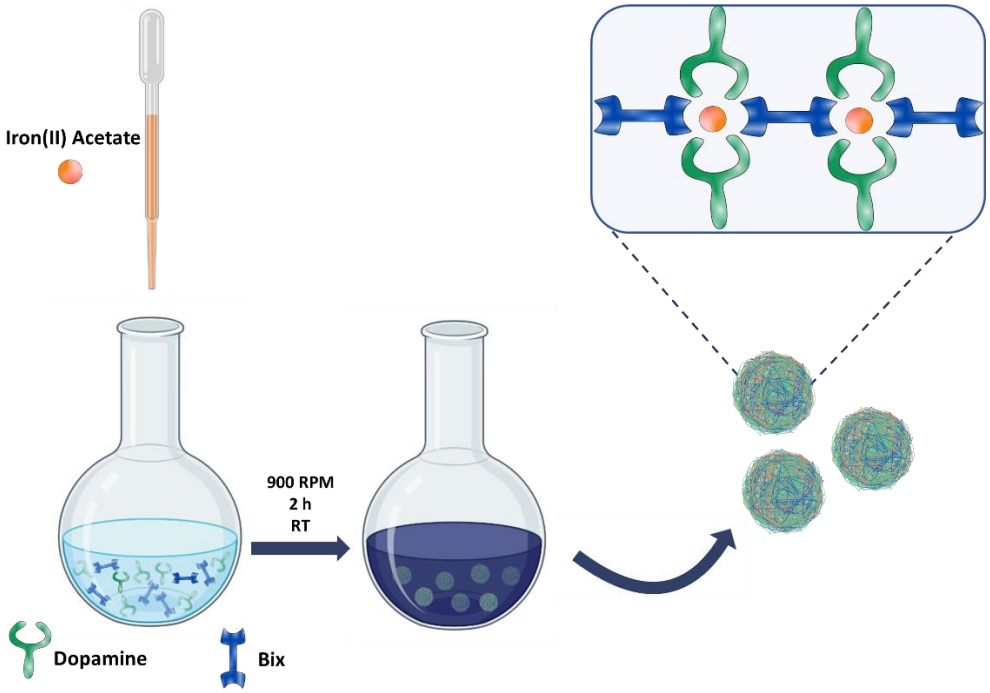

Figure 3.22: Schematic representation of DA-NCPs synthesis.

3.4.2 Morphological characterization

SEM images in Figure 3.23 reveal the formation of round-shaped nanoparticles with a homogenous size of 80.3 ± 15.6 nm. The hydrodynamic diameter was measured by DLS, initially in EtOH, showing a size around 200 nm and a narrow size distribution (Table 3.1). This difference in dimensions with

respect to SEM images suggests that in ethanol the DA-NCPs form stable and small colloidal aggregates quite homogenous in size. On the contrary, once re-suspended in water DA-NCPs suddenly form unstable aggregates, with a consequent drastic PDI increase, and precipitating over time. DA-NCPs presented a positive surface charge, probably due to the protonated free amine groups of DA exposed on the surface, though the positive charge was not enough as to stabilize them over time. However, this can be considered a good aspect for intranasal administration as mucin proteins generally present a low isoelectric point, giving the mucus a negative charge behavior.[67] The positive ξ-potential of DA-NCPs would enhance their permanence in the nasal cavity thanks to the electrostatic interaction with mucus, providing more time for permeation, and avoiding their clearance within the mucus.[68]

Similar aggregation tendency was found in PBS (Table 3.1), where larger particles (due to aggregation) were measured and even a faster precipitation was observed. Finally, when DA-NCPs were suspended to a PBS solution of bovine serum albumin (BSA) at the physiological concentration (0.5 mM), NCPs size increased due to the formation of a protein corona, (with the PDI becoming narrower) and showed much higher stability over time, as no precipitation was observed over time (Table 3.1).

Table 3.1: Comparison of hydrodynamic diameters, PDI, and ξ-potential values of NCPs dispersed in different buffers measured with DLS.

	Size (nm)	PDI	ξ-potential (mV)
EtOH	232.2 ± 1.5	0.122 ± 0.013	ND
Water	219.8 ± 12.2	0.45 ± 0.065	21 ± 0.6
PBS	1648 ± 120	0.29 ± 0.023	-13 ± 0.53
PBS/BSA	422 ± 4.9	0.197 ± 0.02	-8.3 ± 0.22

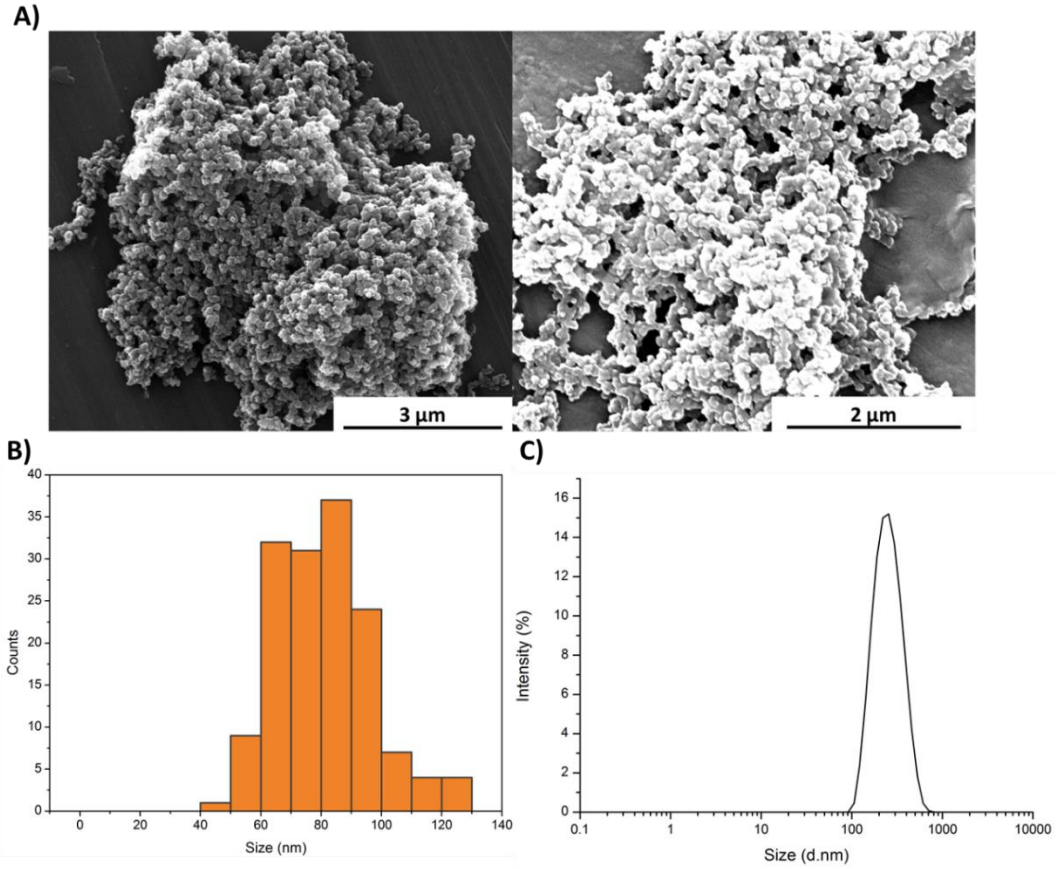

Figure 3.23: A) SEM images, B) size histogram, and C) DLS measurement in EtOH of DA-NCPs.

Worth to mention is that even though our previous experiments showed colloidal stability of small nanoparticles aggregates in EtOH and PBS/BSA, NCPs dimensions were still quite high. So further optimization work was focused to reduce particles dimensions (Figure 3.24). Therefore, different parameters were modulated during the synthesis as they can affect the final nanoparticles dimension: the stirring rate, speed of Fe addition, addition of a stabilizer, and the initial concentration (Figure 3.24). In all cases, size distribution appeared homogeneous and monodisperse, with PDI values always between 0.1 and 0.22, though it was not possible to reach dimensions smaller than 240 nm (Figure 3.24). Surprisingly, the use of polyvinylpyrrolidone (PVP) resulted in a significant increase in particles dimension. Even more, high energy was supplied through ultrasonication after NCPs synthesis, using a bath or a probe, to break or disassemble particle aggregates. However, no drastic size reduction was observed neither in these cases, with the lowest value of 240 nm achieved under high stirring rate (1000 rpm).

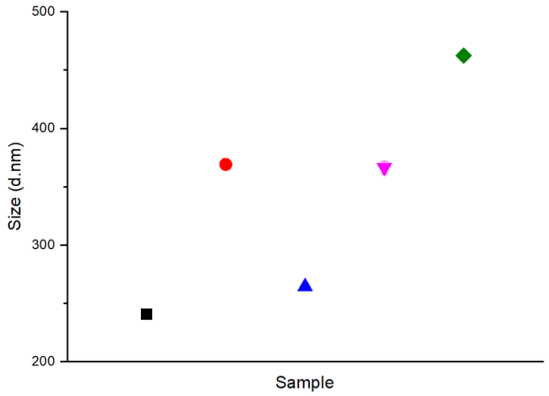

Sample	Condition
Higher RPM	> 11%
Slower Iron Addition	≈ 1 minute
Higher Concentration	> 25% w/w
Lower Concentration	< 27% w/w
Use of PVP	0.1% w/w

Figure 3.24: DA-NCPs size measurement (left side) varying different synthesis conditions, reported in the right table.

As it was not possible to reduce DA-NCPs dimensions, we studied their colloidal stability in EtOH and PBS/BSA over time, to corroborate if the formed aggregated remained stable, and therefore being applicable in further studies. Nanoparticles did not show any significant changes in size after one month (Figure 3.25 A). NCPs re-dispersed in PBS-BSA, instead, remained stable for two days (Figure 3.25 B). Despite the final application is intranasal administration, the absence of aggregation suggests that these nanoparticles could represent a good candidate for intravenous administration as well, even though, their dimensions are in the limit range, where they could be easily removed from the body. Moreover, a small fraction of nanoparticles can still reach the blood stream after intranasal administration, therefore evaluating their colloidal stability could be still of interest. BSA is considered an appropriate model and largely used for particles surface functionalization, simulating the interaction of nanoparticles and proteins which occur in the body, and stabilizing them. However, its biomimetic behavior is still limited, as the human blood contained several types of proteins, fats, and electrolytes, so further experiments with human plasma were performed as a closer physiological environment. For this, DA-NCPs were incubated at 37 ºC and sonified for 10-15 minutes in an ultrasound bath. As shown in Figure 3.25, the PDI value was much higher in comparison to EtOH or PBS suspensions. The DA-NCPs distribution suffered a small shift to larger dimensions ascribed to the progressive formation of the protein corona around the surface of particles; indeed, size distribution was not altered up to 5.5 h, and the shift was approximately of 30 nm, consistent with the proteins dimensions. This time was considered sufficient to assess the colloidal stability of particles, however, an additional measurement was performed after 27 h, where the size distribution drastically changed, suggesting NCPs aggregated, forming particles of micrometer dimensions. On top of that, a new population peak around 40 nm appeared when plasma was used, which comes from the presence of proteins at high concentration which did not surround the nanoparticles, and that justifies the higher PDI value found.

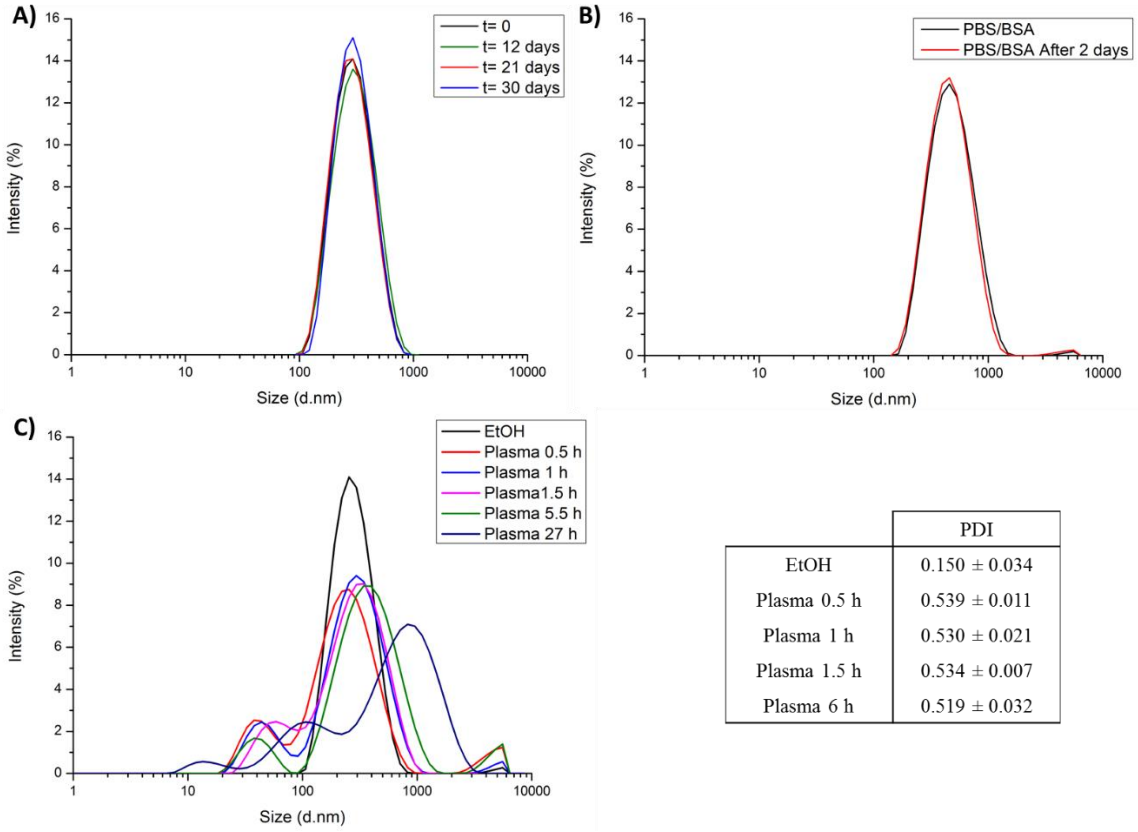

	PDI
EtOH	0.150 ± 0.034
Plasma 0.5 h	0.539 ± 0.011
Plasma 1 h	0.530 ± 0.021
Plasma 1.5 h	0.534 ± 0.007
Plasma 6 h	0.519 ± 0.032

Figure 3.25: Stability study of DA-NCPs. DLS measurements over time using as dispersants: A) EtOH, B) PBS/BSA, and C) human plasma. Correspondents PDI values are reported in the right table.

3.4.3 Chemical characterization

DA-NCPs were characterized by UV-vis spectroscopy (Figure 3.26 A). The absorption spectrum, recorded after the addition of 20 µl of NCPs in 2 ml of deionized water, shows the distinctive DA peak at 290 nm. The bis coordination between DA and Fe was confirmed by the appearance of the peak at 570 nm.[31]

DA-NCPs were further characterized by FT-IR spectroscopy (Figure 3.26 B). The consistent reduction in the intensity of the broad band around ν = 3000-3500 cm^{-1} (-OH) was associated with the deprotonation of catechol groups and their coordination to Fe. Additionally, the vibrational band at 1200-1300 cm^{-1} corroborated the C–O stretching of catechol bonded to metal. The band around 630 cm^{-1} in the DA-NCPs spectrum could be attributed to Bix imide-ring coordinated with iron. Moreover, some characteristic peaks of Bix (1430 and 950 cm^{-1}) can also be recognized.

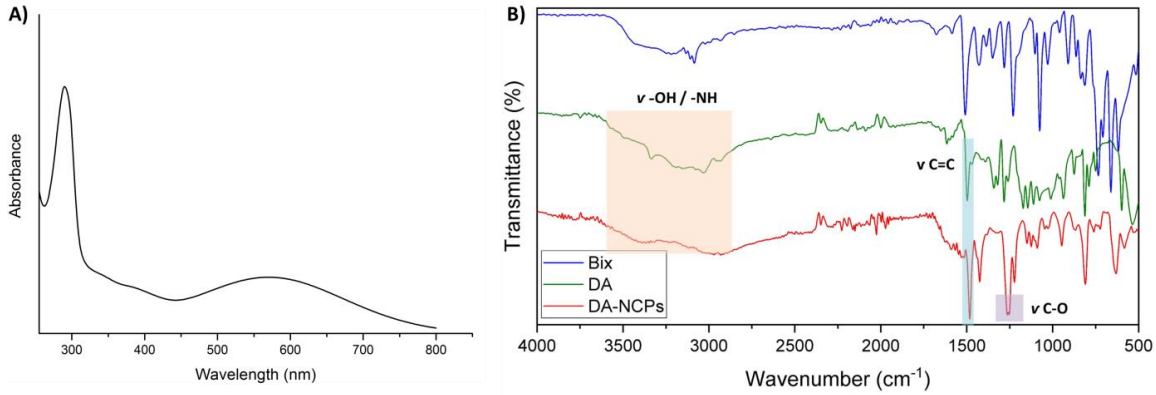

Figure 3.26: A) UV-vis spectrum of DA-NCPs diluted in water. B) FT-IR spectra of: Bix (blue line), DA (green line), and DA-NCPs (red line) (ν: stretching; δ: bending).

DA quantification was performed by HPLC-EDC, resulting in a LE around 50% w/w. A similar result (56% w/w) was found through UV-vis after the complete degradation of DA-NCPs with a strong acid, following the procedure described before. As far as we know this is one of the highest LE value of DA found for nanostructured carriers employed for DA delivery,[47,69] so this outstanding loading capacity made DA-NCPs a unique and powerful carrier for DA replacement treatment. The presence of iron was assessed by ICP-MS and EDX. In this case, the amount of iron present in nanoparticles resulted equal to 15 % wt. This relatively high amount of metal still made DA-NCPs a useful contrast agent in MRI, as it was demonstrated by the phantoms measurement carried out by Dr. Pardo. Taking together, the MRI activity and the high DA loading, DA-NCPs represent a very promising theranostic nanocarrier for PD treatment.

Combining the obtained results with the previous studies performed by Dr. Nador, as elemental analysis, HPLC, and ^{1}H-NMR, the following tentative molecular formula was assigned:

$$Fe(DA)_{1.6}(Bix)_{0.5}(AcO)_{0.2}(H_2O)_{1.9}$$

This formula differs from the expected theoretical one ($Fe(DA)_2(Bix)$), this was attributed to the presence of free DA entrapped within the nanoparticles. Moreover, this difference is a common behaviour for amorphous NCPs, as they are synthetized under out-equilibrium conditions.

3.4.4 Epidermal Growth Factor (EGF) encapsulation

PDs is a complex and multi symptoms disorder. For this reason, although DA replacement remains the primary and selected treatment, other compounds or biomolecules have been employed to contribute to the amelioration of symptoms. For example, the use of antioxidants would help to slow down neurons death,[70] or the use of growth factors could promote the restoration of degenerated neurons.[71,72] With this aim we attempted the co-encapsulation of a second therapeutic agent, the epidermal growth factor (EGF). For the encapsulation, the EGF was mixed with Fe and added to the Bix/DA mixture, then the synthesis was followed as usual.

To corroborate the EGF entrapment in the DA-NCPs-EGF nanoparticles and quantify the encapsulated amount, the supernatant (SN-EGF) of the first cleaning step was collected and freeze-dried. After dissolution in a 0.1% v/v trifluoroacetic acid aqueous solution, the mixture was passed through HPLC coupled with UV detection. The supernatant of nanoparticles synthesized without protein was analyzed as well as control (SN-control) (Figure 3.27). The encapsulated EGF was calculated from the difference between the total protein used for the reaction and the one calculated in the supernatant. Remarkably, a very high encapsulation efficiency of 89.6%, with 7.7 µg of EGF per milligram of particles were found.

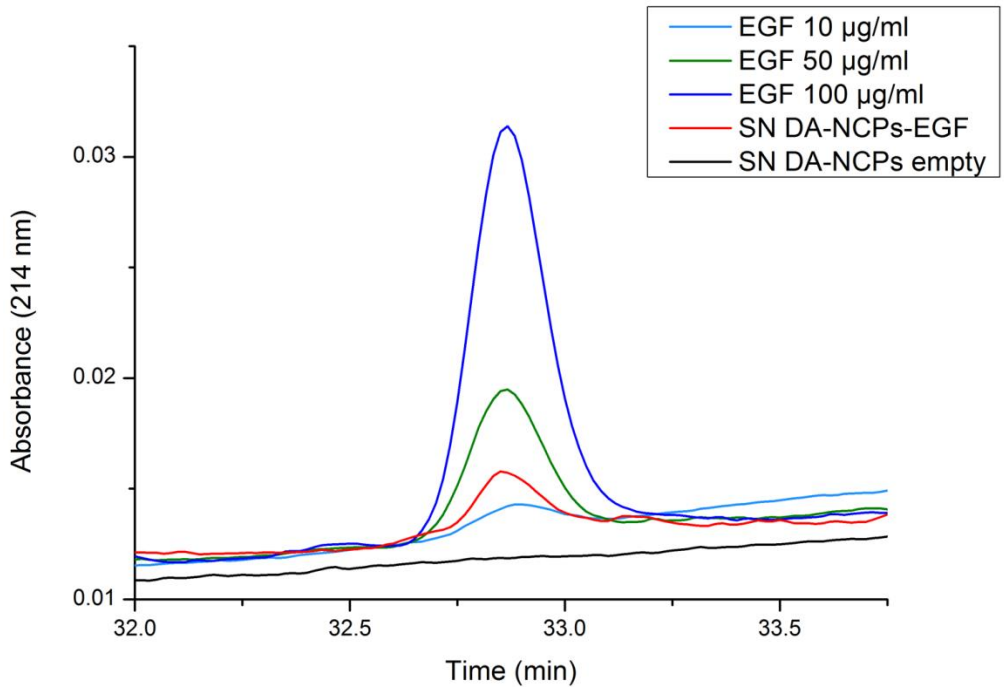

Figure 3.27: HPLC-UV spectra of: EGF at different concentrations (10, 50, and 100 µg/ml), supernatant (SN) of the first cleaning of DA-NCPs with (red line) or without EGF (black line).

3.4.5 *In vitro* experiments

All the *in vitro* experiments described in this section have been performed at the IBB. Initial studies were carried out by Dr. Javier García-Pardo. (BE)2-M17 cells are human neuroblastoma cells and have been extensively used as an *in vitro* model to study the development or progression of neurological diseases like PD or to test the toxicity of compounds or particles.[73,74] Particularly, he evaluated the cytotoxicity of DA and DA-NCPs and their internalization by cells.

Firstly, the cytotoxic effect of free DA and DA-NCPs at increasing concentrations (ranging from 0.01 to 150 µg/ml) was tested for 48 h incubation. The results found are similar as those obtained for the Fe-DA-NPs, previously shown. Both DA and NCPs do not cause a significant reduction in cell viability up to 100 µg/ml. However, the higher free DA concentrations induced drastic cell death. The cytotoxicity effect was more pronounced for free DA than for DA-NCPs, with the corresponding IC50 values being 117 ± 11.8 µg/ml and 177 ± 36.1 µg/ml, respectively. This cell viability reduction at the highest concentration for both DA and DA-NCPs was associated to ROS production. Indeed, both DA and Fe can cause oxidative stress in cells. Despite the non-pronounced cytotoxicity effect of DA and NCPs at lower concentrations, harmful effects could still be expected after more extended times if oxidative stress arises. For this reason, the evaluation of ROS generation is critical to understand the future applicability *in vivo* of DA-NCPs, particularly if repetitive administrations are planned.

In the second place, the internalization by (BE)2-M17 cells of DA and DA-NCPs was studied. Both intracellular and extracellular DA levels were measured by EDC-HPLC after exposure to 1 and 10 µg/ml of DA or DA-NCPs. In the case of free DA, after 2 h of treatment, the intracellular level increased in a dose-dependent manner, most likely due to the abundance of DA transporters. Nevertheless, DA levels dropped to control levels after a longer period of treatment. In the case of NCPs, the neurotransmitter intracellular level was slightly lower than for free DA, following 2 h of treatment with 1 µg/ml NCPs suspension. However, when the higher concentration was used, the amount of DA notably increased.

This behavior dissimilarity suggested that two distinct mechanisms drove DA and NCPs internalization with different uptake rates. For this, a more accurate investigation with additional concentrations treatments was performed.

a) Reactive Oxygen Species production in dopaminergic cells

As mentioned above, the evolution of the oxidative stress is fundamental for the further *in vivo* application of NCPs; thus, intracellular ROS formation in BE (2)-M17 was measured. Cells were treated with different concentration of DA or DA-NCPs, and ROS levels production were measured through the

2′,7′-dichlorofluorescin diacetate (DCFDA) assay.[75] DCFDA is a non-fluorescent and permeable dye that, after cleavage and oxidation by intracellular esterase and ROS, generates dichlorofluorescein (DCF), a fluorescent and non-permeable compound. All conditions were tested in the presence or absence of a powerful natural antioxidant, ascorbic acid (AA), which, additionally, would avoid DA autoxidation. Hydrogen peroxide (H_2O_2) has been used as a positive control at a concentration of 250 µM.

After a 24-hour treatment, strong DCF fluorescence 300-fold increase was observed for the highest free DA concentration (100 µg/ml) (Figure 3.28 A), highlighting the ROS production capabilities of DA, as already reported,[47] and it can be associated to both the degradation and oxidation mechanisms of this neurotransmitter. Indeed, DA is enzymatically converted in DOPAL (3,4-dihydroxyphenylacetaldehyde) by MAO, with H_2O_2 generation. Moreover, by its spontaneous autoxidation, the very reactive o-quinones molecules are produced, which could easily generate ROS.[76] This increase in ROS levels justifies the viability reduction observed in BE (2)-M17, previously mentioned. DA-NCPs showed a lower DCF fluorescence signal (244-fold) for the highest NPs concentration (100 µg/ml), suggesting the gradual and slower release of DA. In the case of free DA, as the DA concentration decrease, lower ROS are produced. However, DA-NCPs did not seem to have a similar trend, showing still moderate oxidative stress even at the lowest concentration, which was attributed to the presence of iron. Since it is known that iron can induce the generation of H_2O_2, metal-induced ROS production was evaluated after the cells treatment with iron(II) acetated as control (Figure 3.28 B), and obtaining high levels of DCF. From the Fe-DA complexes, ferrous iron and aminochrome are released. The further oxidative step of the latter generates the dioxygen superoxide radicals that, in the presence of ferrous iron, is transformed into hydroxyl radicals by the Fenton reaction, generating intense oxidative stress.[77] This consideration aligns with the increased probe fluorescence intensity observed for both DA-NCPs and Fe.

AA was used at its physiological concentration of 20 µg/ml, showing its ability to drastically reduce ROS levels in the case of H_2O_2, and for the highest DA concentration (Figure 3.28 A). However, its effect was not evident for all the other conditions tested. Again, in the case of DA-NCPs, the low antioxidant ability of AA can be ascribed to the contribution of iron. The exact role and behavior of AA in the presence of iron is still unclear; however, it has been reported that AA can have a slight pro-oxidant effect depending on its interaction with quinones and metals.[78,79] It appears that the co-presence of AA and iron can generate a moderate increment in the fluorescence signal of the DCF (Figure 3.28). Despite this ROS production, cytotoxicity results suggest that the conditions tested are not harmful to cells, and DA-NCPs, if used at lower concentrations, could not be considered dangerous.

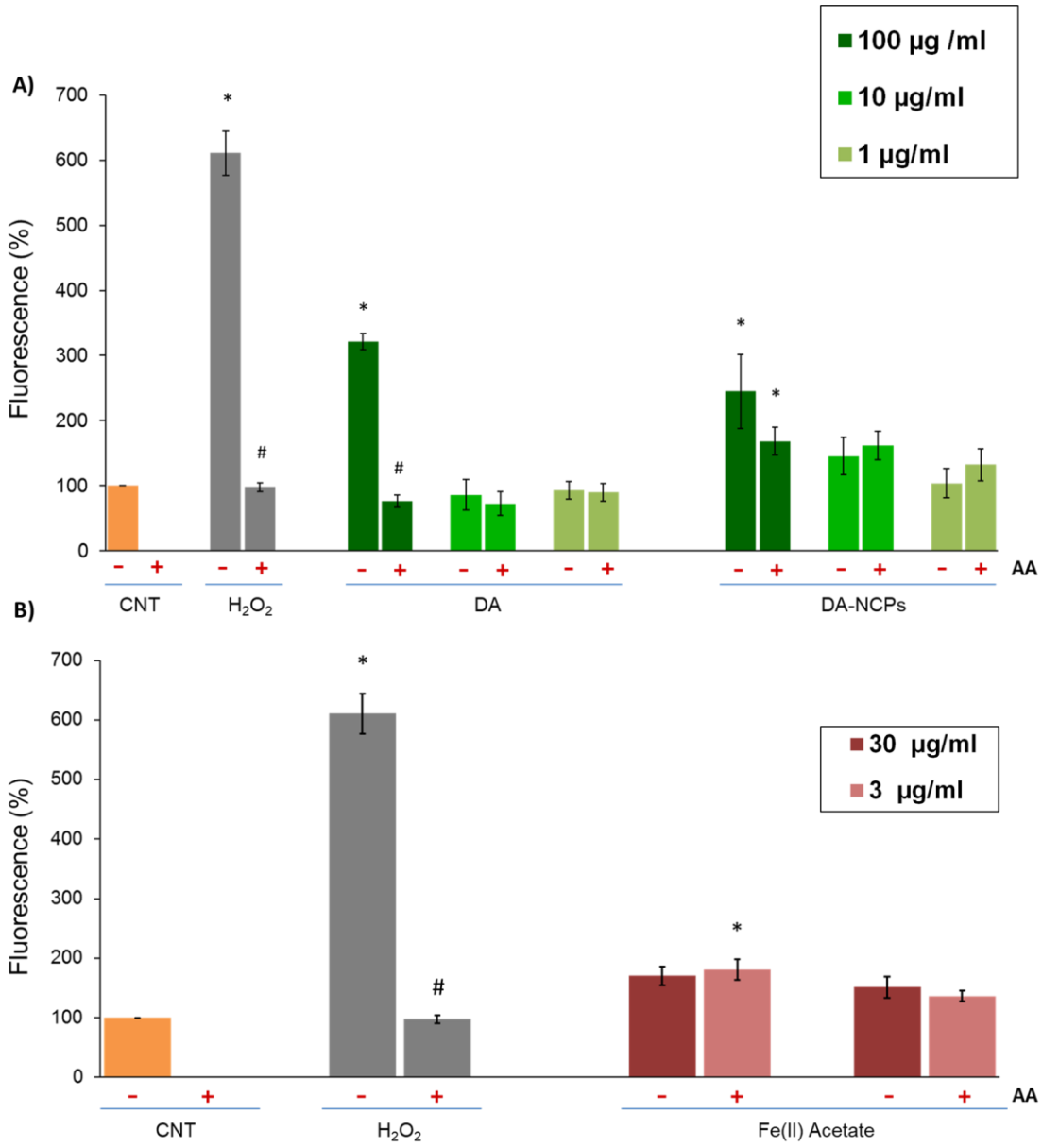

Figure 3.28: ROS production in BE (2)-M17 dopaminergic cells treated for 24 h with: A) H_2O_2, DA, and DA-NCPs (equivalent DA concentrations: 100, 10, and 1 µg/ml); B) H_2O_2, and iron(II) acetate (3 and 30 µg/ml). Experiments were performed in the presence (+) or absence (-) of AA (20 µg/ml). In all the cases, values are mean ± standard deviation (n=2). *$p < 0.05$ compared to the control (CNT), and #$p < 0.05$, compared to the treatment without AA (one-way ANOVA and Tukey-HSD test).

b) Dopamine uptake by dopaminergic cells

Due to the differences in the DA uptake by BE (2)M-17 cells studied by Dr Pardo and described above, the internalization mechanism was studied into more details. Cells were treated for 2 h with different concentrations of DA or DA-NCPs, ranging from 1 to 50 μg/ml (DA equivalent). After cells lysis, the intracellular DA amount was calculated by HPLC-EDC and normalized for the proteins amount found in the cells. This value was plotted as a function of DA concentration (Figure 3.29). For free DA, the smallest concentration induced a rapid rise in DA intracellular level, which tends to stabilize as the concentration increase. This internalization mechanism follows the characteristic saturation kinetics, as it perfectly matches the Michaelis−Menten curve, with approximate K_m and V_{max} values of 0.85 μg/ml and 10 ng/mg_{pro} x min^{-1}, respectively, obeying to a classic receptor mediated internalization mechanism.[80] DA seems to be actively uptake by (BE)2-M17 cells through cell transporters (Figure 3.29 B). On the other hand, a slightly lower value was found for DA-NCPs at the concentration of 1 μg/ml. However, as the concentration increased, the intracellular level of DA reached higher values. Indeed, in the case of 50 μg/ml of DA-NCPs, DA level is almost 4-fold higher than for free DA added at the same concentration. Furthermore, a much more linear response was found (Figure 3.29 C), suggesting that DA-NCPs underwent an entirely different internalization pathway than free DA.

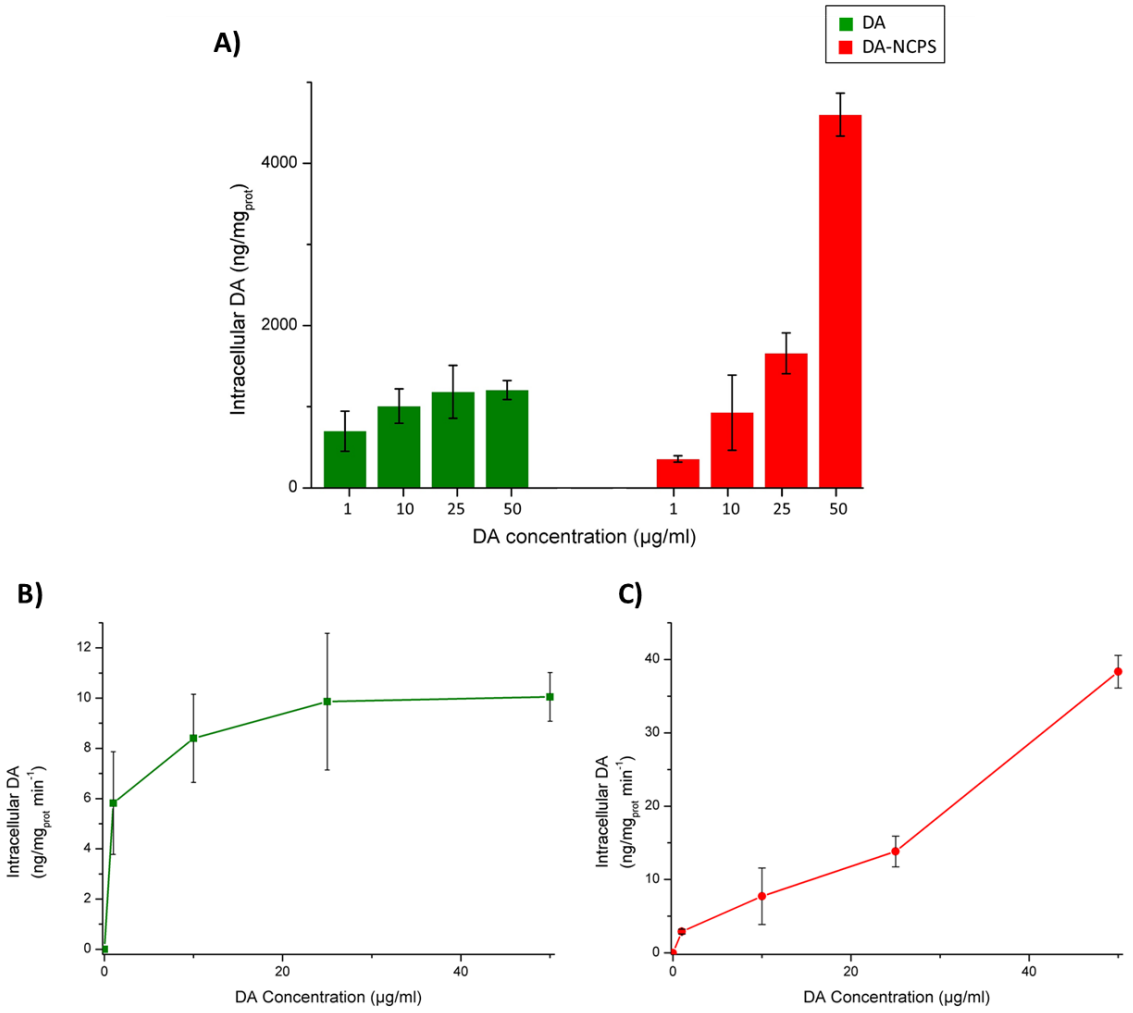

Figure 3.29: A) Intracellular DA levels determined by HPLC-ECD, and normalized by proteins amount, after incubation of (BE)2-M17 cells for 2 h with DA (green bars) or DA-NCPs (red bars) (1, 10, 25, 50, and 10 µg/ml of DA equivalent concentration). The uptake rate of DA after the treatment of (BE)2-M17 cells with: B) DA or C) DA-NCPs. In all the cases, values are mean ± standard deviation and n=2.

3.4.6 *In vivo* studies

The NCPs were tested *in vivo* by Dr. Pardo at the Vall d'Hebron Research Institute. Firstly, a single dose of NCPs was infused in the lateral ventricle of healthy adult rats. No adverse effects or mortality were observed. The DA cerebral distribution was evaluated by ECD-HPLC, after 2 h from administration, a remarkable increase in the neurotransmitter levels was observed in the ipsilateral side of the brain.

Afterward, NCPs were intranasally administrated to evaluate their potentiality for the direct nose-to-brain delivery of DA. The NCPs pathway was followed by MRI, with a strong T1w signal clearly observed in the right nasal cavity of the rat after administration, near the respiratory epithelia. No increase in DA level was found in the plasma after 2 h; on the contrary, an important rise in neurotransmitter quantity was found in the ipsilateral side of the rat brains after only 30 minutes. A similar increase was also found after the unilateral administration of free DA at the same concentration.

The pharmacological effect of NCPs was further investigated by performing behavioral tests on 6-hydroxyDA (6-OHDA)-lesioned rats. This is a commonly used PD model characterized by a unilateral drug-induced degeneration of the nigrostriatal dopaminergic neurons on the same side as neurotoxin injection. When treated with DA agonists or antagonists, the lesioned rats showed a pronounced tendency to rotate in circles for the duration of drug activity. The duration and number of induced rotations were measured after 4 days of nasal administration of DA-NCPs and DA. Exceptionally, a reduction in the motor response was found for rats treated with DA-NCPs, suggesting a continuous presence of the DA in the brain of rats, in accordance with the sustained release of DA from nanoparticles.

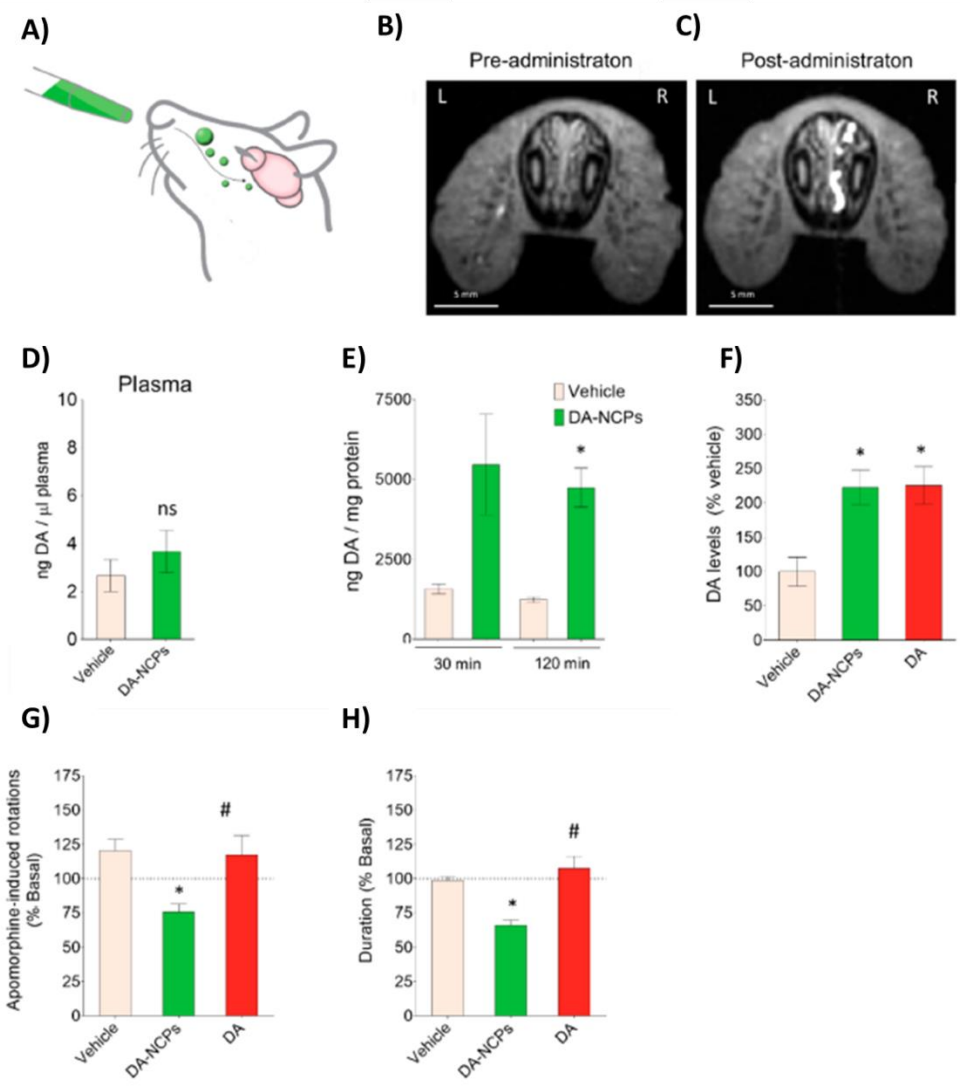

Figure 3.30: A) Schematic representation of intranasal administration. T1w MRI images of the nasal cavity of rat B) before and C) after DA-NCPs intranasal administration. DA concentration measured after treatment with vehicle (PBS with 0.5 mM mouse serum albumin) or a single dose of NCPs D) in plasma of rats after 2 h from administration or E) in the right striatum of rats, after 30 minutes or 2 h from administration (Values are expressed as ng of DA/mg of protein). F) DA level in the right striatum of rats after 2 h of treatment with vehicle, DA-NCPs, or DA G) Apomorphine-induced rotations, and H) duration of the apomorphine-induced rotational behavior of 6-OHDA-lesioned rats after 24 h post administration. Data are expressed as percentage of the time achieved in the basal experiment before treatment. In all cases, data are reported as mean ± standard deviation. ns: nonsignificant when compared to vehicle; *: $p < 0.05$ compared to vehicle; #: $p < 0.05$, compared to treatment with DA-NCPs (one-way ANOVA and Tukey's posthoc test).

3.5 Summary

In summary, in this work we have been able to obtain nanoparticles formed by tris coordinated DA-Fe complex, where no polydopamine formation was identified up to 1 h in water dilution or when stored at -20 and -80 °C. These NPs present a remarkable DA encapsulation efficiency, colloidal stability and do not show significant toxicity toward the nasal cell line. However, the fast oxidation tendency and the chemical lability of Fe-DA-NPs made us evaluate different and more robust candidates as an intranasal delivery carrier for DA. Additionally, considering the high data dispersion in the literature about RPMI2650 and cell monolayers, a more reliable *in vivo* model should be considered to understand the particles behavior once administrated intranasally.

To the best of our knowledge, no previous studies of DA or DA delivery systems using RPMI260 models have been reported. In the case of Caco-2 cell monolayer, the Papp of DA is relatively close to the one calculated in our study, equal to $9.33\ 10^{-6} \pm 3.48 \times 10^{-6}$ cm/s.[81] Trapani *et al.* have studied the use of chitosan for DA delivery across MDCKII-MDR1 cell line. They found close values of Papp between DA and one of their formulations (1.31×10^{-7} and 1.22×10^{-7} cm/s, respectively); however, when nanoparticles were prepared with a higher initial concentration of DA, they were able to enhance the neurotransmitter permeability (3.2×10^{-7} cm/s).[58] It appears clear how Fe-DA-NPs do not have a direct effect as permeation enhancers; nevertheless, the correlation between Papp values against RPMI2650 and the *in vivo* adsorption profiles is still not fully clear. For example, Mistry *et al.* have studied the behavior of carboxylate polystyrene nanoparticles with different sizes and coatings, both with *in vitro* and *in vivo* models. They found that their particles could not cross excised porcine olfactory epithelium mounted on Franz-type diffusion cells after 90 minutes.[82] However, the same nanoparticles were administrated intranasally in mice, showing to be able to pass across the olfactory and respiratory mucosa.[83] These studies suggest how the Papp values can be used only as qualitative indicators and not as replacement markers for the *in vivo* intranasal administration.

In conclusion, these neuromelanin-inspired nanoparticles showed formidable colloidal stability and good encapsulation abilities. They did not induce cytotoxicity effects or significant ROS generation *in vitro* in dopaminergic cells compared with free DA.

Furthermore, DA-NCPs directly administrated by intranasal pathway were able to restore attenuate motor dysfunctions in the parkinsonians rats' model.

DA-NCPs represent a promising tool for dopamine delivery and, thus, for the amelioration of PD's symptoms

3.6 Experimental Section

Materials: EtOH and starting materials were purchased from Sigma–Aldrich (Merck, Madrid, Spain) and used as received, without further purification. Bix was synthesized according to previously reported methodology.[84]

Synthesis nanoparticles: Fe-DA NPs were obtained through a one-pot reaction. 114 mg of DA hydrochloride (0.6 mmol) were dissolved in 20 ml of sodium tetraborate buffer (50 mM, pH 9) through magnetic stirring in a 50 ml flask. 35 mg of iron(II) acetate (0.2 mmol) were dissolved in 2 ml of the same buffer and slowly added to the DA solution, along with 600 µl of NaOH (1 M). The reaction was left stirred at 800 rpm for 30 minutes. The colorless DA solution immediately turns to red/violet after the addition of Fe solution, turning to purple/red-wine color after the addition of NaOH. The final solution was filtered with filtering paper, to remove the undesired iron oxide nanoparticles formed. NPs were freeze-dried for their characterization or were made fresh each time prior to *in vitro* experiments.

Synthesis of DA-NCPs: DA-NCPs were prepared according to previously published method for the synthesis of NCPs with some modifications.[23,85] Briefly, a mixture of dopamine hydrochloride (DA, 0.5 mmol, 95 mg) and Bix (0.25 mmol, 60 mg) was dissolved in 12.5 ml of ethanol. Under constant magnetic stirring (900 rpm), a solution of iron(II) acetate ($Fe(CH_3COO)_2$) (0.25 mmol, 44 mg in 2.5 ml of ethanol) was added to the DA-Bix solution. The mixture was left stirred at room temperature and the suspension rapidly turned from colorless to black. After 2 h, the solution was centrifuged at 8000 rpm for 10 min. The pellet obtained was resuspended and washed three times with ethanol. The resulting DA-NCPs were freeze-dried for their characterization or made fresh every time in case of *in vitro* experiments.

Moreover, EGF was encapsulated within the particles by adding it during the synthesis. 75 µl of EGF solution in PBS at the concentration of 10 mg/ml were mixed with iron acetate solution and quickly added to DA-Bix solution. The reaction was followed as previously described. As control, the same reaction was carried out, replacing the volume of EGF solution with PBS. After the first cleaning centrifugation, the supernatant was collected and freeze-dried. The resulted sample was suspended in 1 ml of 0.1 % v/v of trifluoroacetic acid (TFA) water solution, and a dilution of 1:4 in the same buffer was made.

Characterization:

Scanning Electron Microscopy (SEM): The structural properties of DA-NCPs and Fe-DA-NPs were studied by a high-resolution field emission SEM with a Quanta 650 FEG. Samples were prepared by dilution in ethanol (for DA-NCPs), or water (for Fe-DA-NPs) and placed over an aluminum tape.

Following solvent evaporation, samples were coated with 5 nm of platinum under an argon atmosphere by using a Leica EM ACE600 sputter coater. SEM pictures were acquired at accelerating voltages between 2 and 20 kV under a high-vacuum mode and a distance of the sample of 5 mm.

Dynamic Light Scattering (DLS): Hydrodynamic size and zeta potential of both DA-NCPs and Fe-DA-NPs were determined by dynamic light scattering using a Zetasizer Nano 3600 instrument (Malvern Instruments, UK). In the case of DA-NCPs, samples were diluted in five different solvents: ethanol, PBS, and PBS with 30 mg/ml (0.5 mM) of Bovine Serum Albumin (BSA). Furthermore, to study the colloidal stability in physiological conditions, an aliquot of nanoparticles was dispersed in nontreated human plasma, and the hydrodynamic diameter was measured over 24 h at different time points after incubation at 37 °C. Fe-DA-NPs, nanoparticles were dispersed in water or PBS.

Nanoparticle Tracking Analysis (NTA): Size distribution and concentration of Fe-DA-NPs, expressed as number of nanoparticles for ml, were determined by Nanosight NS300. Nanoparticles were diluted in water before measurements and injected in the sample chamber by syringes.

Fourier-transform infrared spectroscopy (FT-IR): FT-IR spectra of both DA-NCPs and Fe-DA-NPs were recorded by transmission FT-IR on a Bruker Tensor 27 (Bruker Optics) spectrophotometer. Each spectrum was acquired between 400 and 4000 cm^{-1} at a spectral resolution of 2 cm^{-1}.

UV-vis spectroscopy: The absorption spectra of nanoparticles were recorded using a Cary 4000 and Cary 600 spectrophotometers (Agilent), in the 200−800 nm wavelength range, using a matched pair (one for the solvent blank and one for the sample) of quartz cuvettes of 1 cm optical path length. Spectra were recollected diluting or dispersing dried samples in different buffers (water, PBS, EtOH for NCPs, and H_2O or sodium tetraborate buffer for Fe-DA-NPs).

For the spectroscopic DA quantitation, 5 mg of dried DA-NCPs or Fe-DA NPs were dispersed in 5 ml of 1 M HCl aqueous solution, sonicated until the complete particles degradation, and diluted in HCl to a concentration of 0.1 mg/ml. Standards (aqueous solutions) with different DA concentrations (ranging from 0 to 0.4 mM) were prepared by diluting a stock solution (1 mM) of DA hydrochloride in 1 M HCl aqueous solution. The absorbance of the different samples was determined at 280 nm. The amount of loaded DA was calculated from the calibration curve (adjusted to a linear regression model with $R^2 > 0.99$). The loading efficiency (LE) and the entrapment (or encapsulation) efficiency (EE) were calculated using the following equations for both DA-NCPs and Fe-DA NPs:

$$LE(\%) = \frac{Calculated\ Weight\ of\ DA}{Weighted\ of\ NPs}\ x\ 100$$

$$EE(\%) = \frac{Calculated\ Weight\ of\ DA}{Weight\ of\ Total\ DA}\ x\ 100$$

Dopamine quantification by high-pressure liquid chromatography with electrochemical detection (HPLC-ECD): HPLC-ECD analyses were performed using a Chromolith Performance RP-18e (100 mm x 4.6 mm, Merck-Millipore, Darmstadt, Germay) column in an Elite LaChrom system from Hitachi (Tokyo, Japan) coupled to a Coulochem 5100A electrochemical detector from ESA (Chelmsford, MA, USA). The detector was equipped with a 5011 dual-electrode analytical cell with porous graphite electrodes set at +5 and +400 mV (for electrodes 1 and 2, respectively). Before the analysis, the column was preequilibrated in the mobile phase containing 99% v/v of a buffered aqueous solution (0.1 M citric acid, 0.05 mM EDTA, 1.2 mM sodium octyl sulfate) with 1% acetonitrile. The final pH of the solution was adjusted to pH = 2.7 with triethylamine. Elution of the monoamines was performed with an isocratic elution of the mobile phase, at 25 °C and a flow rate of 1 ml/min. 5 mg of dried DA-NCPs or Fe-DA NPs were dispersed in 5 ml of homogenization solution (0.25 M perchloric acid, 100 µM sodium bisulphite, 250 µM EDTA). Before injection, samples were sonicated, diluted in homogenization buffer and centrifuged. Calibration curve was obtained by injecting different concentrations of DA in the range of 50 to 500 pg/µl.

Inductively coupled plasma (ICP) spectroscopy: In the case of Fe-DA-NPs, iron amount was quantified by ICP with optical detection, using a Plasma Emission Spectrometer ICP Perkin Elmer mod. OPTIMA 2100 DV, and samples were digested with nitric acid and hydrochloric acid before measurements. The total amount of iron present in DA-NCPs was determined by ICP with mass spectroscopy (MS) using a Perkin Elmer NexION 300X spectrometer equipped with an S10 autosampler. Samples of dried DA-NCPs nanoparticles were dispersed at a concentration of about 50 µg/mL in concentrated nitric acid solution and incubated at 25 ºC for 2 h. After incubation, samples were diluted (estimated concentration of iron ranging 10-200 ppb) in 0.5% (v/v) HNO_3 aqueous solution and injected into the instrument using a peristaltic pump from 15 ml tubes placed in the autosampler. Calibration curve was prepared with five solutions of different metal ion concentrations (0, 10, 100, 200 and 500 ppb), by diluting certified reference metal ion solutions.

Quantitative magnetic resonance imaging phantoms (MRI-Phantoms): Samples of Fe-DA-NPs were dispersed using agarose (1 % w/w) in phosphate buffer solution (PBS) at pH = 7.4. Five concentrations (0, 1, 5, 10, 25 µg/ml of iron) were prepared in 2 mL Eppendorf tubes. Nanoparticles were well dispersed through an ultrasound bath. Acquisition sequences for assessing longitudinal (T1) and transversal relaxation (T1) were carried out with 7T (300 MHz) Bruker BioSpec 70/30 USR spectrometer (Bruker BioSpin GmbH, Ettlingen, Germany).

Drug release assay: DA release from Fe-DA-NPs was determined using dialysis method. Nanoparticles were resuspended in a biomimetic nasal buffer (7.5 mg/ml of sodium chloride, 1.3 mg/ml of potassium chloride, and 0.3 mg/ml of calcium chloride),[51] supplemented with ascorbic acid (0.3 mg/ml) and inserted in dialysis bags (MWCO = 3500 Da). The dialysis bags were immersed in 150 ml of the same buffer at 37 °C. Aliquots of 500 µl were taken from the beaker at predetermined time periods (0.25, 0.5, 1, 2, 4, 6, 10, and 24 h), followed by the replacement with fresh buffer. The amount of released DA was determined by HPLC-EDC. 90 µl of different samples were mixed with 10 µl of homogenization buffer 10 X (25 M perchloric acid, 10 mM sodium bisulfite, and 25 mM EDTA), sonicated 10 s on ice, centrifuged and analyzed.

Epidermal Growth Factor (EGF) quantification: Protein quantification was performed by reverse phase HPLC through a Nova-Pak C8 cartridge (Waters), 4 µm particle size, 3.9x150 mm (Waters) equipped in a 2695 Separation Module (Waters) and analyzed using a multistep gradient elution. Solution A was 0.1% v/v of TFA in MilliQ® water and solution B was 0.1% of TFA acetonitrile. Elution started at 5% of acetonitrile followed by 30 minutes of linear increasing gradient, up to 35% of acetonitrile solution. Next, acetonitrile was raised to 98% in 5 minutes and it was maintained for 5 more minutes. Its level was then dropped again to 5% in 1-minute and was then maintained for the final 9 minutes. Protein elution was monitored by absorbance at 214 nm and 280 nm using a 2487 dual λ Absorbance Detector (Waters). The calibration curve was carried out by making a series of dilutions (from 10 to 100 µg/ml) of pure EGF

Encapsulation efficiency (EE(%)) and the loading capacity (LC(µg/mg)) of EGF were determined by the two following equations respectively:

$$EE(\%) = \frac{Weight\ of\ EGF\ in\ DA-NCPs}{Weight\ of\ initial\ EGF}$$

$$LC(\mu g/mg) = \frac{Weight\ of\ EGF\ in\ DA-NCPs}{Total\ weight\ of\ DA-NCPs}$$

Cell Cultures: The human BE(2)-M17 (ATCC CRL-2267) cell line were maintained in Opti-MEM supplemented with 10 % (v/v) FBS.

Carcinoma nasal RPMI 2650 (ATCC CCL-30) cell line was maintained in DMEM supplemented with 10 % (v/v) FBS, 1 % v/v not essential amino acids and 1% v/v pen-strep. Cells were grown under a highly humidified atmosphere of 95% air with 5% CO_2 at 37 °C.

***In Vitro* Cytotoxicity Experiments:** the cytotoxicity effects of free DA or Fe-DA-NPs on RPMI 2650 were evaluated by a resazurin-based assay. Briefly, RPMI2650 cells were seeded in 96-well plates at a

concentration of 3 x 104 cells per well and incubated for 24 h. After incubation, cells were washed two times with warmed PBS and treated with DA or Fe-DA-NCPs at different concentrations (ranging from 0.1 to 1000 µg/ml DA equivalent concentration) in cell culture medium. After further 24 h of incubation, cells were washed two times with PBS and 200 µl of resazurin (10% v/v) were added. After 2 h of incubation in absence of light, 100-200 µl were recollected from each well and transferred to a black-walled, transparent-bottom 96-well plate. Fluorescence (λ_{ex} = 530 nm, λ_{em} = 590 nm) of each well was measured using a fluorescence microplate reader (Biotek Synergy 2, Winooski,VT, USA). Cell cytotoxicity was expressed as percent of the control assay.

Reactive oxygen species determination: BE(2)-M17 cells were seeded in a 96-well plate at a density of 10 x 10^4 cells/well. After 24 h, DCFDA was added at a concentration of 25 µM, and cells were incubated at 37 °C in the absence of light, for 30 minutes. All conditions were tested in the presence or absence of a natural antioxidant, ascorbic acid (AA). After incubation, the media was replaced, and cells were exposed for 24 h to DA, DA-NCPs (with an equivalent DA concentration of 100, 10, and 1 µg/ml), and iron acetate (at concentrations corresponding to the same as the iron present in DA-NCPs). Hydrogen peroxide (H_2O_2) was used as a positive control at a concentration of 250 µM. Cell culture medium was supplemented or not with AA at 20 µg/ml. The fluorescence of each well was measured at 535 nm with a Victor3 microplate reader (PerkinElmer), after excitation at 485 nm. Results are reported as the average of two independent experiments. The analysis of variance was evaluated with one-way ANOVA. The comparison between different groups was assessed by applying the Tukey-HSD test. Significance level was set to 0.05.

Cellular Uptake: To study the uptake of free DA and DA-NCPs BE(2)-M17 cells were seeded in 60 mm culture plates at a density of 2.5 x 10^5 cells/plate and let grow for 24 h. Afterwards, cells were treated with different concentration of DA or DA-NCPs (1, 10, 25, 50 µg/ml) for 2 h. To prevent DA oxidation during treatments, media were further supplemented with 20 µg/ml of AA. For intracellular DA determination, cells were washed three times with cold PBS, scraped, and centrifuged at 1000 g for 5 min. The resulting pellets were suspended in a 1X homogenization buffer (2.5 M perchloric acid, 1 mM sodium bisulfite, and 2.5 mM EDTA) and sonicated for 15 s in ice, and centrifuged for 40 min at 4 °C. The supernatants were analyzed by HPLC-EDC, while the pellets were dispersed in PBS, and the total amount of protein was determined by the BCA protein assay kits (Thermo Fisher Scientific, Waltham, MA, USA). HPLC-ECD analyses were performed as described before.

Cells monolayer growth: In order to obtain a cells monolayer model, RPMI 2650 were seeded on the apical chamber of a 12-well Transwell™ insert (transparent polyester membrane, 1 µm pore diameter, 4.67 cm^2) at a density of 2.0 x 10^5 cells/cm^2. Cells were maintained in the same culture conditions for

14-21 days, and cell culture medium was changed every two days both from apical and basolateral sides. From day 7, the transepithelial electrical resistance (TEER) was measured every two days before changing medium, up to the day of the experiment using an EVOM Epithelial Volthometer Instrument equipped with a chopstick electrode (World Precision Instruments, Sarasota, FL, USA).

Permeability study: After 14 days from seeding, to perform the permeability experiment, the medium was removed from both the apical and basolateral sides, and cells were washed twice with warmed Hank's Balanced Salt Solution (BBSS). Then, cells monolayer was left equilibrated with HBSS for 30 minutes at 37 °C, in an orbital shaking incubator (IKA® KS 4000 IC) at 100 rpm. After that, the HBSS from the apical side was replaced with free DA or Fe-DA-NPs at 10 µg/ml. Aliquots of 200 µl were collected from the basolateral side at different time points (15, 30, 60, 120, 180 minutes) and replaced with fresh HBSS. 90 µl of different samples were mixed with 10 µl of homogenization buffer 10 X, sonicated 10 s in ice, centrifuged and analyzed by HPLC-EDC. During the experiment TEER was measured to verify the cells monolayers integrity. Results were expressed as percentage of permeability and drug apparent permeability (Papp (cm/s)) calculated using the following equation:

$$Papp = \frac{dQ}{dt} \; x \; \frac{1}{A \; x \; C_0}$$

where dQ is the amount of cumulative drug quantified in the basolateral side (µg) at the latest time, A is the surface area of the insert (cm^2), C_0 is the initial drug concentration in the apical side (µg/ml) and dt is the experiment duration (seconds).

3.7 References

1. Batten, S. R. *et al.* Terminology of metal–organic frameworks and coordination polymers (IUPAC Recommendations 2013). *Pure Appl. Chem.* **85**, 1715–1724 (2013).
2. Liu, Y., Lv, S., Liu, D. & Song, F. Recent development of amorphous metal coordination polymers for cancer therapy. *Acta Biomater.* **116**, 16–31 (2020).
3. Dey, K., Mohata, S. & Banerjee, R. Covalent Organic Frameworks and Supramolecular Nano-Synthesis. *ACS Nano* **15**, 12723–12740 (2021).
4. Novio, F., Simmchen, J., Vázquez-Mera, N., Amorín-Ferré, L. & Ruiz-Molina, D. Coordination polymer nanoparticles in medicine. *Coord. Chem. Rev.* **257**, 2839–2847 (2013).
5. Solórzano, R. *et al.* Nanoscale coordination polymers for medicine and sensors. in *Advances in Inorganic Chemistry* vol. 76 3–31 (Elsevier, 2020).
6. He, C., Liu, D. & Lin, W. Nanomedicine Applications of Hybrid Nanomaterials Built from Metal–Ligand Coordination Bonds: Nanoscale Metal–Organic Frameworks and Nanoscale Coordination Polymers. *Chem. Rev.* **115**, 11079–11108 (2015).

7. Masoomi, M. Y., Morsali, A., Junk, P. C. & Wang, J. Ultrasonic assisted synthesis of two new coordination polymers and their applications as precursors for preparation of nano-materials. *Ultrason. Sonochem.* **34**, 984–992 (2017).
8. Novio, F. & Ruiz-Molina, D. Coordination Polymers for Medical Applications: Amorphous versus Crystalline Materials. in *Hybrid Organic-Inorganic Interfaces* (eds. Delville, M.-H. & Taubert, A.) 661–694 (Wiley-VCH Verlag GmbH & Co. KGaA, 2017). doi:10.1002/9783527807130.ch15.
9. Wang, J.-L. *et al.* Room-temperature preparation of coordination polymers for biomedicine. *Coord. Chem. Rev.* **411**, 213256 (2020).
10. Zhu, W., Zhao, J., Chen, Q. & Liu, Z. Nanoscale metal-organic frameworks and coordination polymers as theranostic platforms for cancer treatment. *Coord. Chem. Rev.* **398**, 113009 (2019).
11. Guardingo, M. *et al.* Synthesis of Nanoscale Coordination Polymers in Femtoliter Reactors on Surfaces. *ACS Nano* **10**, 3206–3213 (2016).
12. Puigmartí-Luis, J. Microfluidic platforms: a mainstream technology for the preparation of crystals. *Chem Soc Rev* **43**, 2253–2271 (2014).
13. Carné, A., Carbonell, C., Imaz, I. & Maspoch, D. Nanoscale metal–organic materials. *Chem Soc Rev* **40**, 291–305 (2011).
14. Oh, M. & Mirkin, C. A. Chemically tailorable colloidal particles from infinite coordination polymers. *Nature* **438**, 651–654 (2005).
15. Suárez-García, S. *et al.* Antitumour activity of coordination polymer nanoparticles. *Coord. Chem. Rev.* **441**, 213977 (2021).
16. Amorín-Ferré, L. *et al.* Encapsulation and Release Mechanisms in Coordination Polymer Nanoparticles. *Chem. – Eur. J.* **19**, 17508–17516 (2013).
17. Gao, P. F. *et al.* A new type of pH-responsive coordination polymer sphere as a vehicle for targeted anticancer drug delivery and sustained release. *J. Mater. Chem. B* **1**, 3202 (2013).
18. Huxford, R. C., deKrafft, K. E., Boyle, W. S., Liu, D. & Lin, W. Lipid-coated nanoscale coordination polymers for targeted delivery of antifolates to cancer cells. *Chem Sci* **3**, 198–204 (2012).
19. Liu, J. *et al.* Biodegradable Nanoscale Coordination Polymers for Targeted Tumor Combination Therapy with Oxidative Stress Amplification. *Adv. Funct. Mater.* **30**, 1908865 (2020).
20. He, C. *et al.* Core-shell nanoscale coordination polymers combine chemotherapy and photodynamic therapy to potentiate checkpoint blockade cancer immunotherapy. *Nat. Commun.* **7**, 12499 (2016).
21. Mu, X., Yan, C., Tian, Q., Lin, J. & Yang, S. BSA-assisted synthesis of ultrasmall gallic acid–Fe(III) coordination polymer nanoparticles for cancer theranostics. *Int. J. Nanomedicine* **Volume 12**, 7207–7223 (2017).
22. Borges, M. *et al.* Dual T_1 /T_2 MRI contrast agent based on hybrid SPION@coordination polymer nanoparticles. *RSC Adv.* **5**, 86779–86783 (2015).
23. Suárez-García, S. *et al.* Dual T_1 / T_2 Nanoscale Coordination Polymers as Novel Contrast Agents for MRI: A Preclinical Study for Brain Tumor. *ACS Appl. Mater. Interfaces* **10**, 38819–38832 (2018).
24. Cheng, G. *et al.* Ultrasmall Coordination Polymers for Alleviating ROS-Mediated Inflammatory and Realizing Neuroprotection against Parkinson's Disease. *Research* **2022**, 2022/9781323 (2022).
25. Pinna, A. *et al.* A MOF-based carrier for *in situ* dopamine delivery. *RSC Adv.* **8**, 25664–25672 (2018).

26. Holten-Andersen, N. *et al.* Metal-coordination: using one of nature's tricks to control soft material mechanics. *J Mater Chem B* **2**, 2467–2472 (2014).
27. Lee, B. P., Narkar, A. & Wilharm, R. Effect of metal ion type on the movement of hydrogel actuator based on catechol-metal ion coordination chemistry. *Sens. Actuators B Chem.* **227**, 248–254 (2016).
28. Gerlach, M. *et al.* Neuromelanin and its interaction with iron as a potential risk factor for dopaminergic neurodegeneration underlying Parkinson's disease. *Neurotox. Res.* **5**, 35–43 (2003).
29. Holten-Andersen, N. *et al.* pH-induced metal-ligand cross-links inspired by mussel yield self-healing polymer networks with near-covalent elastic moduli. *Proc. Natl. Acad. Sci.* **108**, 2651–2655 (2011).
30. Dong, C. *et al.* Mussel byssus cuticle-inspired ultrastiff and stretchable triple-crosslinked hydrogels. *J. Mater. Chem. B* **9**, 373–380 (2021).
31. Sever, M. J. & Wilker, J. J. Visible absorption spectra of metal–catecholate and metal–tironate complexes. *Dalton Trans* 1061–1072 (2004) doi:10.1039/B315811J.
32. Bijlsma, J. *et al.* Revealing the main factors and two-way interactions contributing to food discolouration caused by iron-catechol complexation. *Sci. Rep.* **10**, 8288 (2020).
33. Lee, B. P., Lin, M.-H., Narkar, A., Konst, S. & Wilharm, R. Modulating the movement of hydrogel actuator based on catechol–iron ion coordination chemistry. *Sens. Actuators B Chem.* **206**, 456–462 (2015).
34. Taghizadeh, A. *et al.* Mussel-inspired biomaterials: From chemistry to clinic. *Bioeng. Transl. Med.* **7**, (2022).
35. Yuan, C. *et al.* Protein-responsive assemblies from catechol–metal ion supramolecular coordination. *Soft Matter* **11**, 2243–2250 (2015).
36. Ganguly, R., Saha, P., Banerjee, S. L., Pich, A. & Singha, N. K. Stimuli-Responsive Block Copolymer Micelles Based on Mussel-Inspired Metal-Coordinated Supramolecular Networks. *Macromol. Rapid Commun.* **42**, 2100312 (2021).
37. Guo, J. *et al.* Engineering Multifunctional Capsules through the Assembly of Metal-Phenolic Networks. *Angew. Chem. Int. Ed.* **53**, 5546–5551 (2014).
38. Nador, F. *et al.* Solvent-Tuned Supramolecular Assembly of Fluorescent Catechol/Pyrene Amphiphilic Molecules. *Chem. - Eur. J.* **24**, 14724–14732 (2018).
39. Krogsgaard, M., Behrens, M. A., Pedersen, J. S. & Birkedal, H. Self-Healing Mussel-Inspired Multi-pH-Responsive Hydrogels. *Biomacromolecules* **14**, 297–301 (2013).
40. Kim, B. J., Cheong, H., Hwang, B. H. & Cha, H. J. Mussel-Inspired Protein Nanoparticles Containing Iron(III)-DOPA Complexes for pH-Responsive Drug Delivery. *Angew. Chem. Int. Ed.* **54**, 7318–7322 (2015).
41. Solórzano, R. *et al.* Versatile iron–catechol-based nanoscale coordination polymers with antiretroviral ligand functionalization and their use as efficient carriers in HIV/AIDS therapy. *Biomater. Sci.* **7**, 178–186 (2019).
42. Sever, M. J. & Wilker, J. J. Absorption spectroscopy and binding constants for first-row transition metal complexes of a DOPA-containing peptide. *Dalton Trans* 813–822 (2006) doi:10.1039/B509586G.
43. Rana, D. *et al.* Strategies to prevent dopamine oxidation and related cytotoxicity using various antioxidants and nitrogenation. *Emergent Mater.* **2**, 209–217 (2019).

44. Lopez, T. Treatment of Parkinson's disease: nanostructured sol-gel silica–dopamine reservoirs for controlled drug release in the central nervous system. *Int. J. Nanomedicine* 19 (2010) doi:10.2147/IJN.S13223.
45. Besenhard, M. O. *et al.* Co-precipitation synthesis of stable iron oxide nanoparticles with NaOH: New insights and continuous production via flow chemistry. *Chem. Eng. J.* **399**, 125740 (2020).
46. Hong, S., Wang, Y., Park, S. Y. & Lee, H. Progressive fuzzy cation-π assembly of biological catecholamines. *Sci. Adv.* **4**, eaat7457 (2018).
47. Pahuja, R. *et al.* Trans-Blood Brain Barrier Delivery of Dopamine-Loaded Nanoparticles Reverses Functional Deficits in Parkinsonian Rats. *ACS Nano* **9**, 4850–4871 (2015).
48. Lopalco, A. *et al.* Transferrin Functionalized Liposomes Loading Dopamine HCl: Development and Permeability Studies across an In Vitro Model of Human Blood–Brain Barrier. *Nanomaterials* **8**, 178 (2018).
49. Kang, Y.-S., Jung, H.-J., Oh, J.-S. & Song, D.-Y. Use of PEGylated Immunoliposomes to Deliver Dopamine Across the Blood-Brain Barrier in a Rat Model of Parkinson's Disease. *CNS Neurosci. Ther.* **22**, 817–823 (2016).
50. Nieto, C., Vega, M. A., Marcelo, G. & Martín del Valle, E. M. Polydopamine nanoparticles kill cancer cells. *RSC Adv.* **8**, 36201–36208 (2018).
51. Masiuk, T., Kadakia, P. & Wang, Z. Development of a physiologically relevant dripping analytical method using simulated nasal mucus for nasal spray formulation analysis. *J. Pharm. Anal.* **6**, 283–291 (2016).
52. Yoo, J. & Won, Y.-Y. Phenomenology of the Initial Burst Release of Drugs from PLGA Microparticles. *ACS Biomater. Sci. Eng.* **6**, 6053–6062 (2020).
53. Shen, Y. *et al.* T1 Relaxivities of Gadolinium-Based Magnetic Resonance Contrast Agents in Human Whole Blood at 1.5, 3, and 7 T: *Invest. Radiol.* **50**, 330–338 (2015).
54. Suárez-García, S. *et al.* Dual T_1 / T_2 Nanoscale Coordination Polymers as Novel Contrast Agents for MRI: A Preclinical Study for Brain Tumor. *ACS Appl. Mater. Interfaces* **10**, 38819–38832 (2018).
55. Costa, C. P. *et al.* In Vitro Studies on Nasal Formulations of Nanostructured Lipid Carriers (NLC) and Solid Lipid Nanoparticles (SLN). *Pharmaceuticals* **14**, 711 (2021).
56. Kürti, L. *et al.* In vitro and in vivo characterization of meloxicam nanoparticles designed for nasal administration. *Eur. J. Pharm. Sci.* **50**, 86–92 (2013).
57. Kürti, L. *et al.* Retinoic acid and hydrocortisone strengthen the barrier function of human RPMI 2650 cells, a model for nasal epithelial permeability. *Cytotechnology* **65**, 395–406 (2013).
58. Trapani, A. *et al.* Characterization and evaluation of chitosan nanoparticles for dopamine brain delivery. *Int. J. Pharm.* **419**, 296–307 (2011).
59. Banerjee, K. *et al.* Dopamine Cytotoxicity Involves Both Oxidative and Nonoxidative Pathways in SH-SY5Y Cells: Potential Role of Alpha-Synuclein Overexpression and Proteasomal Inhibition in the Etiopathogenesis of Parkinson's Disease. *Park. Dis.* **2014**, 1–12 (2014).
60. Jana, S. *et al.* Mitochondrial dysfunction mediated by quinone oxidation products of dopamine: Implications in dopamine cytotoxicity and pathogenesis of Parkinson's disease. *Biochim. Biophys. Acta BBA - Mol. Basis Dis.* **1812**, 663–673 (2011).
61. Reichl, S. & Becker, K. Cultivation of RPMI 2650 cells as an in-vitro model for human transmucosal nasal drug absorption studies: optimization of selected culture conditions. *J. Pharm. Pharmacol.* **64**, 1621–1630 (2012).

62. Dolberg, A. M. & Reichl, S. Expression analysis of human solute carrier (SLC) family transporters in nasal mucosa and RPMI 2650 cells. *Eur. J. Pharm. Sci.* **123**, 277–294 (2018).
63. Schlachet, I. & Sosnik, A. Mixed Mucoadhesive Amphiphilic Polymeric Nanoparticles Cross a Model of Nasal Septum Epithelium in Vitro. *ACS Appl. Mater. Interfaces* **11**, 21360–21371 (2019).
64. Pozzoli, M. *et al.* Application of RPMI 2650 nasal cell model to a 3D printed apparatus for the testing of drug deposition and permeation of nasal products. *Eur. J. Pharm. Biopharm.* **107**, 223–233 (2016).
65. Lungare, S., Bowen, J. & Badhan, R. Development and Evaluation of a Novel Intranasal Spray for the Delivery of Amantadine. *J. Pharm. Sci.* **105**, 1209–1220 (2016).
66. Kreft, M. E. *et al.* The Characterization of the Human Nasal Epithelial Cell Line RPMI 2650 Under Different Culture Conditions and Their Optimization for an Appropriate in vitro Nasal Model. *Pharm. Res.* **32**, 665–679 (2015).
67. Beule, A. G. Physiology and pathophysiology of respiratory mucosa of the nose and the paranasal sinuses. *GMS Curr. Top. Otorhinolaryngol. - Head Neck Surg. 9Doc07 ISSN 1865-1011* (2010)
68. das Neves, J., Bahia, M. F., Amiji, M. M. & Sarmento, B. Mucoadhesive nanomedicines: characterization and modulation of mucoadhesion at the nanoscale. *Expert Opin. Drug Deliv.* **8**, 1085–1104 (2011).
69. Qu, M. *et al.* Dopamine-loaded blood exosomes targeted to brain for better treatment of Parkinson's disease. *J. Controlled Release* **287**, 156–166 (2018).
70. Duarte-Jurado, A. P. *et al.* Antioxidant Therapeutics in Parkinson's Disease: Current Challenges and Opportunities. *Antioxidants* **10**, 453 (2021).
71. Yasuda, T. & Mochizuki, H. Use of growth factors for the treatment of Parkinson's disease. *Expert Rev. Neurother.* **10**, 915–924 (2010).
72. Jarrin, S., Hakami, A., Newland, B. & Dowd, E. Growth Factor Therapy for Parkinson's Disease: Alternative Delivery Systems. *J. Park. Dis.* **11**, S229–S236 (2021).
73. Andres, D. *et al.* Morphological and functional differentiation in BE(2)-M17 human neuroblastoma cells by treatment with Trans-retinoic acid. *BMC Neurosci.* **14**, 49 (2013).
74. Bourdenx, M. *et al.* Nanoparticles restore lysosomal acidification defects: Implications for Parkinson and other lysosomal-related diseases. *Autophagy* **12**, 472–483 (2016).
75. Kalyanaraman, B. *et al.* Measuring reactive oxygen and nitrogen species with fluorescent probes: challenges and limitations. *Free Radic. Biol. Med.* **52**, 1–6 (2012).
76. Farzam, A. *et al.* A functionalized hydroxydopamine quinone links thiol modification to neuronal cell death. *Redox Biol.* **28**, 101377 (2020).
77. Zucca, F. A. *et al.* Interactions of iron, dopamine and neuromelanin pathways in brain aging and Parkinson's disease. *Prog. Neurobiol.* **155**, 96–119 (2017).
78. Li, C.-L., Werner, P. & Cohen, G. Lipid Peroxidation in Brain: Interactions of L-DOPA/Dopamine with Ascorbate and Iron. *Neurodegeneration* **4**, 147–154 (1995).
79. Maharaj, H., Sukhdev Maharaj, D., Scheepers, M., Mokokong, R. & Daya, S. l-DOPA administration enhances 6-hydroxydopamine generation. *Brain Res.* **1063**, 180–186 (2005).
80. Maalmi, M., Strieder, W. & Varma, A. Ligand diffusion and receptor mediated internalization: Michaelis–Menten kinetics. *Chem. Eng. Sci.* **56**, 5609–5616 (2001).

81. Yazdanian, M., Glynn, S. L., Wright, J. L. & Hawi, A. Correlating Partitioning and Caco-2 Cell Permeability of Structurally Diverse Small Molecular Weight Compounds. *Pharm. Res.* **15**, 1490–1494 (1998).
82. Mistry, A., Stolnik, S. & Illum, L. Nose-to-Brain Delivery: Investigation of the Transport of Nanoparticles with Different Surface Characteristics and Sizes in Excised Porcine Olfactory Epithelium. *Mol. Pharm.* **12**, 2755–2766 (2015).
83. Mistry, A. *et al.* Effect of physicochemical properties on intranasal nanoparticle transit into murine olfactory epithelium. *J. Drug Target.* **17**, 543–552 (2009).
84. Adarsh, N. N., Novio, F. & Ruiz-Molina, D. Coordination polymers built from 1,4-bis(imidazol-1-ylmethyl)benzene: from crystalline to amorphous. *Dalton Trans.* **45**, 11233–11255 (2016).
85. Novio, F., Lorenzo, J., Nador, F., Wnuk, K. & Ruiz-Molina, D. Carboxyl Group (CO_2H) Functionalized Coordination Polymer Nanoparticles as Efficient Platforms for Drug Delivery. *Chem. - Eur. J.* **20**, 15443–15450 (2014).

Chapter 4

4. Design of biomimetic ellipsoidal microparticles and their application as a new class of vaccines

In this chapter, biomimetic microparticles were synthesized exhibiting the same size and shape of *Pseudomonas aeruginosa*, and their surface was decorated with a model protein (BSA) or with specific antigens extracted by the bacterium (NrdJ and FliC). Ellipsoidal particles, with dimensions of 1.3 x 0.5 µm, were successfully obtained by the stretching method of spherical particles. The surface of both spherical and ellipsoidal particles was functionalized with the proteins, and the bound amount was calculated by the reliable fast protein liquid chromatographic technique, the stability of NrdJ antigen before its binding was also studied. The immune system activation of *Galleria mellonella* larvae was evaluated, and the NrdJ-functionalized ellipsoidal particles showed an enhanced immunogenic capability, demonstrating how the shape has a crucial role in immunomodulation. These particles pave the way for the evaluation of a new powerful class of bacterial vaccines.

This work was done in collaboration with the Bacterial infections: antimicrobial therapies group, led by Dr. Eduard Torrents, from the Institute for Bioengineering of Catalonia.

4.1 Introduction

4.1.1 Polylactic acid particles in biomedical applications

Biocompatible polymers have found vast applications in biomedicine thanks to their unique properties. Compared to natural polymers, synthetic ones provide higher flexibility as it is possible to tailor their chemical, physical and mechanical properties.[1] Among them, polylactic acid (PLA) occupies an exceptional place in biomedical fields, being used for the fabrication of scaffolds for tissue regeneration, implants, surgical materials, and especially for micro and nanostrucutration.[2,3] This extended use relies on the advantages of this polymer, like intrinsic biocompatibility, low cost, and high versatility. As other polyesters, indeed, the ester bond can be hydrolyzed, forming lactic acids units that can be eliminated by the body as CO2 or water after entering in the Kreb's cycle.[4] Thanks to its biocompatibility and biodegradability PLA, has been approved by FDA, and several products are already available in clinical uses.[5]

PLA can be found in two forms, as it possesses an asymmetric structure, the PDLA or PLLA, which present different features: PLLA, which undergoes to a slower degradation rate, is preferred in biological applications.[2] The PLA properties, such as flexibility, malleability, or its glass transition temperature, can be easily adjusted by adding a plasticizer, by blending, crosslinking or copolymerizing with other polymers, or by mixing it with other organic/inorganic materials to achieve composites.[4]

Considering all these advantages, micro and nanostructuration of PLA has been widely exploited. Particularly, micro and nanoparticles have found several applications, especially for drug delivery and immune modulation (as mentioned in the general introduction). The tunability of their properties allows to achieve the desirable pharmacokinetic and biodegradable features, leading to a controlled release. Moreover, their surface can be easily modified by chemical linking, coating, or plasma treatment.[5] PLA particles can be obtained as solid particles, where the polymer is present in all the particle volumes, or capsules, where a different substant is also present and protected by the polymer.[6-7] Polymeric capsules usually possess a core-shell structure, where the polymer (the shell) surrounds the second substance (the core), which could consist of single or multiple domains. [8,9]

Different synthetic strategies can be used for the fabrication of polymeric particles, which can be carried out by starting from the preformed polymer or from the single monomers. In the case of PLA, the more employed is the emulsion/solvent evaporation method, which allows to obtain both micro and nanoparticle,[5 10] and it has been the one used and selected in this work.

Single emulsion/solvent evaporation method

It consists on the formation of an initial emulsion; in this work, the oil-in-water has been employed (O/W). The polymer is dissolved in a water-immiscible solvent, usually chloroform and dichloromethane, and then added to a water phase containing a stabilizer or surfactant. The mixture is consequently emulsified by a high-energy source, like ultrasounds or homogenizers. After the emulsification process has been carried out, the organic solvent is left to evaporate, which causes the progressive polymer precipitation, that remains entrapped and deposited in the oil droplets. Solvent evaporation can be conducted at room temperature under magnetic agitation or at low pressure or vacuum. Once polymeric particles are obtained, they can be washed to remove residual solvent or excess of surfactant by centrifugation or cross-flow filtration (Figure 4.1).[5]

The use of surfactants is fundamental in order to reduce the interfacial tension between the two phases, making the emulsification process more favorable while reducing the phase separation mechanism like coalescence or repealing phenomena.

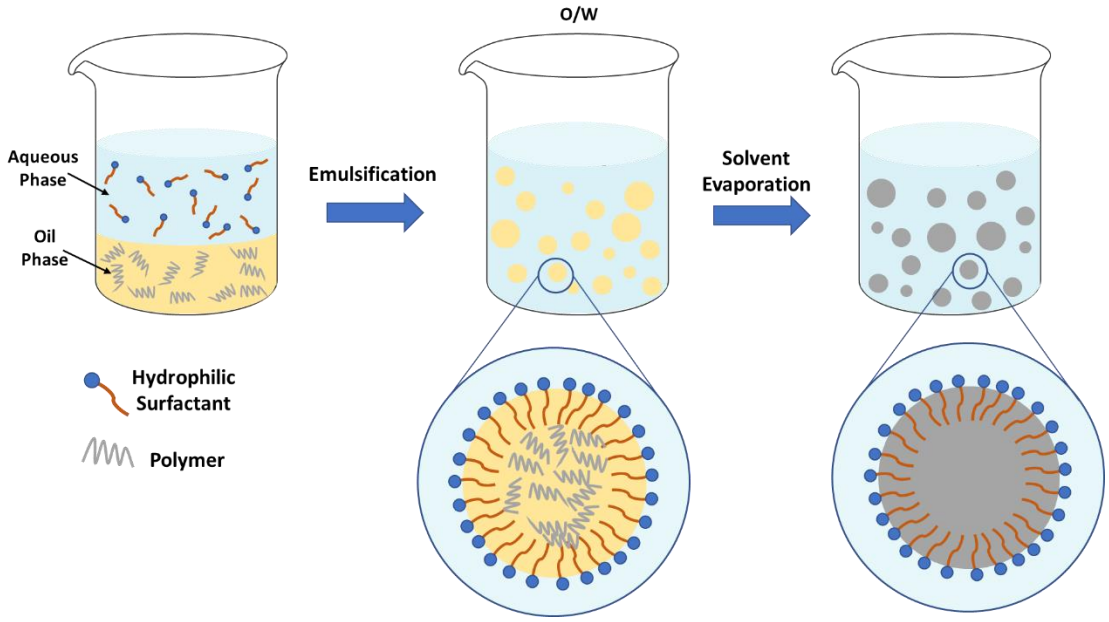

Figure 4.1: Schematic representation of single emulsion/evaporation method.

The encapsulation of several hydrophobic molecules, such as oils, fluorescent dyes or drugs, is achievable by simply adding the desired moiety in the organic phase along with the dissolved polymer. However, especially for biomedical applications, the encapsulation of hydrophilic macromolecules or hydrophilic drugs is desired. Therefore, a modification of this method has been developed.[11]

Double emulsion/solvent evaporation

In this work, a water-in-oil-in-water double emulsion has been used. This strategy is carried out in two steps, making it relatively more complicated than the single emulsion process. As constituted by two separate emulsions, each of them needs to be individually stabilized, thus, the employment of two different surfactants is required. Their selection is a crucial aspect to consider, as they should possess a lipophilic or hydrophilic tendency, for the first and second emulsion respectively, which is expressed by the hydrophilic-lipophilic balance (HBL) value. A first water-in-oil emulsion is made by adding a water phase, which could contain the molecule to be encapsulated, to the organic one, constituted by the polymer dissolution and the lipophilic surfactant. Once the emulsification process is accomplished, this first emulsion is added to a second water phase in the presence of a hydrophilic surfactant, and a further emulsification step is carried out. The evaporation of the organic solvent, even in this case, leads to the formation of solid particles (Figure 4.2).

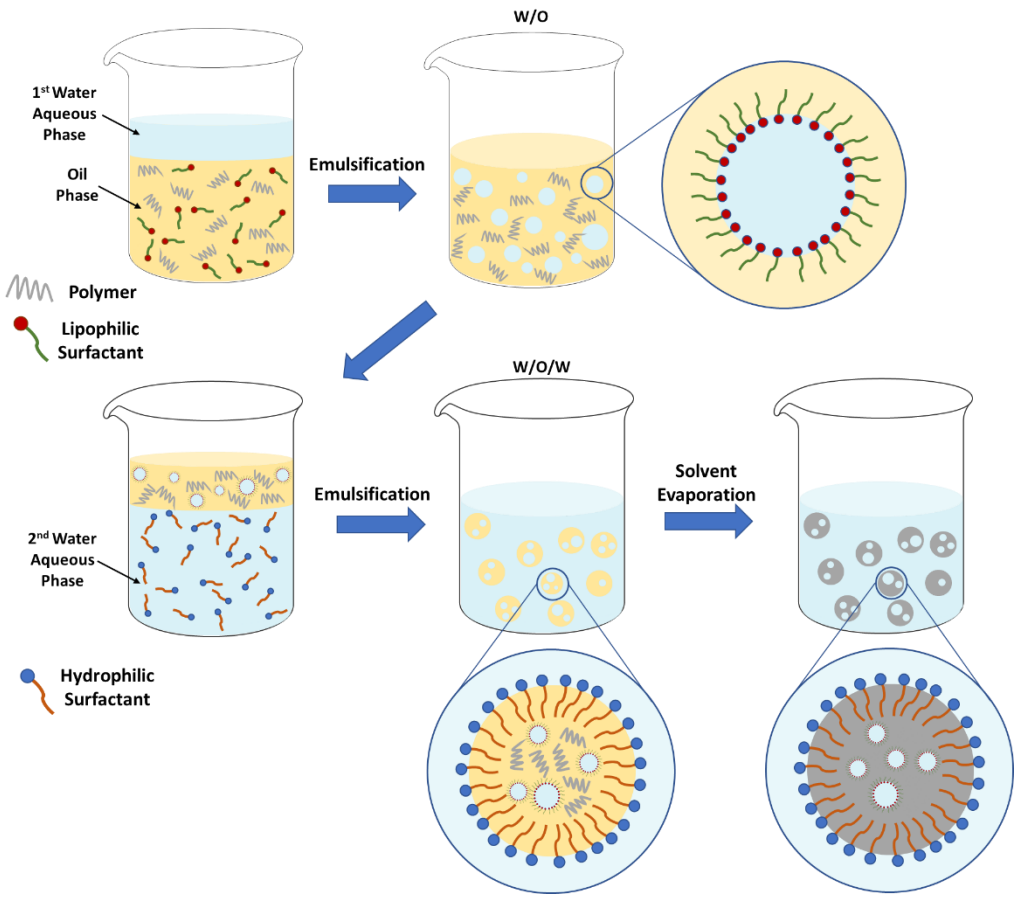

Figure 4.2: Schematic representation of double emulsion/solvent evaporation method.

PLA particles formation has been performed using different stabilizers or surfactants, both ionic[12] and non-ionic. The more used are polyvinyl alcohol (PVA)[13] as stabilizer and Polysorbates, both lipophilic and hydrophilic, as surfactants.[14]

Different parameters can be modulated in both single and double emulsion to control the final particles size and distribution, such as surfactant concertation, solvent evaporation rate, organic and water phase ratio, and viscosity.[13] Nevertheless, the final size of the oil droplets primarily depends on the external energy provided. As nanoemulsion is a more thermodynamically unstable system, a higher energy (e.g. by ultrasounds or high pressure homogenizers) is required to reduce the droplets dimensions.

Through these conventional methods, spherical particles are always obtained; however, the development and study of different geometries has gained increasing interest.

4.1.2 Non-spherical polymeric particles

Several biological systems exhibit a non-spherical shape; for example, as mentioned in the general introduction, many bacteria have an ellipsoidal geometry, while the red blood cells have a discoidal one.[15,15] The display of these inherent geometries led to wonder if the shape of particles could have a significant impact on their interaction with cells or biological components; therefore, the interest in anisotropic particles has exponentially increased in the last 20 years (Figure 4.3).[16]

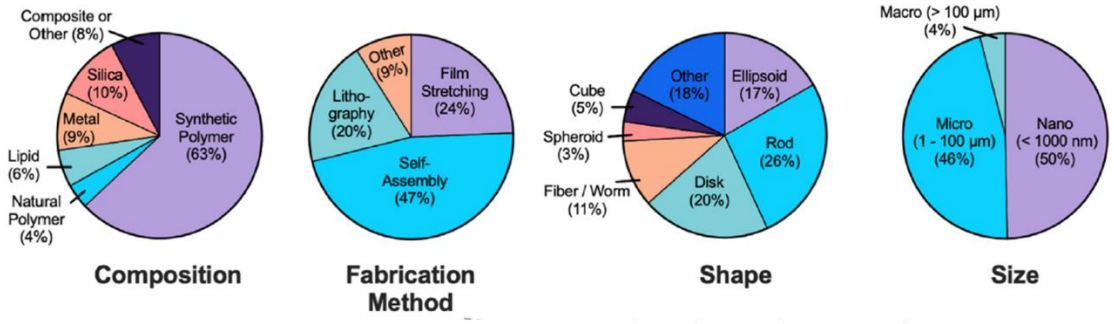

Figure 4.3: Summary statistics studied until 2021 about composition, fabrication method, shape, and dimensions of non-spherical particles (reported as %). Adapted from [17].

Inorganic particles, like iron oxide or gold nanoparticles, can be obtained with different shapes by simply varying synthesis parameters. However, non-spherical organic particles, mainly polymers, have also been produced through several methods. Self-assembly is the most used strategy, and the most common structures obtained are rods or worms.[18] Other possible techniques are layer-by-layer deposition[19] or the more sophisticated photolithography[20] and microfluidics.[21] A different approach,

named film stretching, is based on the mechanical deformation of preformed spherical particles, which has been employed in this thesis. This method was first applied back in 1993 by Ho *et al.*[22] to obtain ellipsoidal particles, but only in 2007, its application was extended to other geometries.[23,24] It relies on the use of an auxiliary water-soluble polymeric film in which spherical particles are embedded. Spherical particles are made plastically deformable (liquefaction) by using temperature or a solvent treatment (usually toluene). In the case of thermal plasticization, the film is immersed in an oil bath heated above the glass transition temperatures of both the film and particles polymer while a mechanical stretching is applied. The polymer chains of particles follow the direction of the external deformation. Finally, non-spherical particles can be collected by simply dissolving the polymeric film in water. Usually, for elongation, two equal forces are applied in opposite directions at the extremities of the film.

Non-spherical micro and nanoparticles have been successfully obtained through this method, both in the form of solid particles and capsules.[25-26] Particularly, polystyrene (PS) and poly(lactic-co-glycolic acid) (PLGA) are the most studied; a few examples of non-spherical PLA are reported.[27] The most employed film-forming polymer is instead the polyvinyl alcohol (PVA).[17]

Several geometries can be obtained by the film stretching strategy by employing a mono or two-dimensional deformation. Though the more straightforward geometry is the ellipsoidal one, achieved by a single-direction stretching; its elongation is evaluated by the aspect ratio, defined as the ratio between the major and the minor axis. However, several other aspects can influence the final shape: [17,23]

- Parameters of the procedure, including the liquefacation method, the temperature, or the stretching rate.
- Film properties, like the type of film-forming polymer, thickness, or concentration of plasticizers.
- Particles properties, such as type of polymer and concentration.
- Method of stretching.

Champion et al., studied the combination of different parameters to modulate the final geometry of PS particles.[24] Moreover, they proposed a possible modification of the method to further extended the possible achievable shapes, where the film stretching was performed before the liquefacation of the particles. In this manner, voids around the embedded particles were formed, which were filled only after the consequent liquefacation performed by solvent or heating. The authors employed initial spherical particles of different sizes, between 0.9 and 5.7 μm. A schematic representation of some of the tested combined parameters and the resulting shapes are reported in Figure 4.4; however, many other shapes were also produced. For instance, it was possible to obtain flat or ticker disks by using different film

thicknesses. Moreover, by modulating the temperature used during the stretching or decreasing the film viscosity, it was possible to control the sharpness of the particles borders.[24] Clearly, this shape variability made challenging the definition of parameters for characterizing and comparing different particles, such as the aspect ratio for ellipsoidal particles.

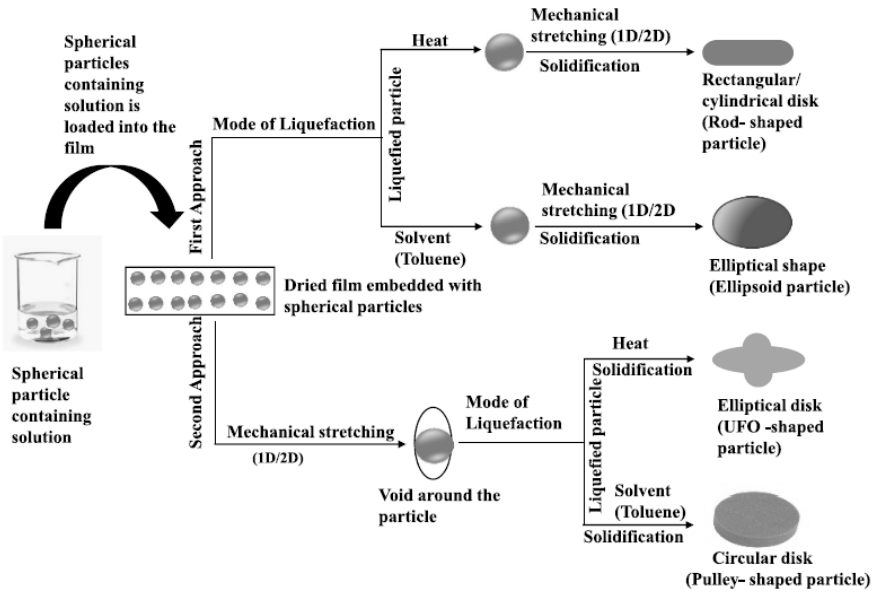

Figure 4.4: Schematic representation of the combination of different film stretching methods and parameters to polymeric particles with different shapes. Reported from [23] and [24].

The stretching method presents several advantages, such as high versatility in the possible achievable shape, and it is straightforward to be carried out. However, it consists of a multi-steps and time-consuming process, reducing scalability. [16,17] Moreover, it could lack reproducibility, mainly due to the stretching method. In most studies, the stretching is performed by employing "home-made" devices, where no standards have been set yet. Moreover, a detailed description of their setups is rarely provided. Some examples of reported custom-made apparatus are pictured in Figure 4.5,[28,29] which appeare bulky, making their use difficult, especially when silicon oil at high temperatures is employed.

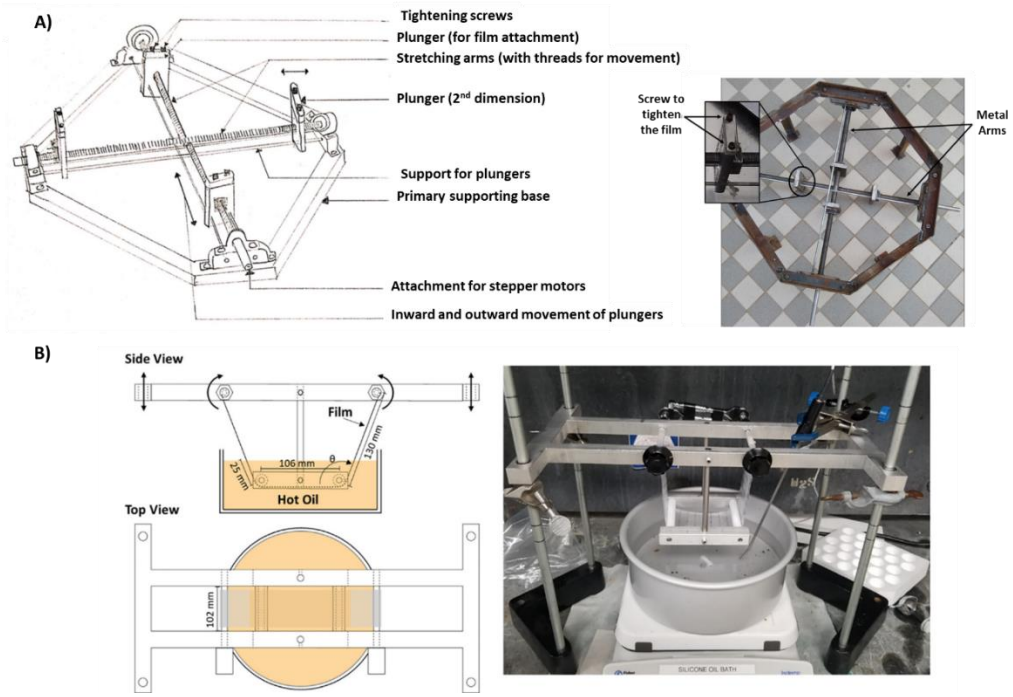

Figure 4.5: Schematic representation and pictures of home-made apparatus. Reported from A) [29], and B) [28].

The anisotropy of particles could influence their biodistribution *in vivo*. On one hand, spherical and non-spherical particles can be uptake differently by cells; on the other, their flow behavior in vasculature could differ. The control of particles shape would permit to inhibit or promote unspecific/specific internalization,[30] and to modulate the blood circulation time.[31] For this, particles with different geometries have been investigated for their uses in immunomodulation, cancer therapy, and target drug delivery.[17] As explained in the introduction, phagocytosis drastically depends on particles local curvature.[32] By escaping macrophages internalization, non-spherical particles would remain longer in blood circulation, with a consequent liver accumulation reduction. Moreover, their shape provides a more complex flow behavior in the blood, which would help to move toward the blood vessels (margination phenomenon), while spherical particles tend to flow along with red blood cells; once attached to the walls, non-spherical particles show a higher binding possibility due to their higher specific surface area.[33] Taken together, all these features permit to enhance the capability of non-spherical particles to reach the targeted organs more easily.

Although the increasing interest in the role of particles shape, more research is still needed to clearly elucidate the interactions with biological systems; furthermore, only few studies have reached clinical trials. Nevertheless, particles shape must always be considered in combination with other parameters, such as size and surface properties.

In our work, ellipsoidal particles were produced and studied. This shape is one of the more interesting as it results biomimetic toward different bacteria, such as *Pseudomonas aeruginosa*.

4.2 Objectives

Antibiotic resistance represents one of the biggest challenges for global health, and the employment of vaccines represents a unique opportunity to face this struggle. The latest developments are mainly based on using live-attenuated pathogens or fragments of them, such as proteins called antigens, obtained by bacteria. However, these approaches are active for specific diseases and for a short period of time, present risks of re-activation or are based on subunits morphologically and dimensionally different from the real pathogen, affecting the efficiency of antibody production. Micro and nanoparticles have also been proposed and synthesized as new vaccines, acting as adjuvants or carriers for the antigens' delivery. Moreover, particles with different shapes have attracted great attention, particularly for immunological purposes.

Pseudomonas aeruginosa is a gram-negative bacterium that, like several other bacteria, is characterized by an elongated ellipsoidal shape. Particularly, it possesses dimensions around 1.5 x 0.5 µm, and an aspect ratio (AR), defined as the ratio of the major and minor axes of an ellipse, of 2.6-2.7 (Figure 4.6). *Pseudomonas aeruginosa* has already demonstrated resistance to a broad spectrum of antibiotics, and effective vaccines are still lacking. Thus, new strategies are urgently needed to obtain impactful vaccines against such bacterium.

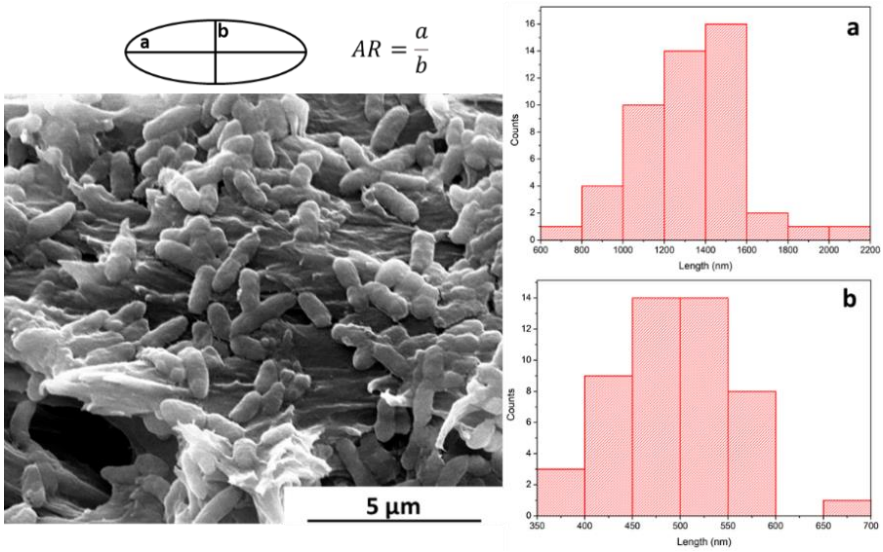

Figure 4.6: Scanning electron microscopy image of *Pseudomonas aeruginosa* and correspondent histograms of the major (a) and minor (b) axes.

Herein, we hypothesized that the bacteria's shape could play a crucial and unique role in activating the immune system. This work aims to realize biomimetic ellipsoidal particles able to induce a specific immunogenic response, fulfilling a new class of vaccines.

The general objective of the work presented in this section is to achieve an artificial vaccine against the bacterium *Pseudomonas aeruginosa* by using microparticles with biomimicry of size, shape, and surface. Therefore, polymeric ellipsoidal particles with the surface decorated with antigens, directly purified from the bacterium, will be developed to study their enhanced immune-activation properties (Figure 4.7).

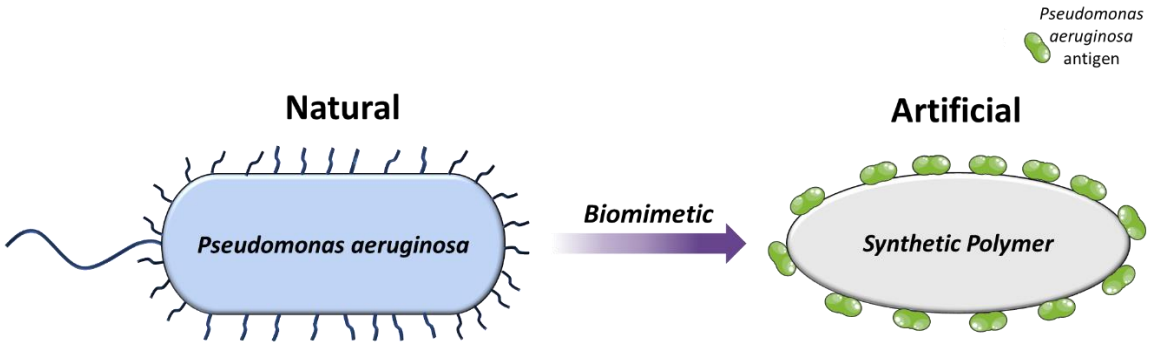

Figure 4.7: Schematic representation of biomimetic polymeric particles with the same size, shape of *Pseudomonas aeruginosa* and with surface functionalized with antigen obtained from the bacterium.

To achieve the defined biomimetic structure, the following specific objectives have been established:

- The spherical particles need to have an average diameter of 1 µm.
- The ellipsoidal particles with an AR of 2.6 and dimensions of 1.5 x 0.5 µm are required; in order to have reproducible dimensions, a finely controlled synthetic protocol has to be designed.
- The surface of both ellipsoidal and spherical particles needs to be decorated with antigens of *Pseudomonas aeruginosa* to confer immunogenicity properties of the synthetic particles.
- The amount of antigens covering the particles surface needs to be known accurately; thus, a reliable determination protocol has to be developed.

4.3 Results and discussion

This project has been carried out in collaboration with the "Bacterial infections antimicrobial therapies" group (BIAT), led by Prof. Eduard Torrents, from IBEC institute, specialized in bacterial infections and antigens' purification.

Based on our hypothesis, to make synthetic particles able to act as a vaccine against the *Pseudomonas aeruginosa* we proposed the following strategy (Figure 4.8):

- First, particles of shape and dimensions like *Pseudomonas aeruginosa* (i.e. ellipsoidal), are prepared. For this, we decided to follow a method previously developed by the Nanosfun group for polyurethane microcapsules[26] which involves two steps: *i)* the preparation of spherical microparticles through emulsion approach, *ii)* the generation of the ellipsoidal shape through stretching method.
- Successively, the obtained particles are functionalized with the antigens to increase the immunoactivity.

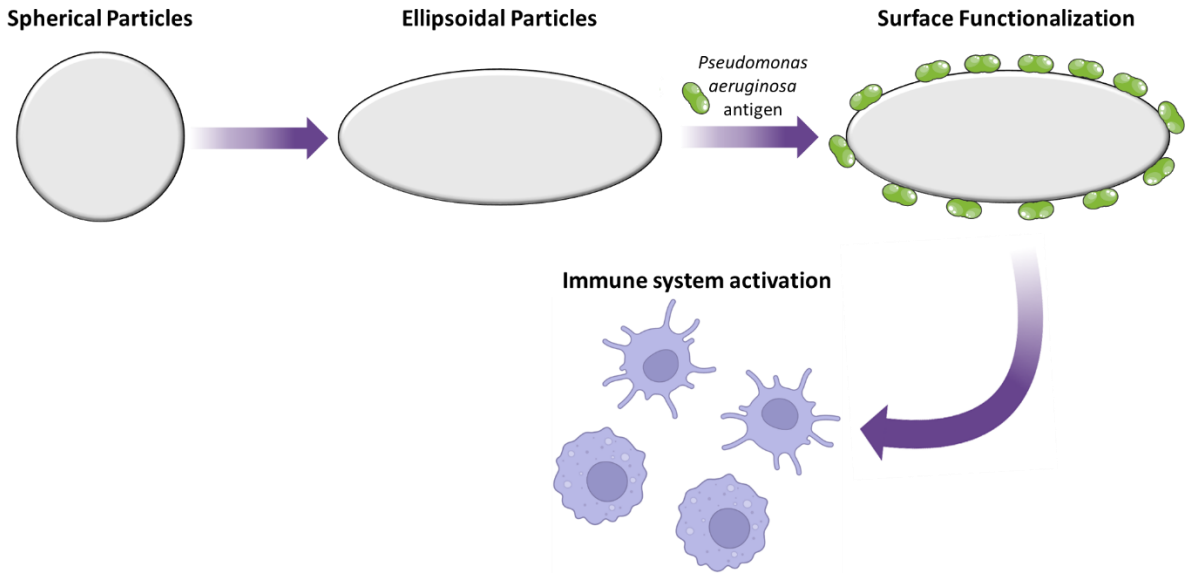

Figure 4.8: Schematic representation of ellipsoidal particles obtained from spherical one. Once their surface is covered with *Pseudomonas aeruginosa* antigens, they could generate an enhanced immune response.

4.3.1 Synthesis of spherical particles: size optimization

The achievement of ellipsoidal particles with narrow size and AR distributions, within the range of the *Pseudomonas aeruginosa*, is one of the main goals of this project. For this, it is important having the parent spherical particles with dimensions around 1 µm and highly homogeneous in size. Therefore, the

size and size distribution optimization of the spherical polymeric microparticles has been one of the most extensive parts of this work.

Polylactic acid (PLA) was selected as the constituent material of our microstructured artificial bacterium as *i)* it is a biocompatible polymer, extensively employed for the synthesis of micro and nanoparticles in biological applications,[3,34,35] *ii)* it has good thermo-mechanical properties, with relatively low glass transition temperature (T_g) (60-65 °C),[36-37] and *iii)* it has low cost.[38]

The emulsion-solvent evaporation method was employed for the synthesis of particles. It is a straightforward technique to obtain micro/nanoparticles and capsules, and it has been largely used by the group,[9,39] and in general for the preparation of PLA particles.[40] As described in the introduction, it consists of a two steps process and two phases: an organic phase, made by volatile organic solvents, not miscible with water, in which the polymer (which will constitute the particles) is dissolved, and an aqueous phase containing the surfactants or stabilizers added to stabilize the emulsion. Initially, the organic phase is mixed and emulsified with the water phase, obtaining a stable emulsion. The formed droplets constitute the template in which the particles are formed upon evaporation of the organic solvent, which induces the polymer precipitation. In this work, oil-in-water (O/W) or water-in-oil-in-water (W/O/W) emulsions have been used as templates. Dichloromethane (DCM) is a good solvent to dissolve PLA and thus was employed in all the experiments as the volatile organic solvent. Different parameters, such as the surfactant concentration, oil/water ratio, and homogenization method, can influence particles formation, size, and distribution.

Single O/W emulsion

Initially, O/W emulsion-solvent evaporation method was employed to obtain the spherical microparticles. First, the emulsification process was carried out using an Ultra-Turrax® homogenizer (UT). High homogenization rates and high surfactant concentrations are typically required to ensure the formation of small droplets size. Surfactants with high hydrophilic/lipophilic balance (HLB) are used to induce O/W emulsions. However, when UT is employed in the presence of high quantities of surfactants, foam might be generated, which inevitably reduces the system stability, negatively affecting the final size distribution. Therefore, the relation between surfactant concentration and homogenization rate was carefully studied. Sodium dodecyl sulfate (SDS) was used as ionic surfactant at a concentration of 0.5 or 2% w/w, while the UT rate was fixed to 10.000 or 8000 rpm (30 minutes), respectively (Table 4.1). However, in both cases, foam formed rapidly, leading to the formation of relatively small particles (~ 2-6 µm) but highly heterogeneous in terms of size (Figure 4.9 A). Moreover, a considerable amount of unstructured PLA was found at the end of the synthesis. This was again ascribed to the foam generation,

as it would result in the faster evaporation of part of the solvent, leading to the solidification of the polymer.

Extended emulsification time (45 minutes) was attempted to further reduce the average size and size distribution, though failed due to the formation of an increasing amount of foam, which reached the top border of the flask, causing loss of emulsified material.

Table 4.1: Synthesis conditions of PLA particles obtained using SDS as surfactant at different concentrations and UT rates.

Sample	UT Rate (rpm)	Surfactant (% w/w)
PLA-SDS-1	10.000	0.5
PLA-SDS-2	8000	2

Much less foam was formed when SDS was replaced by polyvinyl alcohol (PVA) 4-88 (which refers to low molecular weight and low hydrolysis grade) at a concentration of 1% w/. However, it was still not possible to significantly increase the homogenization rate without promoting foam generation, reaching a maximum of only 9000 rpm, which neither yielded significant improvement in terms of size or size distribution.

Thus, a study of the effect of the PVA concentration in the aqueous phase was conducted. A rate of 10.000 rpm was set while the PVA concentration was carefully increased until too much foam was formed (Table 4.2). In all the cases, the homogenization was conducted for 30 minutes, and the solvent was let evaporate at room temperature overnight. For the lowest PVA concentration (0.1 % w/w), more homogeneous particles were found, which is consistent with the fact that it was the case that showed less foam formation (Figure 4.9 B). On the other hand, when higher PVA concentration was employed, smaller particles were observed, though highly heterogenous (Figure 4.9 C). Again, unstructured PLA was found at the end of the synthesis.

Table 4.2: Synthesis condition of PLA particles with different PVA concentrations using 10.000 rpm of UT rate.

Sample	Surfactant (% w/w)
PLA-PVA-1	0.1
PLA-PVA-2	0.25
PLA-PVA-3	0.3
PLA-PVA-4	0.5

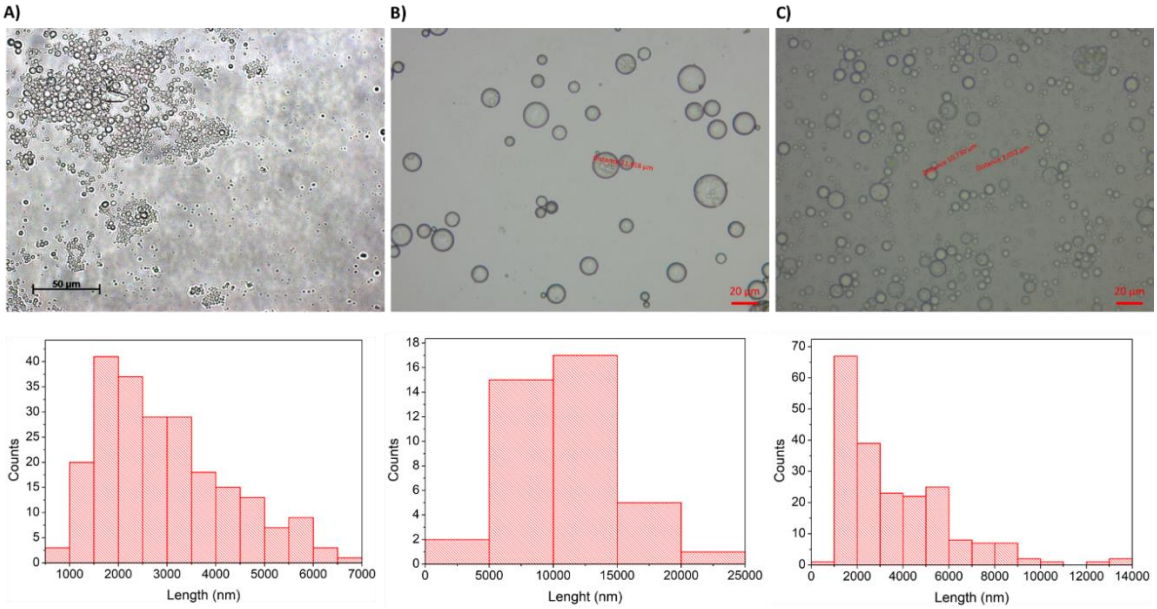

Figure 4.9: Optical microscope images and correspondent size distribution histograms of A) PLA-SDS-2, B) PLA-PVA-1, and C) PLA-PVA-4.

Since particles with micrometric dimensions, never smaller than 2 µm, were consistently obtained in all tested conditions, a different emulsification strategy was attempted. Higher energy was provided to the system by employing ultrasonication (US). Low amplitudes were set since, as a higher energy technique, US is primarily used to form nanoemulsions.[41] A pre-emulsion was formed through magnetic stirring the mixture at 900-1000 rpm for 30 minutes at room temperature.

SDS was initially chosen as surfactant (1% w/w) and US amplitude of 20 and 40 % were set for 2 minutes, with a pulse stimulation composed of US pulses of 30 s, with pauses of 10 s (Table 4.3). The amplitude of 20% led to the formation of highly heterogenous particles with sizes ranging between 200 and 1000 nm, while, at 40%, much more homogeneous particles were obtained, but with dimensions completely shifted to the nanometer range (100-200 nm).

Table 4.3: Synthesis condition for PLA particles obtained by varying the amplitude of US and using SDS as surfactant at 1% w/w.

Sample	Amplitude (%)
PLA-SDS-3	20
PLA-SDS-4	40

Similar attempts were carried out replacing SDS with PVA, at the same concentration (Table 4.4 PLA-PVA-5). Polymer concentration was also reduced (Table 4.4 PLA-PVA-6) since PLA itself tended

to form foam, and in the attempt to avoid the formation of unstructured solid polymer after the solvent evaporation. Moreover, the sonication was conducted with or without pulses to corroborate if the un-continuous stimulation would favor the coalescence of droplets during the off timing resulting in less homogeneous particles (Table 4.4).

Table 4.4: Synthesis condition for PLA particles obtained by using a 20% amplitude of US and changing the polymer concentration while employing or not pulsed stimulation.

Sample	On/Off cycle	PLA concentration (mg/ml)
PLA-PVA-5	✓	100
PLA-PVA-6	✓	50
PLA-PVA-7	X	100
PLA-PVA-8	X	50

Once again, a no homogeneous size distribution was accomplished when pulsated sonication was performed, as both micro- and nanoparticles were observed (Figure 4.10 A). Better results were achieved by combining the continuous ultrasound stimulus with the reduced amount of polymer (Figure 4.10 C), though the main size was centered in the nanometric scale. Moreover, less unstructured material was found, suggesting a more efficient emulsification process occurred.

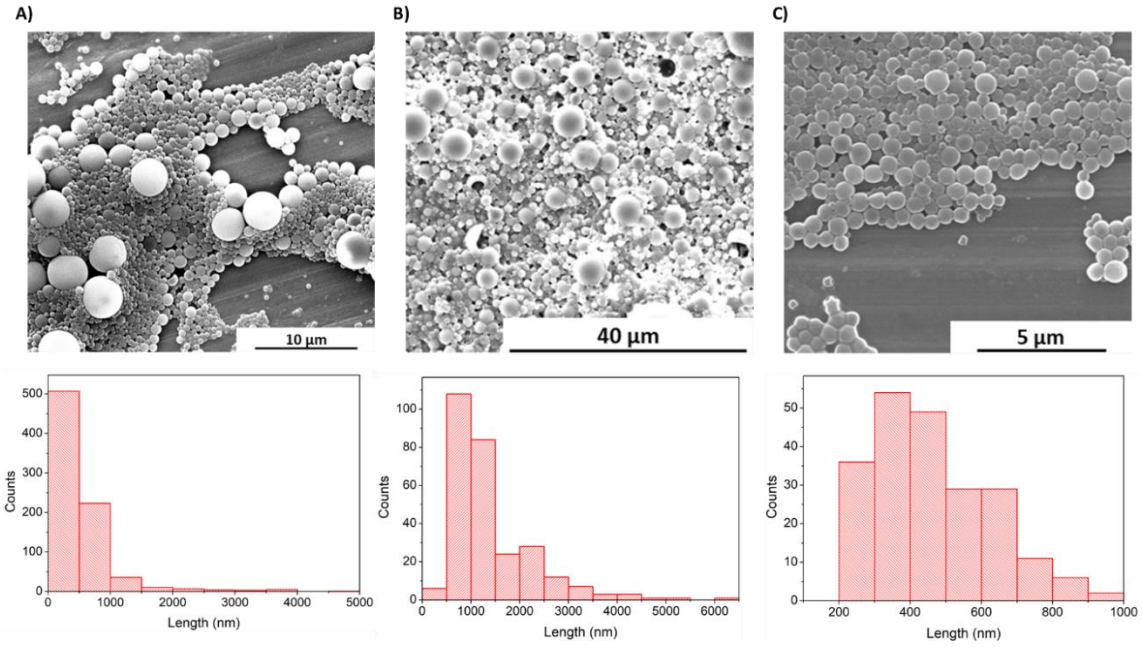

Figure 4.10: SEM images and correspondent size distribution histograms of A) PLA-PVA-6, B) PLA-PVA-7, and C) PLA-PVA-8.

From these experiments, it became evident that by using US homogenization nanoparticles (even with quite homogeneous size) are always obtained, but it was not suitable for homogeneous microparticles formation.

Double emulsion

The double emulsion-solvent evaporation process was evaluated as an alternative synthetic strategy. This method consists on the generation of a first water-in-oil (W/O) emulsion that is then added to a second continuous water phase, followed by a second emulsification step. The thermodynamic stability of the double emulsion is more challenging to achieve than the single one, as it is constituted by two different interfaces which need to be stabilized individually.[42,43] Indeed, two different surfactants with different behavior (opposite solubility, with distinct HLB values) are generally required to guarantee emulsion stability.[44] However, double emulsion has shown excellent kinetic stability,[45,46] most probably since the inner droplets are protected by two interfaces, and the coalescence phenomenon should be reduced. Moreover, the dimension of the final emulsion depends on the size of the first water droplets, which is independent from polymer concentration or solvent evaporation rate. Therefore, finer control over size dimension is expected when a W/O/W emulsion is employed. As an additional advantage, the presence of aqueous and oil domains would allow the encapsulation of both hydrophobic and hydrophilic molecules, such as adjuvants, achieving an even higher immune-response activation capability of particles. Nevertheless, a considerably low foam formation was observed when double emulsion was employed, representing an important advantage in particles synthesis.

Therefore, along with PVA, used to stabilize the final W/O/W, a second surfactant with lyophilic nature was employed. Particularly, Span® (Sorbitane monooleate) 80 (Span) was chosen as it presents a HLB balance value of 4.3.[47] In this case, it was finally possible to achieve much higher homogenization rates, as the foam generation was reduced. Indeed, an homogenization rate of 16.000 was used for both emulsification steps, and the resulting particles size appeared much more homogeneous (around 1.6 µm). With the attempt to further increase the delivered emulsification energy, PVA was replaced by the better surfactant Tween® (Polysorbate) 80 (Tween) for the second emulsion (1% w/w). This non-ionic surfactant is one of the most used in the double emulsion method in combination with Span,[48] as together allow fine regulation of the HLPB. Tween has also been extensively employed in biomedical applications.[11] In this case, the foam-free emulsions could be achievable even with high homogenization (10 minutes) rates (up to 18.000 rpm), kept equal for both the emulsification process (Table 4.5).

Table 4.5: Synthesis condition for PLA particles obtained by employing double-emulsion solvent evaporation method through different UT speeds, using Tween and Span at 1% w/w.

Sample	UT Rate (rpm)
PLA-Twee-1	16.000
PLA-Tween-2	17.000
PLA-Tween-3	18.000

The highest homogenization rate (18.000 rpm) yielded to nanometric size particles, similar to when US was used (Figure 4.11 C). Finally, particles with homogeneous size distribution, around the target 1 µm, were obtained with a homogenization rate of 17.000 (Figure 4.11 B). Double emulsion resulted in a successful strategy for one of the aims of this work.

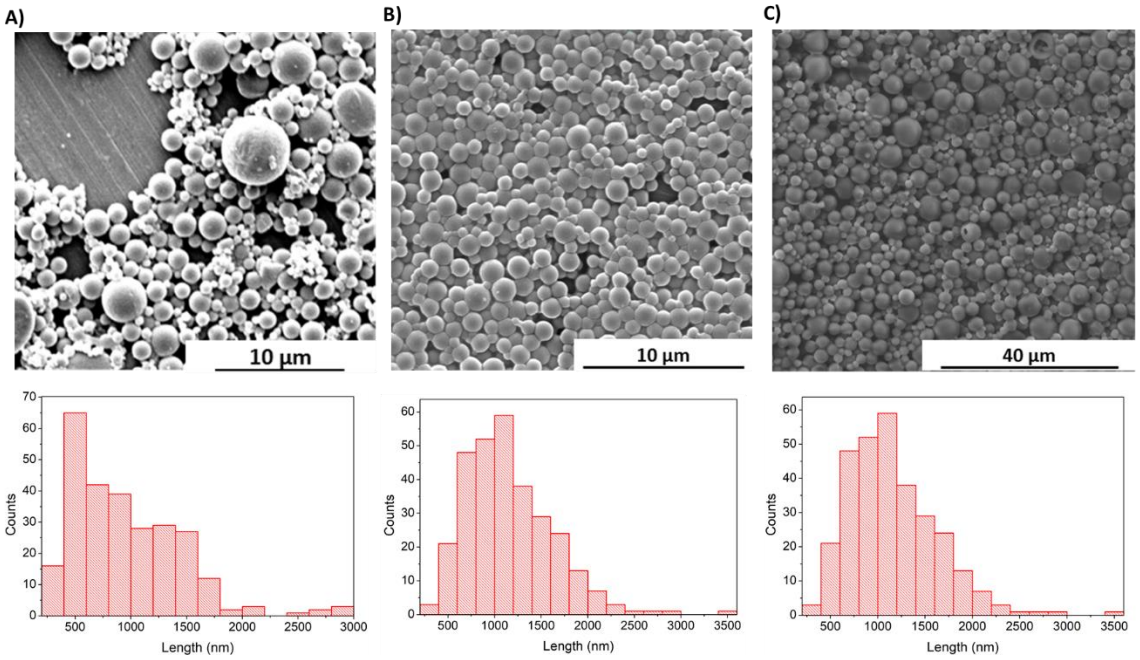

Figure 4.11: SEM images and correspondent size distribution histograms of A) PLA-Tween-1, B) PLA-Tween-2, and C) PLA-Tween-3.

However, Mastersizer measurements of the size distribution of these particles in the aqueous suspension revealed the apperecnce two populations, suggesting the presence of larger particles or aggregates (Figure 4.12). Moreover, as it will be explained in detail below, Tween and Span had to be discarded as surfactants as they generated interferences in the quantification of the protein attached on the surface of particles.

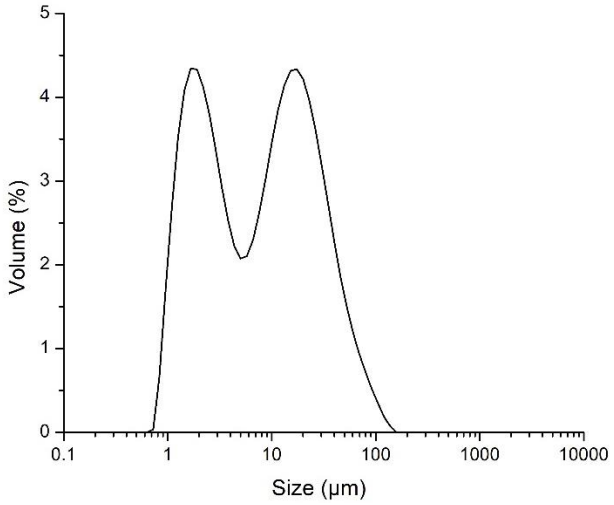

Figure 4.12: Size distribution of PLA-Tween-2 in water.

Therefore, Tween was replaced by the BriJ®S (polyoxyethylene stearyl ether) 100 (BriJS100), and no lipophilic surfactant was used. All the optimized parameters were maintained, but a slightly lower homogenization rate of UT for the first emulsion was set (15.000 rpm). Here, the use of a single surfactant forced to make the emulsion steps close in time. An astonishing size distribution centered around 1 µm (Figure 4.13) was finally achieved. The spherical PLA microparticles obtained using BriJS100 (S-PLA) as surfactant were used for all further experiments. It is important to mention that a large amount of unstructured PLA was still found, which was removed upon filtration; thus, particles were formed with quite low yield.

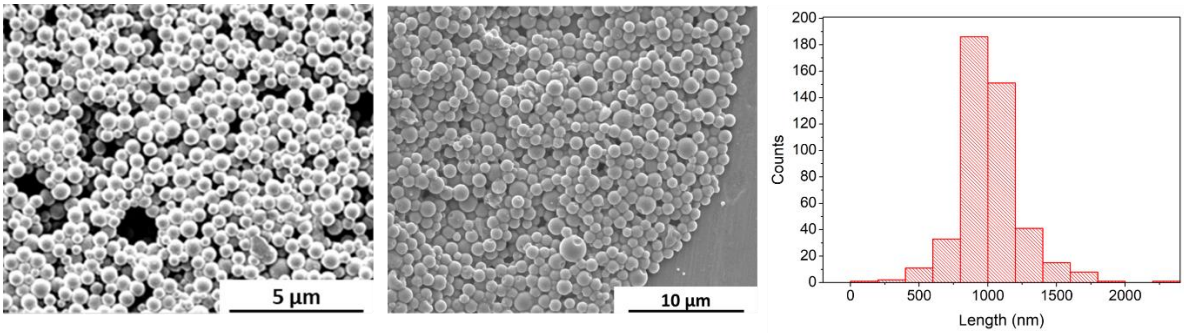

Figure 4.13: SEM images of S-PLA obtained using BriJS100 as surfactant and the corresponding size distribution histogram.

In order to remove the excess of surfactant, it was crucial to design an effective cleaning procedure for the S-PLA. Purification upon centrifugation allowed their sedimentation, though their redispersion

in water was then practically impossible. Indeed, a compact pellet formed even at the slowest centrifugation rates, as consequence of the suffered particles aggregation.

Thus, cross-flow filtration was employed. This method is mainly used for protein purification,[49] even if examples of its use for cleaning particles have been reported.[50,51] It consists of a tangential filtration, where the continuous and tangential motion of the liquid avoids the obstruction of pores, normally observed in standard vacuum or gravity filtration of particles suspensions. Moreover, it is possible to easily recollect the cleaned particles at the desired concentration without inducing their aggregation. Moreover, the permeated liquid, which for simplicity is going to be called supernatant (SN), recalling the centrifugation process, can also be collected at the outlet of the filter. Different cut-off filters and membranes allow cleaning the particles from the surfactant. In this study, a 500 kDa cut-off membrane was employed, to minimize the loss of particles while efficiently removing the excess of BriJS100. However, since BriJS100 is employed at high quantities during the synthesis, having a weight similar to the one of PLA, even after cleanings, part of it is still expected to be found in S-PLA suspension.

4.3.2 Ellipsoidal particles: shape optimization

Ellipsoidal particles were obtained following a method reported in literature,[52-53] and previously employed by our group to obtain ellipsoidal core-shell capsules.[26] It relays on the deformation of spherical polymeric particles while heating them above their T_g and applying an opposite external strain forces along one direction of a film in which the particles were previously embedded (Figure 4.14).

For this, the spherical particles are first entrapped in a PVA film through casting. The film is prepared by dispersing S-PLA particles in a PVA aqueous solution, pouring it on a polystyrene Petri dish, and letting the water evaporate at 35 °C overnight. Once dried, the film, with the particles embedded in it, can be pealed out from the support. Particularly, PVA 4-88 was employed for its high solubility in water, required to form an aqueous suspension containing both the particles and the polymer before casting, its low cost, thermo-conformability, and film-forming properties, and it has been largely exploited by the Nanosfun group to prepare photofunctional films. [9,39,54,55] The obtained film was cut in rectangle shape and immersed in a pre-heated silicon oil at a temperature higher than the T_g of both PLA and PVA (T_g = 70 ºC)[56], while the two opposite edges were subjected to tension forces along the direction of the longer side of the film, resulting in its stretching. Once immersed in the hot oil, both S-PLA and PVA became deformable and stretched along the elongation direction. The PVA film was dissolved in water, and the obtained ellipsoidal particles (E-PLA) were easily recollected by centrifugation.

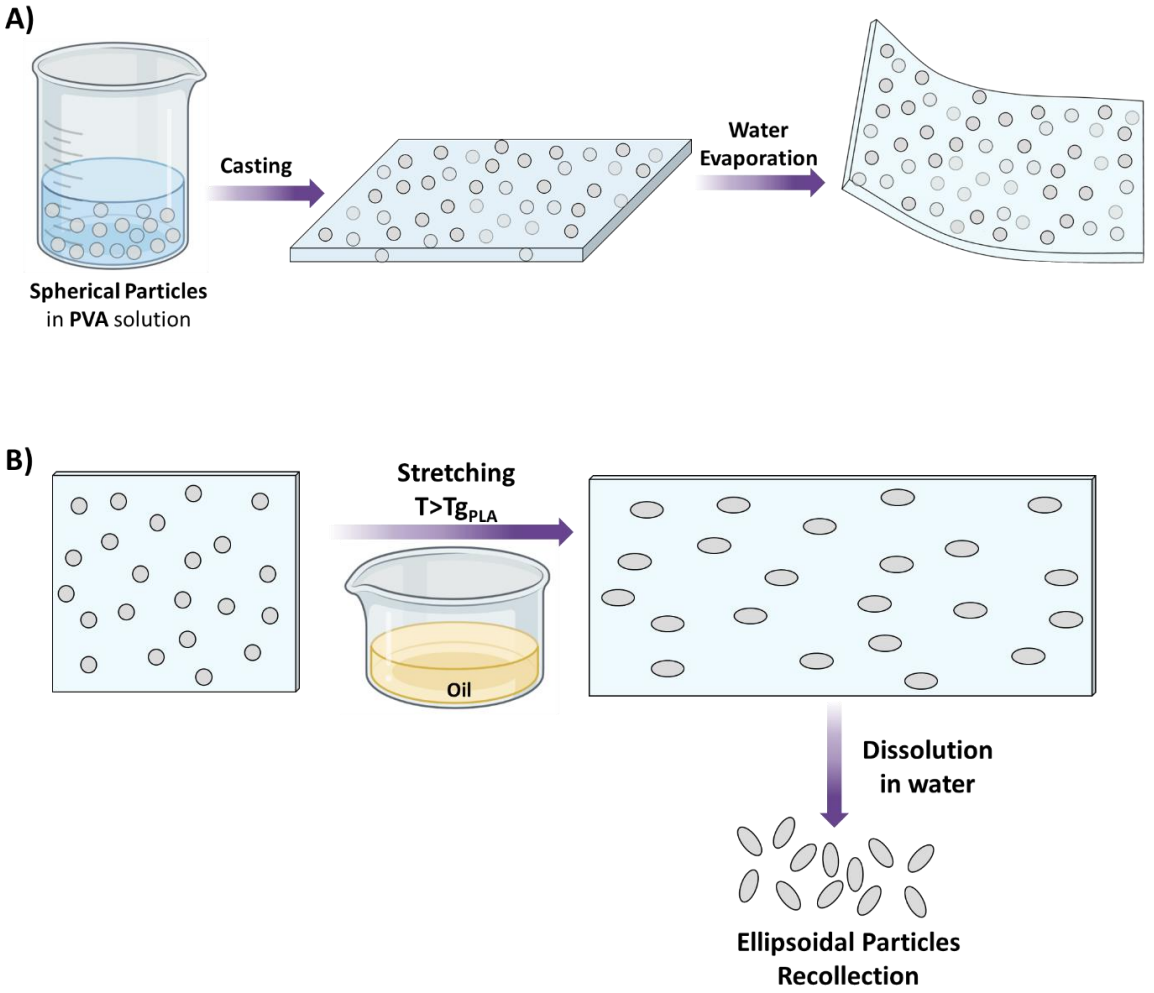

Figure 4.14: Schematic representation of A) PVA film (with S-PLA embedded) preparation and B) general procedure for ellipsoidal particles preparation by film stretching method.

The high concentration of PVA in the suspension of the E-PLA obtained from the films re-dissolution allowed their easy redispersion in water after the first centrifugation processes. However, during the latest cleaning cycles, particles started aggregating due to the removal of PVA, thus, the final cleaning steps were carried out by cross-flow filtration.

Although this stretching method is broadly reported, variability was found in the protocols, which also lacked reproducibility. Indeed, the final shape of the particles depends on the stretching conditions, which themselves depend on several parameters (films material, thickness, particles materials and size, stretching rate and magnitude, etc.), which need to be chosen depending on the desired shape and the polymeric particles used.

Initially, the elongation was performed by manually moving the two extremes of the film in opposite directions after its immersion in the oil. Firstly, the oil temperature was optimized: stretching experiments were carried out varying the temperature in the range of 70-150 °C, every 10 ºC. The film could be very hardly stretched at lower temperatures (70-80 ºC), while at 150 °C, the films become very rigid for the loss of plasticizing water. Thus, a temperature between 90-100 °C was selected as the optimal.

The film thickness is another crucial parameter to consider for the elongation, and it can be modulated depending on the PVA amount dissolved in the suspension prior to the casting. When the film was too thick, its stretching was almost impossible to achieve by hands, independently of the oil bath temperature. Conversely, if the film was too thin, it broke too easily, even applying weak elongation forces. The optimal film thickness was found to be approximately 110 μm, as it could be stretched manually without being broken. The effect of the film flexibility on the stretching properties was also investigated. Hydrophilic plasticizers could be used to modulate the flexibility of PVA. Water is an efficient and cheap plasticizer, though its amount in the film could not be finely controlled, especially while it was immersed in the hot oil, which caused the water evaporation and an increase of rigidity. Glycerol at 5% w/w concentration in the film considerably contributed to improve the flexibility, making the films manipulation much easier.

The S-PLA concentration did not negatively affect the mechanical properties of the films. No relevant differences were observed in the stretching capability/rupture in films of same thickness, prepared with or without the S-PLA particles. A high concentration of the particles in the film would allow a larger production of ellipsoidal particles in each stretching process. However, a too high concentration could promote particles aggregation during the film preparation or stretching. Thus, despite film stretching was successfully achievable even with films prepared with 20% w/w of S-PLA concentration, 5-6 % w/w was the chosen one.

SEM images show the successful formation of ellipsoidal particles when using the optimized parameter for the films stretching (Figure 4.15). However, they appeared largely heterogenous, with some particles showing a pronounced elongated shape, whereas others still presented a spherical geometry. Moreover, the AR was equal to 4.8, being much higher than the one of *Pseudomonas aeruginosa* (2.6), and with a broad variability and distribution. Spherical particles most likely came from portions of the film not stretched, which were re-dissolved during the collection of the particles.

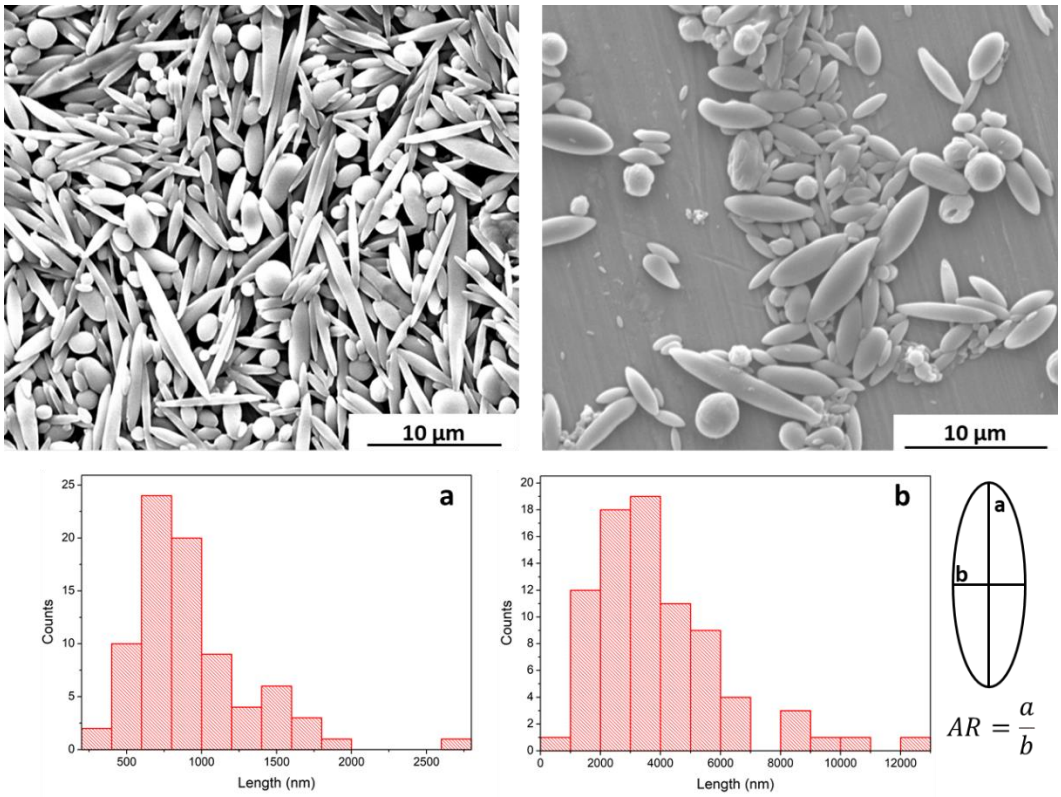

Figure 4.15: SEM images of ellipsoidal particles obtained by stretching spherical ones and the correspondent histograms (a: major axis, b: minor axis).

A more careful study of the stretched films allowed to establish regions with different stretching magnitudes: the central part, suffering the most considerable stretching, as the region where strain forces distribution concentrate, and the areas closer to the film extremities, much less elongated, since to the two fixed extremities, which no suffer any elongation. The stretching magnitude of all intermediate regions increased from the center to the extremities, accordingly (Figure 4.16).

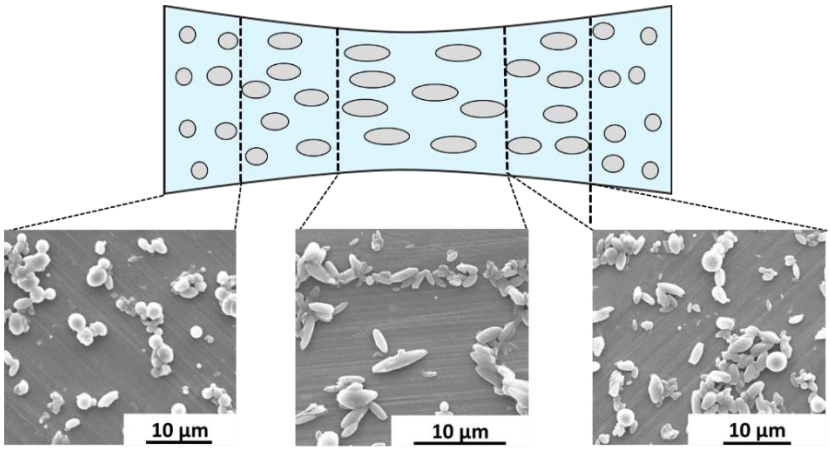

Figure 4.16: Schematic representation and SEM images of particles with different elongation rate depending on their position in the film.

In this way, an easy and more reproducible protocol was established to monitor and quantify the elongation magnitude. The film was divided in different sections marking it with a permanent pen, and the elongation length of each section was measured before and after applying the stretching. After SEM imaging, it was concluded that the sections extending to double the initial length showed the more efficient formation of ellipsoidal particles over spherical ones. Despite such optimization process significantly improved the efficiency of the production of ellipsoidal particles and their homogeneity in terms of size AR, the mechanical deformation was still accomplished by stretching the film with the hands. This (literally) manual elongation was a clear source of lack of reproducibility as it was not possible to control the applied force nor the elongation rate and magnitude.

Thus, it was evident that a more reproducible and reliable stretching method was needed. For this aim, a custom-made apparatus was designed and fabricated in our laboratory, that for convenience we call here "stretcher". The idea of the stretcher is to provide reproducible external forces to pull the edges of the film in opposite directions. The concept is inspired on the Instron instrument, a universal testing machine normally used to measure the mechanical properties of materials, such as shear, bend stresses, flexibility, etc.[57,58] These instruments are based on hydraulic or electromechanical systems that apply different types of forces to the tested materials.

The stretcher was built to have a fixed (top) part and a mobile (bottom) part, both immersed in the oil bath. The two opposite sides of the film could be firmly grabbed to the two parts through clamps by simply tightening a few screws. A mechanism was designed so that upon application of a fully controlled weight, sufficiently high to provoke the elongation of the film, the mobile bottom part is pushed away from the fixed one until reaching the bottom of the oil bath container, yielding the stretching of the film. In a first prototype, the weight was applied directly at the bottom part of the equipment, so within the oil bath. However, this caused the weight to be subjected to forces from the bottom to the top by the displaced liquid, according to the Archimedes principle, significantly reducing the effective weight and thus attenuating the stretching rate and magnitude (Figure 4.17).

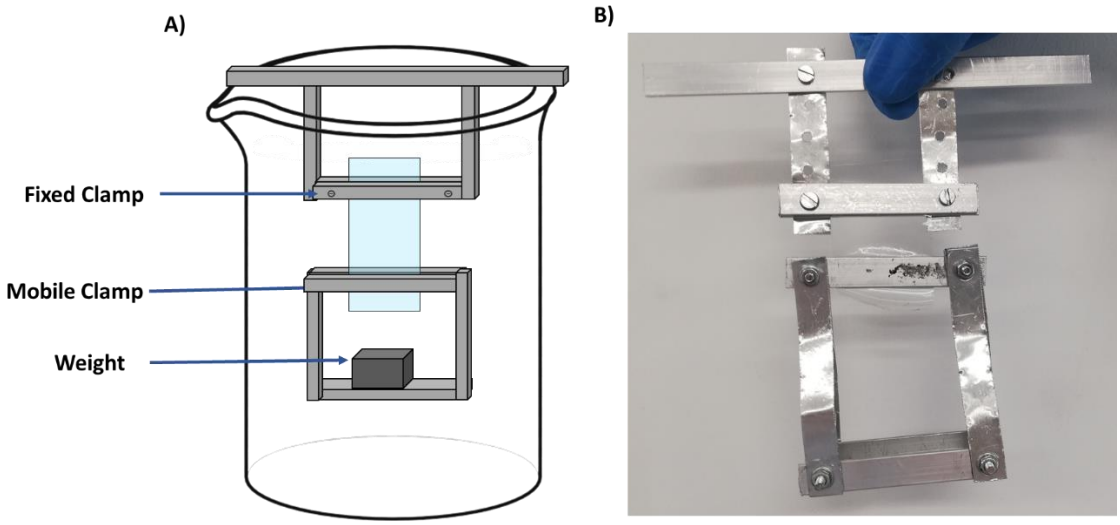

Figure 4.17: A) Schematic illustration and B) pictures of the first protype of the custom-made apparatus (the "stretcher").

Thus, a new mechanism of the stretcher was made, in which the applied force was still directly connected to the bottom and mobile part of the apparatus, but the film was stretched through the application of a weight outside the oil bath. A schematic representation of the final "stretcher" and some pictures are reported in Figure 4.18. In this way, by controlling the weight and the initial distance between the two clamps, it was possible to finely modulate the shape of ellipsoidal particles.

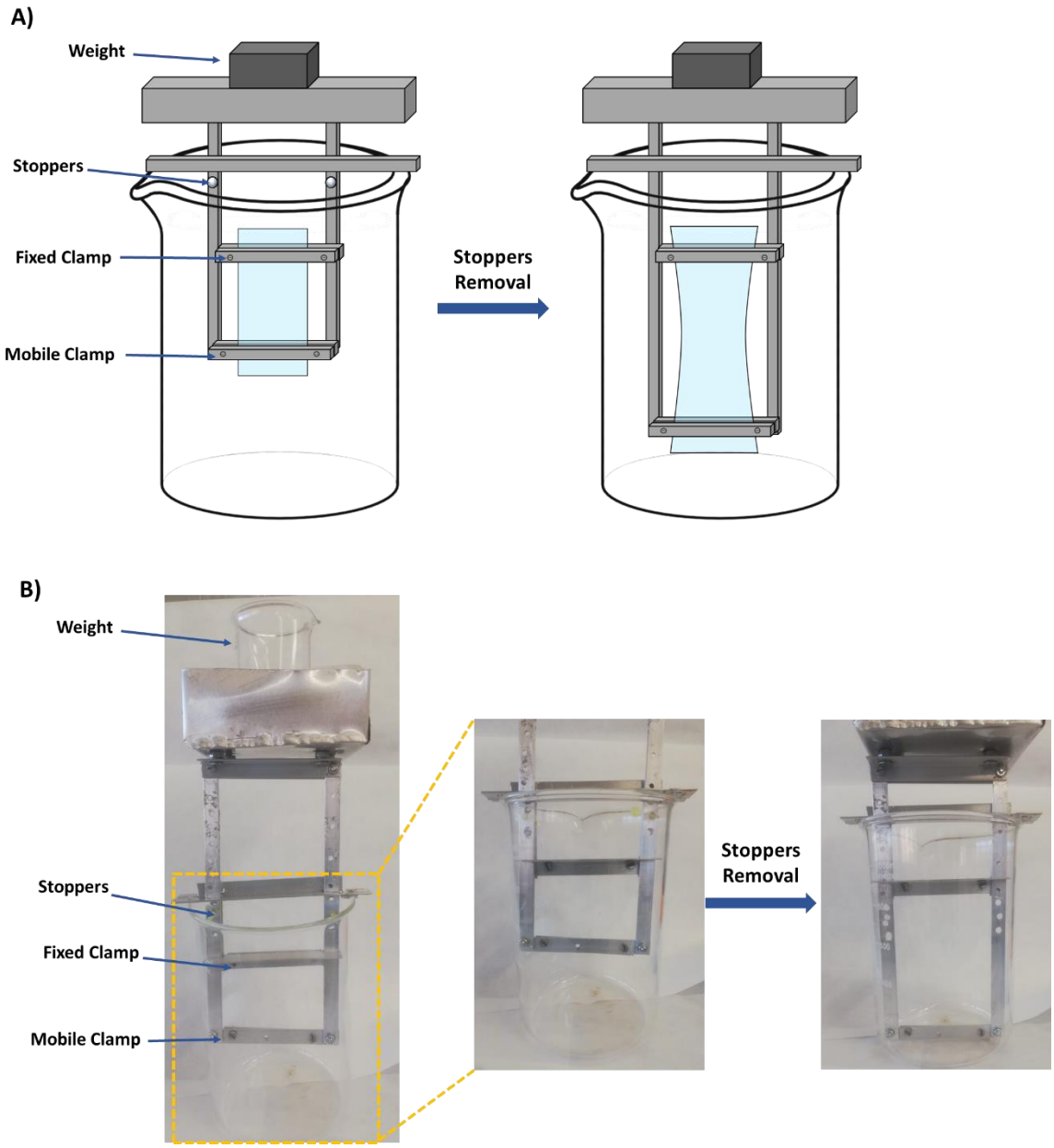

Figure 4.18: A) Schematic illustration and B) pictures of the final designed "stretcher" and its functional principle.

Combining all the optimized parameters for the films preparation and using the "stretcher" to control the elongation, it was possible to achieve very homogeneous ellipsoidal particles with reproducible elongation magnitude (Figure 4.19). In this way, ellipsoidal microparticles with axis dimensions and AR (2.4) close to those of the natural *Pseudomonas aeruginosa* bacterium (2.6) were obtained.

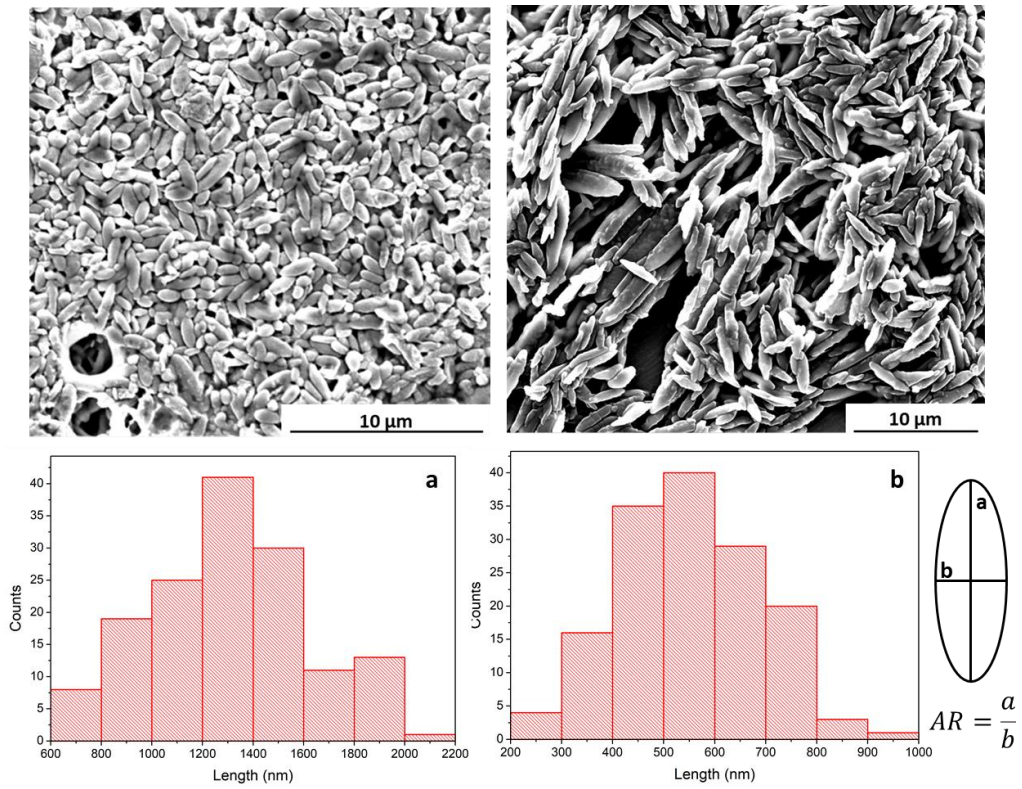

Figure 4.19: SEM images of E-PLA and correspondent histograms.

4.3.3 Determination of particles concentration

Knowing the concentration of particles is extremely important in biological applications. Thus, once the syntheses of both spherical and ellipsoidal particles were optimized, it was decided to develop a method for quantifying particles amount and concentration in aqueous suspensions. Indeed, the standard method, based on the weight of freeze-dried particles, is not applicable for S-PLA because the powder weight has a strong contribution of the surfactant present in the suspension, which would remain even after the cleanings procedure, inducing a quantification error. Moreover, as it will be explained later, particles were subjected to several functionalization and cleaning steps, and the exact concentration is needed to be known after each of them. With this aim, a two-step strategy has been developed.

Firstly, the concentration of S-PLA, right after their synthesis, was calculated using proton nuclear magnetic resonance (^{1}H-NMR). Freeze-dried particles were dissolved in deuterated chloroform, and a known amount of dimethylformamide (DMF) was added as an internal reference. The spectra of pure PLA, BriJS100, and S-PLA are reported in Figure 4.20 to fully assign the ^{1}H-NMR peaks of the particles sample to the components. Through the integrated area of selected peaks and taking into account the

number of equivalent protons (DMF, δ = 8.1 ppm, singlet, CH, area = 1 arb. u., and PLA, δ = 5.2 ppm, multiplet, CH, area = 0.37 arb. u.), it was possible to quantify the amount of PLA, and the final concentration of S-PLA. This calculation was made by assuming that all the PLA present in the sample was structured as particles (strongly supported by the fact that unreacted polymer was filtered away after the formation of particles, and that SEM images did not show any non-structured material), and that PLA was made by only repetitive units of [–CH(CH_3)COO–], which is practically true as only the two terminating moieties show the slightly different acid [–CH(CH_3)COOH structure, not significantly affecting the overall molecular weight.

The amount of PLA calculated was 30-40% w/w, compared to the total weight of the sample.

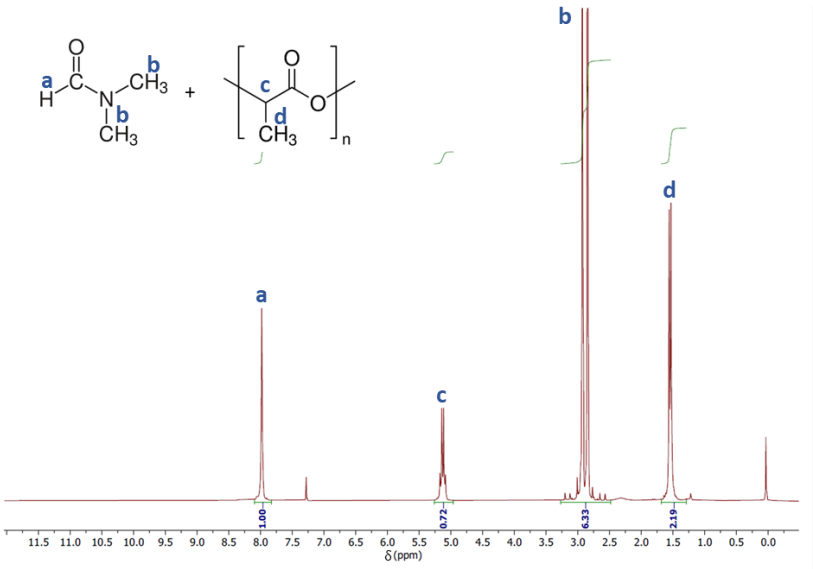
a
b
c
d
1.00
0.72
6.33
2.19
δ (ppm)

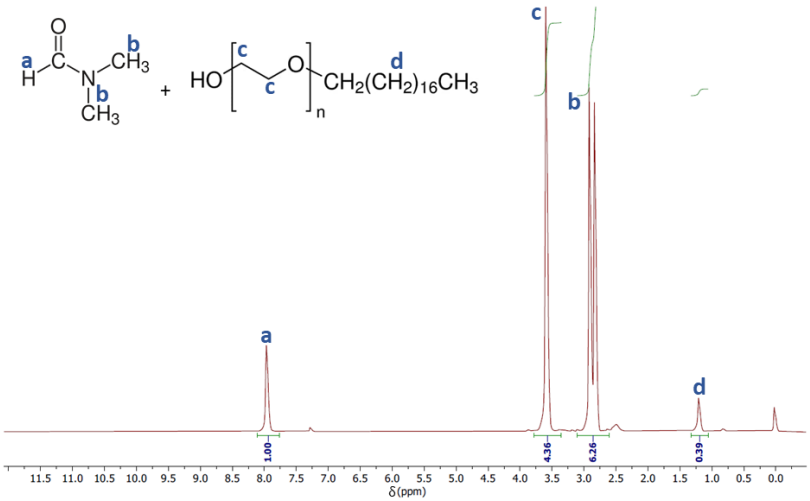
a
b
c
d
HO
CH2(CH2)16CH3
n
1.00
4.36
6.26
0.39
δ (ppm)

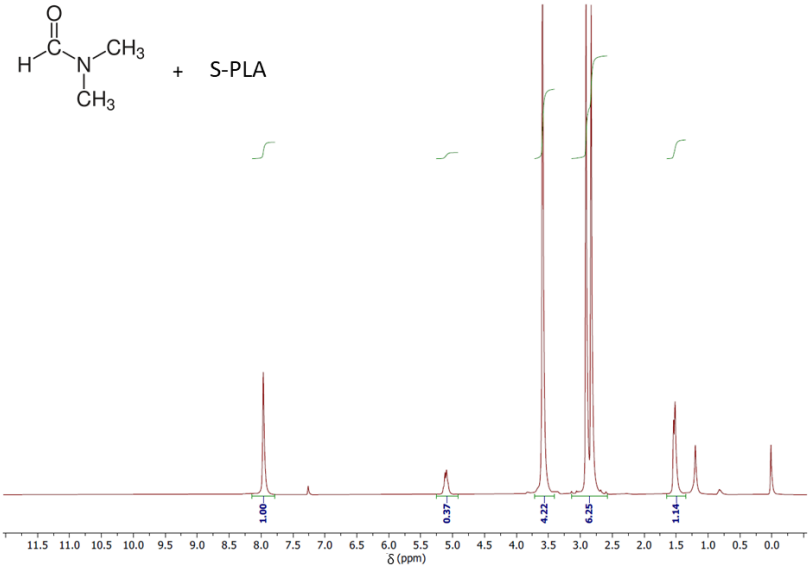
S-PLA
1.00
0.37
4.22
6.25
1.14
δ (ppm)

Figure 4.20: ^{1}H-NMR spectra in deuterated chloroform of PLA, BriJS100, and S-PLA. DMF was used as an internal reference. The characteristic peaks of each component were recognized. PLA: δ =5.12 ppm (m, 1 H, CH), 1.55 ppm (d, 3H, CH3); BriJS100: δ= 1.2 ppm (s, 32H, $(CH_2)_{16}$), 3.59 ppm (t, 400H, $O(CH_2)_{100}$). The peaks at δ= 2.82 ppm (s, 3H, CH_3), 2.90 ppm (s, 3H, CH_3), and 7.96 ppm (s, 1H, CH) were ascribed to DMF. (s: singlet; d: doublet; t: triplet; m: multiples).

The particles quantification through ^{1}H-NMR requires high quantities of material (> 5 mg), making it unsuitable when low concentrations are used, such as in our biological experiments. Consequently, a second method has been developed by using fluorescence measurements. S-PLA particles were turned fluorescent by encapsulating a fluorescent dye, the 9,10-diphenylanthracene (DPA), whose emission quantum yield is close to 1 even when aggregates.[59,60] By using such dye, the fluorescence intensity is not affected by its surrounding or aggregation state and thus could be directly related to the concentration of the particles. Moreover, the dye incorporation would make particles trackable after cells internalization.

By knowing the concentration of a stock S-PLA suspension, determined as described above by ^{1}H-NMR, calibration fluorescence curves were obtained for two different particles concentration ranges upon dilutions with water, to be used in experiments with distinct concentration conditions (Figure 4.21 A, C). Linear responses ($R^2 > 0.998$) of the integrated emission intensity against concentration were obtained (Figure 4.21 B, D). Noticeably, such linearity permitted measuring the particles amount of concentrated solutions, as the signal was not significantly affected by the particles scattering, though some reabsorption effects were noticed. More importantly, the method allowed the quantification even for suspensions with very low concentrations (up to 25 µg/ml).

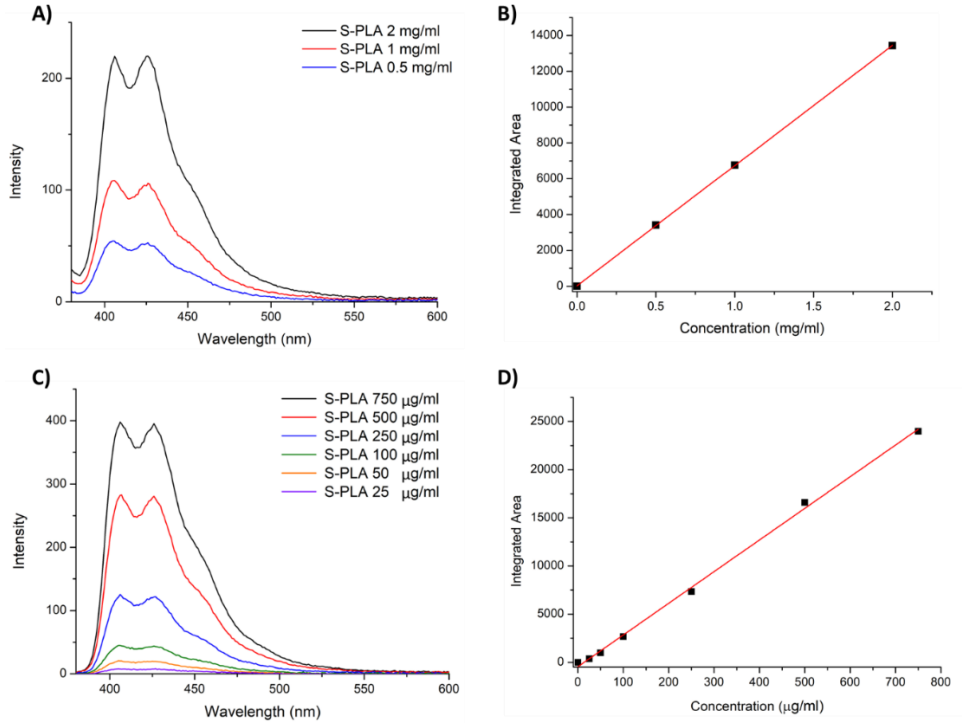

Figure 4.21: Fluorescence spectra of S-PLA at different concentrations ranging between A) 2 and 0.5 mg/ml and C) 750 and 25 µg/ml. B-D) Correspondents fitting linear curve of integrated emission intensity against concentration.

4.3.4 Surface functionalization of spherical and ellipsoidal particles and proteins quantification

Once obtained biomimetic ellipsoidal particles with size and shape similar to those of *Pseudomonas aeruginosa*, the next part of the work consisted of the surface functionalization of PLA particles. Indeed, antigens obtained from the bacterium itself were used to decorate the surface of particles, to generate a specific immune response. With this purpose, the BIAT group purified different proteins extracted from the *Pseudomonas aeruginosa*. Specifically, they purified four antigens: NrdJ (82.7 kDa), FliC (49.2 kDa), PilA (13 kDa), and PrcV (32.2 kDa). In their previous study, the immunogenic behavior of all of them was evaluated and compared *in vivo*, by using *Galleria mellonella* larvae, a well-established animal model commonly used for toxicological screening of new compounds and pathogenicity studies of different bacteria.[61,62] Among them, NrdJ and FliC were the ones able to generate the highest immune response, and thereby selected as the more suitable antigens for this project and used for further experiments. The FliC is a structural protein and is a major component of the flagellum,[63] while NrdJ is an enzymatic protein, the class II ribonucleotide reductase. Thus, in this work, the immune response of

S-PLA and E-PLA, functionalized and non-functionalized, was aimed to be studied in order to evaluate the shape effect and determine the contribution of the surface antigens on the immunogenicity properties.

The physical adsorption of proteins on the surface of the particles was chosen as the functionalization strategy. Indeed, proteins have a strong ability and tendency to adhere to surfaces, which can be exploited to avoid covalent conjugation strategies,[64] which are more complex and require harsher conditions with higher risks of denaturation of the antigens. Moreover, the controlled orientation of proteins is not necessary since their immunogenic properties are not orientation dependent. However, despite the apparent simplicity of the physical adsorption strategy, the efficient coupling between proteins and particles still depends on several factors, such as temperature, pH, and time.[65-66]

The functionalization process was optimized predominantly with S-PLA particles because of the larger available amount. It was assumed that being the particles material the same, the adsorption tendency of the protein was similar in both types of particles and the conditions of functionalization of the S-PLA could then be extrapolated to the E-PLA particles.

In order to quantitatively compare the immune response of functionalized PLA particles with the free antigen, it was essential to ensure the administration of the same dosage of antigens. So, it was important to establish a precise and accurate protocol for quantifying the adsorbed protein on the particles surface.

Direct protein quantification resulted very challenging. In fact, standard protein quantification assays are based on light absorption measurements, where the contribution of scattering from particles could drastically modify the real absorbance values, especially at shorter wavelengths. On the other hand, in chromatographic techniques, the presence of microsized particles could cause the obstruction of columns, with irreversible damages. Therefore, an undirected method was always used, which consisted on the calculation of the difference between the amount of starting protein used for the functionalization and the quantified non-adsorbed protein recollected during the cleaning steps.

In the first attempts of surface functionalization, protein and S-PLA (at a ratio of 1:5 w/w) were let gently stirred overnight in phosphate buffer saline solution (PBS) or Tris (50 mM) buffers. The buffers were expected to provide higher stability conditions to the antigens. Initially, bovine serum albumin (BSA) was used as commercially protein model to optimize the adsorption process.

As mentioned above, S-PLA could not be cleaned through centrifugation as it would induce their irreversible aggregation. Thus, after the functionalization, particles were cleaned by cross-flow filtration. To verify its efficiency in removing the excess of protein, a particles-free solution of a known amount of BSA was filtered three times, the SNs and the internal filtered part were recollected and analyzed by UV-vis. As observed in Figure 4.22, the characteristic peak of BSA, at 280 nm can be recognized in all the recollected SN, with a gradual reduction in the peak intensity after each cleaning, and the recollected

filtered part showed a very low amount of BSA. With three cleanings, most of BSA was efficiently filtered out (almost the 100%).

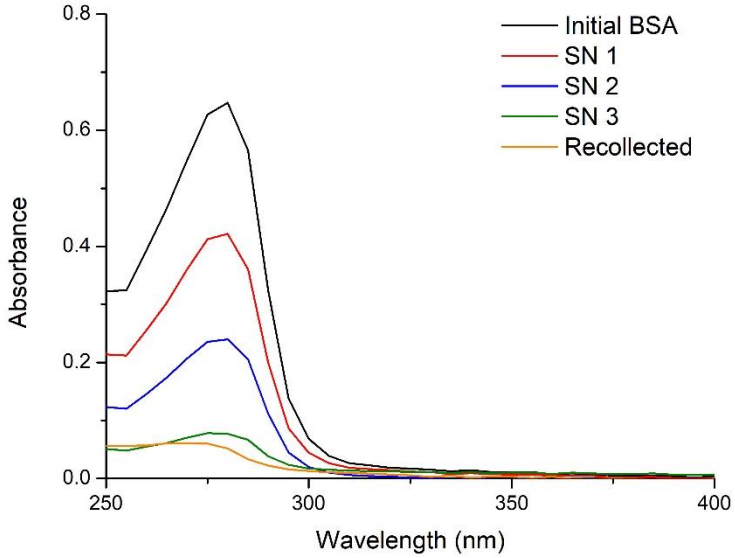

Figure 4.22: Absorption spectra of BSA (1 mg/ml) in water, and the recollected SN after three cross-flow filtrations.

Importantly, S-PLA particles alone, with any functionalization, showed quite good colloidal stability all over the processes to which they were subjected, i.e. after 6 steps of cross-flow filtration, after freezing at -80 ºC, which would be required for the storage and protection of the adsorbed antigens, and after 6 further filtrations (Figure 4.23). The presence of a few large particles was already appreciable in the particles before any treatment.

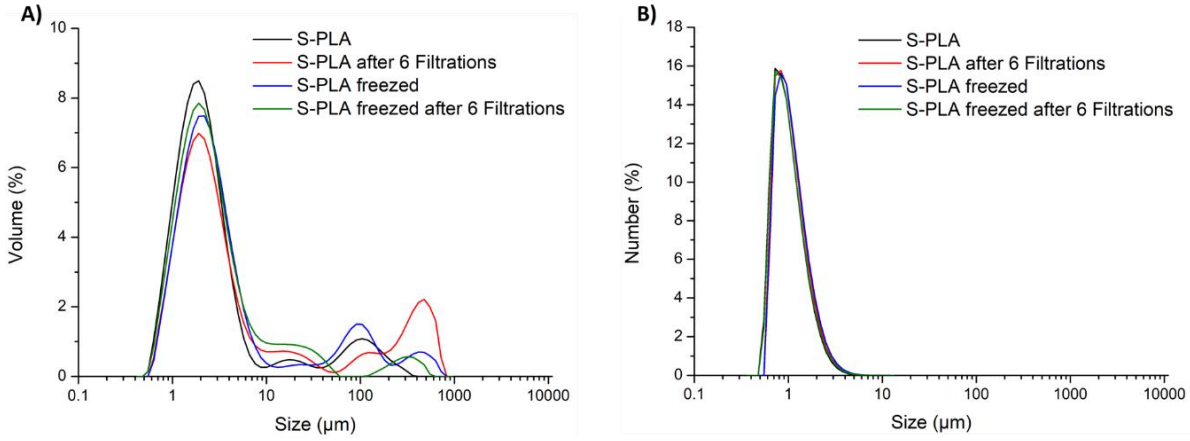

Figure 4.23: Size distribution of S-PLA (black line), S-PLA filtered six times with cross-flow in Tris buffer (red line), S-PLA stored at -80 °C (blue line), and S-PLA stored at -80 °C after six filtrations in Tris buffer (green line). The distribution is reported as A) volume (%) and B) the corresponding calculated number (%).

a) Colorimetric methods

Initially, spherical particles obtained using Tween as surfactant (PLA-Tween-2) were functionalized with BSA. The amount of protein present in the recollected SN was quantified by employing Bradford or bicinchoninic acid (BCA) assays, which are the most common and largely used methods for protein quantification.[67-68] The first one is based on the absorbance shift (from λ_{max} = 465 nm to λ_{max} = 595 nm) of the dye Coomassie brilliant blue G-250 after the binding with protein. The latter method, instead, relies on the reduction of copper by the presence of protein and the absorbance (λ_{max} = 560 nm) of the complex formed by two BCA molecules and the reduced Cu^{+} is directly proportional to the amount of protein. However, no consistent or reproducible results were achieved, despite several attempts were carried out. Indeed, in most cases, a percentage of adsorbed protein over 100% w/w was estimated. This behavior was associated to the possible interference of detergents-like components (surfactants) present in the measured samples, as a consequence of the cross-flow filtration, which allowed a consistent amount of the surfactant to migrate to the SN along with the BSA. Indeed, these assays are known to be sensitive to the concentration of detergents. Polysorbates induce measurable interference in the absorption signal of protein quantification kits, and different attempts to remove or reduce their contribution have been reported.[69,70]

To verify and tentatively quantify the surfactant contribution in the signal of the probing kit, a known and fixed amount of BSA was mixed with aliquots of Tween solutions of different concentrations and the absorption spectra resulting from the addition of Bradford and BCA probes were measured (Figure 4.24). For both assays, the measured absorption spectra revealed an enhancement of absorbance as the amount of Tween increased, when the surfactant concentrations exceeded the protein one, as it might happen in many biological assays. These experiments clearly confirmed the surfactant contributes significantly to the signal, making the methods not very reliable in these concentration ranges. In the case of Bradford, a shift of 15 nm was also observed when Tween was added, and the error calculated for the highest concentration was 83% (Figure 4.24 A). For the BCA, the error found was considerably lower (33 %) (Figure 4.24 B). When the concentration of Tween was reduced (Figure 4.24 C-D) to comparable values to that of BSA, the estimated error decreased drastically, reaching a more reasonable value of 4% for both Bradford and BCA, when Tween was at 1 mg/ml.

As reported in the manual of the assays, and as demonstrated in these experiments, BCA should be less sensitive to the presence of detergents.

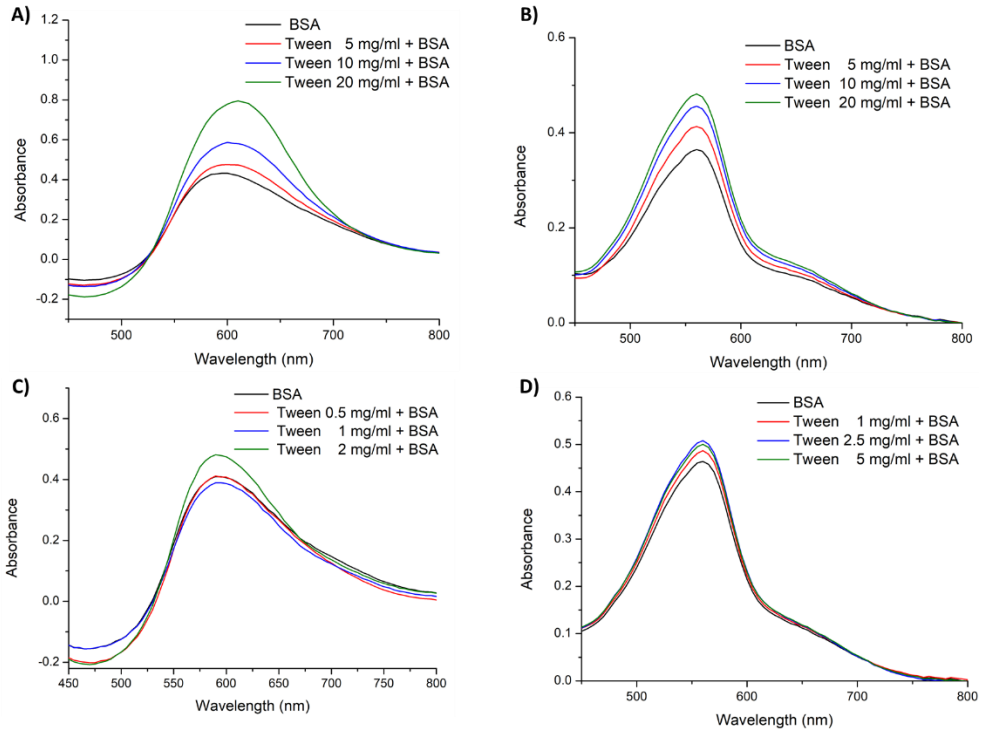

Figure 4.24: Absorption spectra of BSA at 1 mg/ml in the presence of different amounts of Tween and measured after mixing with Bradford or BCA working solutions. A) Bradford and B) BCA measurements with Tween at concentrations of 5, 10, 20 mg/ml. C) Bradford measurements with Tween at 0.5, 1, and 2 mg/ml. D) BCA measurements with Tween at 1, 2.5, and 5 mg/ml.

The SN of three cross-filtration steps of PLA-Tween-2 was recollected and mixed with a known amount of BSA, as confirmation of the effect of the surfactant which would be present in the quantification of protein after particles functionalization. In the BCA measurements (Figure 4.25), a difference between the spectrum of pure protein and the SN was observed, resulting in an error of the 11%, suggesting a considerable presence of the surfactant.

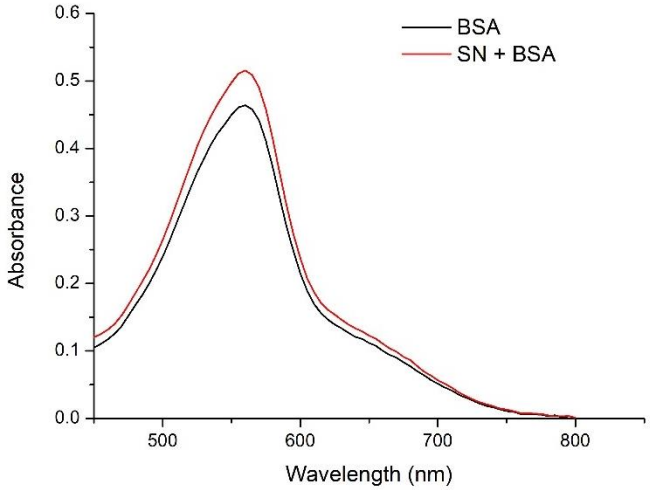

Figure 4.25: Absorption spectra of BCA working solution mixed with BSA (1 mg/ml) or with the SN of three cleaning steps of PLA-Tween-2 mixed with BSA (1 mg/ml).

Thus S-PLA particles obtained with BriJS100 as surfactant were employed to verify the tests since such it should have less intereferences effects, as reported from the manual of the assays. Initially, the effect of pure BriJS100, without being mixed with proteins, was evaluated both for BCA and Bradrord (Figure 4.26). A strong signal was detected in the case of Bradford, while a very low absorbance was found in BCA, suggesting that its use could be compatible only with the second protein quantification assay.

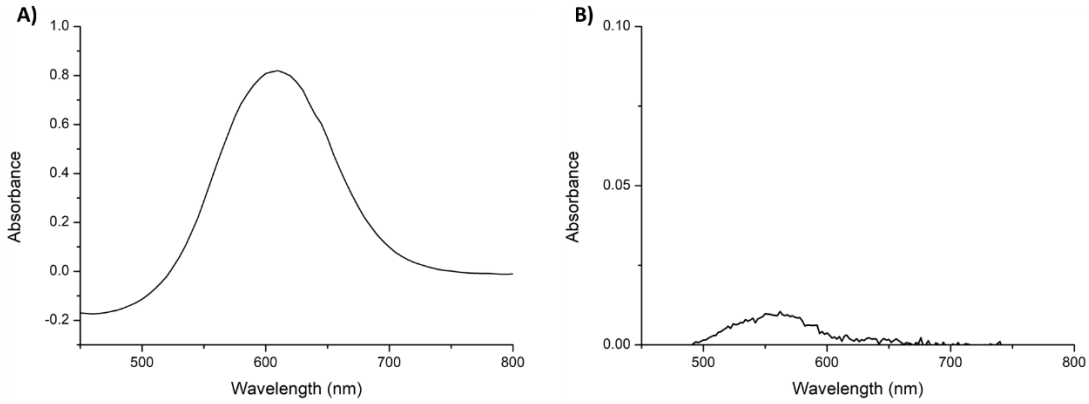

Figure 4.26: Absorption spectra of BriJS100 (5 mg/ml) after mixing with A) Bradford or B) BCA working solutions.

To further verify this possibility, two different and known protein concentrations were combined with BriJS100 and measured through BCA. On one side, a high protein concentration was employed, representative of the worst-case scenario of binding efficiency, where no protein remains attached on the

surface of particles, migrating completely to the SN (1 mg/ml) (Figure 4.27 A). Conversely, the opposite situation was evaluated, where a theoretical 90% w/w of protein would adsorb on the particles surface (0.1 mg/ml) (Figure 4.27 B). When the highest amount of protein was present, only a 2% error was calculated. However, as the protein concentration decreased, the inaccuracy became more consistent (error of 44 %).

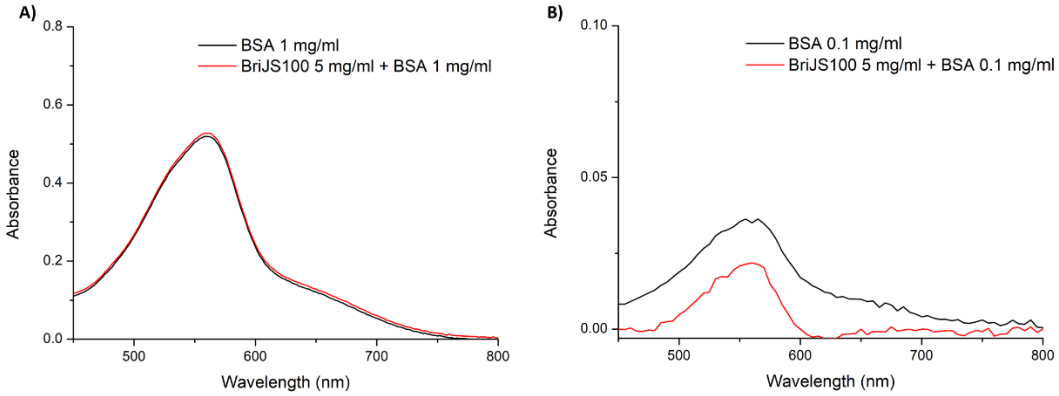

Figure 4.27: Absorption spectra of BCA working solution mixed with A) BSA (1 mg/ml), and BriJS100 mixed with BSA (1 mg/ml) or with B) BSA 0.1 mg/ml, and BriJS100 mixed with BSA (0.1 mg/ml).

Considering that the amount of protein could vary in the different measurements, both colorimetric methods were discarded for the quantification as unreliable due to their excessive variability and dependence on surfactants concentrations.

b) Fast protein liquid chromatography

The use of a more accurate and reliable quantification method was necessary. Accordingly, the fast protein liquid chromatography (FPLC) technique was employed, broadly used for the purification, separation, and analysis of proteins.[71,72] The Superdex® 200 and 200 increase columns were chosen as they present a range of protein recognition from 10 to 600 kDa, which perfectly fit both NrdJ and FliC dimensions. Moreover, they well tolerate surfactants, even at high concentrations. The absorbance at 214 nm was followed over the elution time by a UV detector.

Initially, different dilutions of pure BSA, NrdJ and FliC were injected to verify the viability of this strategy and the linear response of the detector. As shown in Figure 4.28 A, increasing absorption signals were found as the protein concentration raised. By integrating the area of the peaks between 20 and 40 minutes, it was possible to obtain a linear calibration curve (R^2>0.99). Similar behavior and trend were

also found for the FliC. Moreover, the interference effect from BriJS100 was evaluated by injecting a concentrated aliquot (125 µl) of the SN recollected by three cleaning steps of S-PLA, where no signal was detected during the total elution time (Figure 4.28 B).

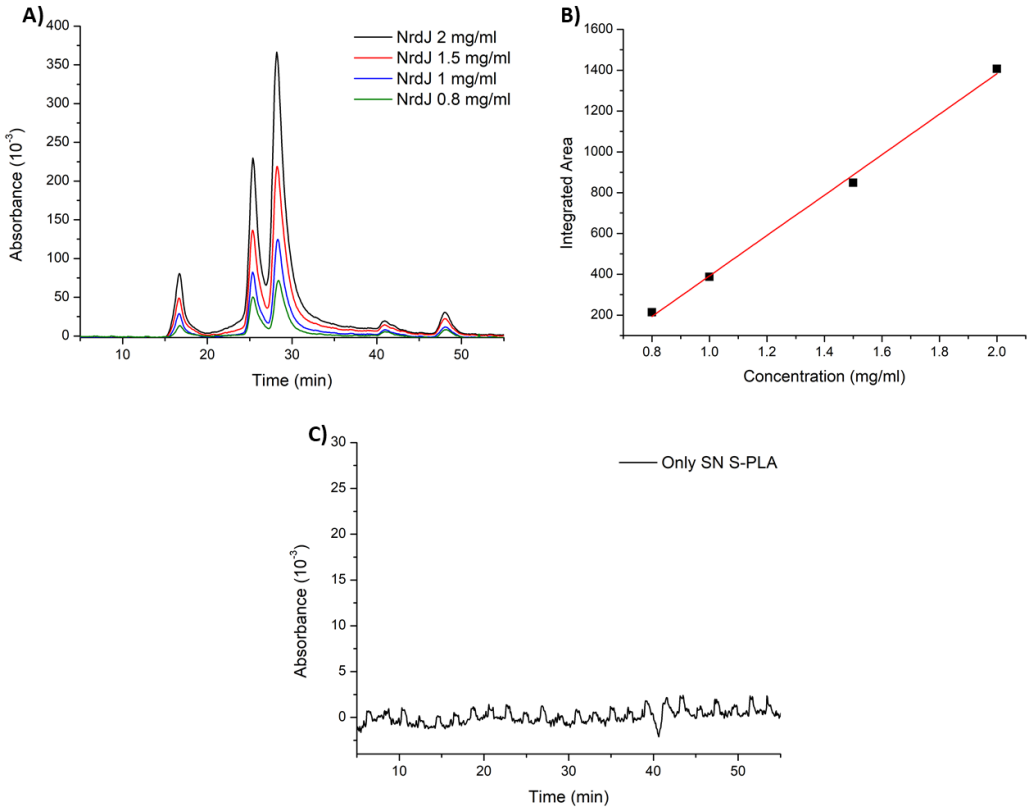

Figure 4.28: FPLC measurements of A) different concentration of NrdJ, and B) SN collected after three cleanings of S-PLA.

Once again, BSA-coated S-PLA (S-PLA-BSA) particles were initially used for the methodology optimization, following similar conditions as described before. Moreover, these S-PLA-BSA particles, as well as the free BSA were used in posterior experiments as comparative control to demonstrate the antigenic effect of proteins isolated from *Pseudomonas aeruginosa* (NrdJ, FliC).

S-PLA particles were stirred overnight at a ratio 5:1 w/w with the protein. As the FPLC methodology needs the employment of high protein concentrations to record signals with proper quality, the SN recollected after the cleanings of S-PLA-BSA was freeze-dried and suspended in a known volume or filtered with an amicon filter (30 kDa), previous its injection. The calculated binding efficiency (defined as the ratio between the bound amount and the initial protein) was surprisingly high (84% w/w), demonstrating an effective adsorption of protein around the surface of particles (Figure 4.29 A).

Considering this promising result, the BSA was replaced with the NrdJ, and the same reaction conditions were followed (S-PLA-NrdJ). However, when the SN was injected, the spectrum of NrdJ drastically changed (Figure 4.29 B). The peaks detected at shorter retention times were associated to a strong aggregation phenomenon. The ones at larger, instead, could be correlated to some nonspecific interaction between the protein and the resin material of the column, or to the loss of the conformational structure of the protein. Indeed, proteins can interact with the stationary phase by electrostatic or hydrophobic interaction, causing elution time shifting.[73]

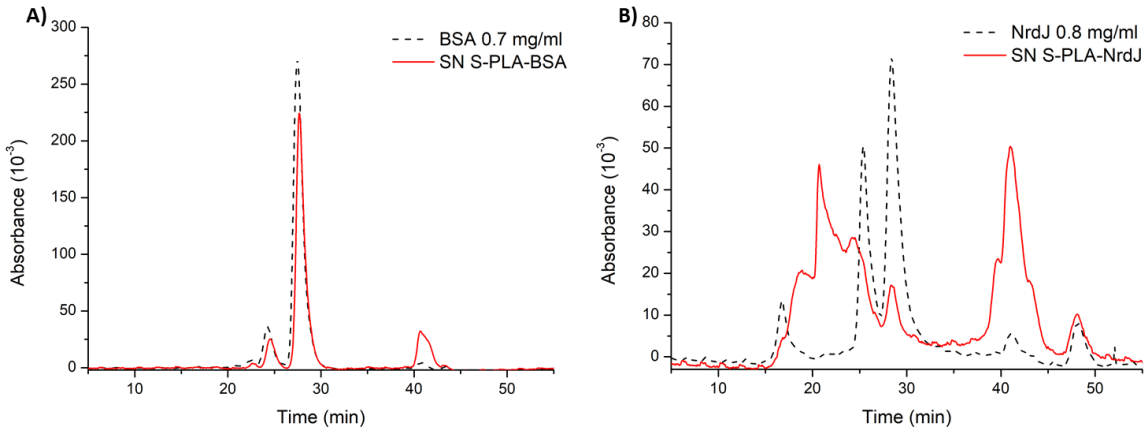

Figure 4.29: FPLC measurements of A) BSA and the SN of S-PLA-BSA, and B) NrdJ and SN S-PLA-NrdJ.

Since the NrdJ chromatogram was not showing any modification of the signal when investigated by its own, it was concluded that the aggregation phenomena and its denaturation occurred during the particles functionalization. It is well known how different conditions can affect protein stability, like temperature variation, agitation, and exposure to interfaces.[73,74] Moreover, the NrdJ, as mentioned before, is an enzymatic protein, and its properties, in terms of physicochemical stability, are widely different from structural proteins, as could be the BSA. Therefore, a broad study was carried out to find which conditions during the particle functionalization could affect the stability of the NrdJ. The different potential factors were studied separately and compared with a fresh antigen dilution, which was not subjected to any stress condition. Firstly, the effect of the cross-flow filtration was examined by filtering three times a NrdJ solution and collecting both the SN and the inner part (Figure 4.30 A). Despite the application of a shear stress, no aggregation of the antigen was detected; indeed, it has been suggested that the shear alone does not cause protein aggregation.[75] On the other hand, it was found that when the NrdJ was let under magnetic stirring, even using low stirring rates, this complete aggregation of the antigen was observed, and no signal from FPLC was found (Figure 4.30 A). On the contrary, the presence of BriJS100 (33% w/w) showed the ability to protect the NrdJ against aggregation (Figure 4.30 A). The

agitation stress is known as a possible cause of protein aggregation.[75] However, since the agitation is needed for the efficient particles functionalization, to maximize the interaction between the particles and the protein, the harsh mechanical stirring was substituted with a milder mixing procedure, using an orbital shaker. In this case, the characteristic chromatogram of the antigen was preserved (Figure 4.30 B). Mechanical stirring, indeed, is known to be a more stressful condition in comparison to shakers.[76-77]

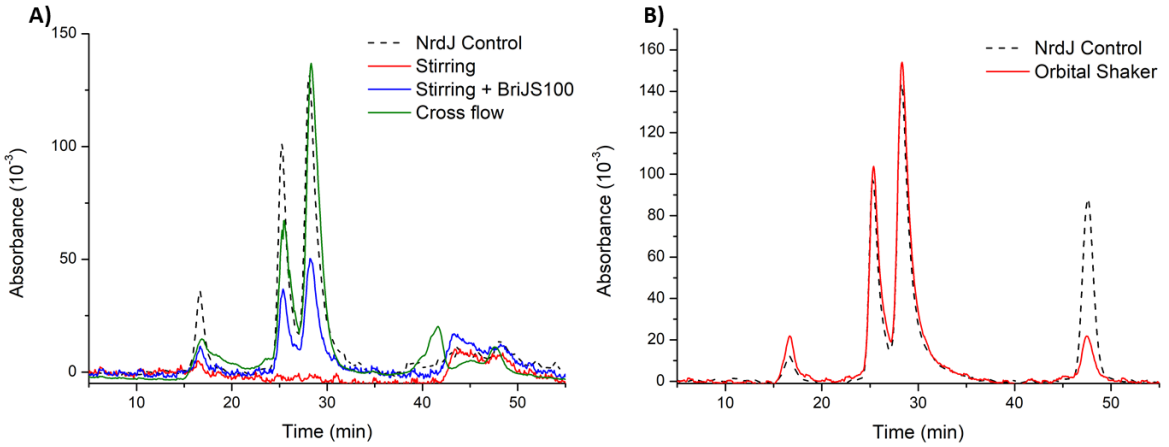

Figure 4.30: FPLC measurements of Nrdj subjected to different stress conditions. A) Pure NrdJ (black dash line), NrdJ after cross-flow filtration (green line), NrdJ magnetically stirred overnight (red line), and NrdJ magnetically stirred overnight in the presence of BriJS100 (33% w/w). B) Pure NrdJ (black dash line), and NrdJ agitate on an orbital shaker overnight (red line).

Moreover, other experimental conditions were modified to additionally protect the protein and avoid denaturation and aggregation. First, further reactions were conducted at a constant temperature of 4 °C, maximizing the antigen protection from environmental factors.[78] Secondly, the reaction time was reduced to only to 4 h, once again, to minimize the NrdJ exposure to harsh conditions. Indeed, it has been demonstrated how the adsorption of proteins on particles surface is a fast process, which starts almost immediately, and the equilibrium is reached in a few hours.[79] Finally, a higher ionic strength was used in the mobile phase of the FPLC column by adding a higher concentration of salts to reduce all possible nonspecific interactions during the running time.[73,80]

Once these parameters were optimized, the surface functionalization with NrdJ of both S-PLA and E-PLA was performed using the same conditions and the SN characterized by FPLC. Surprisingly, the antigen present in the SN of S-PLA still showed significant aggregation, while the SN of E-PLA provided a defined chromatogram (Figure 4.31). This different behavior was attributed to the possible residual presence of PVA in the SN of ellipsoidal particles suspensions. Indeed, as demonstrated before for the BriJS100, the presence of surfactants or stabilizers could help protecting the protein.

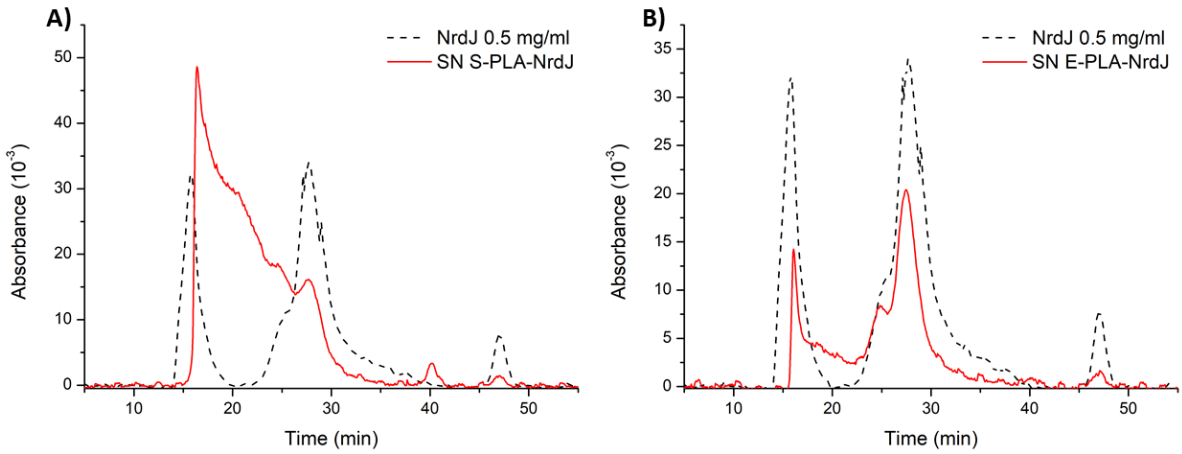

Figure 4.31: FPLC measurements of functionalized S-PLA and E-PLA with NrdJ. A) Pure Nrdj (black line) and SN of S-PLA-Nrdj (red line). B) Pure NrdJ (black line), and SN of E-PLA-NrdJ (red line).

To verify this hypothesis, S-PLA were dispersed in an aqueous solution of PVA, at the same concentration used to obtain the E-PLA (2% w/w), and the same cleaning procedure was followed. This time it was possible to quantify the unbonded protein with no aggregation phenomena for both S-PLA or E-PLA (Figure 4.32 A). Finally, these optimized functionalization conditions were applied for the functionalization with FliC, and BSA, always using a ratio of 5:1 w/w between particles and proteins (Figure 4.32 B,C).

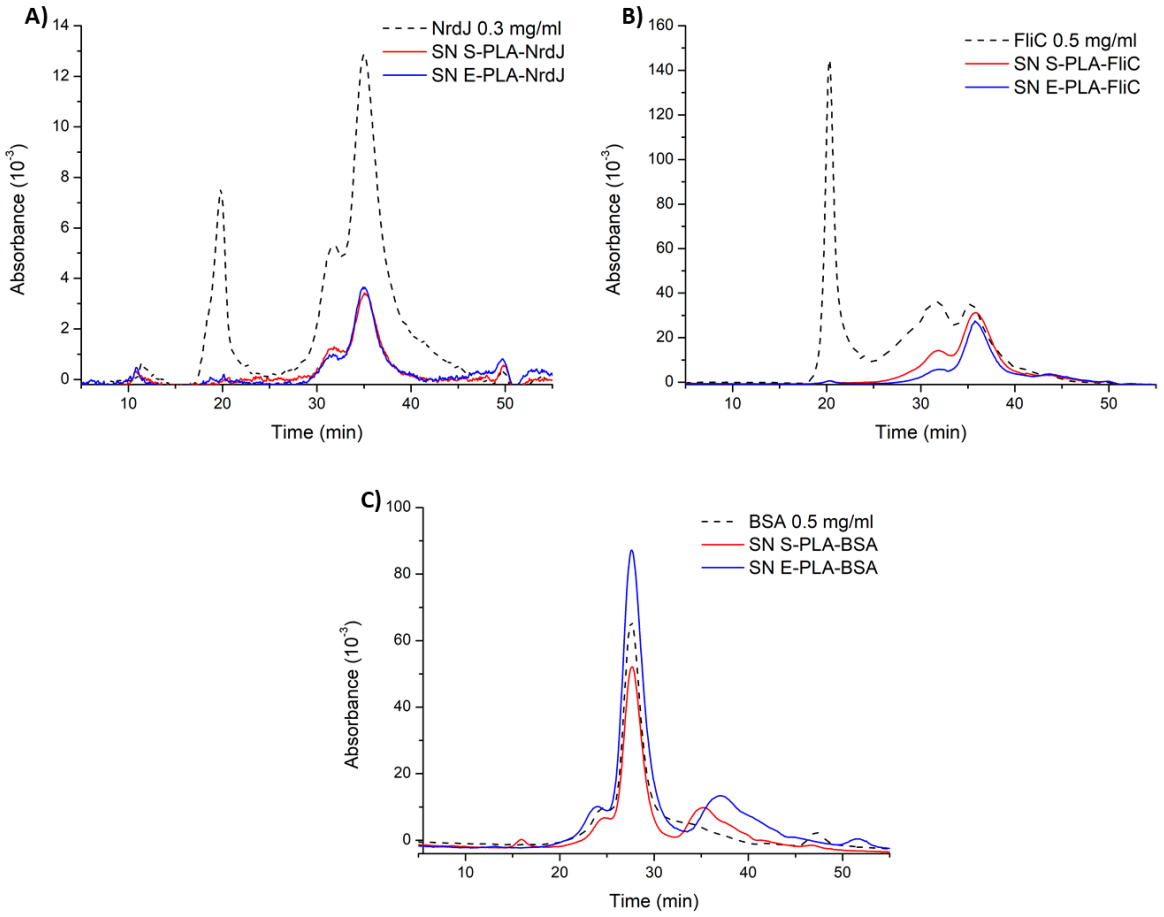

Figure 4.32: FPLC measurements of the final functionalization for both SN of S-PLA and SN of E-PLA with A) NrdJ, B) FliC, and C) BSA.

The bounded protein amounts and the binding efficiency for all three proteins could be obtained (Table 4.6:). In all cases, very high binding efficiencies were found, demonstrating the proteins adsorption as a powerful strategy for the particles functionalization. From fluorescence measurements, the ellipsoidal and spherical particles concentrations were determined. Thus, the ratio of proteins per mg of particles was calculated (Table 3.6) which resulted surprisingly high, with values much higher than the majority found in literature.[81,82] In all cases, higher values were found for E-PLA, as expected, particularly in the case of BSA and FliC. Indeed, the ellipsoidal shape provides a higher available surface for the protein attachment. NrdJ was the one with the highest adsorption ratio, as almost all the amount of protein was found to be attached on the particles surface.

Table 4.6: Binding efficiency values and protein/particles ratio for S-PLA and E-PLA functionalized with BSA, FliC, and NrdJ.

Sample	Binding Efficency (% w/w)	Protein/Particles Ratio (µg/mg):
S-PLA-NrdJ	97.9	425.7
E-PLA-NrdJ	97.6	205
S-PLA-FliC	64.5	145.5
E-PLA-FliC	84.9	167.6
S-PLA-BSA	62	179.8
E-PLA-BSA	79	192

4.3.5 *In vivo* studies

Finally, the toxicity effects and the ability to induce immune response of S-PLA and E-PLA, with and without surface functionalization with the three proteins were evaluated using the *Galleria mellonella* larvae. These experiments were conducted by Joana Admella in the BIAT-IBEC laboratories.

The immune system of the larvae resembles the innate immune response of mammals. Their cellular immune defenses, such as phagocytosis, nodulation, and encapsulation, are mediated by hemocytes, similar to what happens in mammal macrophages.[83]

Initially, the toxicity was studied by injecting high doses (130 mg particles/kg larva) of all particles (with or without functionalization); any mortality was detected for 72 h, showing similar results as pure PBS, used as control (Figure 4.33).

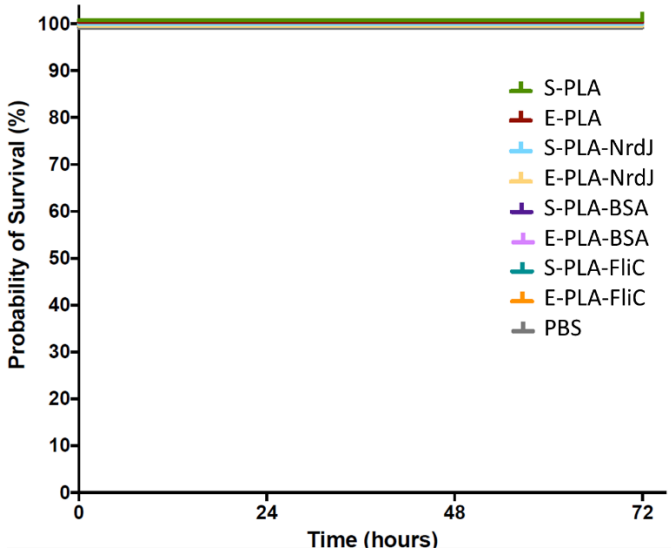

Figure 4.33: Survival curves of *Galleria mellonella* larvae injected with pure PBS, or of spherical or ellipsoidal particles without surface functionalization or functionalized with BSA, FliC, NrdJ (130 mg/kg). Larval mortality was monitored for 72 h with observation every 24 h.

Subsequently, the immune response of the larvae against pure BSA, FliC, and NrdJ, or against the S-PLA and E-PLA with and without proteins functionalization, was evaluated (Figure 4.34). A concentration of 4 mg antigen/kg larva was selected for all the conditions, and BSA was used as a negative control. At 24 h post-injection, the immune response was measured by counting the number of hemocytes present in larvae from each experimental group and by imaging the same hemocytes in the confocal microscope. At 24 h, hemocyte proliferation was appreciable in the cases of pure antigens, while S-PLA and E-PLA without protein or functionalized with BSA did not induce any significant immune response. Interestingly, ellipsoidal particles functionalized with NrdJ and FliC were able to significantly trigger the immune response of the larvae, thus revealing a synergic effect between the antigens and the particles shape. Noticeably, E-PLA-NrdJ appeared to be able excellent hemocyte proliferation promoter, showing even more substantial effect than pure antigen.

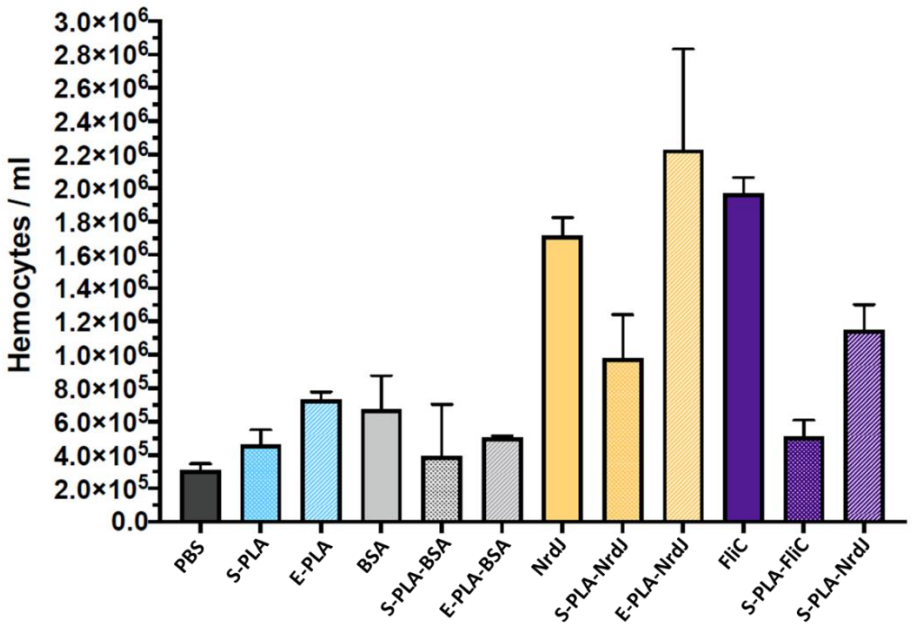

Figure 4.34: Hemocyte proliferation of *Galleria mellonella* after the injection of pure PBS or of spherical and ellipsoidal particles without surface functionalization or functionalized with BSA, FliC, NrdJ (4 mg/kg). Hemocytes were recollected after 24 h from the injection.

Finally, the hemocytes membrane was stained after S-PLA and E-PLA treatment and analyzed under a confocal microscope. Both particles appeared efficiently internalized by the cells, as it is possible to appreciate in the orthogonal views of the confocal images (Figure 4.35).

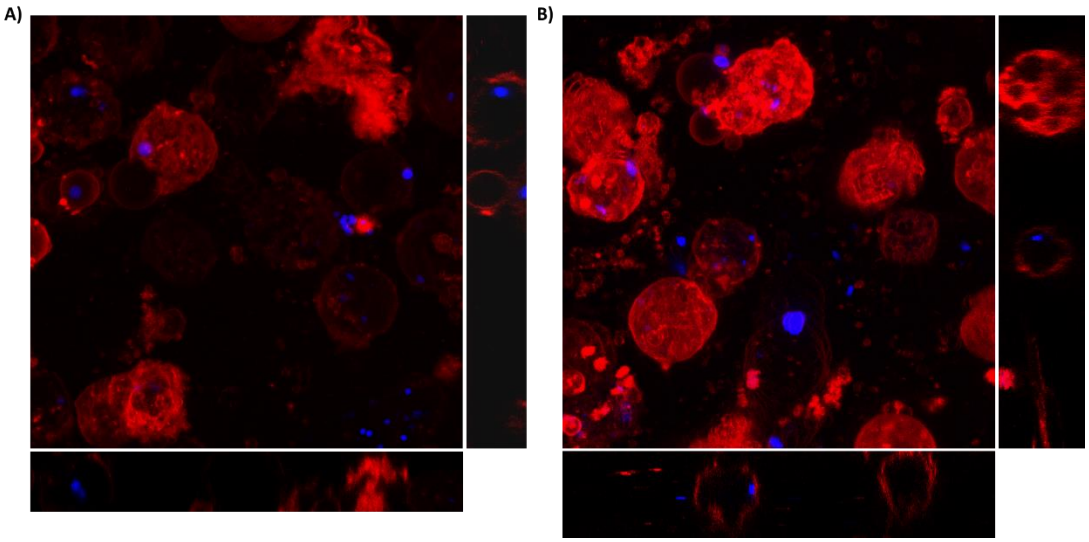

Figure 4.35: Confocal microscope images of *Galleria mellonella* hemocites, with cell membrane stained (red) after the treatment with fluorescent A) S-PLA, and B) E-PLA (blue). Center image is the sum of all stack images and the orthogonal views are seen to the side and underneath.

4.4 Summary

Biomimetic microparticles displaying the same morphological characteristics as *Pseudomonas aeruginosa* were successfully obtained:

i) A narrow size distribution, centered in 1µm, of PLA microparticles was obtained. The employment of double emulsion/solvent evaporation method allowed to significantly reduce the particles dimensions without reaching the nanometric range at the same time. The tuning of parameters and the selection of specific surfactants appeared crucial for achieving homogeneous microparticles.

ii) Ellipsoidal particles with AR of 2.4, and uniformity in shape were produced. The film stretching method was optimized in terms of film properties and stretching method. The design of an efficient stretching apparatus helped in the modulation of the achieved shape and elongation rate.

iii) Particles surface, of both spherical and ellipsoidal, was successfully decorated with antigens obtained by *Pseudomonas aeruginosa*, showing an outstanding binding efficiency. The functionalization was carried out only after the accomplishment of antigen stability, tested under different conditions.

iv) The treatment of *Galleria mellonella* larvae with antigens, or spherical and ellipsoidal particles both functionalized and not, highlighted the important role of particles shape. The functionalized ellipsoidal particles appeared to be the condition able to enhance the immune response more significantly.

The synergetic effect of specific antigens with morphology could represent a new important strategy to pave the way for the development of a new class of vaccines that would help stop the spreading of antibiotic resistance.

4.5 Experimental Section

Materials: Polylactic acid (PLA) was kindly provided by (68-69 kDa, calculated by a Bruker Daltronics Ultraflextreme MALDI-TOF). All the other products were purchased from Sigma Aldrich. Dichloromethane was purchased by Alfa Aesar.

Synthesis of spherical micro-particles (S-PLA): Spherical PLA particles were obtained through a double emulsion solvent evaporation method. For the first emulsion preparation, the organic phase was

made by dissolving 300 mg of PLA in 12 ml of DCM, while the aqueous face was constituted by 6 ml of deionized water. The emulsification process was carried out by employing an Ultra-Turrax® homogenizer (IKA, T-18) at 15.000 rpm for 10 minutes. This first water-in-oil (W/O) emulsion was quickly added to 23 ml of 1% (w/w) BriJS100 water solution and emulsified again at 17.000 rpm for another 10 minutes. The organic solvent was let evaporated overnight at room temperature to induce the polymer precipitation and the consequent particles formation. The unreacted residual polymer was removed by filtration. To make S-PLA fluorescent, 500 µl of a 9,10-diphenylanthracene (DPA) solution (1 mg/ml) were added to the organic phase before emulsification.

Synthesis of ellipsoidal microparticles (E-PLA): Ellipsoidal particles were obtained by adapting a stretching method reported in literature. [26,52] Between 3 and 8 ml of S-PLA were homogeneously mixed with 6 g of PVA water solution (20% w/w). This solution was then casted in a Petri plate of 12 cm of diameter. After water evaporation, conducted at 35 °C overnight, it was possible to obtain a film with particles embedded in it, which was consequently cut into 3 rectangular strips. Each of them was mounted to the two clamps of a custom-made apparatus. After its immersion in a silicon oil bath, pre-heated between 90-100 °C, the film stretching was performed. The film was let to cool down at room temperature, cleaned with isopropanol to remove any residual oil, and then cut in the center, recollecting only the section that had doubled its length. The cut sections were dissolved in deionized water, and ellipsoidal particles were recollected by three centrifugations at 10000 rpm for 10 minutes.

Surface functionalization. S-PLA and E-PLA were cleaned three times by cross-flow filtration (mPES, 500 kDa cut-off) and resuspended in Tris buffer (50 mM with 50 mM NaCl, pH 7.4). Their surface was decorated with BSA, NrdJ, and Flic proteins. As general procedure, 1 ml of protein suspension (0.5-1 mg/ml in Tris) was added to 1 ml of S-PLA or E-PLA (2.5-5 mg/ml) and let gently agitated through an orbital shaker at 4 °C for 4 h. The unbounded protein was removed by three passages through a cross-flow filter; the permeates (supernatant, SN) were recollected and filtered with an amicon filter (30 kDA) for the further quantification of protein, while the filtered particles were recollected in Tris buffer.

Characterization techniques:

Particles size distribution: The size distribution of S-PLA was evaluated by employing a Mastersizer 2000 (Malvern Instruments). Few drops of S-PLA were poured into the dispersion cell of the equipment, and three consecutive measurements were made.

Scanning electron microscopy (SEM): The morphology and size of S-PLA and E-PLA were evaluated by SEM using a Quanta 650 FEG. Samples were diluted in water, a few drops were placed over an

aluminum tape, and water was let evaporated at room temperature. Before analysis, samples were coated with 5 nm of platinum under an argon atmosphere using a Leica EM ACE600 sputter coater. SEM pictures were acquired at accelerating voltages between 2 and 20 kV under a high-vacuum mode and a distance of the sample of 5 mm.

Absorption spectra. All the absorption spectra were acquired by using a Cary 60 spectrophotometer. Water solutions were measured in transmittance mode using a pair of quartz cuvettes (1 cm optical path) and using water as blank.

Fluorescence emission spectra. For S-PLA and E-PLA, fluorescence was recorded on a PTI Quanta Master 300 phosphorescence/fluorescence spectrophotometer (Horiba Ltd.). The excitation (350 nm) for emission measurements was provided from a Xenon lamp (75 W). A filter of 355 nm was used for excitation light to attenuate the signal contribution from scattering.

Proton nuclear magnetic resonance (^{1}H-NMR): ^{1}H-NMR spectra of PLA, BriJS100 and S-PLA, were recorded using a Bruker Avance DPX of 250 MHz and a Bruker Ascend of 300 MHz. Generally, around 20-30 mg of samples were dissolved in $CDCl_3$, and 30 µl of DMF were added as internal reference. Spectra are given in chemical shifts (δ (ppm)). The amount of PLA was quantified using the following equation.

$$\frac{\int DMF}{mmol_{DMF}} = \frac{\int PLA}{mmol_{PLA}}$$

Colorimetric methods: The total micrograms present in the SN, recollected from the S-PLA and E-PLA cleaning, were quantified using the Braford and BCA assays, following the protocols described in the kit. The absorbance values were measured through a UV-vis spectrophotometer Cary 60.

Fast Protein Liquid Chromatography (FPLC). An AKTA purifier (GE Healthcare) system was used to quantify the amount of protein present in the SN of S-PLA or E-PLA, or to study protein stability. The Superdex® 200, and Superdex® 200 increase (GE Healthcare) columns were used. Tris (50 mM, 50-150 mM NaCl, pH 7.4) was used as mobile phase setting a 0.50 ml/min flow rate and using a linear gradient. Before measurements, samples were concentrated using an Amicon filter of 30 kDa. Volumes within 125 and 200 µl of samples were injected in the FPLC, after column equilibration, and absorbance at 214 and 280 nm were measured.

4.6 References

1. Elmowafy, E. M., Tiboni, M. & Soliman, M. E. Biocompatibility, biodegradation and biomedical applications of poly(lactic acid)/poly(lactic-co-glycolic acid) micro and nanoparticles. *J. Pharm. Investig.* **49**, 347–380 (2019).
2. DeStefano, V., Khan, S. & Tabada, A. Applications of PLA in modern medicine. *Eng. Regen.* **1**, 76–87 (2020).
3. Li, G. *et al.* Synthesis and Biological Application of Polylactic Acid. *Molecules* **25**, 5023 (2020).
4. Casalini, T., Rossi, F., Castrovinci, A. & Perale, G. A Perspective on Polylactic Acid-Based Polymers Use for Nanoparticles Synthesis and Applications. *Front. Bioeng. Biotechnol.* **7**, 259 (2019).
5. Lee, B. K., Yun, Y. & Park, K. PLA micro- and nano-particles. *Adv. Drug Deliv. Rev.* **107**, 176–191 (2016).
6. da Luz, C. M. *et al.* Poly-lactic acid nanoparticles (PLA-NP) promote physiological modifications in lung epithelial cells and are internalized by clathrin-coated pits and lipid rafts. *J. Nanobiotechnology* **15**, 11 (2017).
7. Nguyen, A. *et al.* Nanoparticles loaded with ferrocenyl tamoxifen derivatives for breast cancer treatment. *Int. J. Pharm.* **347**, 128–135 (2008).
8. Ramli, R. A., Laftah, W. A. & Hashim, S. Core–shell polymers: a review. *RSC Adv.* **3**, 15543 (2013).
9. Julià-López, A. *et al.* Temperature-Controlled Switchable Photochromism in Solid Materials. *Angew. Chem.* **128**, 15268–15272 (2016).
10. Lassalle, V. & Ferreira, M. L. PLA Nano- and Microparticles for Drug Delivery: An Overview of the Methods of Preparation. *Macromol. Biosci.* **7**, 767–783 (2007).
11. Iqbal, M., Zafar, N., Fessi, H. & Elaissari, A. Double emulsion solvent evaporation techniques used for drug encapsulation. *Int. J. Pharm.* **496**, 173–190 (2015).
12. Belletti, G. *et al.* Preparations of Poly(lactic acid) Dispersions in Water for Coating Applications. *Polymers* **13**, 2767 (2021).
13. Zambaux, M. Influence of experimental parameters on the characteristics of poly(lactic acid) nanoparticles prepared by a double emulsion method. *J. Controlled Release* **50**, 31–40 (1998).
14. Cortés, H. *et al.* Non-Ionic Surfactants for Stabilization of Polymeric Nanoparticles for Biomedical Uses. *Materials* **14**, 3197 (2021).
15. Kinnear, C., Moore, T. L., Rodriguez-Lorenzo, L., Rothen-Rutishauser, B. & Petri-Fink, A. Form Follows Function: Nanoparticle Shape and Its Implications for Nanomedicine. *Chem. Rev.* **117**, 11476–11521 (2017).
16. Mathaes, R., Winter, G., Besheer, A. & Engert, J. Non-spherical micro- and nanoparticles: fabrication, characterization and drug delivery applications. *Expert Opin. Drug Deliv.* **12**, 481–492 (2015).
17. Kapate, N., Clegg, J. R. & Mitragotri, S. Non-spherical micro- and nanoparticles for drug delivery: Progress over 15 years. *Adv. Drug Deliv. Rev.* **177**, 113807 (2021).
18. Madivala, B., Fransaer, J. & Vermant, J. Self-Assembly and Rheology of Ellipsoidal Particles at Interfaces. *Langmuir* **25**, 2718–2728 (2009).
19. Zhou, Z., Anselmo, A. C. & Mitragotri, S. Synthesis of Protein-Based, Rod-Shaped Particles from Spherical Templates using Layer-by-Layer Assembly. *Adv. Mater.* **25**, 2723–2727 (2013).

20. del Barrio, J. & Sánchez-Somolinos, C. Light to Shape the Future: From Photolithography to 4D Printing. *Adv. Opt. Mater*. **7**, 1900598 (2019).
21. Meyer, R. A. & Green, J. J. Shaping the future of nanomedicine: anisotropy in polymeric nanoparticle design. *WIREs Nanomedicine Nanobiotechnology* **8**, 191–207 (2016).
22. Ho, C. C., Keller, A., Odell, J. A. & Ottewill, R. H. Preparation of monodisperse ellipsoidal polystyrene particles. *Colloid Polym. Sci.* **271**, 469–479 (1993).
23. Guha, S. & Jindal, A. B. An insight into obtaining of non-spherical particles by mechanical stretching of micro- and nanospheres. *J. Drug Deliv. Sci. Technol*. **59**, 101860 (2020).
24. Champion, J. A., Katare, Y. K. & Mitragotri, S. Making polymeric micro- and nanoparticles of complex shapes. *Proc. Natl. Acad. Sci.* **104**, 11901–11904 (2007).
25. Mathaes, R., Winter, G., Besheer, A. & Engert, J. Influence of particle geometry and PEGylation on phagocytosis of particulate carriers. *Int. J. Pharm.* **465**, 159–164 (2014).
26. Zhang, F. *et al.* Shape Memory Polyurethane Microcapsules with Active Deformation. *ACS Appl. Mater. Interfaces* **12**, 47059–47064 (2020).
27. Haryadi, B. M. *et al.* Nonspherical Nanoparticle Shape Stability Is Affected by Complex Manufacturing Aspects: Its Implications for Drug Delivery and Targeting. *Adv. Healthc. Mater*. **8**, 1900352 (2019).
28. Trevenen, S. & Beltramo, P. J. Gradient stretching to produce variable aspect ratio colloidal ellipsoids. *J. Colloid Interface Sci.* **583**, 385–393 (2021).
29. Bhide, A. R. & Jindal, A. B. Fabrication and evaluation of artemether loaded polymeric nanorods obtained by mechanical stretching of nanospheres. *Int. J. Pharm.* **605**, 120820 (2021).
30. Kolhar, P. *et al.* Using shape effects to target antibody-coated nanoparticles to lung and brain endothelium. *Proc. Natl. Acad. Sci.* **110**, 10753–10758 (2013).
31. Thompson, A. J., Mastria, E. M. & Eniola-Adefeso, O. The margination propensity of ellipsoidal micro/nanoparticles to the endothelium in human blood flow. *Biomaterials* **34**, 5863–5871 (2013).
32. Champion, J. A. & Mitragotri, S. Role of target geometry in phagocytosis. *Proc. Natl. Acad. Sci.* **103**, 4930–4934 (2006).
33. Lagarrigue, P., Moncalvo, F. & Cellesi, F. Non-spherical Polymeric Nanocarriers for Therapeutics: The Effect of Shape on Biological Systems and Drug Delivery Properties. *Pharmaceutics* **15**, 32 (2022).
34. Vlachopoulos, A. *et al*. Poly(Lactic Acid)-Based Microparticles for Drug Delivery Applications: An Overview of Recent Advances. *Pharmaceutics* **14**, 359 (2022).
35. Tyler, B., Gullotti, D., Mangraviti, A., Utsuki, T. & Brem, H. Polylactic acid (PLA) controlled delivery carriers for biomedical applications. *Adv. Drug Deliv. Rev.* **107**, 163–175 (2016).
36. Chuensangjun, C., Pechyen, C. & Sirisansaneeyakul, S. Degradation Behaviors of Different Blends of Polylactic Acid Buried in Soil. *Energy Procedia* **34**, 73–82 (2013).
37. Middleton, J. C. & Tipton, A. J. Synthetic biodegradable polymers as orthopedic devices. *Biomaterials* **21**, 2335–2346 (2000).
38. Conn, R. E. *et al.* Safety assessment of polylactide (PLA) for use as a food-contact polymer. *Food Chem. Toxicol.* **33**, 273–283 (1995).
39. Julià-López, A., Ruiz-Molina, D., Hernando, J. & Roscini, C. Solid Materials with Tunable Reverse Photochromism. *ACS Appl. Mater. Interfaces* **11**, 11884–11892 (2019).

40. Yeh, M.-K., Chen, J.-L. & Chiang, C.-H. ***In vivo*** and ***in vitro*** characteristics for insulin-loaded PLA microparticles prepared by w/o/w solvent evaporation method with electrolytes in the continuous phase. *J. Microencapsul.* **21**, 719–728 (2004).
41. Ruiz, E., Orozco, V. H., Hoyos, L. M. & Giraldo, L. F. Study of sonication parameters on PLA nanoparticles preparation by simple emulsion-evaporation solvent technique. *Eur. Polym. J.* **173**, 111307 (2022).
42. Bahtz, J. *et al.* Decoupling of Mass Transport Mechanisms in the Stagewise Swelling of Multiple Emulsions. *Langmuir* **31**, 5265–5273 (2015).
43. Tenorio-Garcia, E., Araiza-Calahorra, A., Simone, E. & Sarkar, A. Recent advances in design and stability of double emulsions: Trends in Pickering stabilization. *Food Hydrocoll.* **128**, 107601 (2022).
44. Pays, K., Giermanska-Kahn, J., Pouligny, B., Bibette, J. & Leal-Calderon, F. Coalescence in Surfactant-Stabilized Double Emulsions. *Langmuir* **17**, 7758–7769 (2001).
45. Yafei, W., Tao, Z. & Gang, H. Structural Evolution of Polymer-Stabilized Double Emulsions. *Langmuir* **22**, 67–73 (2006).
46. de Almeida Paula, D. *et al.* Increased thermal stability of anthocyanins at pH 4.0 by guar gum in aqueous dispersions and in double emulsions W/O/W. *Int. J. Biol. Macromol.* **117**, 665–672 (2018).
47. Dinarvand, R., Moghadam, S. H., Sheikhi, A. & Atyabi, F. Effect of surfactant HLB and different formulation variables on the properties of poly-D,L-lactide microspheres of naltrexone prepared by double emulsion technique. *J. Microencapsul.* **22**, 139–151 (2005).
48. Anarakdim, K., Gutiérrez, G., Cambiella, Á., Senhadji-Kebiche, O. & Matos, M. The Effect of Emulsifiers on the Emulsion Stability and Extraction Efficiency of Cr(VI) Using Emulsion Liquid Membranes (ELMs) Formulated with a Green Solvent. *Membranes* **10**, 76 (2020).
49. Pires, I. S. & Palmer, A. F. Selective protein purification via tangential flow filtration – Exploiting protein-protein complexes to enable size-based separations. *J. Membr. Sci.* **618**, 118712 (2021).
50. Tomsen-Melero, J. *et al.* Impact of Chemical Composition on the Nanostructure and Biological Activity of α-Galactosidase-Loaded Nanovesicles for Fabry Disease Treatment. *ACS Appl. Mater. Interfaces* **13**, 7825–7838 (2021).
51. Han, Z. *et al.* Highly efficient exosome purification from human plasma by tangential flow filtration based microfluidic chip. *Sens. Actuators B Chem.* **333**, 129563 (2021).
52. Yoo, J.-W. & Mitragotri, S. Polymer particles that switch shape in response to a stimulus. *Proc. Natl. Acad. Sci.* **107**, 11205–11210 (2010).
53. Mathaes, R., Winter, G., Siahaan, T. J., Besheer, A. & Engert, J. Influence of particle size, an elongated particle geometry, and adjuvants on dendritic cell activation. *Eur. J. Pharm. Biopharm.* **94**, 542–549 (2015).
54. Vázquez-Mera, N. A. *et al.* Color-Tunable White-Light-Emitting Materials Based on Liquid-Filled Capsules and Thermally Responsive Dyes. *ACS Appl. Mater. Interfaces* **11**, 17751–17758 (2019).
55. Torres-Pierna, H., Ruiz-Molina, D. & Roscini, C. Highly transparent photochromic films with a tunable and fast solution-like response. *Mater. Horiz.* **7**, 2749–2759 (2020).
56. Strawhecker, K. E. & Manias, E. Structure and Properties of Poly(vinyl alcohol)/Na^+ Montmorillonite Nanocomposites. *Chem. Mater.* **12**, 2943–2949 (2000).

57. Abu-Huwaij, R., Assaf, S., Salem, M. & Sallam, A. Mucoadhesive Dosage form of Lidocaine Hydrochloride: I. Mucoadhesive and Physicochemical Characterization. *Drug Dev. Ind. Pharm.* **33**, 855–864 (2007).
58. Stevens, E. S. & Poliks, M. D. Tensile Strength Measurements on Biopolymer Films. *J. Chem. Educ.* **80**, 810 (2003).
59. Heinrich, G., Schoof, S. & Gusten, H. 9,10-diphenylanthracene as a fluorescence quantum yield standard. *J. Photochem.* **3**, 315–320 (1974).
60. Wang, R., Liang, Y., Liu, G. & Pu, S. Aggregation-induced emission compounds based on 9,10-diheteroarylanthracene and their applications in cell imaging. *RSC Adv.* **10**, 2170–2179 (2020).
61. Champion, O. L., Wagley, S. & Titball, R. W. *Galleria mellonella* as a model host for microbiological and toxin research. *Virulence* **7**, 840–845 (2016).
62. Benthall, G. *et al.* Evaluation of antibiotic efficacy against infections caused by planktonic or biofilm cultures of Pseudomonas aeruginosa and Klebsiella pneumoniae in Galleria mellonella. *Int. J. Antimicrob. Agents* **46**, 538–545 (2015).
63. Haiko, J. & Westerlund-Wikström, B. The Role of the Bacterial Flagellum in Adhesion and Virulence. *Biology* **2**, 1242–1267 (2013).
64. Moore, K. M. *et al.* Injectable, Ribbon-Like Microconfetti Biopolymer Platform for Vaccine Applications. *ACS Appl. Mater. Interfaces* **12**, 38950–38961 (2020).
65. Sharpe, J. R., Sammons, R. L. & Marquis, P. M. Effect of pH on protein adsorption to hydroxyapatite and tricalcium phosphate ceramics. *Biomaterials* **18**, 471–476 (1997).
66. Hlady, V. & Buijs, J. Protein adsorption on solid surfaces. *Curr. Opin. Biotechnol.* **7**, 72–77 (1996).
67. Goldring, J. P. D. Measuring Protein Concentration with Absorbance, Lowry, Bradford Coomassie Blue, or the Smith Bicinchoninic Acid Assay Before Electrophoresis. in *Electrophoretic Separation of Proteins* (eds. Kurien, B. T. & Scofield, R. H.) vol. 1855 31–39 (Springer New York, 2019).
68. Harlow, E. & Lane, D. Bradford Assay. *Cold Spring Harb. Protoc.* **2006**, pdb.prot4644 (2006).
69. Cheng, Y. *et al.* Quantitation of low concentrations of polysorbates 80 in protein formulations by Coomassie brilliant blue. *Anal. Biochem.* **573**, 67–72 (2019).
70. Cheng, Y., Wei, H., Sun, R., Tian, Z. & Zheng, X. Rapid method for protein quantitation by Bradford assay after elimination of the interference of polysorbate 80. *Anal. Biochem.* **494**, 37–39 (2016).
71. Kent, U. M. Purification of Antibodies Using Protein A-Sepharose and FPLC. in *Immunocytochemical Methods and Protocols* vol. 115 29–34 (Humana Press, 1999).
72. Madadlou, A., O'Sullivan, S. & Sheehan, D. Fast Protein Liquid Chromatography. in *Protein Chromatography* (eds. Walls, D. & Loughran, S. T.) vol. 681 439–447 (Humana Press, 2011).
73. Fekete, S., Beck, A., Veuthey, J.-L. & Guillarme, D. Theory and practice of size exclusion chromatography for the analysis of protein aggregates. *J. Pharm. Biomed. Anal.* **101**, 161–173 (2014).
74. Roberts, C. J., Das, T. K. & Sahin, E. Predicting solution aggregation rates for therapeutic proteins: Approaches and challenges. *Int. J. Pharm.* **418**, 318–333 (2011).
75. Mahler, H.-C., Friess, W., Grauschopf, U. & Kiese, S. Protein aggregation: Pathways, induction factors and analysis. *J. Pharm. Sci.* **98**, 2909–2934 (2009).
76. Kiese, S., Papppenberger, A., Friess, W. & Mahler, H.-C. Shaken, Not Stirred: Mechanical Stress Testing of an IgG1 Antibody. *J. Pharm. Sci.* **97**, 4347–4366 (2008).

77. Sediq, A. S., van Duijvenvoorde, R. B., Jiskoot, W. & Nejadnik, M. R. No Touching! Abrasion of Adsorbed Protein Is the Root Cause of Subvisible Particle Formation During Stirring. *J. Pharm. Sci.* **105**, 519–529 (2016).
78. Wang, W., Nema, S. & Teagarden, D. Protein aggregation—Pathways and influencing factors. *Int. J. Pharm.* **390**, 89–99 (2010).
79. Welsch, N., Lu, Y., Dzubiella, J. & Ballauff, M. Adsorption of proteins to functional polymeric nanoparticles. *Polymer* **54**, 2835–2849 (2013).
80. Hong, P., Koza, S. & Bouvier, E. S. P. A REVIEW SIZE-EXCLUSION CHROMATOGRAPHY FOR THE ANALYSIS OF PROTEIN BIOTHERAPEUTICS AND THEIR AGGREGATES. *J. Liq. Chromatogr. Relat. Technol.* **35**, 2923–2950 (2012).
81. Kumar, S., Anselmo, A. C., Banerjee, A., Zakrewsky, M. & Mitragotri, S. Shape and size-dependent immune response to antigen-carrying nanoparticles. *J. Controlled Release* **220**, 141–148 (2015).
82. Raudszus, B., Mulac, D. & Langer, K. A new preparation strategy for surface modified PLA nanoparticles to enhance uptake by endothelial cells. *Int. J. Pharm.* **536**, 211–221 (2018).
83. Ohta, M. *et al.* Mechanism by which Bombyx mori hemocytes recognize microorganisms: direct and indirect recognition systems for PAMPs. *Dev. Comp. Immunol.* **30**, 867–877 (2006).

Chapter 5

5. Encapsulation of magnetic nanocubes: bioinspired and biomimetic nanoparticles and their uses in hyperthermia, nanothermometry and magnetic orientation.

This chapter is divided into two subsections. In the first part, ellipsoidal particles containing magnetic nanocubes were developed. The resulting microparticles exhibited magnetic anisotropy, demonstrated by their ability to locate themselves along the force lines of an external static magnetic field, and to align in the direction of an alternating one. Moreover, by applying a rotatory magnetic field, the ellipsoidal particles were able to follow the rotation in real time. These particles would represent a promising strategy for cancer therapy being able to induce the magneto-mechanical effect.

In the second section, bioinspired magnetic nanocubes, composed of iron oxide, were encapsulated in core-shell polymeric particles, where their confinement in the liquid core permitted their movement. The photo-responsiveness of this system was evaluated by NIR irradiation, demonstrating heating capabilities suitable for photothermal treatment. Moreover, these particles acted as a nanothermometer, as the free rotation of the encapsulated nanocubes allowed measuring real-time slight temperature changes taking advantage from the magneto-optical effect. The internalization of the polymeric nanoparticles was evaluated *in vitro*. This system could constitute a powerful theragnostic tool in cancer treatment.

This work was carried out in collaboration with the Magnetic Nanostructures group led by Dr. Josep Nogués from the Catalan Institute of nanoscience and nanotechnology.

5.1 Introduction

As mentioned in the General Introduction, iron oxide magnetic nanoparticles (IOMNPs) require a coating layer to guarantee their stability, avoiding aggregation. Moreover, the coating would help improve the biodistribution of IOMNPs and reduce cytotoxicity. It would allow the functionalization with (bio)molecules, e.g., for targeting, without chemically modifying the IOMNPs and, therefore, without altering their properties.[1]

However, a single IOMNP could exhibit magnetic properties, such as the magnetic moment, although it is not strong enough. Nevertheless, having a high magnetic moment, for instance, is an indispensable requirement in biomedical applications, especially for magnetic targeting. Therefore, new strategies have been employed where aggregates, not individual particles, are coated together. In this way, single magnetic moments would sum in the magnetic cluster. This behavior is because the final magnetic properties depend on the interparticle interactions, like the dipole-dipole ones, and the exchange coupling between surface atoms, which are regulated by the size and morphology of clusters.[2] In addition, optimizing inter-particle interactions could enhance the heating efficiency of the resulting clusters.[3]

Furthermore, an even more powerful strategy could be achieved by encapsulating IOMNPs in polymeric micro- or nanoparticles. In this case, it would be possible to combine the magnetic properties of IOMNPs with all the advantages of polymeric particles, such as high biocompatibility, and versatility in size, shape, and physicochemical properties.[4] Moreover, this strategy would allow for the co-encapsulation of a possible therapeutic drug or a fluorescent dye for particle tracking, which would remain protected from the exterior simultaneously.[5] In a simple coating, it would remain exposed as if attached to the external surface. By taking advantage of the heating capabilities of IOMNPs, it would be possible to further modulate the release of the encapsulated drug by employing thermosensitive polymers.[6]

Different polymers or techniques have been investigated to develop hybrid functional materials. Solid particles with IOMNPs dispersed all over the particle's volume, and core-shell capsules encapsulating IOMNPs in the inner core have been extensively studied.[7] One of the main techniques employed for encapsulating IOMNP is miniemulsion polymerization. The magnetic nanoparticles are usually first coated with oleic acid to make them highly hydrophobic, and poly(methyl methacrylate) (PMMA) has been one of the most widely used polymers for encapsulation purposes.[7,8]

Ronco *et al*. employed crodamol, as a co-stabilizer, and oleic acid, evaluating their role in the

efficiency of IOMNPs encapsulation.[7] They discovered that a reduced amount of oleic acid, or using crodamol, helped incorporate magnetic particles in the liquid core of PMMA nanocapsules, as the oleic acid at high concentrations appeared to be able to react with the PMMA radical, participating in the polymerization. The authors further confirmed the preservation of superparamagnetic properties of IOMNPs, demonstrating their ability to be attracted towards an external magnet (Figure 5.1).[7] In a similar study, Feuser *et al*. encapsulated IOMNPs in a PMMA capsule along with zinc (II) phthalocyanine, a promising second-generation photosensitizer. The authors demonstrated the synergetic effect of photothermia and photodynamic therapy for efficient cancer treatment by employing a human glioblastoma cell line.[9] Machado and co-workers, instead, obtained solid PMMA particles with incorporated IOMPNs, and they further formed a coating layer of vinyl pivalate through seeded emulsion polymerization.[10] Other polymers, such as polyurea[11] or polystyrene[12], have also been employed to obtain polymeric particles or capsules with magnetic properties.

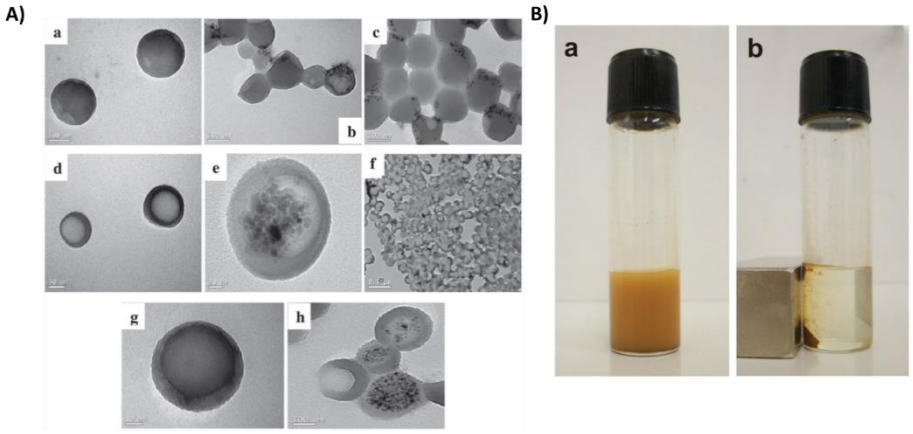

Figure 5.1: A) Transmission electron microscopy (TEM) images of PMMA magnetic nanocapsules obtained by varying the co-stabilizer used (oleic acid or crodamol) and the percentage employed. B) PMMA magnetic nanocapsules in distilled water without (a) or with (b) the application of an external magnetic field [7].

However, PMMA is not biodegradable, even though it is known to be biocompatible; therefore, its use in biological applications still has significant limitations. Therefore, the use of biodegradable polymers, such as Polylactic acid (PLA) or poly(lactic-co-glycolic acid) (PLGA), is fundamental. Nevertheless, fewer studies have been reported compared to PMMA.[5]

Lee and co-workers obtained PLA nanoparticles (around 160 nm) incorporating MIONPs by the oil-in-water solvent evaporation method. They varied the amount of encapsulated magnetic nanoparticles in order to evaluate if the different interactions between IOMNPs (concentration-dependent) could enhance the efficiency towards hyperthermia.[3] The authors found that polymeric

particles containing an intermediate amount of IOMNPs (2:6) resulted in higher magnetization and heating efficiency, suggesting they possessed more favorable magnetic interparticle interactions. They further demonstrated their particles' great cytocompatibility and biocompatibility *in vitro* and *in vivo* (Figure 5.2).[3]

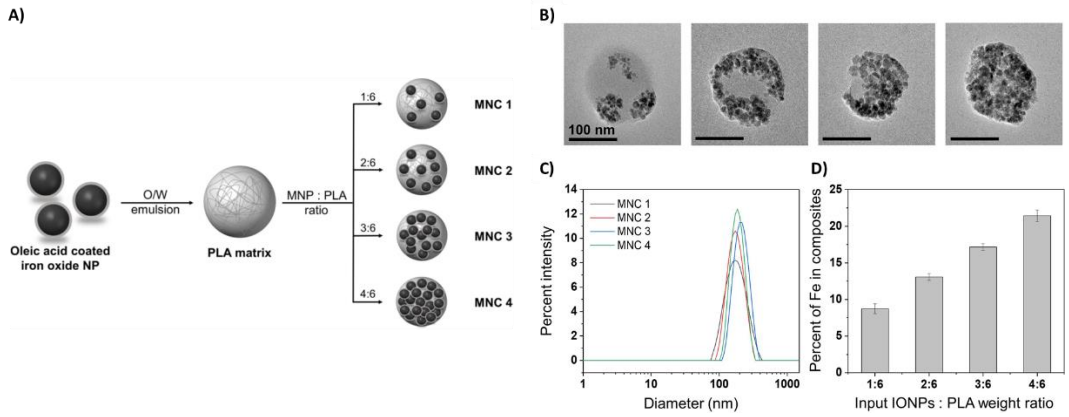

Figure 5.2: A) Schematic representation of IOMNPs embedded in PLA particles via oil-in-water emulsion by varying the concentration of IOMNPs (MNC). B) TEM of IOMNPs-PLA nanoparticles at different magnetic nanoparticles concentrations. C) size distributions, and D) percentage of iron contained in IOMNPs-PLA [3].

Mosafer *et al*. employed the multiple emulsion solvent evaporation method to obtain uniform PLGA nanoparticles with encapsulated IOMNPs. The authors demonstrated the preserved magnetic properties and their potential activity as contrast agents in MRI *in vivo*.[13] Similar results were also achieved by Jong-Duk and co-workers, following an emulsification-diffusion method, and they also functionalized the surface of PLGA particles with a monoclonal antibody for the specific targeting of breast cancer.[14] Cui *et al*., on the other side, co-encapsulated anticancer drugs, such as paclitaxel and curcumin, in PLGA nanoparticles along with IOMNPs via the single emulsion/solvent evaporation method. Moreover, they functionalized the surface of particles with a specific peptide able to bind to the transferrin receptors. Therefore, they obtained a dual targeting mechanism: by an external magnetic guide, and by the receptor-mediated, which allowed the particles to cross the blood-brain barrier *in vivo*, demonstrating improved glioma therapy efficacy.[15]

Overall, using a core-shell system would also help the thermally induced drug delivery, as only a thinner polymer shell would need to be broken to release the drug.[16] Moreover, many fluorescent dyes present an easier aggregation process in solid materials, drastically reducing the fluorescent quantum yield.[17] Despite the advances in the latest years, the controlled encapsulation of IOMNPs remains challenging. Indeed, their confinement in a specific and desired part of the capsules (such

as the core, the shell, or both) is difficult to assess and demonstrate.

Another critical aspect to be considered in biomedical applications of IOMNPs is magnetic anisotropy, which has been particularly vital in the case of nanomotors, to obtain the system's directionality; indeed, an external magnetic field can easily torque anisotropic particles. The anisotropy can depend on several factors, such as the crystallinity or the shape of IOMNPs. Therefore, several studies have been employed to obtain anisotropic magnetic particles,[18] such as the direct chemical synthesis or the assembly of single isotropic particles. Among them, the "surface/bulk modification" is quite interesting, where the anisotropy is achieved by depositing IOMNs on particles templates, obtaining Janus surfaces, or modifying the particle in which the IOMNPs are encapsulated.[18] Despite being one of the less explored methods, the latter allows for preserving all the advantages of having IOMNPs encapsulated in polymeric particles.

Tierno *et al.* performed the film stretching method of commercial spherical paramagnetic polystyrene particles and covered one face of the particles with platinum. This layer was made to provide a directional motion to the particle. They demonstrated that ellipsoidal particles could be guided by the external magnetic field, being able to move toward its direction by linear trajectories, which always developed normal to their long axis. Moreover, their anisotropy allowed the particles to perceive a torque effect from the magnetic field and, therefore, change directionality. Instead, their spherical counterparts could not change their directionality as the magnetic moment rotated inside the particles (Figure 5.3 A).[19] Another intriguing example was proposed by Kim *et al.*, involving the deposition of IOMNPs on top of pre-formed ellipsoidal polystyrene nanoparticles via the layer-by-layer method. The authors demonstrated the achieved magnetic anisotropy since, under the influence of an external magnetic field, the particles assembled into column-like structures parallel to its direction (Figure 5.3 B).[20]

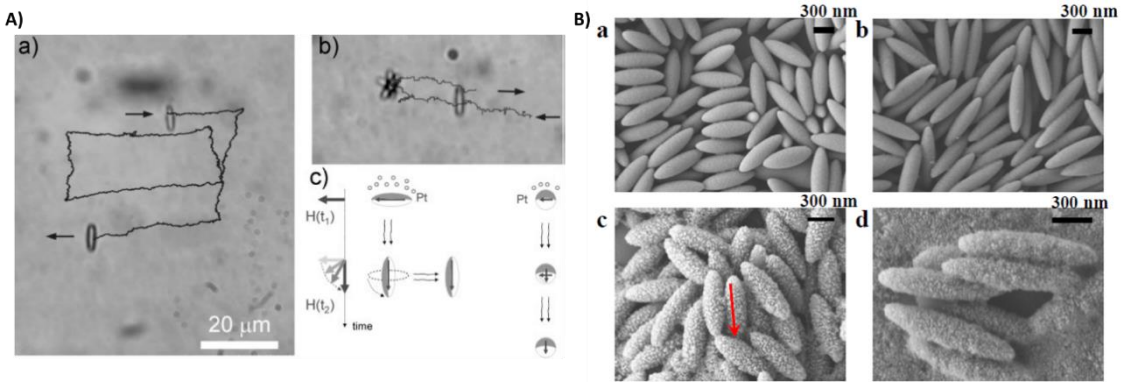

Figure 5.3: A) a,b) Optical microscopy images showing the guided motion of ellipsoidal magnetic

particles under a dynamic magnetic field. (black lines indicated the drawn trajectories) c) Schematic representation of the effect of the magnetic torque on ellipsoidal (left) and spherical (right) particles. On the first line, the magnetic field allows control over versus and direction of motion, while the spherical particles are not perturbated as the magnetic moment rotates inside the particles [19]. B) Scanning electron microscopy images (SEM) of ellipsoidal polystyrene particles before (a,b), and after (c,d) the deposition of IOMNPs. [20]

However, to our knowledge, the movement ability of an anisotropic particle achieved by modifying the polymeric particle's shape without varying IOMNPs, has not been studied for possible applications *in vitro* or *in vivo*.

Achieving controlled magnetic anisotropy by simply tuning IOMNPs' shape or properties is still challenging. Therefore, the induction of anisotropy from the "exterior" would offer fundamental advances in cancer therapy, both to move and attract more efficiently magnetic particles to the tumor and to apply magnetic torque and induce magneto-mechanical stress on cancer cells.

5.2 Objectives

Magnetic nanoparticles (MNPs) are promising tools for bioimaging and biotherapy. On the one hand, many of these have the capability of generating hyperthermia upon the application of light stimulus (photothermia) or external alternating magnetic field (magnetic hyperthermia). These nano-heaters can be used to induce apoptosis of cancer cells in which have been internalized. On the other hand, magnetic nanoparticles, of certain anisotropy, can rotate under an alternating magnetic field. Such rotation can also be exploited to induce mechanical damage to cancer cells inducing their death or as a tool for magneto-optical nano-thermometry. The latter takes advantage of the intensity modulation of an incident light induced by the rotation of the magnetic nanoparticles subjected to low-intensity and low-frequency magnetic fields, which is highly related to the viscosity variations in the surrounding medium. In this way, it is also possible to monitor and finely control the local temperature at the nanoscale while applying light or magnetic field stimuli.

So far, several different examples of MNPs have been described in the literature. Among them, recently the Magnetic Nanostructures Group (MN), led by Prof. Josep Nogues at ICN2, reported magnetite (Fe_3O_4) nanocubes with high magnetic moment, optical anisotropy, and intense absorbance in the second biological window, enabling them as nanoheaters as well as nanosensors. Magnetic nanocubes (NCs), composed of Fe_3O_4, were chosen as magnetic nanostructures inspired by the magnetic crystals present in the magnetosomes, nanocubes of size between 30 and 120 nm, which are permanently magnetic at ambient temperature (ferromagnetic behavior) [21]. Nevertheless, superparamagnetic nanoparticles (they recover their magnetic properties when the external

magnetic field is removed, with no residual magnetic moment) are less prone to aggregation, so their magneto-optical properties are more easily preserved. Thus, for our application, we aimed for superparamagnetic behavior. Nevertheless, synthetic magnetic nanoparticles present a critical size of approximately 20 nm, around which their magnetic behavior changes from superparamagnetic to ferromagnetic as their dimension increase [22].

However, before these applications become real, the following aspects must be faced:

- They should preserve very high colloidal stability when entering a biological environment as aggregation would affect their hyperthermia efficiency
- Their optical properties vary depending on the viscosity of the medium. Therefore, their use as nanothermometer is ensured if the surrounding viscosity variation only depends on temperature fluctuation.
- These nanocubes can only be used to induce cell apoptosis under external stimulation but can hardly be used to co-deliver drugs unless they are chemically functionalized.
- Magnetic anisotropy should be favored in order to enhance the effect of the external alternating magnetic field.

The general objective of the work reported in this chapter is then to overcome the challenges previously described via the encapsulation of the MNPs within bioinspired/biomimetic micro/nanocarriers. Specifically, two main structures were designed and developed along this project.

1. *Solid ellipsoidal polymeric particles* with encapsulated magnetic nanocubes, inspired by the anisotropic shape of magnetotactic bacteria. Afterwards, the ellipsoidal shape of the nanoparticles is achieved by embedding them into a polymeric thin film and applying shear forces. Ideally,

   The stretching process will also distribute the magnetic nanoparticles along the long axis inducing magnetic anisotropy, even if the each nanocube does not show it itself. As a result, the ellipsoidal particles can be directionally oriented under an external static magnetic field or rotate following an oscillating magnetic one (Figure 5.4). The magnetic-field rotational effect could be exploited for theranostic applications; indeed, the rotation of the ellipsoidal particles could induce mechanical stress in cells, causing their membrane rupture and death.

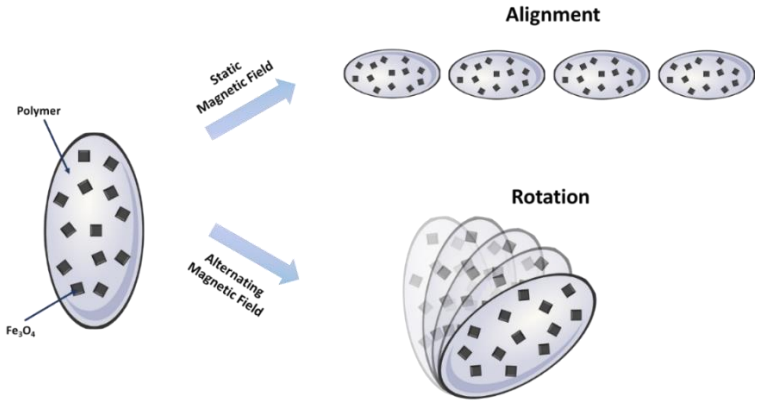

Figure 5.4: Schematic representation of ellipsoidal microparticles with magnetic nanocubes in the interior. Under a static magnetic field, microparticles can align following the field lines. If an alternating magnetic field is applied, microparticles rotate by following the direction of the external field.

2. *Biocompatible core-shell polymeric nanocapsules* containing an oil suspension of the Fe_3O_4 magnetic nanocubes (Figure 5.5). The synthetic magnetic nanocubes were employed as bioinspired nanoparticles; natural magnetosomes, as described in the introduction, often present a rough cubic shape.

   This core-shell nanostructure presents several advantages:

   - The oil core ensures the colloidal stability of the nanocubes, independently on the location of the nanocapsules, guaranteeing the preservation of the optical and hyperthermia properties.
   - The liquid core of the capsules allows the free rotation of the nanocubes under the presence of an external alternating magnetic field, enabling them as nanothermometers. The oil viscosity variation in the nanocapsules upon temperature variation should be enough to be detectable.
   - The polymeric shell isolates and protects the oil from the external environment avoiding so any viscosity variation would depend exclusively on the temperature increase produced by the nanocubes. In turn, knowing the viscosity-temperature dependence would allow the precise and real-time measurement of the local heating effect.
   - Such core-shell nanostructure would also permit the co-encapsulation of drugs, which would be released upon photothermal heating and destruction of the nanocapsules.

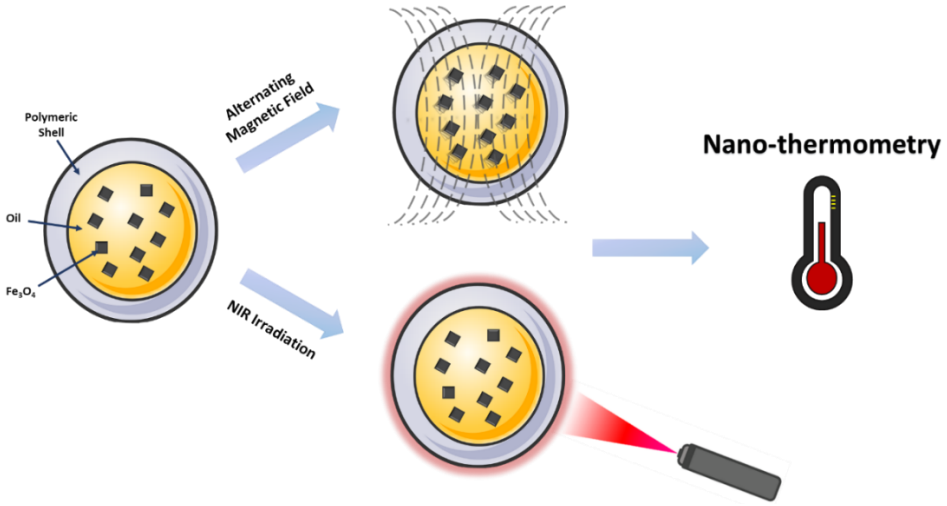

Figure 5.5: Schematic representation of polymeric core-shell nanocapsules with encapsulated magnetic nanocubes. The application of alternating magnetic field results in the rotation of the nanocubes, while the near-infrared (NIR) irradiation generates a temperature increase. Combining the two effects allows polymeric nanocapsules to be used as a nanothermometer.

5.3 Results and Discussion

Superparamagnetic NCs were synthesized and provided by Dr. Alejandro Gomez (MN group) by thermal decomposition of the precursor iron(III) acetylacetonate in the presence of oleic acid as stabilizing agent [23]. Transmission electron microscopy (TEM) showed cubic nanoparticles with an average side length of 16 nm (Figure 5.6 A) and the chloroform absorption spectrum is similar those already reported for cubical magnetic nanoparticles,[5] with a broad band around 800 nm (Figure 5.6 B).

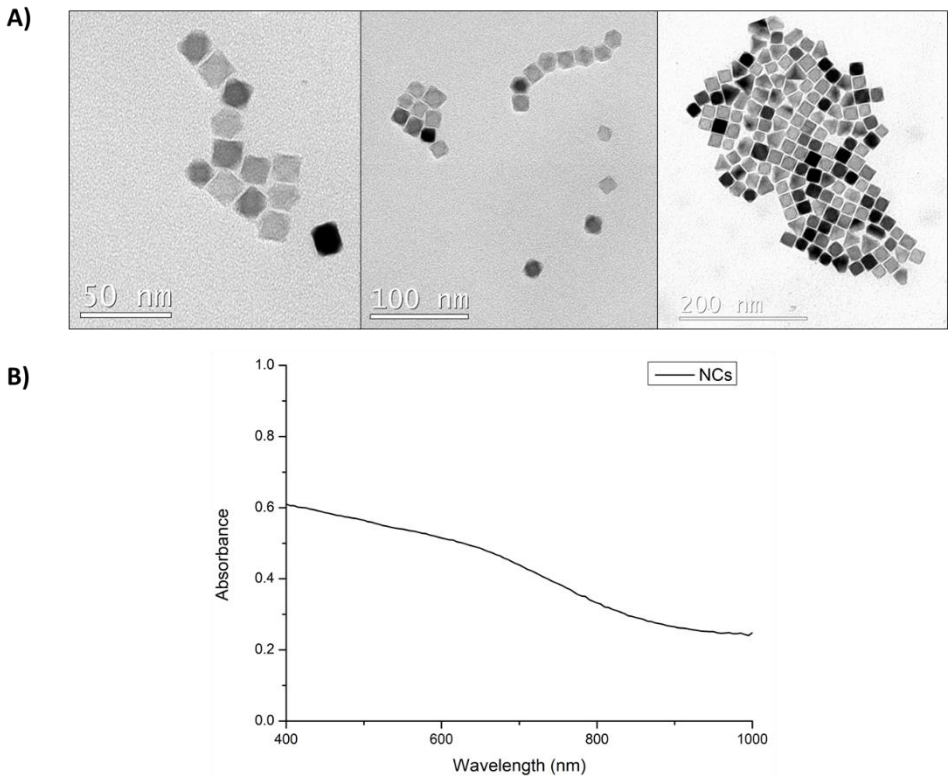

Figure 5.6: A) TEM images of NCs, B) absorption spectrum of NCs dispersed in chloroform.

5.4 Synthesis and characterization of solid ellipsoidal microparticles containing Fe_3O_4 nanocubes

Ellipsoidal PLA solid microparticles, with encapsulated NCs (PLA-NCs), were chosen as the initial model at the beginning of this work. Indeed, the micrometric size would make their monitoring easier, for instance, by optical microscopy. Moreover, contrary to the previous case, solid microparticles, without a liquid core, were selected for this study since the intrinsic rotation of NCs must be blocked in order to induce the rotation of the whole ellipsoidal particles. Of course, if the hypothesis is verified, these particles must be scaled down to the nanometer size for their further applications in biological systems. Furthermore, ellipsoidal microparticles were synthesized in a two-step process, following combined procedures described in the previous sections of this chapter. The detailed synthesis is described in the experimental section. First, spherical particles encapsulating the NCs were obtained through phase separation-solvent evaporation method. Successively ellipsoidal PLA-NCs particles were achieved through film stretching method. BPA dye was added in the organic phase during the synthesis of the spherical microparticles to make the

final ellipsoidal microparticles observable through fluorescence microscopy.

PLA-NCs with approximately 550 x 150 nm dimension and an aspect ratio of 3.5 (defined as the ratio between the major and the minor axes of ellipsoids) were observed by TEM and STEM (Figure 5.7). Through both techniques, it is possible to appreciate the presence of NCs throughout the whole microparticle volume without aggregation, yielding an overall anisotropic distribution (ellipsoidal).

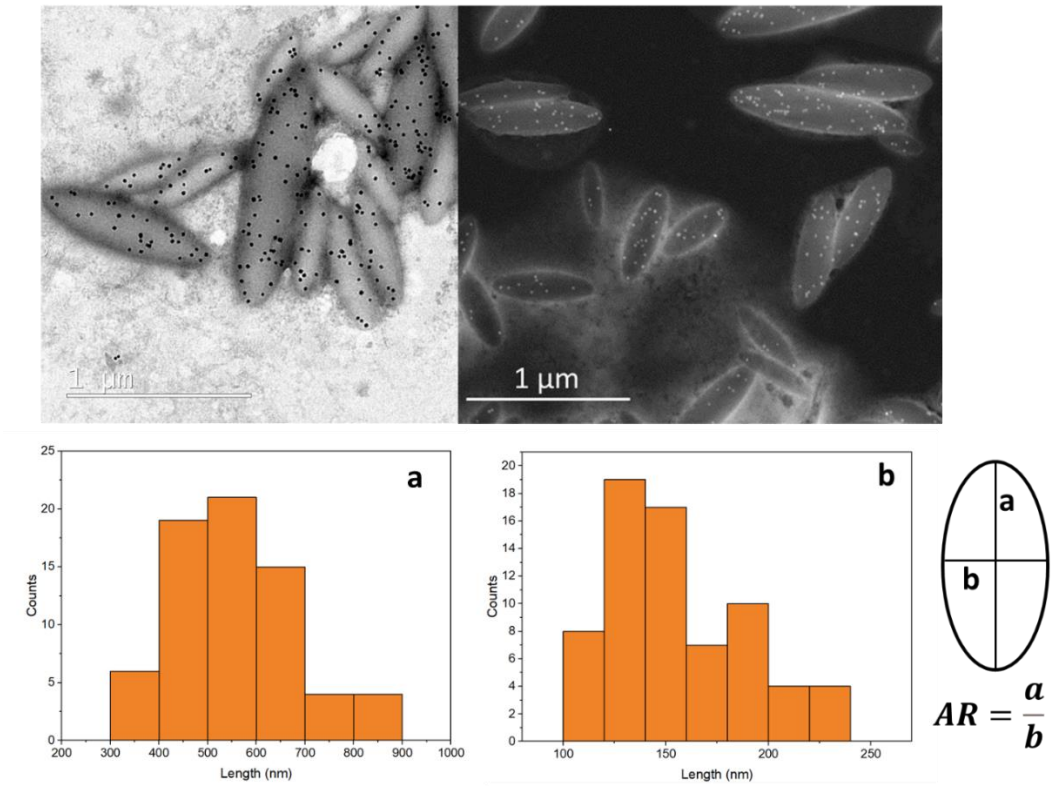

Figure 5.7: TEM images (left side) and STEM images (right side) of PLA-NCs, with the corresponding size histograms. a: major axe of ellipsoids, b: minor axe of ellipsoidal, the AR (aspect ratio) is calculated as their ratio.

5.4.1 Magnetic properties of the microparticles

The magnetic behavior of PLA-NCs was evaluated under magnetic fields. The initial study was carried out under a static magnetic field. To be able to analyze the effect of the magnetic field on the microparticles orientation, a set-up was designed. The PLA-NCs suspension was dispersed in an aqueous solution of PVA (20 % w/w) and casted on a Petri plate. When below the plate a magnet of spherical or rectangular shape was placed (Figure 5.8), no changes at naked eye were observed. However, after evaporating the water (while keeping the magnet), a PVA film was formed, trapping

the polymeric particles. As a result, the film presented an opaque pattern that followed the magnetic field lines (**Errore. L'origine riferimento non è stata trovata.**Figure 5.8). Such opacity was ascribed to the light scattering of the microparticles in the films, suggesting that the microparticles were positioned along the magnetic field lines when the medium was in the liquid state and then remained frozen in the forced position once the film dried.

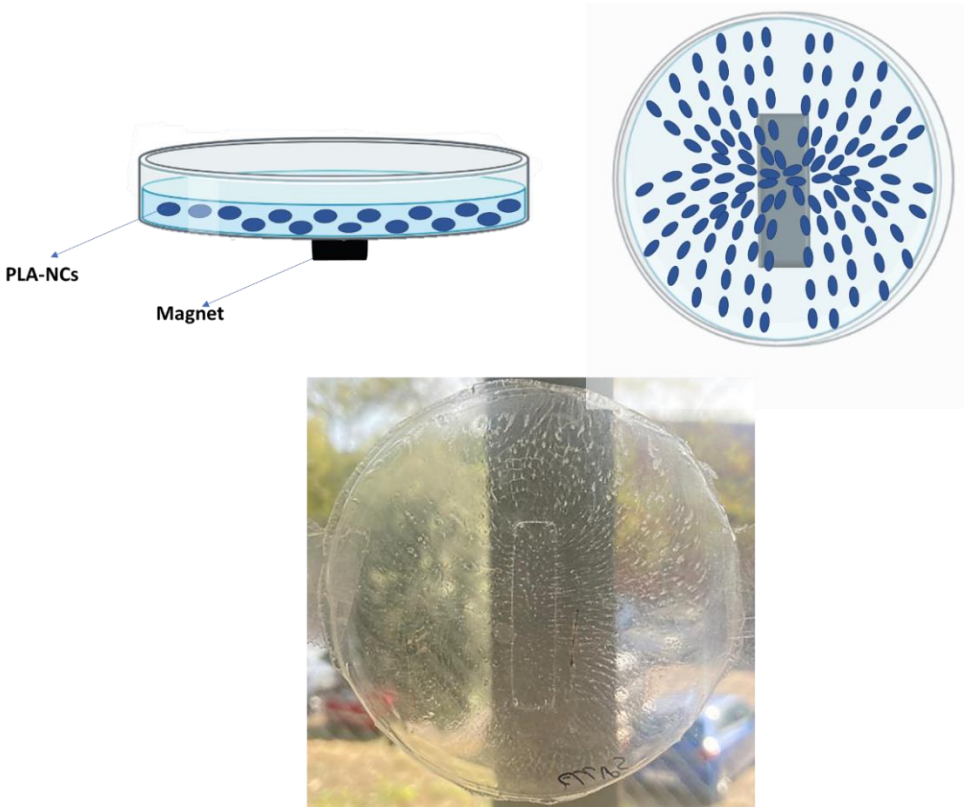

Figure 5.8: Schematic representation of PLA-NCs entrapped in PVA films and oriented with a magnet (upper side) and picture of the resulting film (bottom side).

A closer inspection of the film via fluorescence microscopy confirmed not only that the PLA-NCs were distributed in discrete rows within the film, but also that they were aligned in the same direction, along the magnetic field lines (Figure 5.9 A). A similar alignment was also found for spherical particles, made as a control, but it was absent in the case of films obtained without the presence of the magnet (Figure 5.9 B, C).

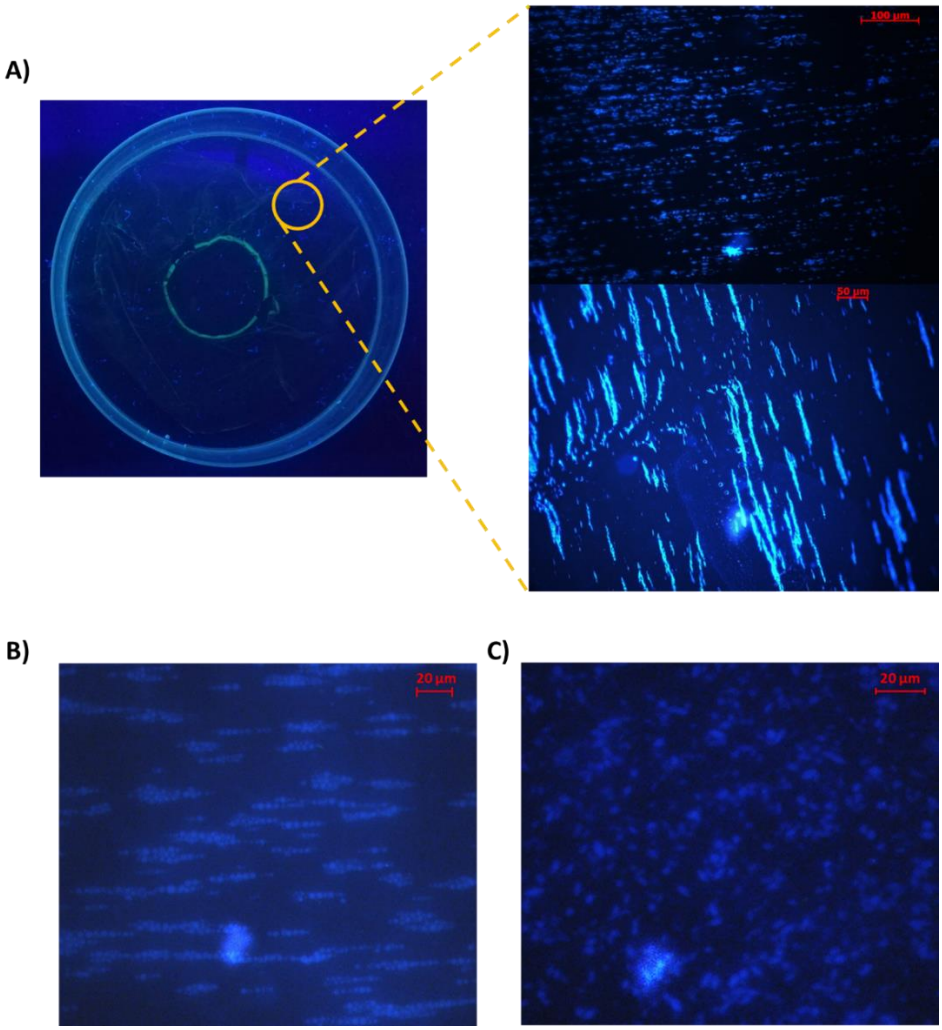

Figure 5.9: A) Picture of PVA film of oriented PLA-NCs entrapped inside observed under a UV lamp (left side), and correspondents fluorescence microscope images (right side). Fluorescence microscope images of PVA films with B) oriented spherical particles and C) not oriented PLA-NCs.

The results above clearly demonstrate that polymeric microparticles can be oriented by an external static magnetic field. As discussed above, TEM images showed that the NCs did not form anisotropic aggregates, which means the resultant magnetic anisotropy is dictated by the overall distribution of the NCs in the anisotropic ellipsoidal particles.

The next step consisted in investigating the magnetic response of the PLA-NCs to an alternating magnetic field. Initially, the PLA-NCs behavior in suspension was monitored in real-time with fluorescence microscopy under the manual motion of a magnet around the sample. Interestingly, it could be observed as the PLA-NCs started aligning toward the magnet within a few seconds. When the magnet was changed in position, the particles followed its movement with a short delay (Figure 5.10). Since the movement of the magnet was relativity slow, microparticles could rotate

accordingly. When the same experiment was carried out with spherical nanoparticles, the change of direction could not be detected upon variation of the magnet position.

Successively, a controlled alternating magnetic field was applied (10 Hz, 15 Vpp) through a coil. As soon as it was turned on, the PLA-NCs immediately aligned along the magnetic field lines. Noticeably, it was possible to align the microparticles in planar (parallel to the film plane) and homeotropic (perpendicular to the film plane) modes upon variation in the direction of the magnetic fields (Figure 5.10). When the magnetic field was turned off, the microparticles recovered random orientation and position as they were able to freely move through Brownian motions. It must be mentioned that when the alternating frequency of the magnetic field was too high, the PLA-NCs could not follow it. This was ascribed to the slow rotation rate of the microparticles, possibly caused by their large dimensions. It is expected that a faster rotation can be achieved by making the particles of nanoscale dimension, which is also the size required for them to be internalized in cells. However, this perspective study has shown how NCs could be assembled in anisotropic non-magnetic responsive polymeric microparticles to achieve magnetic anisotropic particles that respond to the magnetic field direction variation.

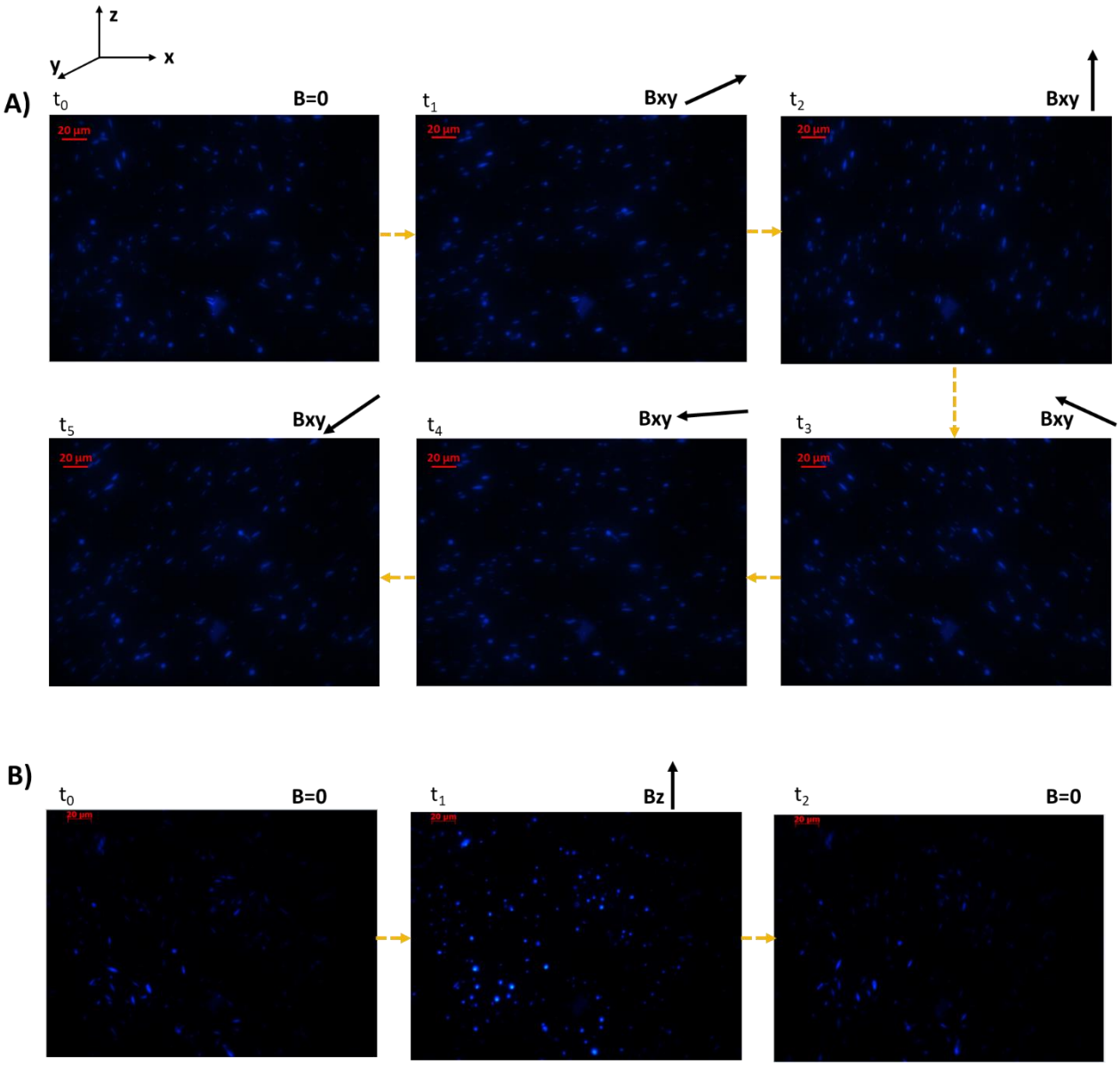

Figure 5.10: Frames of acquired videos under fluorescence microscopy of PLA-NA-NCs movement when A) a magnet is applied in different positions (Bxy), or when B) an alternating magnetic field is applied (Bz). The movement of particles is followed over time (t_n).

5.5 Synthesis and characterization of polymeric nanocapsules

Core-shell nanocapsules, containing oil nanocubes suspensions as core material, were synthesized by solvent-evaporation method, adapting a protocol reported in literature and developed in the group [26]. Basically, the organic phase constituted by polylactic acid (PLA), a nontoxic polymer approved by the FDA employed in several studies to form nanocapsules,[27,28] and the oil-

NCs suspension mixed together in dichloromethane was emulsified by ultrasonication to ensure the formation of nanodroplets. The final nanocapsules (PLA-NA-NCs) were obtained after organic solvent evaporation, which was accelerated by using a rotary evaporator. The optimization protocol was done initiated by Ylenia Martin, a bachelor student working under my supervision. During this study, several parameters were investigated, such as the surfactant type and concentration, oil core (i.e. hexadecane, oleic acid, Miglyol® 812, and nonanoic acid), oil/water ratio, homogenization rate, etc.

According to the previous results, nonanoic acid (NA) appeared to be the most promising oil for the efficient encapsulation of NCs as its OH groups are expected to substitute the oleic acid surfactant, favoring their good colloidal dispersion. Other oils manifested a reduced capability of redispersion, forcing the NCs to migrate to the oil/water interface during the emulsification process, where they remained trapped after the shell formation. Moreover, this oil is expected to be well tolerated, as it shears remarkable chemical similarities with decanoic or dodecanoic acids, known for their low cytotoxicity.[29-30] Therefore, the final fabrication protocol consisted of a PLA and NA-NCs (2:1 w/w) dichloromethane sonicated suspension, using polyvinyl alcohol (PVA) as a stabilizer. The excess of NA could act as a co-stabilizer, reducing nanodroplet size and distribution. The final nanocapsules (PLA-NA-NCs) were obtained after dichloromethane evaporation using a rotary evaporator. To remove the non-encapsulated NA-NCs suspension, PLA-NA-NCs were first centrifuged. However, flocculation of nanocapsules was observed on the top of the suspension, making impossible their separation from the excess of NA. This result also suggests the core-shell structure of the nanocapsules, as the NA core makes them less dense than water. Thus, a cleaning procedure was implemented by taking advantage of the low melting point of NA (12 °C). Indeed, at relatively low temperatures, the non-encapsulated NA resulted as a solid easily separable from the liquid water PLA-NA-NCs colloidal suspension. Once cleaned, freeze-dried nanocapsules appeared as brown dry solid powder, color originated from the presence NCs, without residual non-encapsulated oil. Both nanoparticles with NCs but without NA and nanocapsules without NCs (PLA-NA) were synthesized as control samples for comparative purposes, using similar conditions.

Dynamic light scattering (DLS) of PLA-NA-NCs diluted in water, revealed an average hydrodynamic diameter of 228 nm with a sharp size distribution and a very low PDI (0.05) (Figure 5.11 A). Scanning electron microscopy (SEM) images showed spherical nanoparticles with an average diameter of 300 nm, in good agreement with DLS analysis (Figure 5.11 B, C). Moreover, no unstructured oil material was observed, corroborating the successful cleaning of any residual NA from the nanoparticles. During the SEM sample inspection, indirect evidence of the core-shell

structure of PLA-NA-NCs was also extrapolated. Indeed, after a few seconds of focusing the electron beam on the nanocapsules, a significant and rapid rupture was observed (Figure 5.11 D).

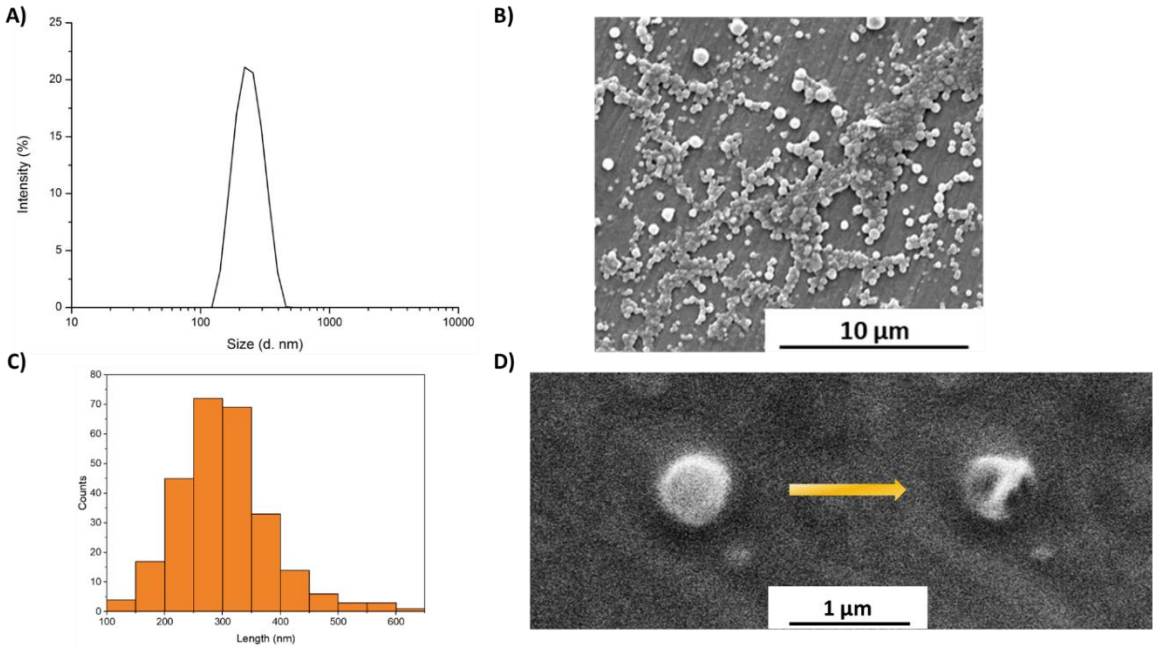

Figure 5.11: A) SEM image of PLA-NA-NCs, and B) the correspondent size histogram. C) DLS measurement of PLA-NA-NCs in water, and D) a SEM image taken over time before (left) and after (right) the focusing of the electron beam on the surface of a nanocapsule.

In any case, to ascertains and quantify the encapsulated NA (payload), proton nuclear magnetic resonance (^{1}H-NMR) of PLA-NA capsules without NCs (to avoid any possible NMR interference caused by the magnetic field induced by the nanocubes) was done. For this, freeze-dried nanocapsules were dissolved in deuterated chloroform, and a known amount of dimethylformamide (DMF) was used as an internal reference. The acquired spectra of controls (PLA and NA) and nanocapsules are reported in Figure 5.12. For PLA-NA-NCs, the characteristic peaks of both PLA and NA were recognized, and the amount of NA was quantified from the ratio of the integrated areas of the selected peaks of DMF (δ = 8.1 ppm, singlet, CH, area = 1 arb. u.) and NA (δ = 1.2 ppm, broad singlet, $(CH_2)_5$), area = 1.93 arb. u.), considering the number of protons assigned for each selected peak. Thus, by knowing the amount of DMF, it was possible to calculate the number of moles of NA, resulting in a payload of 21% w/w.

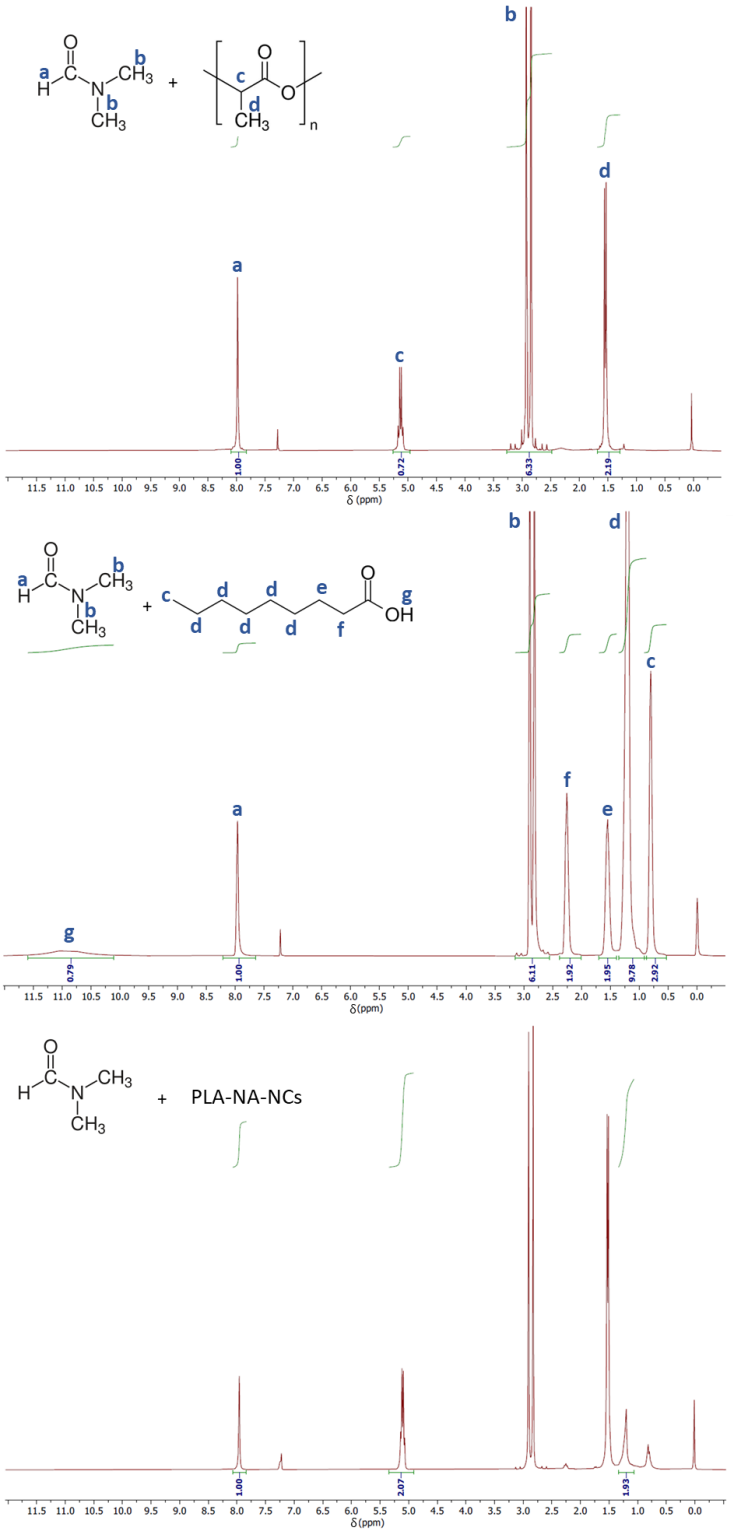

Figure 5.12: ^{1}H-NMR spectra in deuterated chloroform of PLA, NA, and PLA-NA-NCs. DMF was used as an internal reference. The characteristic peaks of each component were recognized. PLA: δ =5.13 ppm (m, 1 H, CH), 1.55 ppm (d, 3H, CH3); NA: δ= 0.79 ppm (t, 3H, CH_3), 1.2 ppm (s, 10H, $(CH_2)_5$), 1.54 ppm (m, 2H, CH_2), 2.25 ppm (t, 2H, $COCH_2$), and 10.8 ppm (br s, 1H, OH), The peaks at δ = 2.82 ppm (s, 3H, CH_3),

2.90 ppm (s, 3H, CH_3) and 7.96 ppm (s, 1H, CH) were ascribed to DMF. (s: singlet; d: doublet; t: triplet; m: multiples; br: broad).

Afterward, differential scanning calorimetry (DSC) was used to confirm the core-shell structure of PLA-NA-NCs. Five different heating up and cooling down processes are represented in Figure 5.13 (upward peaks correspond to exothermic processes). If the heating process does not reach the T_g and T_m of PLA,[31 32] only the melting point (T_m) of NA is recognized at 16 °C, close to the value reported in literature (12 °C)[33]. The absence of displacement demonstrates that the NA preserved a separated phase with respect to the PLA, and, thus, the thermal transition properties; this further indirectly indicates that a core-shell structure is achieved in the nanocapsules, with the NA occupying a separated core portion within the capsules. Indeed, if the polymer and the oil would mix, forming a homogeneous plasticized polymer matrix, a shift in the NA T_m would be expected. A second peak at -4ºC was also found ascribed to the melting of water trapped within the sample powder. On the other side, in the cooling process a peak at 4 ºC was found, associated to the crystallization process of NA (the difference between the crystallization and melting peaks was ascribed to supercooling).[34] Finally, when a third heating process is performed, this time up to 80 °C (over PLA Tg), forcing the mixing and plasticization of the polymer and the oil, a slight shift in the crystallization temperature of NA was found.

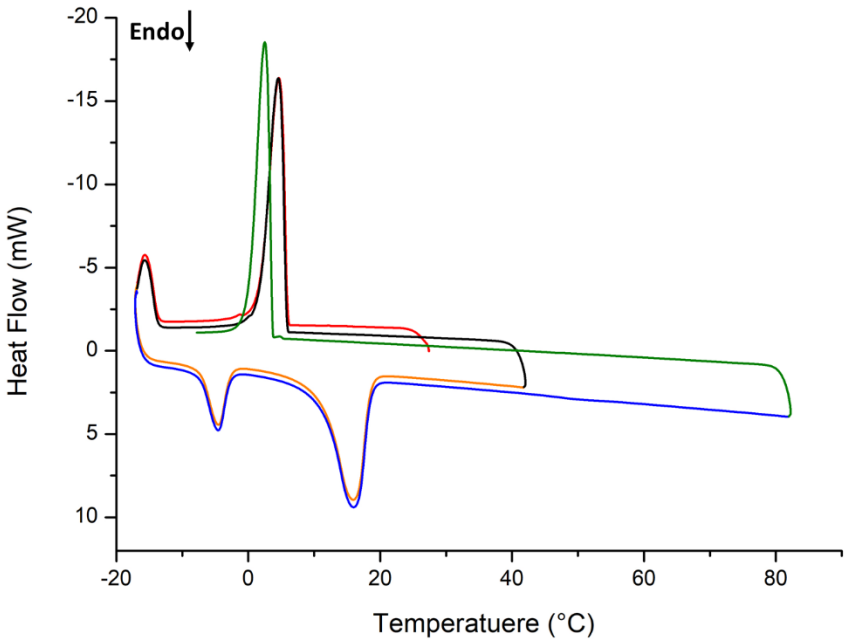

Figure 5.13: DSC of PLA-NA-NCs. The endothermic processes are represented as downward peaks. 5 different temperature heating and cooling processes were carried out: 1) cooling from 25 °C to -17 °C (red curve), 2) heating from -17 °C to 42 °C (orange curve), 3) cooling from 42 °C to -17 °C (black curve), 4)

heating from -17 °C to 82 °C (blue curve), and 5) cooling down from 82 °C to -8 °C (green curve).

The core-shell structure of the nanocapsules was supported by TEM images; as can be seen there, the oil phase is mostly located in the center (Figure 5.14 A). Noticeably, NCs appeared mostly located in the center as small aggregates. However, the confirmation of the exact localization of NCs in the inner core material, is not completely achievable by TEM, indeed, they could also be trapped in or deposited on the shell material, in the top or bottom position, with respect to the incident electron beam.

To partially discard that NCs were positioned on the surface of the nanocapsules, scanning transmission electron microscopy (STEM) was employed and carried out on larger capsules, as these were the only ones able to stand the electron beam irradiation without incurring in rupture (Figure 5.14 B). STEM image showed the NCs appeared, with strong contrast, predominantly at the center of the capsules volume (indicated with yellow circles) and, in less extent, near the particle borders. On the other hand, the corresponding SEM images show a quite smooth surface with just few roughness on the surface of PLA-NA-NCs associated with the presence of NCs (pointed out by yellow circles). These results indicate how most NCs are not located on the top surface of the nanocapsules (and for extrapolation on the bottom surface), concluding that the majority of them were in the core material.

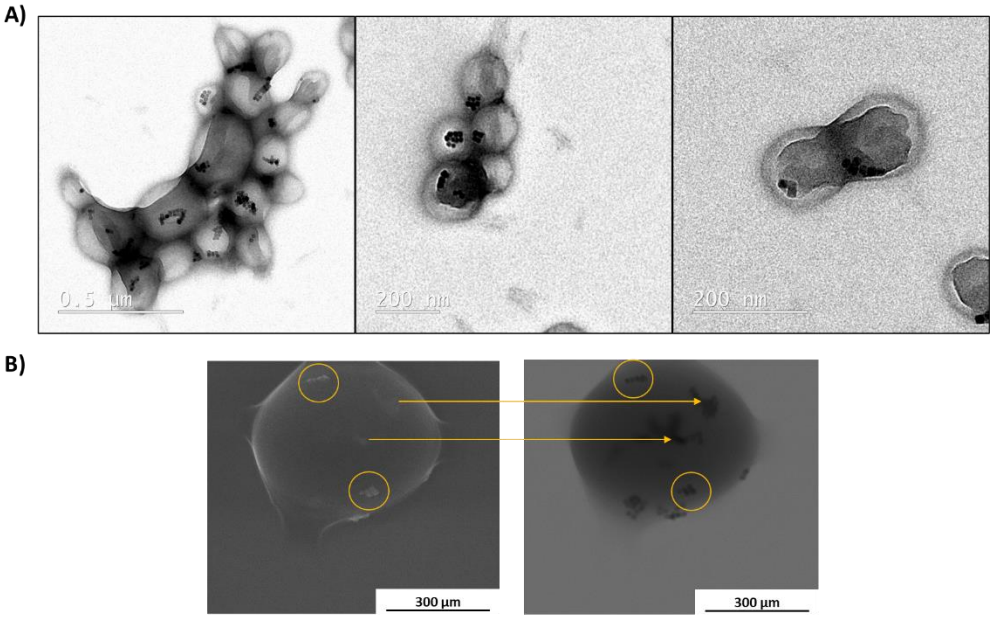

Figure 5.14: A) TEM images of PLA-NA-NCs. B) STEM and SEM images of PLA-NA-NCs. SEM image on the left side, STEM image on the right side. The yellow arrows indicate the encapsulated NCs, while the yellow circles indicate the NCs present on the surface of nanocapsules.

Therefore, to have a more definitive conclusion on where NCs were located, TEM images of PLA-NA-NCs were acquired at different tilting angle degrees. As shown in Figure 5.15, the NCs, clearly appreciable for their high contrast, appeared to be confined entirely in the inner part of nanocapsules, indicating they are positioned predominantly in the core oil medium. Combining the results described above, it is possible to state that NCs are mostly well encapsulated inside the PLA nanocapsules and appear confined in their inner liquid core. Finally, the amount of encapsulated NCs was quantified by Inductively Coupled Plasma Optical Emission Spectroscopy (ICP-OES), resulting in an outstanding encapsulation efficiency (EE) of almost 70% w/w.

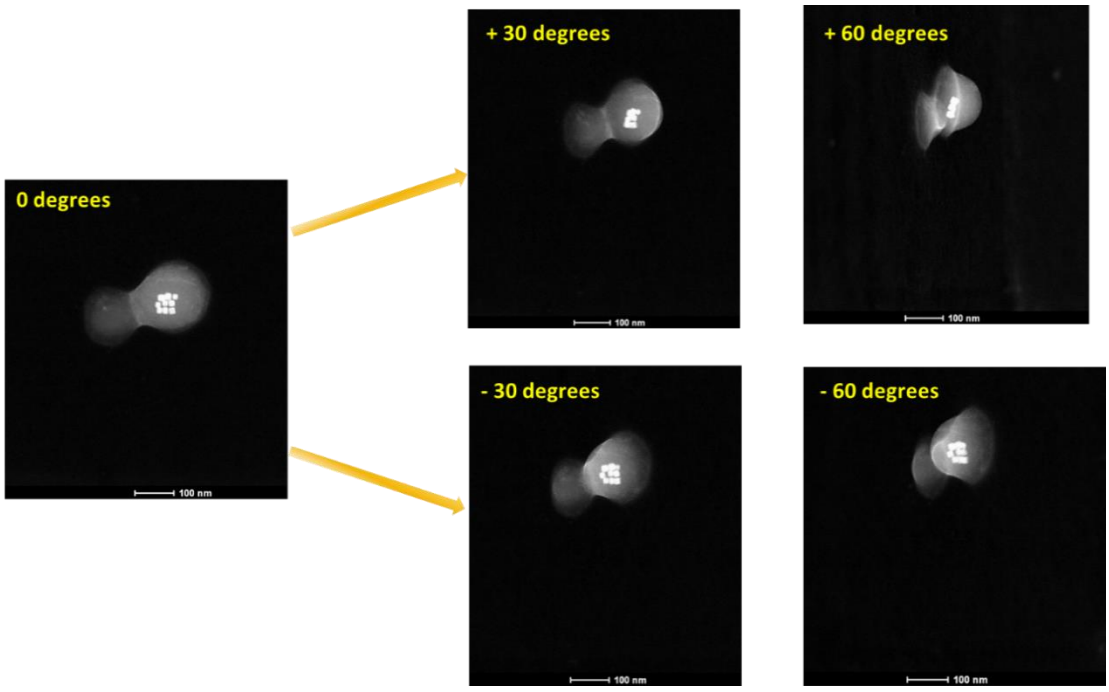

Figure 5.15: TEM images of PLA-NA-NCs acquired at different angulations.

The magnetic properties of PLA-NA-NCs were studied by Dr. A. Gomez (MN group). As control, free NCs suspended in chloroform were also studied and showed the expected superparamagnetic behavior, characterized by a saturated magnetic moment at high magnetic fields and a saturation magnetization (Ms) of 77 emu/g_{sample}. On the contrary, PLA-NA-NCs showed a magnetization curve with a decreasing slope as the external magnetic field increased (Figure 5.16). This tendency can be associated to a double contribution, the superparamagnetic behavior of the NCs, and a diamagnetic one of the organic material (PLA and NA). This two-phase magnetic behavior has been described and attributed to core-shell systems.[35,36] By subtracting the diamagnetic

component, which corresponds to a straight line with a negative slope, it is possible to demonstrate how the superparamagnetic behavior of NCs was kept after encapsulation. The Ms resulted equal to 0.86 emu/g_{sample}, much lower in comparison to free NCs; however, PLA-NA-NCs were still sensitive to the external magnetic field.

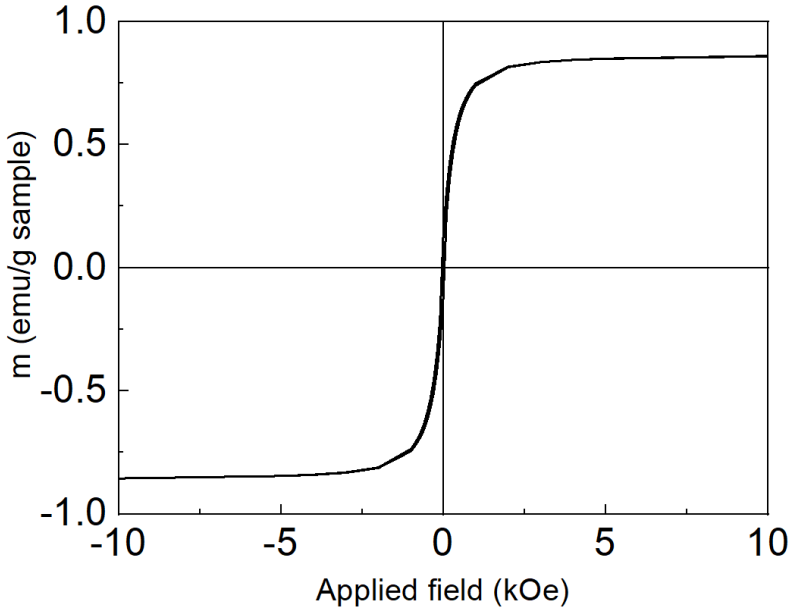

Figure 5.16: Normalized magnetization curve of PLA-NA-NCs.

a) Applications of PLA-NA-NCs

Once the core-shell structure of the PLA nanocapsules and the confinement of the NCs within the oil core were demonstrated, we investigated their properties for their potential use as theranostic nanomaterials.

Initially, the response of PLA-NA-NCs under magnetic stimulation was evaluated while measuring the local temperature. However, despite the application of strong alternating magnetic fields, any heating capability from nanocapsules was observed, most probably due to the relatively low concentration of NCs. Therefore, their use in magnetic hyperthermia was excluded.

The photoresponse of PLA-NA-NCs was studied. Fe_3O_4 nanoparticles are well known to perform as photothermal agents when irradiated in the near-infrared (NIR) region.[37] They can absorb NIR irradiation in the biological window, where tissues are more transparent, allowing the highest light penetration.

Firstly, the heat generation ability of PLA-NA-NCs was studied upon irradiation with a pulsed laser (10 Hz) of 1064 nm, using an average power of 1.86 W (2.9 W/cm^2) and positioning a

thermocouple inside the nanocapsules suspension to measure *in-situ* the light-induced temperature increase, taking care that it was not directly hit by the laser beam. After 30 minutes of irradiation, the sample temperature increased up to 48 °C. It must be considered that this is the average temperature of the water suspension. The local heat produced by the NCs decreases quickly with the distance from the nanocapsules due to thermal equilibrium with the water medium. The sample also suffered a drastic color change from brown to white upon irradiation (Figure 5.17); the reason of this notable modification still needs to be understood. The use of high-power pulsed laser, with a very high peak intensity during the pulse, might have favored the degradation of some of the NCs, reducing their coloration.

A second irradiation experiment was conducted, in collaboration with Aritz Lafuente (MN group), using a continuous wave (CW) laser at 1064 nm, at 400 mW (3.2 W/cm^2). Although the average power density was higher than in the previous experiment, the continuous mode avoids the very high peak intensity output of pulsed laser irradiations. Indeed, the measured power density in the pulsed laser irradiation is an average of power during the laser pulse in the on state (lasting a few ns) and the off state (ms), thus, the real power in the on state is much higher than the average one.

The temperature increase of PLA-NA-NCs suspension was measured over time during the CW laser irradiation using a thermochromic camera (IR camera). In this case, PLA-NA-NCs suspension showed a progressive temperature increase over time until reaching (in 8 minutes) a photo-stationary state at 47 °C (Figure 5.17), with an overall temperature increase of 22 ºC. This NIR radiation is in the second biological window, where partial light absorption from water could occur. However, the heat contribution from the water absorption in the final temperature is much less significant than that of the PLA-NA-NCs, as shown by the only 9 °C increase in a control experiment where the same volume of just water was irradiated in the same conditions (Figure 5.17). The heating conversion efficiency of PLA-NA-NCs guarantees an increase of 13 °C compared to water, which could be considered sufficient for cancer therapeutic purposes.

It is worth to mention that similar results were obtained for NIR irradiation at 808 nm; however, the 1064 nm irradiation would be more relevant in cancer treatment as it has a deeper tissue penetration due to reduced scattering losses.[38,39]

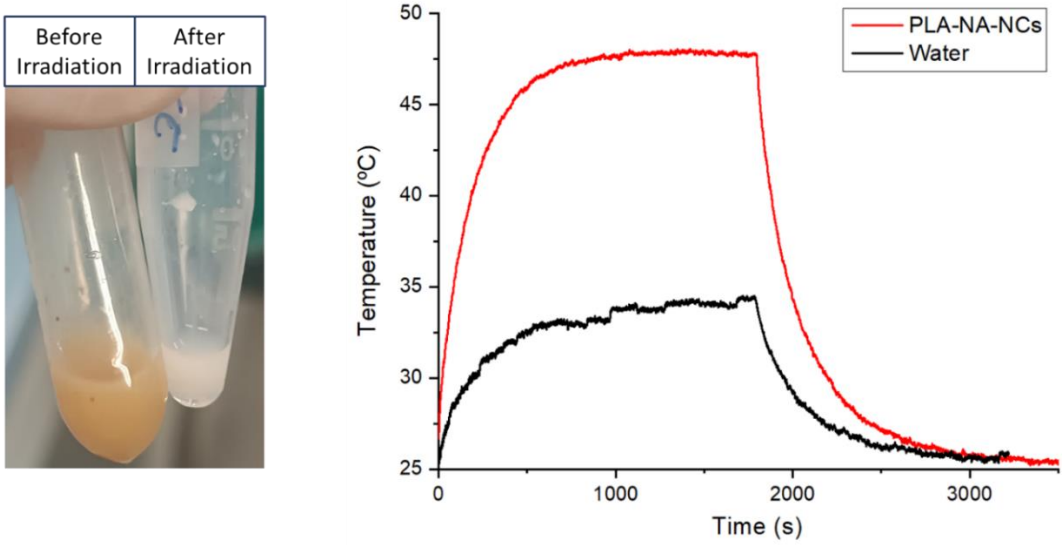

Figure 5.17: Photothermal effect of PLA-NA-NCs. Color change before and after irradiation at 1086 nm at 2.9 W/cm^2 (left side). Temperature increase measured with an IR camera over time of PLA-NA-NCs (red line) and water (black line) irradiated with a 1064 nm laser and 3.2 W/cm^2 of power density (right side).

b) Nano-thermometry

After demonstrating the ability of PLA-NA-NCs to convert light irradiation into heat, their use as local nanothermometers was evaluated. As aforementioned, the real-time monitoring of the temperature increase induced by photothermal agents is crucial to monitor the heat generation ensuring its localization only on the site of interest and avoiding adverse effects in biological regions that do not need to be treated.

A measurement set-up was designed by the MN group, following one of their previous works.[40] The sample is subject to an alternating magnetic field (with ω frequency) while irradiated with a linearly polarized light beam in a region where the NCs absorb (808 nm). The free rotation of NCs strongly modulates the intensity of the transmitted light with the frequency of the magnetic field (opto-magnetic effect). When the NCs are dispersed in a viscous medium (e.g. the oil of the core material of the nanocapsules), they are subjected to a delay of the rotation and thus on the light intensity modulation. From the transmitted light, it is possible to extract the light modulation amplitude and the phase lag (Φ2ω) with respect to the magnetic field. The amplitude and the phase lag depend on the viscosity of the surrounding medium and, when the frequency of the external field increases, more difficulty would result for the NCs to follow it. Thus, by monitoring the phase lag at a given frequency of the external magnetic field it is possible to measure the local viscosity. In this way, the temperature of the medium in which the NCs are dispersed, can be indirectly

determined by knowing the medium viscosity dependence on the temperature.

As the NCs also undergo photothermal heating upon irradiation at 808 nm, with the same light source it is possible to induce and measure the localized temperature increase.

Therefore, a water suspension of PLA-NA-NCs was irradiated at 808 nm, while measuring the phase lag, under an alternating magnetic field. Low irradiation powers were used, as to demonstrate the high sensitivity of the nanocapsules as nanothermometer only a slight temperature increase had to be induced. The temperature increase was also measured by an IR camera for reference comparison. The sample was irradiated at 0.12 W/cm^2 until the temperature reached a photo-stationary state, which was set as t = 0. Then, the laser power was increased to 1.04 W/cm^{2,} and the temperature of PLA-NA-NCs increased, as expected. The temperature decreased once the laser was turned off. Two conclusions could be made from this experiment: on one side, the profiles of temperature variation (both increase and decrease) measured over time with phase lag or IR camera nearly overlapped, with no significant delay (Figure 5.18), validating PLA-NA-NCs as photothermal agent and nanothermometer; on the other, the technique was able to detect slight real-time temperature variations caused by low-power laser irradiations.

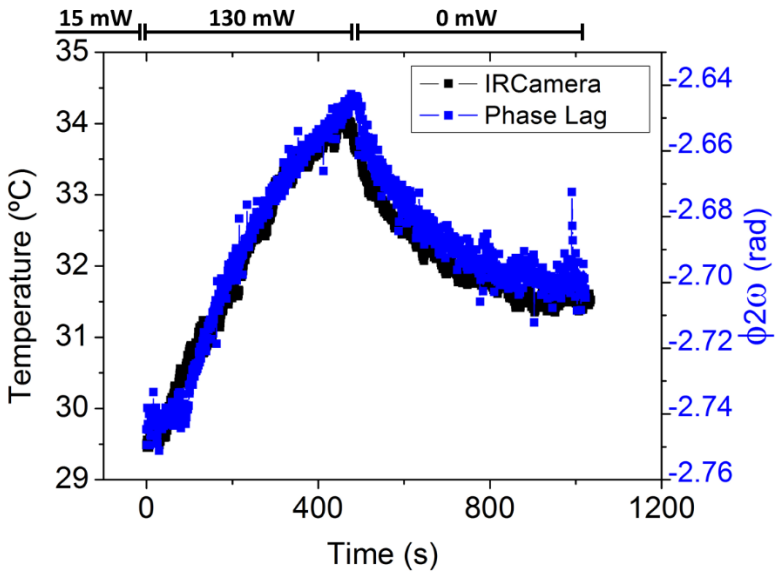

Figure 5.18: Comparison of real-time temperature detection by the phase lag measurement (blue line) and the IR camera (black line) in PLA-NA-NCs sample.

c) *In vitro* internalization

Finally, in collaboration with Aritz Lafuente, a first preliminary study of cells internalization of

PLA-NA-NCs was evaluated by confocal microscopy. The nanocapsules were made fluorescent by co-encapsulating a fluorescent dye, the 9,10-bis(phenylethynyl)anthracene (BPA). To achieve this, a small amount of dye (500 µl at 1 mg/ml) solution in dichloromethane solvent was added to the organic phase before the emulsification process. The dye is expected to remain both in the core and in the shell material of the nanocapsules as it presents similar solubility for the polymer and the oil.

THP-1 (TIB-202), human monocyte cells, were treated with approximately 1 mg/ml of PLA-NA-NCs for 4 h, and then their membrane was stained. By acquiring images at the different focal planes, it was possible to detect a high number of nanocapsules in the extracellular space; however, a considerable amount of blue fluorescent PLA-NA-NCs were also found inside the cells (Figure 5.19). The high quantity of non-internalized nanocapsules can be attributed to the short incubation time (4 h) and the high concentration of nanocapsules used. Treating cells for a longer period at a lower concentration would probably lead to higher internalization. It is important to mention that monocytes tend to uptake the majority of external nanoparticles. However, similar behavior can also be expected for cancer cells, considering the known enhanced permeability and retention (EPR) effect.

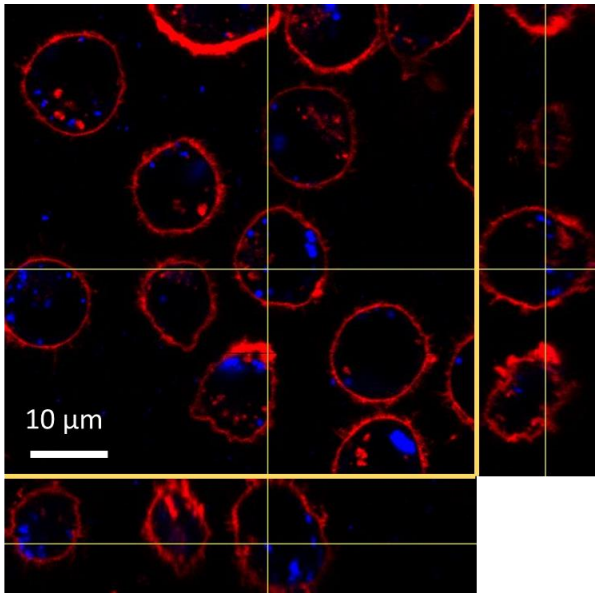

Figure 5.19: A confocal image of THP-1 (TIB-202), human monocyte treated with PLA-NA-NCs (blue spots). The cell membrane was treated with CellMaskTM Deep Red (red circles). Different projections of the same plane are presented on the right and in the bottom.

This cell line was chosen as it can grow in suspension conditions, which would make more accessible the evaluation of the nano-thermometry capability of PLA-NA-NCs. Nevertheless, a

complementary measurement set-up would be needed in order to monitor the temperature increase in adherent cell culture conditions. Since this set-up is being optimized, no further measurements were carried out on cells. Also, further *in vitro* experiments for the evaluation of PLA-NA-NC cytotoxic effect are planned for the near future.

5.6 Summary

In this chapter, bioinspired NCs have been used in two different applications.

On one side, ellipsoidal microparticles, which display morphology like magnetotactic bacteria, can respond to an external magnetic field, both static and alternate. As an anisotropic system, they present a preferential orientation and can rotate if a low-frequency magnetic field is applied. Future works will focus on scaling to nanometer dimensions and demonstrating their rotational effect *in vitro*.

On the other side, it has been possible to obtain well-defined core-shell nanocapsules, with encapsulated magnetic NCs in their core. Moreover, these PLA-NA-NCs can act as an efficient photothermal agent, and NCs seemed able to rotate freely. Moreover, these nanocapsules have shown great potential as nano-thermometry tools. The next work will aim to demonstrate these properties *in vitro*.

5.7 Experimental Section

Materials:

PLA was kindly provided by (68-69 kDa, calculated by a Bruker Daltronics Ultraflextreme MALDI-TOF). All the other products were purchased from Sigma Aldrich. DCM was purchased by Alfa Aesar.

Synthesis of ellipsoidal particles containing magnetic nanocubes (PLA-NCs): Initial spherical particles were obtained by single emulsion/solvent evaporation method. Between 200 and 600 µl of NCs suspension in chloroform were added to PLA dissolution in DCM (250 mg in 5 ml). The organic phase was added to a 15 ml aqueous solution of PVA (1% w/w) and homogenized using a T18 Ultra-Turrax® IKA at 7000 rpm for 10 minutes at room temperature. The solvent was evaporated using a rotary evaporator, at 40 °C for 20 minute. To make nanocapsules fluorescent 500 µl of a BPA solution in DCM (1 mg/ml) were added to the organic phase. 3-4 ml of the resulting particles were homogeneously mixed with 6 g of PVA water solution (20% w/w). This solution was

then casted in a Petri plate of 12 cm of diameter. After water evaporation, conducted at 35 °C overnight, it was possible to obtain a film with particles embedded in it, which was consequently cut into 3 rectangular strips. Each of them was mounted to the two clamps of a custom-made apparatus. After its immersion in a silicon oil bath, preheated between 90-100 °C, the film stretching was performed. The film was let to cool down at room temperature, cleaned with isopropanol to remove any residual oil, and then cut in the center, recollecting only the section that had doubled its length. The cut sections were dissolved in deionized water, and ellipsoidal particles were recollected by three centrifugations at 10000 rpm for 10 minutes.

Synthesis of PLA nanocapsules containing magnetic nanocubes (PLA-NA-NCs): Nanocapsules were obtained by single emulsion/solvent-evaporation method. Briefly, 250 mg of PLA and 500 mg of NCs dispersed in NA were dissolved in 5 ml DCM through magnetic stirring. This organic phase was added to 15 ml of 1% w/w of PVA water solution and left to agitate for 20 minutes at room temperature to form an oil-in-water (O/W) pre-emulsion. The pre-emulsion was ultrasonicated with a Branson Ultrasonic Sonifier for 2 minutes at 70% of amplitude (with sonication impulses on/off of 30/10 seconds). The organic solvent was evaporated using a rotary evaporator, at 40 °C for 20 minutes. The obtained particles were left at 4 °C for 30 minutes, and the liquid particles suspension was separated from the solidified NA. To make nanocapsules fluorescent 500 µl of a BPA solution in DCM (1 mg/ml) were added to the organic phase. Moreover, capsules without NCs (PLA-NA) were synthesized as control by following the same procedure described but replacing the NCs suspension with pure NA.

Characterization techniques:

Dynamic Light Scattering (DLS): Hydrodynamic diameter of PLA-NA-NCs was determined by dynamic light scattering using a Zetasizer Nano 3600 instrument (Malvern Instruments, UK) after dilution (1:10 or 1:100) in water.

Scanning electron microscopy (SEM): The morphology and size of PLA-NA-NCs, and PLA-NCs were evaluated by SEM using a Quanta 650 FEG. Samples were diluted in water, and few drops were placed over an aluminum tape, and water was let evaporated at room temperature. Before analysis, samples were coated with 5 nm of platinum under an argon atmosphere using a Leica EM ACE600 sputter coater. SEM pictures were acquired at accelerating voltages between 2 and 20 kV under a high-vacuum mode and a distance of the sample of 5 mm.

Transmission electron microscopy (TEM): PLA-NA-NCs and PLA-NCs morphology, size, and NCs localization were studied by TEM. Samples were prepared by depositing few drops on a carbon

copper grid after dilution in water. After water evaporation, samples were analyzed using a JOEL JEM-1400 microscope applying a voltage of 120 kV under high vacuum.

Scanning Transmission Electron Microscopy (STEM): STEM images of PLA-NA-NCs and PLA-NCs were acquired using a Magellan 400L from FEI operated at 20 kV and 100 pA. The samples were prepared as in the case of TEM.

Fluorescence microscope: Fluorescence microscopy images of PLA-NCs in suspension or embedded in a PVA film were acquired by a Axio Observer Z-1m (Zeiss) inverted optical/fluorescence microscope equipped with a motorize XY stage, a halogen lamp (Philips 7724) for transmission and reflection mode, a Hg lamp source (HBO 103/2 of 100W) for fluorescence images, and an AxioCam HRc digital camera. A DAPI filter was used for fluorescence images acquisition (Exitaion: BP 365/12, Emission: LP 397).

Absorption spectra: The absorption spectrum of NCs suspension in chloroform was acquired by a Cary 60 spectrophotometer in transmittance mode using a pair of quartz cuvettes (1 cm optical path) and using chloroform as blank.

Differential Scanning Calorimetry (DSC). Calorimetric measurements were performed using a DSC equipment (Perkin Elmer DSC8500 LAB SYS). Approximately 2-4 mg of freeze-dried PLA-NA-NCs were deposited on a 0.5 cm aluminum pam, while an equivalent empty pan was used as reference. The scanning rate used was 10 °C/min, both for the cooling and heating process, and the temperature ranged from -17 °C to 80 °C.

Proton nuclear magnetic resonance (^{1}H-NMR): ^{1}H-NMR spectra of PLA, NA, and PLA-NA were recorded using a Bruker Avance DPX of 250 MHz and a Bruker Ascend of 300 MHz. Generally, around 20-30 mg of samples were dissolved in $CDCl_3$, and 30 µl of DMF were added as internal reference. Spectra are given in chemical shifts (δ (ppm)). The amount of NA was quantified using the following equation.

$$\frac{\int DMF}{mmol_{DMF}} = \frac{\int NA}{mmol_{NA}}$$

NA payload was calculated as:

$$\frac{mg_{encapsulated\ NA}}{mg_{PLA-NA-NCs}}\ x\ 100$$

Inductively Coupled Plasma Optical Emission Spectroscopy (ICP-OES): The amount of encapsulated NCs in PLA-NA-NCs was calculated by quantifying the iron presence. The equipment used was a Plasma Emission Spectrometer ICP Perkin Elmer mod. OPTIMA 2100 DV, and samples were digested with nitric acid and hydrochloric acid.

The encapsulation efficiency of NCs was calculated by the following equation:

$$EE(\%) = \frac{Weight\ of\ NCs\ in\ PLA-NA-NCs}{Weight\ of\ initial\ NCs}$$

Magnetization measurement: The magnetic response and the saturation magnetization of PLA-NA-NCs were studied by using a Vibrating Sample SQUID Magnetometer Quantum Design MPMSR3. For sample preparation, a small amount of freeze-dried powder was deposited inside a gelatin capsule. Magnetization curve was obtained, showing the magnetic behavior of the particles as function of the magnetic field applied.

Near-Infrared (NIR) response: Pure water or diluted sample of PLA-NA-NCs were irradiated with pulsate NIR laser at 1064 (2.9 3.2 W/cm^2) or with a continuous NIR laser at 1064 nm or 808 nm, (3.2 W/cm^2) for different periods of time. Temperature was monitored by a thermocouple for pulsating irradiation or with an infrared camera for continuous stimulation.

Nano-thermometry measurements: A custom-made setup was constituted by a polarized NIR laser diode at 808 nm, an optical collimating and aligning system, a Helmholtz coil (3 cm diameter), a signal generator (SDG1025, Siglent) and a modulated power supply (TS200, ACCEL Instruments), a Si photodiode (PDA36A-EC, THORlabs), an infrared camera, and data acquisition card (National Instruments). For the analysis, PLA-NA-NCs diluted in water were irradiated with NIR laser, which was linearly polarized, and the temperature solution was continuously monitored by infrared camera and the photodiode. A sinusoidal magnetic induction, with frequency of 133 Hz and strength of 2.7 mT was used. The transmitted light intensity was acquired and then processed via FFT analysis in a Labview program, and the amplitude and phase were extracted.

Cell internalization. THP-1 cells were cultured in RPMI 1640 medium supplemented with 10% FBS. 150 µg of fluorescent PLA-NA-NCs were added to 10^5 cells and incubated for 4 h. Cells were subsequently stained with CellMaskTM Deep Red (ThermoFisher) and observed in a confocal microscope (Leica DCM 3D).

5.8 References

1. Li, X., Li, W., Wang, M. & Liao, Z. Magnetic nanoparticles for cancer theranostics: Advances and prospects. *J. Controlled Release* **335**, 437–448 (2021).
2. Socoliuc, V. *et al.* Magnetic Nanoparticle Systems for Nanomedicine—A Materials Science Perspective. *Magnetochemistry* **6**, 2 (2020).
3. Ryu, C. *et al.* Highly Optimized Iron Oxide Embedded Poly(Lactic Acid) Nanocomposites for Effective Magnetic Hyperthermia and Biosecurity. *Int. J. Nanomedicine* **Volume 17**, 31–44 (2022).
4. Pich, A., Bhattacharya, S., Ghosh, A. & Adler, H.-J. P. Composite magnetic particles: 2.

Encapsulation of iron oxide by surfactant-free emulsion polymerization. *Polymer* **46**, 4596–4603 (2005).
5. Shapiro, E. M. Biodegradable, polymer encapsulated, metal oxide particles for MRI-based cell tracking: Polymer Particles for MRI. *Magn. Reson. Med.* **73**, 376–389 (2015).
6. Shen, B. B., Gao, X. C., Yu, S. Y., Ma, Y. & Ji, C. H. Fabrication and potential application of a di-functional magnetic system: magnetic hyperthermia therapy and drug delivery. *CrystEngComm* **18**, 1133–1138 (2016).
7. Ronco, L. I. *et al.* Incorporation of Magnetic Nanoparticles in Poly(Methyl Methacrylate) Nanocapsules. *Macromol. Chem. Phys.* **219**, 1700424 (2018).
8. Hong, R. Y. *et al.* Double-miniemulsion preparation of Fe_3O_4 /poly(methyl methacrylate) magnetic latex. *J. Appl. Polym. Sci.* **112**, 89–98 (2009).
9. Feuser, P. E. *et al.* Simultaneous encapsulation of magnetic nanoparticles and zinc phthalocyanine in poly(methyl methacrylate) nanoparticles by miniemulsion polymerization and in vitro studies. *Colloids Surf. B Biointerfaces* **135**, 357–364 (2015).
10. Resende, G. *et al.* Well Defined Poly(Methyl Methacrylate)-Fe3O4/Poly(Vinyl Pivalate) Core–Shell Superparamagnetic Nanoparticles: Design and Evaluation of In Vitro Cytotoxicity Activity Against Cancer Cells. *Polymers* **12**, 2868 (2020).
11. Natour, S., Levi-Zada, A. & Abu-Reziq, R. Magnetic Polyurea Nano-Capsules Synthesized via Interfacial Polymerization in Inverse Nano-Emulsion. *Molecules* **24**, 2663 (2019).
12. Landfester, K. & Ram rez, L. P. Encapsulated magnetite particles for biomedical application. *J. Phys. Condens. Matter* **15**, S1345–S1361 (2003).
13. Mosafer, J., Abnous, K., Tafaghodi, M., Jafarzadeh, H. & Ramezani, M. Preparation and characterization of uniform-sized PLGA nanospheres encapsulated with oleic acid-coated magnetic-Fe 3 O 4 nanoparticles for simultaneous diagnostic and therapeutic applications. *Colloids Surf. Physicochem. Eng. Asp.* **514**, 146–154 (2017).
14. Lee, S.-J. *et al.* Functionalized Magnetic PLGA Nanospheres for Targeting and Bioimaging of Breast Cancer. *J. Nanosci. Nanotechnol.* **18**, 1542–1547 (2018).
15. Cui, Y. *et al.* Dual-Targeting Magnetic PLGA Nanoparticles for Codelivery of Paclitaxel and Curcumin for Brain Tumor Therapy. *ACS Appl. Mater. Interfaces* **8**, 32159–32169 (2016).
16. Kumar, R. *et al.* Core–shell nanostructures: perspectives towards drug delivery applications. *J. Mater. Chem. B* **8**, 8992–9027 (2020).
17. Otaegui, J. R., Rubirola, P., Ruiz-Molina, D., Hernando, J. & Roscini, C. Solid Materials with Near-Infrared-Induced Fluorescence Modulation. *Adv. Opt. Mater.* **8**, 2001063 (2020).
18. Tierno, P. Recent advances in anisotropic magnetic colloids: realization, assembly and applications. *Phys Chem Chem Phys* **16**, 23515–23528 (2014).
19. Tierno, P., Albalat, R. & Sagués, F. Autonomously Moving Catalytic Microellipsoids Dynamically Guided by External Magnetic Fields. *Small* **6**, 1749–1752 (2010).
20. Kim, H. & Furst, E. M. Magnetic properties, responsiveness, and stability of paramagnetic dumbbell and ellipsoid colloids. *J. Colloid Interface Sci.* **566**, 419–426 (2020).
21. Vargas, G. *et al.* Applications of Magnetotactic Bacteria, Magnetosomes and Magnetosome Crystals in Biotechnology and Nanotechnology: Mini-Review. *Molecules* **23**, 2438 (2018).
22. Revia, R. A. & Zhang, M. Magnetite nanoparticles for cancer diagnosis, treatment, and treatment monitoring: recent advances. *Mater. Today* **19**, 157–168 (2016).

23. Muro-Cruces, J. *et al.* Precise Size Control of the Growth of Fe_3O_4 Nanocubes over a Wide Size Range Using a Rationally Designed One-Pot Synthesis. *ACS Nano* **13**, 7716–7728 (2019).
24. Sharma, V. K., Alipour, A., Soran-Erdem, Z., Aykut, Z. G. & Demir, H. V. Highly monodisperse low-magnetization magnetite nanocubes as simultaneous $T_1 - T_2$ MRI contrast agents. *Nanoscale* **7**, 10519–10526 (2015).
25. Liang, X. *et al.* Synthesis of Nearly Monodisperse Iron Oxide and Oxyhydroxide Nanocrystals. *Adv. Funct. Mater.* **16**, 1805–1813 (2006).
26. Julià-López, A., Ruiz-Molina, D., Hernando, J. & Roscini, C. Solid Materials with Tunable Reverse Photochromism. *ACS Appl. Mater. Interfaces* **11**, 11884–11892 (2019).
27. Li, G. *et al.* Synthesis and Biological Application of Polylactic Acid. *Molecules* **25**, 5023 (2020).
28. Nguyen, A. *et al.* Nanoparticles loaded with ferrocenyl tamoxifen derivatives for breast cancer treatment. *Int. J. Pharm.* **347**, 128–135 (2008).
29. Mett, J. & Müller, U. The medium-chain fatty acid decanoic acid reduces oxidative stress levels in neuroblastoma cells. *Sci. Rep.* **11**, 6135 (2021).
30. Lappano, R. *et al.* The lauric acid-activated signaling prompts apoptosis in cancer cells. *Cell Death Discov.* **3**, 17063 (2017).
31. Chuensangjun, C., Pechyen, C. & Sirisansaneeyakul, S. Degradation Behaviors of Different Blends of Polylactic Acid Buried in Soil. *Energy Procedia* **34**, 73–82 (2013).
32. Middleton, J. C. & Tipton, A. J. Synthetic biodegradable polymers as orthopedic devices. *Biomaterials* **21**, 2335–2346 (2000).
33. Wang, Z., Sun, J., Xie, S., Ma, G. & Jia, Y. Thermal Properties and Reliability of a Lauric Acid/Nonanoic Acid Binary Mixture as a Phase-Change Material for Thermal Energy Storage. *Energy Technol.* **5**, 2309–2316 (2017).
34. Wang, Z. *et al.* A novel binary mixture of caprylic acid/nonanoic acid as latent heat storage for air conditioning and cooling. *Energy Build.* **145**, 259–266 (2017).
35. Thi N'Goc, H. L. *et al.* Surface-Driven Magnetotransport in Perovskite Nanocrystals. *Adv. Mater.* **29**, 1604745 (2017).
36. Zhang, T., Wang, X. P., Fang, Q. F. & Li, X. G. Magnetic and charge ordering in nanosized manganites. *Appl. Phys. Rev.* **1**, 031302 (2014).
37. Lu, A.-H. *et al.* Precise synthesis of discrete and dispersible carbon-protected magnetic nanoparticles for efficient magnetic resonance imaging and photothermal therapy. *Nano Res.* **9**, 1460–1469 (2016).
38. Cabana, S., Curcio, A., Michel, A., Wilhelm, C. & Abou-Hassan, A. Iron Oxide Mediated Photothermal Therapy in the Second Biological Window: A Comparative Study between Magnetite/Maghemite Nanospheres and Nanoflowers. *Nanomaterials* **10**, 1548 (2020).
39. Hemmer, E., Benayas, A., Légaré, F. & Vetrone, F. Exploiting the biological windows: current perspectives on fluorescent bioprobes emitting above 1000 nm. *Nanoscale Horiz.* **1**, 168–184 (2016).
40. Li, Z. *et al.* Simultaneous Local Heating/Thermometry Based on Plasmonic Magnetochromic Nanoheaters. *Small* **14**, 1800868 (2018).

Chapter 6

6. General Conclusions

In the present thesis, we demonstrated that bioinspiration or biomimicry could represent a promising strategy for developing powerful tools for different biomedical applications. Three different structured materials were studied in this work.

1) Bacteria-like particles were prepared. The inherent characteristics of *Pseudomonas aeruginosa*, such as size, shape, and immunogenic properties, were translated into synthetic particles. Ellipsoidal polymeric particles were obtained by the mechanical stretching of spherical ones, and their surfaces were functionalized with specific antigens. We demonstrated that the shape had a role as an immune stimulator, inducing a much higher response.
2) Neuromelanin-like nanoparticles, made by supramolecular interaction of iron-dopamine complexes, or by nanostructuration of coordination polymer, possess an outstanding content of dopamine, being able to deliver it after intranasal administration.
3) Magnetic nanocubes, bioinspired by natural magnetosomes crystals, were encapsulated in core-shell polymeric particles and confined in the liquid core. The rotation of nanocubes was guaranteed and helpful for real-time thermal measurements, while nanocapsules were able to act as heat nanogenerators. Biomimetic ellipsoidal particles containing magnetic nanocubes, recalling the magnetotactic bacteria features, could align or rotate following an external magnetic field, demonstrating both shape and magnetic anisotropy.

Encouraging results were achieved for all the studied systems, offering promising approaches for several pressing biomedical issues, such as vaccine development, Parkinson's disease therapy, and cancer treatment. Nevertheless, considering the complexity of biological systems, further work and research will be needed before achieving clinical translation.